

Real-Time State Estimation and Voltage Stability Assessment of Power Grids: From Theoretical Foundations to Practical Applications

Thèse N° 9464

Présentée le 21 juin 2019

à la Faculté des sciences et techniques de l'ingénieur
Laboratoire des systèmes électriques distribués
Programme doctoral en énergie

pour l'obtention du grade de Docteur ès Sciences

par

Andreas Martin KETTNER

Acceptée sur proposition du jury

Dr S.-R. Cherkaoui, président du jury
Prof. M. Paolone, directeur de thèse
Prof. T. Van Cutsem, rapporteur
Dr C. Y. Evrenosoglu, rapporteur
Prof. J.-Y. Le Boudec, rapporteur

2019

To my parents, Dora and Claus, and my brother, Stefan.



I firmly believe that most people have a longing to do something for their fellow men,
in order that it may be said, when they have passed on,
that their lives have not been spent in vain.

— William “Bill” Kettner

Acknowledgements

This thesis has been made possible thanks to the support of many people, whom I hereby want to acknowledge and thank.

I am deeply grateful to my supervisor, Prof. Mario Paolone, whose expertise and mentorship have helped me to grow both as a researcher and as a person. Moreover, I am much obliged to Dr. Rachid Cherkaoui, Prof. Farhad Rachidi, and Prof. Jean-Yves Le Boudec, who have fostered the inspiring research environment in which I have had the pleasure to work.

I thank all my friends and colleagues for the great time we have had inside and outside of work: Sadegh Azizi, Juan Becerra Tobar and Yury Estepa Avellaneda, Fabrizio Cortesi, Sophie Flynn, Sherif Fahmy, Guglielmo Frigo, Rahul Gupta, Christoph Kammer and Johanna Nowotny, Ueli Koch, Berenika Koźbiał, Michael Meier, Emil Namor and Sara Braidotti, Marco Pignati, Thomas Pidancier and Noémie Beaupain, Lorenzo Reyes Chamorro and Dayana Gómez Alvear, Christian Saner, Enrica Scolari, Oliver Vogler, Thomas Willi and Ursula Krug, Ji-Hyun Yi, and anyone I forgot to mention. I look forward to many more adventures with you.

My heartfelt gratitude goes to my parents, Dora and Claus Kettner, and my brother, Stefan, who have always supported me unconditionally. Finally, I commemorate my grandparents, Hildegard and Egon Kettner, as well as my grandaunts, Berta, Emma, and Frieda Schlatter, who sparked my interest in the workings of our world.

Sünikon, 15 May 2019

Andreas Kettner

Abstract

The operators of power distribution systems strive to lower their operational costs and improve the quality of the power service provided to their customers. Furthermore, they are faced with the challenge of accommodating large numbers of *Distributed Energy Resources* (DERs) into their grids. It is expected that these problems will be tackled with a large-scale deployment of automation technology, which will enable the real-time monitoring and control of power distribution systems (i.e., similar to power transmission systems). For this purpose, real-time situation awareness w.r.t. the state and the stability of the system is needed. In view of the deployment of such automation functions into power distribution grids, there are two binding requirements. Firstly, the system models have to account for the inherent unbalances of power distribution systems (i.e., w.r.t. the components of the grid and the loads). Secondly, the analysis methods have to be real-time capable when deployed into low-cost embedded systems platforms, which are the cornerstones of automation. In other words, the analysis methods need to be computationally efficient.

This thesis focuses on the modeling of unbalanced polyphase power systems, as well as the development, validation, and deployment of real-time methods for *State Estimation* (SE) and *Voltage Stability Assessment* (VSA) for such systems. More precisely, the following theoretical and practical contributions are made to the field of power system engineering.

1. Fundamental properties of the compound admittance matrix of polyphase power grids are identified. Specifically, theorems w.r.t. the rank of the compound admittance matrix, the feasibility of *Kron Reduction* (KR), and the existence of compound hybrid matrices are stated and formally proven. These theorems hold for generic polyphase power grids (i.e., which may be unbalanced, and have an arbitrary number of phases).
2. A *Voltage Stability Index* (VSI) for real-time VSA of polyphase power systems is proposed. The proposed VSI is a generalization of the well-known *L*-index, which is achieved by integrating more generic models of the power system components. More precisely, the grid is represented by a compound hybrid matrix, slack nodes by Thévenin equivalents, and resource nodes by polynomial load models. In this regard, the theorems mentioned under item 1 substantiate the applicability of the proposed VSI.

-
3. A *Field-Programmable Gate Array* (FPGA) implementation for real-time SE of polyphase power systems is presented. This state estimator is based on a *Sequential Kalman Filter* (SKF), which – in contrast to the standard *Kalman Filter* (KF) – is suitable for implementation in such dedicated hardware. In this respect, it is formally proven that the SKF and the standard KF are equivalent if the measurement noise variables are uncorrelated. To achieve high computational performance, the grid model is reduced through KR, and the SKF calculations on the FPGA are parallelized and pipelined.
 4. The methods stated under items 1–3 are deployed into an industrial real-time controller, which is used to control a real-scale microgrid. This microgrid is equipped with a metering system composed of *Phasor Measurement Units* (PMUs) coupled with a *Phasor Data Concentrator* (PDC). The real-time capability of the developed methods is validated experimentally by measuring the latencies of the PDC-SE-VSA processing chain w.r.t. the PMU timestamps.

Keywords: power distribution systems, automation, active distribution networks, microgrids, polyphase power systems, unbalanced power grids, compound admittance matrix, compound hybrid matrix, Kron reduction, state estimation, sequential Kalman filter, phasor measurement units, voltage stability assessment, voltage stability index, L -index, Thévenin equivalent, polynomial load model, embedded systems, field-programmable gate arrays, COMMELEC.

Zusammenfassung

Verteilnetzbetreiber sind bestrebt, ihre Betriebskosten zu senken und die Qualität der Dienstleistungen für ihre Kunden zu verbessern. Ausserdem sehen sie sich gegenwärtig mit dem Problem konfrontiert, eine grosse Zahl *verteilter Energieanlagen* (*Distributed Energy Resources*, DERs) ins Netz zu integrieren. Um dieser Probleme Herr zu werden, werden die Betreiber voraussichtlich die Automatisierung der Verteilnetze in Angriff nehmen, um diese dann in Echtzeit überwachen und regeln zu können (d.h., ähnlich wie dies bei Übertragungsnetzen bereits der Fall ist). Die Grundvoraussetzungen hierfür sind die Erfassung des Zustandes und der Stabilität des Stromnetzes in Echtzeit. Im Hinblick auf den Einsatz in Verteilnetzen gilt es hierbei, die folgenden Anforderungen zu erfüllen. Erstens müssen die Systemmodelle den Asymmetrien elektrischer Verteilnetze (d.h., des Netzes und der Lasten) Rechnung tragen. Zweitens müssen die Analyseverfahren den Echtzeitanforderungen eingebetteter Systeme genügen, da diese das technische Rückgrat der Automatisierung bilden. Dies verlangt nach Recheneffizienz.

Die vorliegende Doktorarbeit befasst sich mit der Modellierung asymmetrischer Mehrphasensysteme, sowie mit der Entwicklung, Validierung, und dem Einsatz von Echtzeitmethoden zur *Zustandsbeobachtung* (*State Estimation*, SE) und *Spannungsstabilitätsanalyse* (*Voltage Stability Assessment*, VSA) solcher Systeme. In diesem Zusammenhang leistet diese Arbeit die folgenden Beiträge auf dem Gebiet der elektrischen Energietechnik:

1. Grundlegende Eigenschaften der Verbundmittanzmatrix von Mehrphasensystemen werden identifiziert. Genauer gesagt, es werden Lehrsätze aufgestellt und bewiesen, welche sich mit dem Rang der Verbundmittanzmatrix, der Durchführbarkeit der *Kron-schen Reduktion* (*Kron Reduction*, KR), und der Existenz von Verbundhybridmatrizen beschäftigen. Die besagten Lehrsätze sind für allgemeine Mehrphasensysteme gültig (d.h., asymmetrisch und mit einer beliebigen Anzahl Phasen).
2. Ein Spannungsstabilitätsindex (*Voltage Stability Index*, VSI), welcher die Analyse von Mehrphasensystemen in Echtzeit ermöglicht, wird vorgestellt. Der besagte VSI ist eine Verallgemeinerung des bekannten *L-Index*, welche allgemeinere Modelle der Systembestandteile verwendet. Genauer gesagt wird das Netz durch eine Verbundhybridmatrix, Bilanzknoten durch Théveninsche Äquivalente, und Generator- sowie Lastschienen durch polynomielle Modelle dargestellt. Hierbei werden die unter Punkt 1 aufgeführten Lehrsätze hinzugezogen, um die Anwendbarkeit des VSI zu untermauern.

-
3. Ein auf einer anwenderprogrammierbaren logischen Schaltung (*Field-Programmable Gate Array*, FPGA) basierender, echtzeitfähiger Zustandsbeobachter für Mehrphasensysteme wird vorgestellt. Dieser Zustandsbeobachter fusst auf einem *sequentiellen Kalmanschen Filter* (*Sequential Kalman Filter*, SKF), welches sich – im Gegensatz zum herkömmlichen *Kalmanschen Filter* (*Kalman Filter*, KF) – für derlei Geräte eignet. Hierfür wird ein weiterer Lehrsatz aufgestellt und bewiesen, welcher für unkorreliertes Messrauschen die Äquivalenz der besagten Filter garantiert. Um hohe Rechenleistung zu erreichen, wird das Netzmodell durch KR reduziert, und der Durchsatz des SKF mittels Parallelisierung und Pipelining auf dem FPGA optimiert.
 4. Die unter Punkt 1–3 erwähnten Verfahren werden in einen Echtzeitregler integriert und in einem realen Inselnetz getestet. Dieses Inselnetz ist mit einem Messsystem ausgerüstet, welches sich aus *Phasormesseinheiten* (*Phasor Measurement Units*, PMUs) und einem *Phasordatenkonzentrator* (*Phasor Data Concentrator*, PDC) zusammensetzt. Die Echtzeitfähigkeit der entwickelten Verfahren wird experimentell nachgewiesen, nämlich durch Messung der Latenzzeiten der PDC-SE-VSA-Verarbeitungskette im Bezug auf die Zeitmarken der PMUs.

Stichwörter: Stromverteilnetze, Automatisierung, Inselnetze, Mehrphasensysteme, Phasenasymmetrie, Verbundadmittanzmatrix, Verbundhybridmatrix, Kronsche Reduktion, Zustandsbeobachtung, sequentielles Kalmansches Filter, Phasormesseinheiten, Spannungsstabilitätsanalyse, Spannungsstabilitätsindex, *L*-Index, Théveninsches Äquivalent, polynomielles Lastmodell, eingebettete Systeme, programmierbare logische Schaltungen, COMMELEC.

Résumé

Les gestionnaires des réseaux de distribution d'électricité s'efforcent de réduire les coûts d'exploitation et d'améliorer la qualité de service à la clientèle. En plus, l'intégration d'un grand nombre de ressources énergétiques distribuées (*Distributed Energy Resources*, DERs) dans les réseaux de distribution pose un grand défi. Ce problème peut être maîtrisé avec des technologies d'automation, qui permettront la surveillance et le pilotage des réseaux de distribution en temps réel (c.-à-d., avec une approche similaire à celle utilisée dans les réseaux de transport). Cela requiert la connaissance situationnelle quant à l'état et à la stabilité du système. Des outils d'automation pour des réseaux de distribution doivent répondre aux critères suivants. Premièrement, les modèles de systèmes doivent prendre en compte les déséquilibres qui existent dans les réseaux de distributions (c.-à-d., déséquilibres du réseau et des charges). Deuxièmement, les méthodes d'analyse doivent être capable d'être exécutées en temps réel dans des systèmes embarqués, qui constituent l'épine dorsale de l'automation. Par conséquence, les méthodes d'analyse doivent être computationnellement efficaces.

Cette thèse traite la modélisation de systèmes électriques polyphasés déséquilibrés, ainsi que le développement, la validation, et la mise en service de méthodes pour l'observation de l'état (*State Estimation*, SE) et l'analyse de la stabilité de tension (*Voltage Stability Assessment*, VSA) de ce genre de systèmes électriques. Plus précisément, les contributions théoriques et pratiques de la thèse sont les suivantes :

1. Des attributs fondamentaux de la matrice d'admittance composite de systèmes électriques polyphasés sont identifiés. Plus précisément, des théorèmes concernant le rang de la matrice d'admittance composite, la faisabilité de la réduction de Kron, et l'existence des matrices hybrides composites sont formulés et démontrés. Ces théorèmes sont valides pour des réseaux polyphasés généraux (c.-à-d., déséquilibrés et avec un nombre quelconque de phases).
2. Un indice de stabilité de tension (*Voltage Stability Index*, VSI) pour des systèmes électriques polyphasés est proposé. Ce VSI est une généralisation du L -indice, qui employes des modèles plus génériques des composants du réseau. Plus précisément, le réseau est décrit par une matrice hybride composite, les noeuds pivots par des équivalents de Thévenin, et les noeuds de ressources par des modèles polynomiales. Les théorèmes mentionnés dans le point 1 sont utilisés pour certifier l'applicabilité du VSI.

-
3. Une implementation en temps réel d'un observateur d'état dans un réseau de portes programmables à la demande (*Field-Programmable Gate Array*, FPGA) est présentée. Cet observateur d'état est basé sur un filtre de Kalman séquentiel (*Sequential Kalman Filter*, SKF), qui est approprié pour ce genre de dispositifs – contrairement au filtre de Kalman (*Kalman Filter*, KF) standard. Dans ce contexte, il est démontré que ces filtres sont équivalents au cas où les variables aléatoires qui représentent le bruit soient décorrélées. Afin d'atteindre de bonne performance, le modèle de réseau est réduit via la méthode KR, et les calculs pour le SKF sont parallélisés et expédiés par pipeline.
 4. Les méthodes listées dans les points 1–3 sont mises en service dans un contrôleur industriel, qui gère en temps réel un microréseau à l'échelle réelle. Ce microréseau est équipé avec un système de mesure qui se compose d'unités de mesure de phaseurs (*Phasor Measurement Units*, PMUs) et d'un concentrateur de données de phaseurs (*Phasor Data Concentrator*, PDC). Le fonctionnement en temps réel de ces méthodes est validée expérimentalement en mesurant les latences de la chaîne de calcul PDC-SE-VSA par rapport aux chronotimbres issues des PMUs.

Mots clefs : systèmes de distribution d'électricité, automation, microréseaux, systèmes électriques polyphasés, réseaux électriques déséquilibrés, matrice d'admittance composite, matrice hybride composite, réduction de Kron, observation d'état, filtre de Kalman séquentiel, unités de mesure de phaseurs, analyse de stabilité de tension, indice de stabilité de tension, L -indice, équivalent de Thévenin, modèles polynomiales, systèmes embarqués, réseaux de portes programmables à la demande, COMMELEC.

Contents

Acknowledgements	vii
Abstract (English/Deutsch/Français)	ix
List of Figures	xvii
List of Tables	xxi
1 Introduction	1
1.1 Motivation	1
1.2 Contributions	3
1.3 Document Outline	5
2 Review of the State of the Art	7
2.1 Circuit Analysis of Power Systems	7
2.1.1 Equivalent Circuits of Polyphase Power Systems	7
2.1.2 Kron Reduction of Electrical Circuits	10
2.1.3 Hybrid Matrices of Electrical Circuits	10
2.2 State Estimation of Power Systems	12
2.2.1 Static Approaches	12
2.2.2 Quasi-Static Approaches	13
2.3 Voltage Stability Assessment of Power Systems	14
2.3.1 Continuation Power Flow	14
2.3.2 Maximum Loadability	15
2.3.3 Maximum Power Transfer	15
2.3.4 Formal Analysis of the Solvability of the Power-Flow Equations	16
2.4 Contributions of this Thesis	17
3 Analysis of Equivalent Circuits of Polyphase Power Grids	19
3.1 Modeling of Polyphase Power Grids	20
3.1.1 Hypotheses with Respect to the Electrical Components of the Grid	20
3.1.2 Mathematical Description of the Equivalent Circuit of the Grid	21
3.1.3 Hypotheses with Respect to the Equivalent Circuit of the Grid	25
3.1.4 Construction of the Compound Admittance Matrix	26
3.2 On the Rank Properties of the Compound Admittance Matrix	29

Contents

3.2.1	The Rank of the Overall Matrix	29
3.2.2	The Rank of the Diagonal Blocks	32
3.3	On the Feasibility of Kron Reduction	35
3.3.1	Reduction of a Single Set of Zero-Injection Nodes	35
3.3.2	Sequential Reduction of Multiple Sets of Zero-Injection Nodes	37
3.4	On the Existence of Compound Hybrid Matrices	38
3.4.1	The Case of Unreduced Grid Models	38
3.4.2	The Case of (Partially) Reduced Grid Models	39
4	Real-Time Estimation of the Grid State by a Sequential Kalman Filter	41
4.1	Formulation of the Measurement Model	43
4.1.1	Structure of the Measurement Model	43
4.1.2	Hypotheses with Respect to the Measurement Noise	44
4.1.3	The Necessary Condition for Observability	45
4.2	Formulation of the Process Model	46
4.2.1	Structure of the Process Model	46
4.2.2	Hypotheses with Respect to the Process Noise	46
4.3	Estimation of the System State using Kalman Filters	48
4.3.1	Recall of the Standard Kalman Filter	48
4.3.2	The Sequential Kalman Filter	53
4.4	Equivalence of the Considered Kalman Filters	55
4.4.1	Estimation Error Covariance Matrix	55
4.4.2	Estimated State Vector	56
4.5	Computational Complexity of the Considered Kalman Filters	58
4.5.1	Performance Limitations due to Matrix Inversions	58
4.5.2	Assumption of Uncorrelated Measurement Noise Variables	58
4.5.3	Analysis of the Computational Complexity	59
4.6	Implementation of the Sequential Filter into an FPGA	62
4.6.1	Prototype Implementation	62
4.6.2	Test Bench	65
4.7	Validation of the Hardware Prototype	66
4.7.1	Verification of the Functionality	66
4.7.2	Analysis of the Scalability	72
5	Real-Time Assessment of the Voltage Stability by a Voltage Stability Index	75
5.1	The System Model	77
5.1.1	Electrical Grid	77
5.1.2	Aggregate Behavior of the Polyphase Nodes	77
5.2	Recall of the Continuation Power Flow Approach	79
5.2.1	Parametrization of the Power-Flow Equations	79
5.2.2	Determination of Loadability Limits via Numerical Continuation	80
5.3	The Generalized Formulation of the L-Index	82
5.3.1	Reformulation of the System Model	82

5.3.2	Development of the Voltage Stability Index	84
5.4	Validation of the Proposed Voltage Stability Index	87
5.4.1	Description of the Benchmark Power Grid	87
5.4.2	Validation Method	88
5.4.3	Discussion of the Results	88
6	Practical Deployment into a Real-Scale Microgrid	93
6.1	Overview of the Microgrid Setup	94
6.1.1	Architecture	94
6.1.2	Metering System	97
6.1.3	COMMELEC Framework	98
6.2	Experimental Validation of the Real-Time Capability	101
6.2.1	Description of the Method	101
6.2.2	Discussion of the Results	102
7	Conclusions	105
7.1	Synopsis of the Main Findings	105
7.2	Outlook on Future Work	107
A	Appendix	109
A.1	Essentials of Linear Algebra	109
A.1.1	Rank and Inverse	109
A.1.2	Positive-Definite and Negative-Definite Matrices	109
A.1.3	Unitary Matrices	110
A.1.4	Block Matrices	110
A.2	Modeling of Power System Components	111
A.2.1	Transmission Lines	111
A.2.2	Transformers	115
A.2.3	Series Compensators and Shunt Compensatorss	119
A.3	Measurement Noise in Different Coordinate Systems	121
A.4	Properties of the Kalman Filter	122
A.4.1	Joseph's Form of the Error Covariance Update	122
A.4.2	Positive Definiteness of the Estimation Error Covariance Matrix	122
A.4.3	Equivalent Formulations of the Estimation Step	123
A.5	Benchmark Power Grid	125
	Bibliography	139

List of Figures

1.1	Functionality and interaction of EMS, SCADA, and power system apparatus.	2
2.1	Phase-domain model of a three-phase circuit in sinusoidal steady state.	8
2.2	Sequence-domain model in case the compound impedance matrix is circulant (i.e., the sequence components are decoupled): (2.2a) positive-sequence, (2.2b) negative-sequence, and (2.2c) homopolar-sequence equivalent circuit.	9
3.1	Polyphase two-port equivalent circuits of the electrical components of the grid: (3.1a) Π -section equivalent circuit, (3.1b) T-section equivalent circuit.	22
3.2	Topology of the overall equivalent circuit of the grid: (3.2a) vertices \mathcal{N} and \mathcal{G} , (3.2b) edges \mathcal{L} of the branch graph \mathfrak{B} , (3.2c) edges \mathcal{T} of the shunt graph \mathfrak{S}	23
3.3	Compound electrical parameters of the overall equivalent circuit of the grid: compound branch impedance matrices \mathbf{Z}_ℓ ($\ell \in \mathcal{L}$) and shunt admittance matrices \mathbf{Y}_t ($t \in \mathcal{T}$). For the sake of clarity, polyphase terminals and wires are shown by bundles only.	24
3.4	Vectors of voltage and current phasors: phase-to-ground voltages \mathbf{V}_n ($n \in \mathcal{N}$), nodal injected currents \mathbf{I}_n ($n \in \mathcal{N}$), branch currents \mathbf{I}_ℓ ($\ell \in \mathcal{L}$), and shunt currents \mathbf{I}_t ($t \in \mathcal{T}$). For the sake of clarity, polyphase terminals and wires are shown by bundles only.	26
3.5	Proof of Theorem 1: (3.5a) case 1: $\mathbf{Y}_t = \mathbf{0} \forall t \in \mathcal{T}$, (3.5b) case 2: $\exists t \in \mathcal{T}$ s.t. $\mathbf{Y}_t \neq \mathbf{0}$. The surfaces indicate weakly connected graphs.	29
3.6	Proof of Theorem 2: branch graphs, cut-sets, and connectivity in the fictitious grid. The surfaces indicate weakly connected graphs.	33
3.7	Proof of Theorem 2: compound branch impedances $\tilde{\mathbf{Z}}_\ell$ and compound shunt admittances $\tilde{\mathbf{Y}}_t$ in the fictitious grid (i.e., where the polyphase nodes $(\mathcal{M}_k)_\mathbb{C}$ are grounded).	34
4.1	Architecture of the FPGA prototype of the SKF. Dedicated modules take care of communication, computation, memory, and control (i.e., of the first three modules).	62
4.2	Parallelized implementation of the inner product.	63
4.3	Architecture of the TB setup.	65
4.4	Schematic of the benchmark power grid. Note that the 24.9 kV subsystem is a modified version of the IEEE 34-node distribution feeder.	66

List of Figures

4.5	Power profiles used for the validation of the SKF prototype: (4.5a) aggregate generation, (4.5b) aggregate load, and (4.5c) power balance of the benchmark power grid.	67
4.6	Statistical distribution of the estimation error: (4.6a) magnitude and (4.6b) phase. The distributions are shown for selected nodes (i.e., 1, 12, and 20), and for the sets \mathcal{Z}_C and \mathcal{Z} . The edges of the boxes correspond to the 25th and 75th percentile, respectively.	70
4.7	Statistical distribution of the normalized residuals of selected measurements in \mathbf{y}_k . The edges of the boxes correspond to the 25th and 75th percentile, respectively.	70
4.8	Statistical distribution of the numerical mismatch between SKF and standard KF: (4.8a) $\hat{\mathbf{x}}_k^+$ and (4.8b) \mathbf{P}_k^+ . The distributions are shown for selected elements, and for the entire vector/matrix. The edges of the boxes correspond to the 25th and 75th percentile, respectively.	71
4.9	Execution time of the SKF prototype for $S < 256$ and $M = S$. The quadratic fit and the cubic fit are calculated from the measurements for which $S \leq 80$	72
5.1	Representation of the aggregate behavior of the nodes: (5.1a) Thévenin equivalent of a slack node $s \in \mathcal{S}$, (5.1b) polynomial model of phase $p \in \mathcal{P}$ in a resource node $r \in \mathcal{R}$	77
5.2	Schematic of the system model for the derivation of the voltage stability index.	82
5.3	Schematic of the benchmark power grid. Note that the 24.9 kV subsystem is a modified version of the IEEE 34-node distribution feeder.	87
5.4	Evolution of the proposed voltage stability index at the critical node (i.e., node 25), and comparison with the loadability limit computed with the continuation power flow method.	89
5.5	Evolution of the singular values of the Jacobian matrix of the power-flow equations.	90
5.6	Nose curves and characteristic curves of the loads at the critical node (i.e., node 25).	90
6.1	Schematic diagram of the real-scale microgrid of DESL at EPFL.	94
6.2	Conceptual diagram of the metering system. The PMUs stream encapsulated synchrophasor data, which are decapsulated and time-aligned by the PDC. . . .	97
6.3	Flow chart of the COMMELEC framework. The GA calculates requests based on the advertisements of its follower RAs, measurements of the grid state, and the request of its leader agent (in case there is one).	98
6.4	Real-time dispatch using the COMMELEC framework: (6.4a) active powers, (6.4b) reactive powers, and (6.4c) current in line L01.	100
6.5	Assessment of the latencies of the PDC/SE/VSA applications.	103
6.6	Assessment of the latencies of the COMMELEC applications.	103
A.1	Schematic of a polyphase transmission line. The conductors are parallel to each other and to the ground plane. The x -axis and the y -axis are perpendicular to the conductors, and the z -axis is parallel to the conductors.	111

A.2	Polyphase equivalent circuit of an infinitesimal line segment.	112
A.3	Polyphase Π -section equivalent circuit of a short line.	114
A.4	Polyphase equivalent circuit of a lossless transformer in absolute units.	116
A.5	Polyphase T-section equivalent circuit of a lossless transformer in relative units.	117
A.6	Polyphase T-section equivalent circuit of a lossy transformer in relative units.	118
A.7	Equivalent circuit of a line equipped with a series compensator.	120
A.8	Equivalent circuit of a line equipped with shunt compensators. For the sake of simplicity, only one compensator is shown.	120
A.9	Schematic of the benchmark power grid.	125

List of Tables

4.1	Computational complexity of the prediction step.	59
4.2	Computational complexity of the estimation step of the standard KF.	60
4.3	Computational complexity of one iteration of the estimation step of the SKF.	60
4.4	Comparison of the computational complexity of the standard KF and the SKF.	61
4.5	Specifications of the fundamental arithmetic blocks.	64
4.6	Occupation of FPGA resources for DOP = 4.	64
5.1	Reference values of the utilized polynomial models.	88
5.2	Normalized coefficients of utilized polynomial models.	88
5.3	Magnitudes of the phase-to-ground voltages at the load nodes for $\zeta = \zeta_{\max}$	91
5.4	Magnitudes of the conductor currents in selected lines for $\zeta = \zeta_{\max}$	91
6.1	Data of the cables installed in the microgrid.	96
A.1	Specification of the nodes.	126
A.2	Specification of the lines.	126
A.3	Specification of the transformers.	126
A.4	Sequence parameters of the transposed lines.	126

1 Introduction

1.1 Motivation

As known, the operation of power transmission systems is automated to a very high degree. This automation relies on the integration of *Supervisory Control and Data Acquisition* (SCADA) and *Energy Management Systems* (EMSs) [1] (see Figure 1.1). The EMS is a centralized platform of computer-aided tools which perform different functions like state estimation, contingency analysis, stability assessment, voltage/frequency monitoring, economic dispatch, and so forth. These applications are facilitated by a library of numerical methods for (standard, optimal, or continuation) power flow, least-squares regression, Kalman filtering, and the like. Conversely, the SCADA is a distributed infrastructure composed of instrumentation and communication systems, which acquires measurement data and may send control signals. That is, the SCADA interfaces the EMS with the power system apparatus.

Historically, power distribution systems did not have a part in this automation effort. Instead, operational issues were solved entirely during the planning stage (e.g., [2], [3–5], and [6–8]). Recently, automation technology has found its way into power distribution systems, because the operators strive to keep the operational costs low, and improve the quality and reliability of the services provided to their customers. This development is fostered further by the massive integration of *Distributed Energy Resources* (DERs), such as distributed generators (e.g., solar cells or wind turbines), energy storage systems (e.g., supercapacitor, battery, or power-to-gas technologies), and novel loads (e.g., electric vehicles). That is, the power distribution systems of the future are envisioned as *Active Distribution Networks* (ADNs), which allow to manage the electricity flows through control of the DERs and the grid topology (cf. [9]). In this regard, automation tools for real-time monitoring and control are practicable solutions to operate ADNs safely (i.e., keep the voltages within specified bounds, avoid line congestions, etc.) and enable dispatchability along with the provision of ancillary services to the bulk power system.

Of course, real-time control requires real-time situation awareness w.r.t. the state (e.g., [10]) and the stability (e.g., [11]) of the system. This has driven the development and standardization of methods for monitoring [12] and control [13] of ADNs. In view of large-scale utilization,

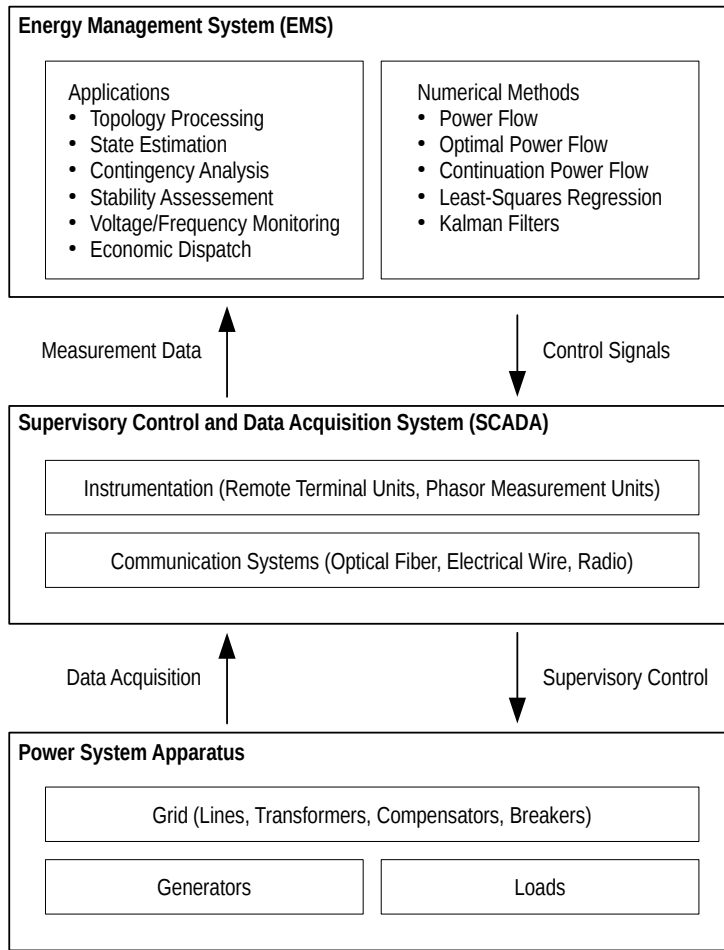


Figure 1.1 – Functionality and interaction of EMS, SCADA, and power system apparatus.

these methods have to be deployed into low-cost embedded systems, for instance based on *Field-Programmable Gate Arrays* (FPGAs), and run in real time (i.e., at refresh rates of tens of frames per second) with highly deterministic execution time. Thus, they have to be computationally efficient. Moreover, the inherent unbalances of power distribution systems w.r.t. the components of the grid and the loads have to be considered – as opposed to power transmission systems, which are typically balanced.

Within this context, this thesis continues the research activities carried out at the *Distributed Electrical Systems Laboratory* (DESL) of the *École Polytechnique Fédérale de Lausanne* (EPFL) in terms of real-time monitoring [14–16] and control [17] of power distribution grids. Specifically, this thesis deals with the modeling of unbalanced polyphase power grids, as well as the development, validation, and deployment of real-time methods for *State Estimation* (SE) and *Voltage Stability Assessment* (VSA) for such systems. To this end, model reduction techniques are applied, computationally efficient algorithms are proposed, and implementations of these algorithms are developed in dedicated hardware and software.

1.2 Contributions

The contributions of this thesis are as follows.

1. Fundamental properties of the equivalent circuits of unbalanced polyphase grids are rigorously identified. Namely, conditions that determine the rank of the compound admittance matrix¹ of polyphase circuits and its diagonal subblocks are established. In particular, it is shown that the diagonal blocks of the compound admittance matrix have full rank, if the branch graph is weakly connected and the compound electrical parameters of the polyphase lumped elements are symmetric, invertible, and lossy. Based on this property, it is proven that *Kron Reduction* (KR) (i.e., the elimination of nodes with zero injected currents) is feasible for any set of zero-injection nodes, and that a compound hybrid matrix exists for any partition of the nodes. These findings are the cornerstones for the further contributions to SE and VSA.
2. An *Voltage Stability Index* (VSI) for unbalanced polyphase power systems is proposed. To this end, the grid is described by a compound hybrid matrix, and slack and resource nodes² are represented by *Thévenin Equivalents* (TEs) and *Polynomial Models* (PMs), respectively. The proposed VSI is a generalization of the well-known *L-index* [18], which is achieved by incorporating the aforementioned models into the classical formulation of the *L-index*. In this regard, the aforesaid properties w.r.t. the feasibility of KR and the existence of compound hybrid matrices are used to substantiate the applicability of the proposed VSI. This establishes a rigorous theoretical foundation for the *L-index* and its descendants.
3. A prototype of a real-time state estimator for power distribution grids, which is hosted in the FPGA of an industrial real-time controller, is presented. This prototype is based on a *Sequential Kalman Filter* (SKF), which is suitable for implementation in such dedicated hardware – as opposed to the standard *Kalman Filter* (KF). In this context, it is proven that the standard KF and the SKF yield identical estimates if the noise variables associated with different measurements are uncorrelated. Furthermore, the computational complexity of the SKF is analyzed in detail, in order to substantiate its suitability for implementation into embedded systems. To achieve high computational performance, the developed real-time state estimator relies on KR of the grid model, as well as parallelization and pipelining of the SKF calculations on the FPGA level.

¹The compound admittance matrix is the polyphase analogon of the positive-sequence admittance matrix used in classical power system analysis.

²Slack/resource nodes correspond to $V\delta/PQ$ buses in classical power system analysis.

4. The applicability of the methods described under 1.–3. is verified numerically. Moreover, their real-time capability is demonstrated experimentally. To this end, the developed methods are deployed into the microgrid facility of the DESL at the EPFL in Lausanne, Switzerland. This setup is a real-scale implementation of the low-voltage benchmark grid defined by the *Conseil International des Grands Réseaux d'Électricité* (CIGRÉ) [19]. The metering system consists of high-accuracy *Phasor Measurement Units* (PMUs) [14], which are coupled with a low-latency *Phasor Data Concentrator* (PDC) [15]. The SKF and the VSI are embedded into modular applications for SE and VSA, which are deployed into an industrial real-time controller together with the PDC. The real-time capability of the PDC-SE-VSA pipeline is validated by assessing the latencies w.r.t. the PMU timestamps.

1.3 Document Outline

The remainder of this thesis is organized as follows:

In Chapter 2, the state of the art in modeling, state estimation, and voltage stability assessment of power systems is discussed. With regard to the applicability to polyphase power systems, special emphasis is put on the treatment of grid unbalances.

In Chapter 3, the essentials of modeling polyphase power grids are discussed. Specifically, it is shown that such grids can be represented by polyphase branch and shunt elements, whose compound electrical parameters (i.e., impedance/admittance matrices) are symmetric, invertible, and lossy. Based on these properties, theorems concerning the rank of the compound admittance matrix, the feasibility of KR, and the existence of compound hybrid matrices are proposed and formally proven.

In Chapter 4, the prototype real-time state estimator is presented. The working hypotheses w.r.t. the measurement and process model, as well as the essentials of KF theory are recalled. Based on these fundamentals, the equivalence of the SKF and the standard KF is postulated and formally proven. Moreover, their computational complexity is analyzed to substantiate the suitability of the SKF (as opposed to the standard KF) for implementation in FPGA hardware. Finally, the design and validation of the FPGA implementation of the SKF are discussed.

In Chapter 5, the proposed VSI is presented. First, the system model is defined. Specifically, it is shown that slack and resource nodes can be represented by TEs and PMs, respectively. Furthermore, the *Continuation Power Flow* (CPF) approach, which is commonly used for VSA, is recalled. Afterwards, the proposed VSI is derived by incorporating the TEs and the PMs, along with the compound hybrid matrix of the grid, into the classical formulation of the L -index. Through comparison with the classical CPF approach, it is confirmed that the proposed VSI correctly detects voltage instability.

In Chapter 6, the deployment of the developed methods into the microgrid facility of the DESL, which is a real-scale implementation of the low-voltage benchmark grid defined by CIGRÉ, is illustrated. The SKF and the VSI are embedded into modular applications for SE and VSA, respectively, which are deployed into an industrial real-time controller. These applications are coupled with a PDC in order to use PMUs installed in the microgrid. The real-time capability of this setup is confirmed by assessing the latencies of the PDC-SE-VSA processing chain w.r.t. the PMU timestamps.

Finally, the thesis is concluded with a synopsis of the findings and an outlook on future work.

2 Review of the State of the Art

This chapter reviews the state of the art in power systems engineering w.r.t. circuit analysis, state estimation, and voltage stability assessment. These topics are covered in Sections 2.1, 2.2, and 2.3, respectively. For illustration purposes, some basic concepts and notation are introduced on the fly. Rigorous definitions are provided in Chapters 3, 4, and 5, respectively, in function of the subject treated in the respective chapter.

2.1 Circuit Analysis of Power Systems

Techniques for power system analysis inherently need an analytical description of the grid. This description is derived from equivalent circuits of its electrical components (e.g., lines and transformers). For instance, in power-flow study (e.g., [20]), state estimation (e.g., [21–23]), and voltage stability assessment (e.g., [24–26]), the grid is described by the nodal admittance or impedance matrix, or by hybrid matrices. The numerical methods used for these applications are computationally intensive. Therefore, model reduction techniques like Ward reduction [27] or *Kron Reduction* (KR) [28] are often employed in order to reduce the number of unknowns. In this way, the execution speed can be improved without having to use of high-performance computers (e.g., [29]). However, neither the applicability of KR nor the existence of hybrid parameters are guaranteed a priori. In the following, the state of the art in circuit analysis is reviewed with a specific focus on these subjects.

2.1.1 Equivalent Circuits of Polyphase Power Systems

Traditionally, power system analysis deals with three-phase grids. Supposing that the system is in *sinusoidal steady state*, voltages and currents can be represented by phasors, and resistors, inductors, and capacitors by impedances or admittances [30].

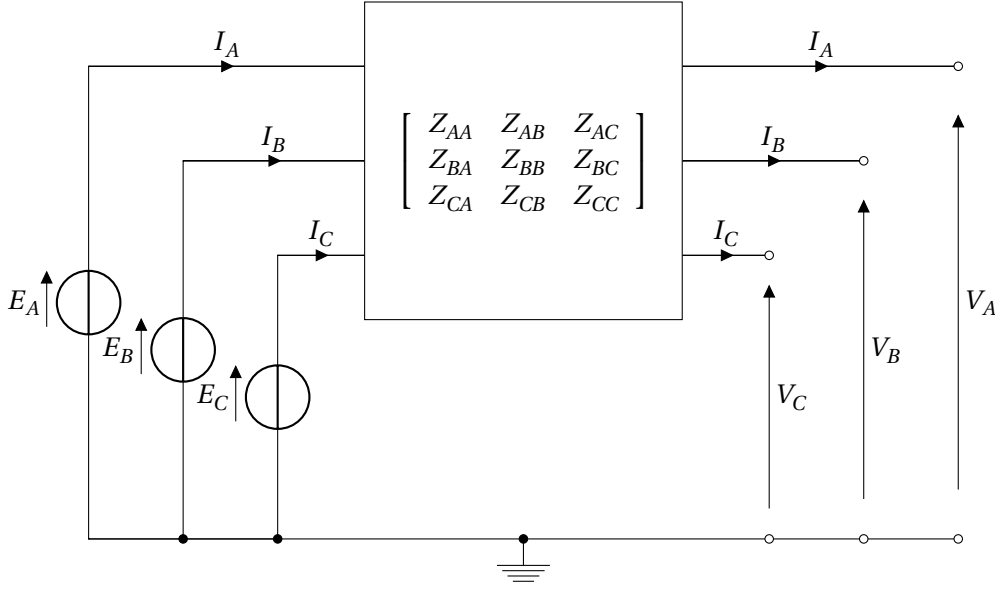


Figure 2.1 – Phase-domain model of a three-phase circuit in sinusoidal steady state.

Consider the three-phase circuit shown in Figure 2.1. In *phase domain* (i.e., *ABC* coordinates), this circuit is described by

$$\begin{bmatrix} V_A \\ V_B \\ V_C \end{bmatrix} = \begin{bmatrix} E_A \\ E_B \\ E_C \end{bmatrix} - \begin{bmatrix} Z_{AA} & Z_{AB} & Z_{AC} \\ Z_{BA} & Z_{BB} & Z_{BC} \\ Z_{CA} & Z_{CB} & Z_{CC} \end{bmatrix} \begin{bmatrix} I_A \\ I_B \\ I_C \end{bmatrix} \quad (2.1)$$

Note that the matrix on the right-hand side of (2.1) is a *compound impedance matrix* [31] (i.e., the off-diagonal terms represent the electromagnetic coupling between the phases).

Typically, power transmission grids are electrically *balanced*. That is, the compound electrical parameters of the electrical components (e.g., lines and transformers) are *circulant*:

$$Z_{AA} = Z_{BB} = Z_{CC} \quad (2.2)$$

$$Z_{AB} = Z_{BC} = Z_{CA} \quad (2.3)$$

$$Z_{AC} = Z_{BA} = Z_{CB} \quad (2.4)$$

In this case, the method of *symmetrical components* [32] can be used to simplify the circuit equations. Namely, the system is represented by *positive-sequence* (*P*), *negative-sequence* (*N*), and *homopolar-sequence* (*H*) components, which are defined by the transformation¹

$$\mathbf{T}: \begin{bmatrix} A \\ B \\ C \end{bmatrix} \mapsto \begin{bmatrix} P \\ N \\ H \end{bmatrix}, \quad \mathbf{T} := \frac{1}{3} \begin{bmatrix} 1 & \alpha & \alpha^2 \\ 1 & \alpha^2 & \alpha \\ 1 & 1 & 1 \end{bmatrix}, \quad \alpha := \exp\left(j\frac{2\pi}{3}\right) \quad (2.5)$$

¹This follows directly from the fact that the columns of \mathbf{T} are eigenvectors of the circulant matrices of size 3×3 (note that the elements of \mathbf{T} are the cube roots of unity).

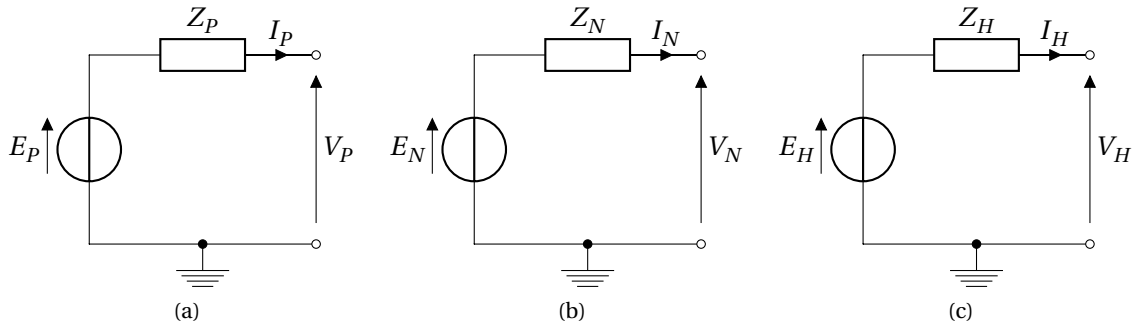


Figure 2.2 – Sequence-domain model in case the compound impedance matrix is circulant (i.e., the sequence components are decoupled): (2.2a) positive-sequence, (2.2b) negative-sequence, and (2.2c) homopolar-sequence equivalent circuit.

Applying this transformation to (2.1) yields the circuit equations in *sequence domain*:

$$\begin{bmatrix} V_P \\ V_N \\ V_H \end{bmatrix} = \begin{bmatrix} E_P \\ E_N \\ E_H \end{bmatrix} - \begin{bmatrix} Z_P & 0 & 0 \\ 0 & Z_N & 0 \\ 0 & 0 & Z_H \end{bmatrix} \begin{bmatrix} I_P \\ I_N \\ I_H \end{bmatrix} \quad (2.6)$$

where

$$\begin{bmatrix} Z_P & 0 & 0 \\ 0 & Z_N & 0 \\ 0 & 0 & Z_H \end{bmatrix} = \mathbf{T}^{-1} \begin{bmatrix} Z_{AA} & Z_{AB} & Z_{AC} \\ Z_{BA} & Z_{BB} & Z_{BC} \\ Z_{CA} & Z_{CB} & Z_{CC} \end{bmatrix} \mathbf{T} \quad (2.7)$$

Note that the sequence-domain impedance matrix is diagonal *iff* the phase-domain impedance matrix is circulant. In this case, Z_P , Z_N , and Z_H are the eigenvalues of the phase-domain impedance matrix. The diagonal structure of the sequence-domain impedance matrix implies that (2.6) can be represented by three independent equivalent circuits as shown in Figure 2.2. In fact, this is the main advantage of sequence-domain analysis over phase-domain analysis.

In contrast to power transmission grids, power distribution grids are typically *unbalanced*. That is, the compound electrical parameters are symmetric, but not necessarily circulant:

$$Z_{AA} \neq Z_{BB} \neq Z_{CC} \quad (2.8)$$

$$Z_{AB} = Z_{BA} \neq Z_{AC} = Z_{CA} \neq Z_{BC} = Z_{CB} \quad (2.9)$$

As a result, the circuit equations in sequence domain cannot be decoupled in general. Hence, it is incorrect (rigorously speaking) to use symmetrical components. In fact, various works acknowledge that it is more meaningful to analyze unbalanced three-phase grids in phase-domain (e.g., [33,34]). This is even more true for generic polyphase power grids with more than three phases, because balancedness is difficult to achieve in practice [35]. However, this case is seldom examined in the literature.

2.1.2 Kron Reduction of Electrical Circuits

Now, consider an electrical circuit whose nodes are partitioned into two sets labeled 1 and 2. The admittance equations of this circuit can be written in block form as

$$\begin{bmatrix} \mathbf{I}_1 \\ \mathbf{I}_2 \end{bmatrix} = \begin{bmatrix} \mathbf{Y}_{11} & \mathbf{Y}_{12} \\ \mathbf{Y}_{21} & \mathbf{Y}_{22} \end{bmatrix} \begin{bmatrix} \mathbf{V}_1 \\ \mathbf{V}_2 \end{bmatrix} \quad (2.10)$$

Suppose that the current injections in the second set of nodes are strictly zero. That is

$$\mathbf{I}_2 = \mathbf{Y}_{21}\mathbf{V}_1 + \mathbf{Y}_{22}\mathbf{V}_2 = \mathbf{0} \quad (2.11)$$

Obviously, \mathbf{V}_1 and \mathbf{V}_2 are linearly dependent. If \mathbf{Y}_{22} is invertible, \mathbf{V}_2 can be expressed as

$$\mathbf{V}_2 = -\mathbf{Y}_{22}^{-1}\mathbf{Y}_{21}\mathbf{V}_1 \quad (2.12)$$

Substituting this formula into (2.10) yields

$$\mathbf{I}_1 = \left(\mathbf{Y}_{11} - \mathbf{Y}_{12}\mathbf{Y}_{22}^{-1}\mathbf{Y}_{21} \right) \mathbf{V}_1 \quad (2.13)$$

This process is known as KR [28].

As previously mentioned, the invertibility of \mathbf{Y}_{22} is a prerequisite for the applicability of KR. Although KR is commonly used in the field, users hardly ever verify whether this condition actually holds. Apparently, even the inventor himself (i.e., the author of [28]) did not take this issue into account. According to practical experience, KR is indeed feasible, but there was no theoretical proof for this empirical evidence until recently. One work [36] investigates the particular case of single-phase grids. Specifically, it is shown that KR is feasible if \mathbf{Y} is strictly diagonally dominant. However, this reasoning is based on the assumption that the circuit is purely resistive or inductive, which is unrealistic for power grids. Two other works [37,38] examine the more generic case of unbalanced three-phase grids. Specifically, it is proven that a block of the admittance matrix, which is obtained by removing only the rows and columns associated with one node, is invertible. However, it is not straightforward to extend this finding to the elimination of several nodes.

2.1.3 Hybrid Matrices of Electrical Circuits

In circuit theory and power system analysis, it is often more convenient to describe a circuit by hybrid instead of admittance equations (e.g., [39,40]). For instance, (2.10) could be restated as

$$\begin{bmatrix} \mathbf{V}_1 \\ \mathbf{I}_2 \end{bmatrix} = \begin{bmatrix} \mathbf{H}_{11} & \mathbf{H}_{12} \\ \mathbf{H}_{21} & \mathbf{H}_{22} \end{bmatrix} \begin{bmatrix} \mathbf{I}_1 \\ \mathbf{V}_2 \end{bmatrix} \quad (2.14)$$

where \mathbf{H} is the hybrid matrix. The term “hybrid” refers to the fact that voltages and currents appear both on the left-hand and the right-hand side of the aforesaid equation.

In general, the existence of hybrid matrices depends on the electrical properties of the circuit, and on the partition of the nodes for which the hybrid equations are to be formulated [41]. There are works which have investigated this matter for single-phase circuits. Many authors simply propose methods for building \mathbf{H} , but do not substantiate their feasibility (e.g., [42–44]). Other authors do formulate criteria for the feasibility, but only for “some” (i.e., at least one) partition of the nodes (e.g., [45–47]).

2.2 State Estimation of Power Systems

State Estimation (SE) is the process of inferring the states of a system from noisy measurements and known inputs. In the case of power systems, the *state vector* \mathbf{x} and *measurement vector* \mathbf{y} consist of nodal and branch quantities (i.e., voltages, currents, and powers). Assuming that the system is in sinusoidal (quasi-)steady state, these quantities are represented by phasors [30]. Depending on the application, the *input vector* \mathbf{u} may be considered or neglected.

2.2.1 Static Approaches

Static approaches neglect any time evolution of the state. The estimated state is calculated as the maximum likelihood fit to the measurements available at a given point in time [48]. Usually, this problem is solved through *Weighted Least-Squares Regression* (WLSR) [22,23].

Recall that the states and measurements are phasors, which can be expressed in rectangular or polar coordinates. Therefore, in general, the *measurement model* is nonlinear [21,49]:

$$\mathbf{y} = \Psi(\mathbf{x}, \mathbf{u}) + \mathbf{v} \quad (2.15)$$

where $\Psi(\cdot)$ is the *output function*, and \mathbf{v} is the *measurement noise*. The nonlinear regression problem has to be solved numerically using iterative methods (e.g., [50,51]). Every iteration requires the calculation and inversion of the Jacobian matrix of $\Psi(\cdot)$, which is computationally intensive. Alternatively, the measurement model can be linearized locally around the present operating point (e.g., [52–54]).

If the states and measurements consist of voltage and current phasors, which are expressed in rectangular coordinates, the measurement model is exactly linear [55,56]:

$$\mathbf{y} = \mathbf{C}\mathbf{x} + \mathbf{D}\mathbf{u} + \mathbf{v} \quad (2.16)$$

where \mathbf{C} is the *output matrix*, and \mathbf{D} is the *feedthrough matrix*. In contrast to the nonlinear regression problem, the linear one can be solved analytically. This is more efficient from the computational point of view [57]. In particular, the use of *Phasor Measurement Units* (PMUs) yields linear measurement models [58].

Finally, it is worth mentioning measurement model can be used to identify so-called *bad data* (i.e., grossly erroneous measurements). Namely, using the *estimated state* $\hat{\mathbf{x}}$, the measurement noise can be approximately reconstructed as

$$\hat{\mathbf{v}} = \mathbf{y} - \Psi(\hat{\mathbf{x}}, \mathbf{u}) \quad (2.17)$$

Whether a measurement is bad can be determined based on the statistical distribution of the elements of $\hat{\mathbf{v}}$ [59,60]. This approach is known as *Hypothesis Testing Identification* (HTI).

2.2.2 Quasi-Static Approaches

Quasi-static approaches do consider the time evolution of the state to some extent. Namely, the system is assumed to change between quasi-steady operating points². This is represented by a *process model*, which links the states at successive instants k and $k + 1$.

Like the measurement model, the process model is nonlinear in general:

$$\mathbf{x}_{k+1} = \Phi(\mathbf{x}_k, \mathbf{u}_k) + \mathbf{w}_k \quad (2.18)$$

where $\Phi(\cdot)$ is the *system function*, and \mathbf{w}_k is the *process noise*. The complete system model

$$\mathbf{x}_{k+1} = \Phi(\mathbf{x}_k, \mathbf{u}_k) + \mathbf{w}_k \quad (2.19)$$

$$\mathbf{y}_k = \Psi(\mathbf{x}_k, \mathbf{u}_k) + \mathbf{v}_k \quad (2.20)$$

can be treated using nonlinear *Kalman Filter* (KF) theory. If $\Phi(\cdot)$ and $\Psi(\cdot)$ are differentiable, the extended KF can be used (e.g., [61–63]). Essentially, the system model is linearized around the present operating point, and the standard KF [64] is applied. In case the system model is strongly nonlinear, the linearization yields a poor approximation, though. The unscented KF, which does not approximate $\Phi(\cdot)$ and $\Psi(\cdot)$ in this way, can avoid this problem (e.g., [65]).

If the system model is (exactly or approximately) linear, that is

$$\mathbf{x}_{k+1} = \mathbf{A}\mathbf{x}_k + \mathbf{B}\mathbf{u}_k + \mathbf{w}_k \quad (2.21)$$

$$\mathbf{y}_k = \mathbf{C}\mathbf{x}_k + \mathbf{D}\mathbf{u}_k + \mathbf{v}_k \quad (2.22)$$

where \mathbf{A} is the *system matrix*, the standard KF [64] can be used (e.g., [66–68]). Notably, the standard KF performs better than WLSR [58] in terms of estimation accuracy, provided that the statistical distribution of the process noise is known exactly [69,70].

Some works suppose that the elements of \mathbf{y}_k can be processed sequentially (i.e., one by one), since this enables computationally efficient implementations (e.g., [68,71]). This formulation is known as the *Sequential Kalman Filter* (SKF). However, the authors of these works do not verify whether the SKF and the standard KF yield the same results, or under which conditions this may be the case.

²In the literature, these approaches are often called *dynamic*. In this thesis, the term *quasi-static* is preferred, because it avoids confusion with truly dynamic approaches (i.e., based on differential equations).

2.3 Voltage Stability Assessment of Power Systems

IEEE and CIGRÉ define voltage stability as “*the ability of a power system to maintain steady voltages at all buses in the system after being subjected to a disturbance from a given initial operating condition*”, and note that “*it depends on the ability to maintain/restore equilibrium between load demand and load supply from the power system*” [72]. Accordingly, *Voltage Stability Assessment* (VSA) is the study of equilibrium points of power systems w.r.t. the (nodal) voltages. For this purpose, one can use *dynamic* methods, such as time-domain simulation, or *static* methods, such as *Power-Flow Study* (PFS) [24–26].

This thesis focuses on static analysis. Specifically, voltage instability is considered to be due to *loadability limits* only. As known, loadability limits are critical points w.r.t. the loading of a power system, beyond which the grid cannot support the transfer of power [73]. Assuming that the device dynamics (i.e., control loops of generators/loads) can be neglected and the device ratings (e.g., generator reactive power limits) are respected, a loadability limit implies that the Jacobian matrices of the power-flow equations and the dynamic equations, respectively, are singular [74–76]. That is, the power-flow equations are “borderline solvable”, and the (linearized) dynamic system is marginally stable. Hence, if the aforesaid assumptions hold, loadability limits are critical points w.r.t. voltage stability.

2.3.1 Continuation Power Flow

Loadability limits can be determined graphically using *nose curves* (a.k.a. *PV/QV* curves), which describe the relation between active/reactive power and voltage. At a loadability limit, the load/generation cannot be increased further, which means that the characteristic curve of the load/generation is tangent to the nose curve of the system [26].

Nose curves are obtained using *Continuation Power Flow* (CPF) methods. For this purpose, the power-flow equations are parametrized w.r.t. a predefined change of the load/generation. That is, the power-flow equations are expressed in the form

$$\mathbf{g}(\mathbf{x}, \xi) = \mathbf{0} \tag{2.23}$$

where \mathbf{x} is the state, and ξ a parameter that represents the loading of the grid [73]. CPF methods track a solution path in (\mathbf{x}, ξ) -space using a predictor-corrector scheme (e.g., [77–79]). That is, starting from a known solution, the next solution is first guessed using a prediction method, and then refined using a correction method. The corrector step involves the solution of the system of nonlinear equations (2.23). As a results, CPF methods are computationally intensive and hence slow, even if advanced predictors/correctors (e.g., [80]) or adaptive stepsize control (e.g., [81]) are used to accelerate the calculation.

In principle, both generation and load can cause voltage instability. However, if the grid is lossy, instability due to generation is of little relevance, as it occurs at very high power injections [82].

That is, thermal ratings of lines or transformers are reached prior to instability. In contrast, instability due to load can occur while respecting these ratings [11]. CPF methods usually operate with positive-sequence equivalent circuits of balanced three-phase systems, but the concept can be extended to unbalanced three-phase systems (e.g., [83,84]).

2.3.2 Maximum Loadability

Instead of tracing the whole solution path to a loadability limit via numerical continuation, the loadability limit can also be determined directly through nonlinear programming [85]. Namely, one can solve the nonlinear program

$$\begin{aligned} \max \quad & \xi \\ \text{s.t.} \quad & \mathbf{g}(\mathbf{x}, \xi) = \mathbf{0} \end{aligned} \tag{2.24}$$

This corresponds to the maximization of the loading factor ξ (e.g., in one single node, an area, or the entire system) subject to the power-flow equations.

The nonlinear program (2.24) can be solved using iterative methods. *Direct methods* account for the constraints explicitly, so each intermediate solution is feasible w.r.t. the constraints. For example, interior-point methods (e.g., [86]) belong to this category. *Indirect methods* solve a series of unconstrained nonlinear programs, whose objective functions include a term which penalizes constraint violations. Thus, only the final solution (if it exists), but not the intermediate ones, is ensured to be feasible. For instance, augmented Lagrangian methods (e.g., [87]) and penalty methods (e.g., [88]) belong to this family.

2.3.3 Maximum Power Transfer

If the load is of *Constant-Power* (CP) type, the loadability limit lies at the tip of the nose curve, which corresponds to maximum power transfer. As known, the power delivered by a source to a load is maximum when the *source impedance* Z_S (i.e., output impedance of the source) matches the *load impedance* Z_L (i.e., the input impedance of the load) [89]:

$$Z_S = Z_L^* \tag{2.25}$$

This is the well-known *impedance-matching criterion*.

Typically, the impedance matching criterion is applied to equivalent two-node systems, each of which consists of the local CP load and a *Thévenin Equivalent* (TE) of the external system [90]. The loads can also be represented by *Polynomial Models* (PMs), whose *Constant-Current* (CI) and *Constant-Impedance* (CZ) components are incorporated into the aforementioned TEs [91]. Alternatively, the impedance-matching criterion can be used to construct the loadability surfaces of the equivalent two-node systems in the *PQ*-plane [92,93]. It is important to note that these approaches tacitly assume that the TEs reasonably reproduce the behavior of the

external systems seen by the local loads over the whole relevant range of operating conditions. A priori, this is a coarse approximation. In order to solve this problem, the concept of coupled single-port circuits has been proposed [94]. Essentially, additional terms which account for the interaction between the loads are added to the equivalent two-node systems. For example, the TEs can be refined with information from sensitivity coefficients [95], or Ward equivalents can be used instead of TEs [96].

2.3.4 Formal Analysis of the Solvability of the Power-Flow Equations

Recall that, under the assumptions made, a loadability limit corresponds to an operating point at which the power-flow equations are “borderline solvable”. The solvability of the power-flow equations can be analyzed formally. For instance, one can formulate necessary conditions for solvability [97], or approximate the solvability set [98–100]. However, these approaches tend to be mathematically intricate.

Hence, most works instead exploit the fact that the Jacobian matrix is singular if the power-flow equations are unsolvable [74]. That is, the determinant [11], eigenvalues [101], and singular values [102] of the Jacobian matrix can serve as *Voltage Stability Indices* (VSIs). Another family of VSIs descends from the well-known *L*-index [18]. Essentially, the power-flow equations are locally approximated by complex quadratic equations, whose discriminant is used to derive the *L*-index. In the original formulation [18], generators are represented by constant voltage sources, loads by constant power sources, and the grid by the hybrid matrix. Moreover, there exist extended formulations, which model generators by TEs [103] or loads by PMs [104].

Finally, it is worth noting that the aforementioned VSIs vary nonlinearly with the load. Hence, it may be challenging to infer the absolute loadability margin (i.e., in kW/kVAR) from the VSI. However, for special cases, such as CP loads [105] or PMs with constant power factor [106], VSIs with reasonably linear behavior have been proposed. In these cases, there is a one-to-one correspondence between the VSI and the absolute loadability margin.

2.4 Contributions of this Thesis

In view of the state of the art that has been discussed in this chapter, the contributions of this thesis are further detailed here below.

1. Fundamental properties of the equivalent circuits of unbalanced polyphase power grids are identified. Specifically, theorems w.r.t. the rank of the compound admittance matrix, the feasibility of KR, and the existence of compound hybrid matrices, are stated and formally proven. In comparison to the existing theorems [37,38] (admittance matrix), [36] (KR) and [45–47] (hybrid matrix), the proposed ones make weaker hypotheses (i.e., the compound electrical parameters do not have to be circulant) and give stronger conclusions (i.e., which are valid for arbitrary subsets or partitions of the nodes).
2. A VSI for unbalanced polyphase power systems is developed. More precisely, the grid is described by a compound hybrid matrix, and slack and resource nodes are represented by TEs and PMs, respectively. This VSI is a generalization of the known L -index [18], which incorporates the aforementioned models. In this regard, the theorems w.r.t. the feasibility of KR and the existence of compound hybrid matrices are used to substantiate the applicability of the proposed VSI. This establishes a rigorous theoretical foundation for the L -index [18] and its descendants (e.g., [103,104]), which – to the best of the author’s knowledge – is truly original.
3. A real-time state estimator for power distribution grids is presented. This state estimator is based on a SKF, which is implemented into an FPGA. It is formally proven that the SKF and the standard KF produce identical estimates if the measurement noise variables are uncorrelated. To the best of the author’s knowledge, this is the first complete and rigorous proof of equivalence in the literature. Notably, this finding establishes a rigorous theoretical foundation for existing works that use the SKF without justifying its applicability (e.g., [68,71]). Moreover, the suitability of the SKF for implementation into dedicated hardware is substantiated by detailed analysis of its computational complexity (in comparison with the standard KF).
4. It is experimentally demonstrated that the developed methods are real-time capable. To this end, they are deployed into an industrial embedded systems platform, which is used for real-time control of a real-scale experimental microgrid.

3 Analysis of Equivalent Circuits of Polyphase Power Grids

Contributions: This chapter lays the theoretical foundations for the analysis of unbalanced polyphase power grids in the phase domain. First, it is shown that polyphase power grids can be represented by equivalent circuits composed of polyphase branch and shunt elements, which are characterized by compound electrical parameters. Specifically, it is demonstrated that these compound electrical parameters are symmetric, invertible, and lossy. Using these properties, plus the assumption that the branch graph of the grid is weakly connected, conditions that determine the rank of the compound admittance matrix of the grid, as well as its diagonal blocks, are stated and formally proven. More precisely, it is shown that the compound admittance matrix has full rank if there is at least one shunt element, and that its diagonal blocks always have full rank. Building upon these findings, it is formally proven that *Kron Reduction* (KR) is feasible for any set of zero-injection nodes, and that a compound hybrid matrix exists for any partition of the nodes. The theorems w.r.t. the rank of the compound admittance matrix, the feasibility of KR, and the existence of compound hybrid matrices establish a rigorous theoretical foundation for the methods developed in the rest of this thesis.

Keywords: polyphase power systems, unbalanced power grids, compound admittance matrix, compound hybrid matrix, Kron reduction.

Publications:

- [107] A. M. Kettner and M. Paolone, "On the properties of the power system nodal admittance matrix", IEEE Trans. Power Syst., vol. 33, no. 1, pp. 1130–1131, Jan. 2018.
- [108] A. M. Kettner and M. Paolone, "On the properties of the compound nodal admittance matrix of polyphase power systems", IEEE Trans. Power Syst., vol. 34, no. 1, pp. 444–453, Jan. 2019.

3.1 Modeling of Polyphase Power Grids

3.1.1 Hypotheses with Respect to the Electrical Components of the Grid

Neutral Conductor and Earthing System

Consider a generic polyphase power system, which is equipped with a neutral conductor. Label the *ground node* as $\mathcal{G} := \{0\}$ and the *phases* as $\mathcal{P} := \{1, \dots, |\mathcal{P}|\}$, where $|\cdot|$ is the *cardinality*. A *polyphase node* consists of a full set of phase terminals that belong to the same bus. In this respect, the terminals of the grid define the *physical polyphase nodes* $\mathcal{N}_{\text{physical}}$. Regarding the wiring and the earthing of the neutral conductor, the following hypothesis is made:

Hypothesis 1 (Neutral Conductor). *The reference points of all sources (i.e., voltage or current sources) are connected to the neutral conductor. Moreover, the neutral conductor is grounded by means of an effective earthing system. That is, the earthing system is able to establish a null voltage between the neutral conductor and the physical ground (see [6,109,110]).*

Given that the neutral-to-ground voltages are effectively zero, the phase-to-neutral voltages directly correspond to phase-to-ground voltages, and fully describe the grid¹.

Electrical Components Interconnecting the Polyphase Nodes

The grid is built of electrical components which connect the physical polyphase nodes with each other and the ground node. With respect to these electrical components, the following hypothesis is made:

Hypothesis 2 (Electrical Components). *The grid consists of electrical components which are linear and passive. Moreover, only the electromagnetic coupling among the phases of the same component is significant. That is, in a per-unit model, they can be represented by polyphase Π -section or T-section equivalent circuits, whose branch and shunt elements are described by compound electrical parameters (see Figure 3.1).*

Let $m, n \in \mathcal{N}_{\text{physical}}$ be two polyphase nodes that are connected by an electrical component. A polyphase Π -section equivalent circuit is described by one compound impedance matrix $\mathbf{Z}_{\Pi,(m,n)}$ and two compound admittance matrices $\mathbf{Y}_{\Pi,m|(m,n)}$, $\mathbf{Y}_{\Pi,n|(m,n)}$ (see Figure 3.1a):

$$\mathbf{Z}_{\Pi,(m,n)}, \mathbf{Y}_{\Pi,m|(m,n)}, \mathbf{Y}_{\Pi,n|(m,n)} \in \mathbb{C}^{|\mathcal{P}|\times|\mathcal{P}|} \quad (3.1)$$

A polyphase T-section equivalent circuit is described by one compound admittance matrix $\mathbf{Y}_{T,x}$ and two compound branch impedance matrices $\mathbf{Z}_{T,(m,x)}$, $\mathbf{Z}_{T,(n,x)}$ (see Figure 3.1b):

$$\mathbf{Y}_{T,x}, \mathbf{Z}_{T,(m,x)}, \mathbf{Z}_{T,(n,x)} \in \mathbb{C}^{|\mathcal{P}|\times|\mathcal{P}|} \quad (3.2)$$

¹In practice, neutral-to-ground voltages are seldom measured, since they are only used to check human safety.

Note that the off-diagonal elements of the aforesaid matrices represent the coupling between the phases (see Section 2.1).

It is important to note that the electrical components are not necessarily *reciprocal*. That is, the transfer functions from m to n and vice versa can be different. So, in general

$$\mathbf{Y}_{\Pi,m|(m,n)} \neq \mathbf{Y}_{\Pi,n|(m,n)} \quad (3.3)$$

$$\mathbf{Z}_{\text{T},(m,x)} \neq \mathbf{Z}_{\text{T},(n,x)} \quad (3.4)$$

The polyphase two-port equivalent circuits of the electrical components constitute the overall equivalent circuit of the grid. This equivalent circuit may contain *virtual polyphase nodes* $\mathcal{N}_{\text{virtual}}$, which are present in the model, but do not exist in reality. Namely, every T-section equivalent circuit contributes one virtual polyphase node (see Figure 3.1b).

3.1.2 Mathematical Description of the Equivalent Circuit of the Grid

Branch Graph and Shunt Graph

Let \mathcal{N} contain all polyphase nodes (i.e., physical and virtual ones):

$$\mathcal{N} := \mathcal{N}_{\text{physical}} \cup \mathcal{N}_{\text{virtual}} \quad (3.5)$$

The topology of the equivalent circuit of the grid is described by *directed graphs*, whose *vertices* and *edges* correspond to the nodes (i.e., polyphase nodes plus ground node, see Figure 3.2a) and the lumped elements of the equivalent circuit, respectively.

The *polyphase branches* \mathcal{L} are connections between pairs of polyphase nodes (see Figure 3.2b). More precisely, \mathcal{L} consists of two subsets \mathcal{L}_{Π} and \mathcal{L}_{T} , which are associated with the Π -section and T-section equivalent circuits, respectively. Namely (see Figure 3.1)

$$\mathcal{L} = \mathcal{L}_{\Pi} \cup \mathcal{L}_{\text{T}} \quad (3.6)$$

$$\mathcal{L}_{\Pi} \subseteq \mathcal{N}_{\text{physical}} \times \mathcal{N}_{\text{physical}} \quad (3.7)$$

$$\mathcal{L}_{\text{T}} \subseteq \mathcal{N}_{\text{physical}} \times \mathcal{N}_{\text{virtual}} \quad (3.8)$$

where \times is the *Cartesian product*. Jointly, \mathcal{N} and \mathcal{L} span the *branch graph* \mathfrak{B}

$$\mathfrak{B} := (\mathcal{N}, \mathcal{L}) \quad (3.9)$$

Let $E(\cdot)$ be the function which returns the edges of a graph. The *incoming branches* $E_{\text{in}}(\mathfrak{B}, n)$ and the *outgoing branches* $E_{\text{out}}(\mathfrak{B}, n)$ of \mathfrak{B} w.r.t. n are defined as

$$E_{\text{in}}(\mathfrak{B}, n) := \{\ell \in E(\mathfrak{B}) \mid \ell = (u, n), u \in V(\mathfrak{B})\} \quad (3.10)$$

$$E_{\text{out}}(\mathfrak{B}, n) := \{\ell \in E(\mathfrak{B}) \mid \ell = (n, v), v \in V(\mathfrak{B})\} \quad (3.11)$$

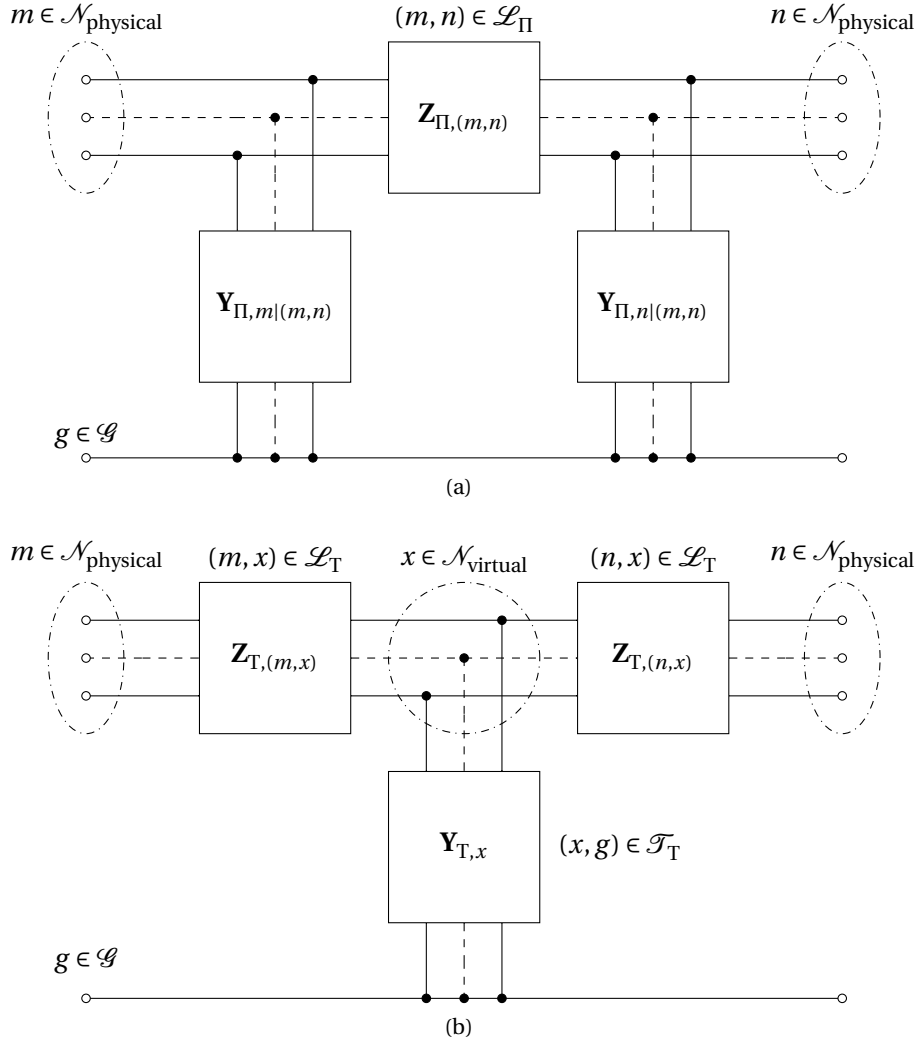


Figure 3.1 – Polyphase two-port equivalent circuits of the electrical components of the grid: (3.1a) Π -section equivalent circuit, (3.1b) T-section equivalent circuit.

The connectivity of \mathfrak{B} is described by the *incidence matrix* $\mathbf{A}_{\mathfrak{B}}$, which is defined as

$$\mathbf{A}_{\mathfrak{B}} : A_{\mathfrak{B},kn} = \begin{cases} -1 & \text{if } \ell_k \in E_{\text{in}}(\mathfrak{B}, n) \\ +1 & \text{if } \ell_k \in E_{\text{out}}(\mathfrak{B}, n) \\ 0 & \text{otherwise} \end{cases} \quad (3.12)$$

A directed graph is *weakly connected* if there exists a path, which need not respect the directions of the edges, between any pair of vertices. Let $V(\cdot)$ be the function which returns the vertices of a graph. As known from graph theory, it holds that (for proof, see [111])

Lemma 1. *If the branch graph \mathfrak{B} is weakly connected, then $\text{rank}(\mathbf{A}_{\mathfrak{B}}) = |V(\mathfrak{B})| - 1$.*

Now, consider a nonempty subset $\mathcal{M} \subsetneq \mathcal{N}$ of the nodes. The *internal branches* $E_{\text{int}}(\mathfrak{B}, \mathcal{M})$ of

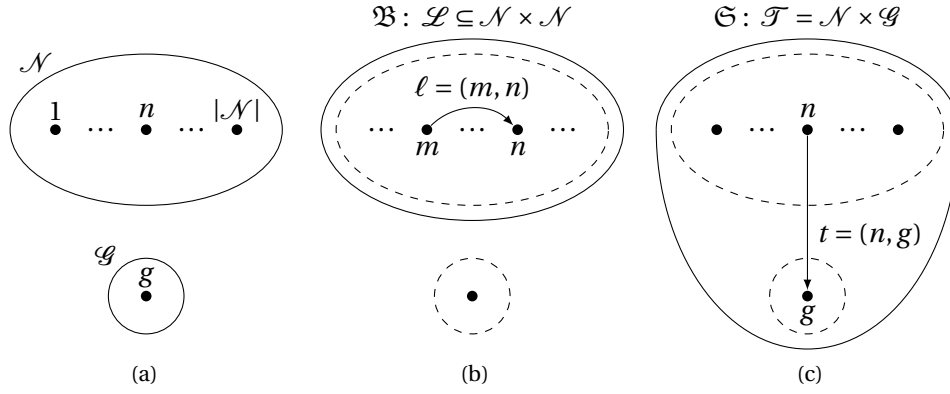


Figure 3.2 – Topology of the overall equivalent circuit of the grid: (3.2a) vertices \mathcal{N} and \mathcal{G} , (3.2b) edges \mathcal{L} of the branch graph \mathcal{B} , (3.2c) edges \mathcal{T} of the shunt graph \mathcal{S} .

\mathcal{B} w.r.t. \mathcal{M} are the branches which start and end in \mathcal{M} :

$$E_{\text{int}}(\mathcal{B}, \mathcal{M}) := \{(u, v) \in V(\mathcal{B}) \mid u, v \in \mathcal{M}\} \quad (3.13)$$

Let $\mathcal{M}_c := \mathcal{N} \setminus \mathcal{M}$ be the *complement* of \mathcal{M} in \mathcal{N} . The *cut-set* $E_{\text{cut}}(\mathcal{B}, \mathcal{M})$ of \mathcal{B} w.r.t. \mathcal{M} consists of the branches which start in \mathcal{M} and end in \mathcal{M}_c :

$$E_{\text{cut}}(\mathcal{B}, \mathcal{M}) := \{(u, v) \in V(\mathcal{B}) \mid u \in \mathcal{M}, v \in \mathcal{M}_c\} \quad (3.14)$$

The *polyphase shunts* \mathcal{T} are connections between the polyphase nodes and the ground node (see Figure 3.2c). \mathcal{T} includes the subset \mathcal{T}_T , which is associated with the virtual polyphase nodes originating from the T-section equivalent circuits. So (see Figure 3.1)

$$\mathcal{T} := \mathcal{N} \times \mathcal{G} \quad (3.15)$$

$$\mathcal{T}_T := \mathcal{N}_{\text{virtual}} \times \mathcal{G} \subsetneq \mathcal{T} \quad (3.16)$$

In analogy to the branch graph \mathcal{B} , the *shunt graph* \mathcal{S} is defined as

$$\mathcal{S} := (\mathcal{N} \cup \mathcal{G}, \mathcal{T}) \quad (3.17)$$

Associated Compound Electrical Parameters

The polyphase branches are related to the *longitudinal electrical parameters* of the electrical components of the grid. Every polyphase branch $\ell \in \mathcal{L}$ is associated with a *compound branch impedance matrix* \mathbf{Z}_ℓ . The \mathbf{Z}_ℓ directly correspond to the compound impedance matrices of the branch elements of the polyphase two-port equivalent circuits. More precisely, they are

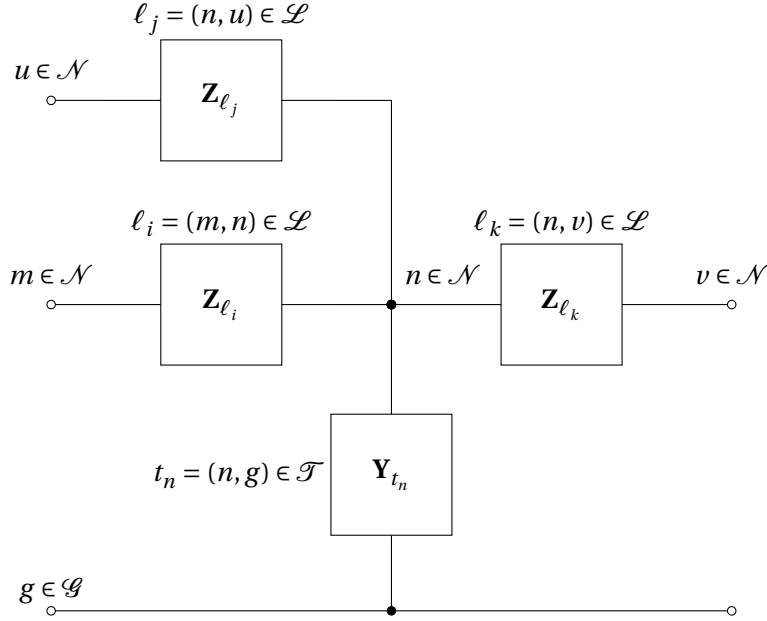


Figure 3.3 – Compound electrical parameters of the overall equivalent circuit of the grid: compound branch impedance matrices \mathbf{Z}_ℓ ($\ell \in \mathcal{L}$) and shunt admittance matrices \mathbf{Y}_t ($t \in \mathcal{T}$). For the sake of clarity, polyphase terminals and wires are shown by bundles only.

given by (see Figures 3.1 and 3.3)

$$\mathbf{Z}_\ell = \begin{cases} \mathbf{Z}_{\Pi,(m,n)} & \text{if } \ell = (m, n) \in \mathcal{L}_\Pi \\ \mathbf{Z}_{\text{T},(u,v)} & \text{if } \ell = (u, v) \in \mathcal{L}_\text{T} \end{cases} \quad (3.18)$$

Likewise, the polyphase shunts are related to the *transversal electrical parameters* of the electrical components of the grid. Every polyphase shunt $t \in \mathcal{T}$ is associated with a *compound shunt admittance matrix* \mathbf{Y}_t . In general, several Π -section equivalent circuits can be connected to the same node, and contribute to its shunt admittance. Define the aggregate compound shunt admittance matrix $\mathbf{Y}_{\Pi,n}$ due to the polyphase Π -section equivalent circuits connected to the polyphase node n as (see Figure 3.1a)

$$\mathbf{Y}_{\Pi,n} := \sum_{(n,m) \in \mathcal{L}_\Pi} \mathbf{Y}_{\Pi,n|(n,m)} + \sum_{(m,n) \in \mathcal{L}_\Pi} \mathbf{Y}_{\Pi,n|(m,n)} \quad (3.19)$$

Then, somewhat analogous to the \mathbf{Z}_ℓ , the \mathbf{Y}_t are given by (see Figures 3.1 and 3.3)

$$\mathbf{Y}_t = \begin{cases} \mathbf{Y}_{\Pi,n} & \text{if } t = (n, g) \in \mathcal{T} \setminus \mathcal{T}_\text{T} \\ \mathbf{Y}_{\text{T},x} & \text{if } t = (x, g) \in \mathcal{T}_\text{T} \end{cases} \quad (3.20)$$

3.1.3 Hypotheses with Respect to the Equivalent Circuit of the Grid

As to the compound electrical parameters \mathbf{Z}_ℓ and \mathbf{Y}_t , the following hypothesis is made:

Hypothesis 3 (Properties of \mathbf{Z}_ℓ and \mathbf{Y}_t). *The compound branch impedance matrices \mathbf{Z}_ℓ given by (3.18) are symmetric, invertible, and lossy:*

$$\forall \ell \in \mathcal{L} : \begin{cases} \mathbf{Z}_\ell = \mathbf{Z}_\ell^\top & (\text{symmetry}) \\ \exists \mathbf{Y}_\ell = \mathbf{Z}_\ell^{-1} & (\text{invertibility}) \\ \Re \{ \mathbf{Z}_\ell \} \geq \mathbf{0} & (\text{lossiness}) \end{cases} \quad (3.21)$$

Notably, this implies $\mathbf{Z}_\ell \neq \mathbf{0}$. The compound admittance matrices \mathbf{Y}_t given by (3.20), on the other hand, may be zero. Otherwise, they are also symmetric, invertible, and lossy:

$$t \in \mathcal{T} \text{ for which } \mathbf{Y}_t \neq \mathbf{0} : \begin{cases} \mathbf{Y}_t = \mathbf{Y}_t^\top & (\text{symmetry}) \\ \exists \mathbf{Z}_t = \mathbf{Y}_t^{-1} & (\text{invertibility}) \\ \Re \{ \mathbf{Y}_t \} \geq \mathbf{0} & (\text{lossiness}) \end{cases} \quad (3.22)$$

It is worth noting that the properties stated above are related to fundamental laws of physics. The symmetry property refers to the reciprocity of electromagnetism (which follows from Maxwell's equations), and the lossiness property is an inherent characteristic of real systems. Hypotheses 2–3 may not hold generally, but they do apply to a broad variety of components in practice. For instance, transmission lines, transformers, and various *Flexible Alternating-Current Transmission Systems* (FACTS) devices, such as series or shunt compensators, satisfy Hypotheses 2–3 (see Appendix A.2). Phase-shifting transformers, on the other hand, do not satisfy the symmetry property of Hypothesis 3.

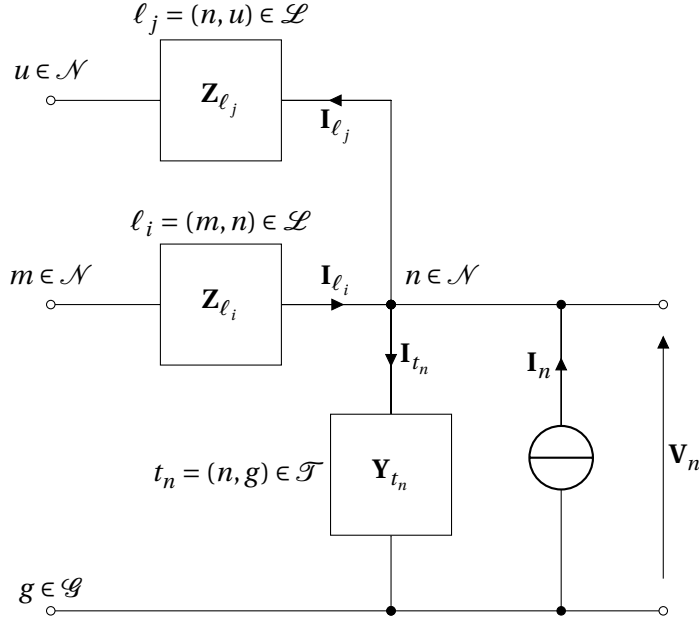


Figure 3.4 – Vectors of voltage and current phasors: phase-to-ground voltages \mathbf{V}_n ($n \in \mathcal{N}$), nodal injected currents \mathbf{I}_n ($n \in \mathcal{N}$), branch currents \mathbf{I}_ℓ ($\ell \in \mathcal{L}$), and shunt currents \mathbf{I}_t ($t \in \mathcal{T}$). For the sake of clarity, polyphase terminals and wires are shown by bundles only.

3.1.4 Construction of the Compound Admittance Matrix

Definition of Voltage and Current Phasors

Let $V_{n,p}$ and $I_{n,p}$ be the phasors of the phase-to-ground voltage and the nodal injected current, respectively, in phase $p \in \mathcal{P}$ of node $n \in \mathcal{N}$. Moreover, define \mathbf{V}_n and \mathbf{I}_n as the column vectors composed of all $V_{n,p}$ and $I_{n,p}$ of n (see Figure 3.4):

$$\mathbf{V}_n := \text{col}_{p \in \mathcal{P}}(V_{n,p}) \quad (3.23)$$

$$\mathbf{I}_n := \text{col}_{p \in \mathcal{P}}(I_{n,p}) \quad (3.24)$$

Analogously, define \mathbf{V} and \mathbf{I} as the block column vectors composed of all \mathbf{V}_n and \mathbf{I}_n :

$$\mathbf{V} := \text{col}_{n \in \mathcal{N}}(\mathbf{V}_n) \quad (3.25)$$

$$\mathbf{I} := \text{col}_{n \in \mathcal{N}}(\mathbf{I}_n) \quad (3.26)$$

Let $I_{\ell,p}$ and $I_{t,p}$ denote the phasors of the currents in phase $p \in \mathcal{P}$ of the branch $\ell \in \mathcal{L}$ and the shunt $t \in \mathcal{T}$, respectively. Moreover, analogous to \mathbf{I}_n , define \mathbf{I}_ℓ and \mathbf{I}_t as the column vectors containing all $I_{\ell,p}$ of ℓ or $I_{t,p}$ of t , respectively (see Figure 3.4):

$$\mathbf{I}_\ell := \text{col}_{n \in \mathcal{N}}(I_{\ell,p}) \quad (3.27)$$

$$\mathbf{I}_t := \text{col}_{n \in \mathcal{N}}(I_{t,p}) \quad (3.28)$$

Further, analogous to \mathbf{I} , define $\mathbf{I}_{\mathcal{L}}$ and $\mathbf{I}_{\mathcal{T}}$ as the block column vectors containing all \mathbf{I}_{ℓ} and \mathbf{I}_t , respectively:

$$\mathbf{I}_{\mathcal{L}} := \text{col}_{\ell \in \mathcal{L}}(\mathbf{I}_{\ell}) \quad (3.29)$$

$$\mathbf{I}_{\mathcal{T}} := \text{col}_{t \in \mathcal{T}}(\mathbf{I}_t) \quad (3.30)$$

Formulation of Kirchhoff's Current Law

By Kirchhoff's current law, the current injected into a node is the sum of all branch currents entering or leaving the said node plus the shunt current. Formally (see Figure 3.4)

$$\mathbf{I}_n = - \left(\sum_{\ell \in \mathbb{E}_{\text{in}}(\mathfrak{B}, n)} \mathbf{I}_{\ell} \right) + \left(\sum_{\ell \in \mathbb{E}_{\text{out}}(\mathfrak{B}, n)} \mathbf{I}_{\ell} \right) + \mathbf{I}_t \quad \forall n \in \mathcal{N}, t = (n, g) \quad (3.31)$$

Whether a branch current is entering or leaving the node is given by the corresponding entries of the branch incidence matrix $\mathbf{A}_{\mathfrak{B}}$ (3.12). Define the *polyphase branch incidence matrix* $\mathbf{A}_{\mathfrak{B}}^{\mathcal{P}}$ as the polyphase analogon of $\mathbf{A}_{\mathfrak{B}}$. More precisely

$$\mathbf{A}_{\mathfrak{B}}^{\mathcal{P}} := \mathbf{A}_{\mathfrak{B}} \otimes \text{diag}(\mathbf{1}_{|\mathcal{P}|}) \quad (3.32)$$

where $\text{diag}(\mathbf{1}_{|\mathcal{P}|})$ is the identity matrix of size $|\mathcal{P}| \times |\mathcal{P}|$, and \otimes is the Kronecker product. Then, (3.31) can be written compactly as (see [111])

$$\mathbf{I} = \left(\mathbf{A}_{\mathfrak{B}}^{\mathcal{P}} \right)^{\top} \mathbf{I}_{\mathcal{L}} + \mathbf{I}_{\mathcal{T}} \quad (3.33)$$

Formulation of Ohm's Law

Ohm's law relates the nodal injected currents \mathbf{I} with the phase-to-ground voltages \mathbf{V} through the *compound (nodal) admittance matrix* \mathbf{Y} (i.e., if it is formulated in admittance form).

$$\mathbf{I} = \mathbf{YV} \quad (3.34)$$

Subsequently, \mathbf{Y} is derived by transforming Kirchhoff's current law (3.33) into Ohm's law (3.34). To this end, $\mathbf{I}_{\mathcal{L}}$ and $\mathbf{I}_{\mathcal{T}}$ need to be expressed in function of \mathbf{V} .

Since the compound branch admittance matrices $\mathbf{Y}_{\ell} = \mathbf{Z}_{\ell}^{-1}$ do exist according to Hypothesis 3, and the polyphase shunts are characterized by compound shunt admittance matrices \mathbf{Y}_t , the currents flowing through the branches ℓ and the shunts t can be expressed as (see Figure 3.4)

$$\mathbf{I}_{\ell} = \mathbf{Y}_{\ell}(\mathbf{V}_m - \mathbf{V}_n) \quad \forall \ell = (m, n) \in \mathcal{L} \quad (3.35)$$

$$\mathbf{I}_t = \mathbf{Y}_t \mathbf{V}_n \quad \forall t = (n, g) \in \mathcal{T} \quad (3.36)$$

The *primitive compound branch admittance matrix* $\mathbf{Y}_{\mathcal{L}}$ and the *primitive compound shunt*

Chapter 3. Analysis of Equivalent Circuits of Polyphase Power Grids

admittance matrix $\mathbf{Y}_{\mathcal{F}}$ are block-diagonal matrices composed of the \mathbf{Y}_{ℓ} and \mathbf{Y}_t , respectively:

$$\mathbf{Y}_{\mathcal{L}} := \text{diag}_{\ell \in \mathcal{L}}(\mathbf{Y}_{\ell}) \quad (3.37)$$

$$\mathbf{Y}_{\mathcal{F}} := \text{diag}_{t \in \mathcal{F}}(\mathbf{Y}_t) \quad (3.38)$$

Using these definitions, (3.35) and (3.36) can be written compactly as (see [111])

$$\mathbf{I}_{\mathcal{L}} = \mathbf{Y}_{\mathcal{L}} \mathbf{A}_{\mathcal{B}}^{\mathcal{P}} \mathbf{V} \quad (3.39)$$

$$\mathbf{I}_{\mathcal{F}} = \mathbf{Y}_{\mathcal{F}} \mathbf{V} \quad (3.40)$$

These are the desired formulas for $\mathbf{I}_{\mathcal{L}}$ and $\mathbf{I}_{\mathcal{F}}$ in function of \mathbf{V} . Substitute (3.39) and (3.40) into Kirchhoff's current law (3.33) to obtain

$$\mathbf{I} = \left(\left(\mathbf{A}_{\mathcal{B}}^{\mathcal{P}} \right)^{\top} \mathbf{Y}_{\mathcal{L}} \mathbf{A}_{\mathcal{B}}^{\mathcal{P}} + \mathbf{Y}_{\mathcal{F}} \right) \mathbf{V} \quad (3.41)$$

By comparison with Ohm's law (3.34), it follows straightforward that (see [31,111])

$$\mathbf{Y} = \left(\mathbf{A}_{\mathcal{B}}^{\mathcal{P}} \right)^{\top} \mathbf{Y}_{\mathcal{L}} \mathbf{A}_{\mathcal{B}}^{\mathcal{P}} + \mathbf{Y}_{\mathcal{F}} \quad (3.42)$$

Properties of the Block Form of the Matrix

According to (3.25)–(3.26), \mathbf{V} and \mathbf{I} consist of blocks that correspond to the polyphase nodes. Hence, \mathbf{Y} can be written in block form as $\mathbf{Y} = (\mathbf{Y}_{mn})$, where $\mathbf{Y}_{m,n}$ is the block which relates \mathbf{I}_m with \mathbf{V}_n . As known from circuit theory (for proof, see [31,111])

Lemma 2. *The summation over a block row or column of the compound admittance matrix \mathbf{Y} produces the compound shunt admittance matrices \mathbf{Y}_t of the corresponding polyphase node. Formally*

$$\sum_{m \in \mathcal{N}} \mathbf{Y}_{nm} = \sum_{m \in \mathcal{N}} \mathbf{Y}_{ms} = \mathbf{Y}_t \quad \forall t = (n, g) \in \mathcal{F} \quad (3.43)$$

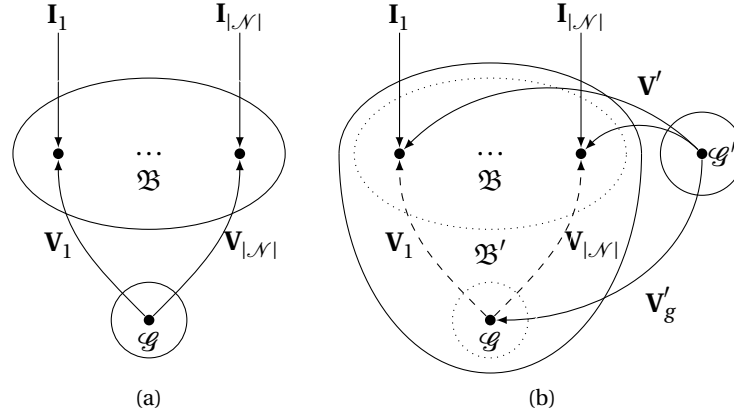


Figure 3.5 – Proof of Theorem 1: (3.5a) case 1: $\mathbf{Y}_t = \mathbf{0} \forall t \in \mathcal{T}$, (3.5b) case 2: $\exists t \in \mathcal{T}$ s.t. $\mathbf{Y}_t \neq \mathbf{0}$. The surfaces indicate weakly connected graphs.

3.2 On the Rank Properties of the Compound Admittance Matrix

3.2.1 The Rank of the Overall Matrix

The properties listed in Hypotheses 1–3, along with the connectivity of the branch graph \mathcal{B} , allow to determine the rank of the compound admittance matrix \mathbf{Y} . Namely

Theorem 1 (Rank of \mathbf{Y}). *If the Hypotheses 1–3 are satisfied, and the branch graph $\mathcal{B} = (\mathcal{N}, \mathcal{L})$ is weakly connected, then it holds that*

$$\text{rank}(\mathbf{Y}) = \begin{cases} (|\mathcal{N}| - 1) |\mathcal{P}| & \text{if } \mathbf{Y}_t = \mathbf{0} \forall t \in \mathcal{T} \\ |\mathcal{N}| |\mathcal{P}| & \text{otherwise} \end{cases} \quad (3.44)$$

Proof. (Case 1: $\mathbf{Y}_t = \mathbf{0} \forall t \in \mathcal{T}$, see Figure 3.5a). $\mathbf{Y}_t = \mathbf{0} \forall t \in \mathcal{T}$ implies that $\mathbf{Y}_{\mathcal{L}} = \mathbf{0}$, see (3.38). Therefore, according to (3.42), \mathbf{Y} is given by

$$\mathbf{Y} = \left(\mathbf{A}_{\mathcal{B}}^{\mathcal{P}} \right)^{\top} \mathbf{Y}_{\mathcal{L}} \mathbf{A}_{\mathcal{B}}^{\mathcal{P}} \quad (3.45)$$

Recall from (3.37) that $\mathbf{Y}_{\mathcal{L}}$ is block-diagonal. Moreover, by Hypothesis 3, its blocks \mathbf{Y}_{ℓ} ($\ell \in \mathcal{L}$) are symmetric and invertible. Therefore, $\mathbf{Y}_{\mathcal{L}}$ is also symmetric and invertible. By consequence, the matrix $\mathbf{Y}_{\mathcal{L}}$ can be factorized into a unitary matrix $\mathbf{D}_{\mathcal{L}}$ and a positive diagonal matrix $\mathbf{D}_{\mathcal{L}}$ using the so-called Autonne-Takagi factorization (see Lemma 10 in Appendix A.1.3):

$$\mathbf{Y}_{\mathcal{L}} = \mathbf{U}_{\mathcal{L}}^{\top} \mathbf{D}_{\mathcal{L}} \mathbf{U}_{\mathcal{L}} \quad (3.46)$$

The matrix $\mathbf{D}_{\mathcal{L}}$ can be written as the square of a positive diagonal matrix $\mathbf{E}_{\mathcal{L}}$:

$$\mathbf{D}_{\mathcal{L}} = \mathbf{E}_{\mathcal{L}}^{\top} \mathbf{E}_{\mathcal{L}} \quad (3.47)$$

Chapter 3. Analysis of Equivalent Circuits of Polyphase Power Grids

Note that the diagonal elements of $\mathbf{E}_{\mathcal{L}}$ are the square roots of the diagonal elements of $\mathbf{D}_{\mathcal{L}}$. Substitute (3.46) and (3.47) into (3.45), and express \mathbf{Y} as

$$\mathbf{Y} = \mathbf{M}_{\mathcal{L}}^{\top} \mathbf{M}_{\mathcal{L}}, \quad \mathbf{M}_{\mathcal{L}} := \mathbf{E}_{\mathcal{L}} \mathbf{U}_{\mathcal{L}} \mathbf{A}_{\mathfrak{B}}^{\mathcal{P}} \quad (3.48)$$

The product of a matrix and its transpose has the same rank as the original matrix (see Lemma 4 in Appendix A.1.1). Accordingly

$$\text{rank}(\mathbf{Y}) = \text{rank}(\mathbf{M}_{\mathcal{L}}^{\top} \mathbf{M}_{\mathcal{L}}) = \text{rank}(\mathbf{M}) = \text{rank}(\mathbf{E}_{\mathcal{L}} \mathbf{U}_{\mathcal{L}} \mathbf{A}_{\mathfrak{B}}^{\mathcal{P}}) \quad (3.49)$$

Note well that $\mathbf{E}_{\mathcal{L}}$ and $\mathbf{U}_{\mathcal{L}}$ are nonsingular, because they are positive diagonal and unitary, respectively. As known, the multiplication of an arbitrary matrix with a nonsingular matrix preserves the rank of the former (see Lemma 5 in Appendix A.1.1). Therefore

$$\text{rank}(\mathbf{Y}) = \text{rank}(\mathbf{E}_{\mathcal{L}} \mathbf{U}_{\mathcal{L}} \mathbf{A}_{\mathfrak{B}}^{\mathcal{P}}) = \text{rank}(\mathbf{A}_{\mathfrak{B}}^{\mathcal{P}}) \quad (3.50)$$

Recall from (3.32) that $\mathbf{A}_{\mathfrak{B}}^{\mathcal{P}} := \mathbf{A}_{\mathfrak{B}} \otimes \text{diag}(\mathbf{1}_{|\mathcal{P}|})$. As known, the rank of the Kronecker product of two matrices is given by the product of the ranks of the said matrices (see Lemma 13 in Appendix A.1.4). Accordingly

$$\text{rank}(\mathbf{Y}) = \text{rank}(\mathbf{A}_{\mathfrak{B}}^{\mathcal{P}}) = \text{rank}(\mathbf{A}_{\mathfrak{B}} \otimes \text{diag}(\mathbf{1}_{|\mathcal{P}|})) = \text{rank}(\mathbf{A}_{\mathfrak{B}}) \cdot |\mathcal{P}| \quad (3.51)$$

The graph $\mathfrak{B} = (\mathcal{N}, \mathcal{L})$ is assumed to be weakly connected. Therefore, according to Lemma 1 (see Section 3.1), $\text{rank}(\mathbf{A}_{\mathfrak{B}}) = |\mathcal{N}| - 1$. By consequence

$$\text{rank}(\mathbf{Y}) = \text{rank}(\mathbf{A}_{\mathfrak{B}}) \cdot |\mathcal{P}| = (|\mathcal{N}| - 1) |\mathcal{P}| \quad (3.52)$$

This proves the first part of the claim. \square

Proof. (Case 2: $\exists t \in \mathcal{T}$ s.t. $\mathbf{Y}_t \neq \mathbf{0}$, see Figure 3.5b). Introduce the virtual ground node \mathcal{G}' , and build an augmented grid, in which the physical ground node \mathcal{G} is treated as polyphase node:

$$\mathcal{N}' := \mathcal{N} \cup \mathcal{G} \quad (3.53)$$

Moreover, let \mathbf{V}' and \mathbf{V}'_g be the voltages of the polyphase nodes \mathcal{N} and physical ground \mathcal{G} , respectively, referenced w.r.t. the virtual ground \mathcal{G}' . Obviously, polyphase shunts are treated as polyphase branches in the augmented grid. Define

$$\mathcal{L}' := \mathcal{L} \cup \{t \in \mathcal{T} \mid \mathbf{Y}_t \neq \mathbf{0}\} \quad (3.54)$$

which is the analogon of \mathcal{L} for the augmented grid. By construction

$$\mathbf{Z}_{\ell'} = \begin{cases} \mathbf{Z}_{\ell} & \text{if } \ell' = \ell \in \mathcal{L} \\ \mathbf{Y}_t^{-1} & \text{if } \ell' = t \in \mathcal{L}' \setminus \mathcal{L} \end{cases} \quad (3.55)$$

3.2. On the Rank Properties of the Compound Admittance Matrix

Recall Hypothesis 3, which states that \mathbf{Z}_ℓ ($\ell \in \mathcal{L}$) and \mathbf{Y}_t ($t \in \mathcal{T}$) are symmetric and invertible. Therefore, the $\mathbf{Z}_{\ell'}$ ($\ell' \in \mathcal{L}'$) are symmetric and invertible. Define

$$\mathfrak{B}' := (\mathcal{N}', \mathcal{L}') \quad (3.56)$$

which is the analogon of \mathfrak{B} for the augmented grid. Note that \mathfrak{B}' is obtained from \mathfrak{B} by adding one vertex (i.e., the virtual ground) and at least one edge (i.e., a polyphase shunt). Therefore, since \mathfrak{B} is weakly connected, \mathfrak{B}' is weakly connected. Define

$$\mathcal{T}' := \mathcal{N}' \times \mathcal{G}' \quad (3.57)$$

which is the analogon of \mathcal{T} for the augmented grid. By construction

$$\mathbf{Y}_{t'} = \mathbf{0} \quad \forall t' \in \mathcal{T}' \quad (3.58)$$

In that sense, the augmented grid corresponds to case 1, which has already been proven. By consequence, the compound admittance matrix \mathbf{Y}' of the augmented grid has rank

$$\text{rank}(\mathbf{Y}') = (|\mathcal{N}'| - 1)|\mathcal{P}| = |\mathcal{N}||\mathcal{P}| \quad (3.59)$$

Now, it is shown that \mathbf{Y}' and \mathbf{Y} have the same rank. For this purpose, Ohm's law is formulated for the augmented grid using the voltages \mathbf{V}' and \mathbf{V}'_g , which are referenced w.r.t. \mathcal{G}' :

$$\mathbf{Y}' : \begin{bmatrix} \mathbf{I} \\ \mathbf{I}_g \end{bmatrix} = \begin{bmatrix} \mathbf{Y} & -\text{col}_{t \in \mathcal{T}}(\mathbf{Y}_t) \\ -\text{row}_{t \in \mathcal{T}}(\mathbf{Y}_t) & \sum_{t \in \mathcal{T}} \mathbf{Y}_t \end{bmatrix} \begin{bmatrix} \mathbf{V}' \\ \mathbf{V}'_g \end{bmatrix} \quad (3.60)$$

It is known from linear algebra that elementary row/column operations preserve the rank. Thus, the first $|\mathcal{N}|$ block rows/columns of \mathbf{Y}' can be added to the last one without changing the rank. By Lemma 2, the summation of the block rows or block columns of \mathbf{Y} yields $\text{row}_{t \in \mathcal{T}}(\mathbf{Y}_t)$ and $\text{col}_{t \in \mathcal{T}}(\mathbf{Y}_t)$, respectively. Therefore

$$\left[\begin{array}{c|c} \mathbf{Y} & -\text{col}_{t \in \mathcal{T}}(\mathbf{Y}_t) \\ \hline -\text{row}_{t \in \mathcal{T}}(\mathbf{Y}_t) & \sum_{t \in \mathcal{T}} \mathbf{Y}_t \end{array} \right] \left| \begin{array}{l} \text{row}_{|\mathcal{N}|+1} += \sum_{n \in \mathcal{N}} \text{row}_n \end{array} \right. \quad (3.61)$$

$$\left[\begin{array}{c|c} \mathbf{Y} & -\text{col}_{t \in \mathcal{T}}(\mathbf{Y}_t) \\ \hline \mathbf{0} & \mathbf{0} \end{array} \right] \left| \begin{array}{l} \text{col}_{|\mathcal{N}|+1} += \sum_{n \in \mathcal{N}} \text{col}_n \end{array} \right. \quad (3.62)$$

$$\left[\begin{array}{c|c} \mathbf{Y} & \mathbf{0} \\ \hline \mathbf{0} & \mathbf{0} \end{array} \right] \quad (3.63)$$

So, $\text{rank}(\mathbf{Y}') = \text{rank}(\mathbf{Y})$. Recall from (3.59) that $\text{rank}(\mathbf{Y}') = |\mathcal{N}||\mathcal{P}|$. By consequence

$$\text{rank}(\mathbf{Y}') = \text{rank}(\mathbf{Y}) = |\mathcal{N}||\mathcal{P}| \quad (3.64)$$

This proves the second part of the claim. \square

3.2.2 The Rank of the Diagonal Blocks

If the compound impedance matrices \mathbf{Z}_ℓ are even *strictly lossy* (i.e., $\Re\{\mathbf{Z}_\ell\} > 0 \forall \ell \in \mathcal{L}$), then the diagonal blocks of the compound admittance matrix \mathbf{Y} have full rank. Namely

Theorem 2 (Rank of the Diagonal Blocks of \mathbf{Y}). *Suppose that Hypotheses 1–3 are satisfied, and that the branch graph $\mathfrak{B} = (\mathcal{N}, \mathcal{L})$ is weakly connected. If the compound branch impedance matrices \mathbf{Z}_ℓ ($\ell \in \mathcal{L}$) are strictly lossy*

$$\Re\{\mathbf{Z}_\ell\} > 0 \quad \forall \ell \in \mathcal{L} \quad (3.65)$$

then the diagonal blocks of the compound admittance matrix \mathbf{Y} have full rank

$$\text{rank}(\mathbf{Y}_{\mathcal{M} \times \mathcal{M}}) = |\mathcal{M}| |\mathcal{P}| \quad \forall \mathcal{M} \subsetneq \mathcal{N} \quad (3.66)$$

Proof. Define $\mathcal{M}_\mathcal{C} := \mathcal{N} \setminus \mathcal{M}$, and write Ohm's law (3.34) in block form:

$$\begin{bmatrix} \mathbf{I}_{\mathcal{M}} \\ \mathbf{I}_{\mathcal{M}_\mathcal{C}} \end{bmatrix} = \begin{bmatrix} \mathbf{Y}_{\mathcal{M} \times \mathcal{M}} & \mathbf{Y}_{\mathcal{M} \times \mathcal{M}_\mathcal{C}} \\ \mathbf{Y}_{\mathcal{M}_\mathcal{C} \times \mathcal{M}} & \mathbf{Y}_{\mathcal{M}_\mathcal{C} \times \mathcal{M}_\mathcal{C}} \end{bmatrix} \begin{bmatrix} \mathbf{V}_{\mathcal{M}} \\ \mathbf{V}_{\mathcal{M}_\mathcal{C}} \end{bmatrix} \quad (3.67)$$

$\mathbf{Y}_{\mathcal{M} \times \mathcal{M}}$ relates $\mathbf{I}_{\mathcal{M}}$ and $\mathbf{V}_{\mathcal{M}}$ for $\mathbf{V}_{\mathcal{M}_\mathcal{C}} = \mathbf{0}$. Since $\mathbf{V}_{\mathcal{M}}$ and $\mathbf{V}_{\mathcal{M}_\mathcal{C}}$ are referenced w.r.t. the ground (Hypothesis 1), $\mathbf{Y}_{\mathcal{M} \times \mathcal{M}}$ can be interpreted as compound admittance matrix of a fictitious grid, in which the polyphase nodes $\mathcal{M}_\mathcal{C}$ are short-circuited. The internal branches $\mathcal{E}_{\text{int}}(\mathfrak{B}, \mathcal{M})$ of \mathfrak{B} w.r.t. \mathcal{M} are not affected by this fictitious process. The cut-sets $\mathcal{E}_{\text{cut}}(\mathfrak{B}, \mathcal{M})$ and $\mathcal{E}_{\text{cut}}(\mathfrak{B}, \mathcal{M}_\mathcal{C})$ of \mathfrak{B} w.r.t. \mathcal{M} , which connect \mathcal{M} and $\mathcal{M}_\mathcal{C}$, are turned from polyphase branches into shunts. The branch graph \mathcal{C} of the fictitious grid is given by

$$\mathcal{C} := (\mathcal{M}, \mathcal{E}_{\text{int}}(\mathfrak{B}, \mathcal{M})) \quad (3.68)$$

In general, \mathcal{C} is disconnected (see Figure 3.6). However, as \mathfrak{B} is weakly connected as a whole, there exists a partition $\{\mathcal{M}_k \mid k \in \mathcal{K}\}$ of \mathcal{M} , such that the subgraphs \mathcal{C}_k of \mathfrak{B} w.r.t. \mathcal{M}_k

$$\mathcal{C}_k := (\mathcal{M}_k, \mathcal{E}_{\text{int}}(\mathfrak{B}, \mathcal{M}_k)) \quad (3.69)$$

are each weakly connected, but mutually disconnected (see Figure 3.6). By consequence, $\mathbf{Y}_{\mathcal{M} \times \mathcal{M}}$ is block-diagonal with blocks $\mathbf{Y}_{\mathcal{M}_k \times \mathcal{M}_k}$:

$$\mathbf{Y}_{\mathcal{M} \times \mathcal{M}} = \text{diag}_{k \in \mathcal{K}} \left(\mathbf{Y}_{\mathcal{M}_k \times \mathcal{M}_k} \right) \quad (3.70)$$

The blocks $\mathbf{Y}_{\mathcal{M}_k \times \mathcal{M}_k}$ can be interpreted as compound admittance matrices of fictitious grids, in which the polyphase nodes $(\mathcal{M}_k)_\mathcal{C} := \mathcal{N} \setminus \mathcal{M}_k$ are short-circuited. Define \mathcal{L}_k and \mathcal{T}_k as the polyphase branches and shunts of the fictitious grid associated with \mathcal{M}_k :

$$\mathcal{L}_k := \mathcal{E}(\mathcal{C}_k) = \mathcal{E}_{\text{int}}(\mathfrak{B}, \mathcal{M}_k) \quad (3.71)$$

$$\mathcal{T}_k := \mathcal{M}_k \times \mathcal{G} \quad (3.72)$$

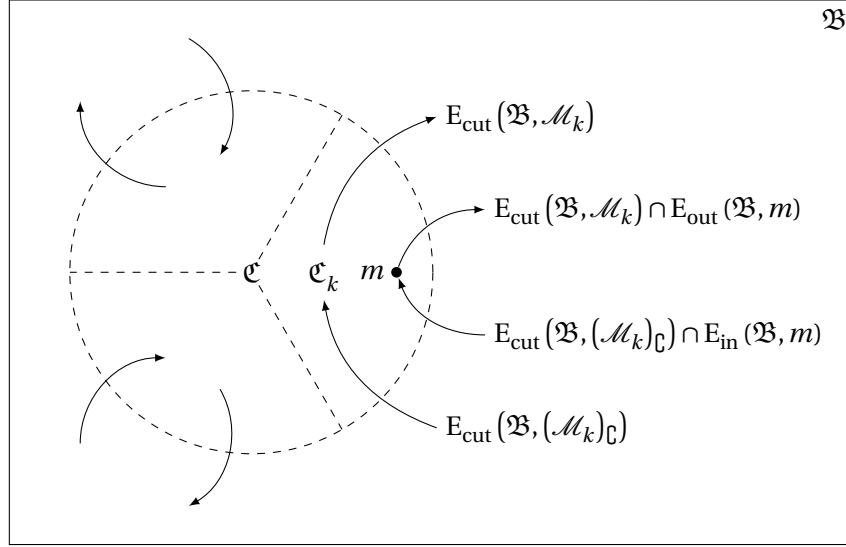


Figure 3.6 – Proof of Theorem 2: branch graphs, cut-sets, and connectivity in the fictitious grid. The surfaces indicate weakly connected graphs.

Furthermore, let $\tilde{\mathbf{Z}}_\ell$ and $\tilde{\mathbf{Y}}_t$ be the associated compound branch impedance matrices and compound shunt admittance matrices, respectively. Now, it is shown that $\tilde{\mathbf{Z}}_\ell$ and $\tilde{\mathbf{Y}}_t$ satisfy Hypothesis 3. Since the branches \mathcal{L}_k are internal w.r.t. the nodes \mathcal{M}_k , they are not affected by the fictitious short-circuiting of other nodes $(\mathcal{M}_k)_C$. By consequence

$$\tilde{\mathbf{Z}}_\ell = \mathbf{Z}_\ell \quad \forall \ell \in \mathcal{L}_k \quad (3.73)$$

Obviously, the properties of Hypothesis 3 w.r.t. \mathbf{Z}_ℓ also apply to $\tilde{\mathbf{Z}}_\ell$. The branches $E_{\text{cut}}(\mathfrak{B}, \mathcal{M}_k)$ and $E_{\text{cut}}(\mathfrak{B}, (\mathcal{M}_k)_C)$, which connect the nodes \mathcal{M}_k and $(\mathcal{M}_k)_C$, become shunts (see Figure 3.6). Let $\mathcal{X}(\mathfrak{B}, \mathcal{M}_k, m)$ be the branches starting or ending in the node $m \in \mathcal{M}_k$, which are turned into shunts by the fictitious short-circuiting of the nodes $(\mathcal{M}_k)_C$. Formally (see Figure 3.6)

$$\mathcal{X}(\mathfrak{B}, \mathcal{M}_k, m) := \{E_{\text{cut}}(\mathfrak{B}, \mathcal{M}_k) \cap E_{\text{out}}(\mathfrak{B}, m)\} \cup \{E_{\text{cut}}(\mathfrak{B}, (\mathcal{M}_k)_C) \cap E_{\text{in}}(\mathfrak{B}, m)\} \quad (3.74)$$

By consequence, the $\tilde{\mathbf{Y}}_t$ are given by (see Figure 3.7)

$$t = (m, g) \in \mathcal{T}_k: \quad \tilde{\mathbf{Y}}_t = \mathbf{Y}_t + \sum_{\ell \in \mathcal{X}(\mathfrak{B}, \mathcal{M}_k, m)} \mathbf{Z}_\ell^{-1} \quad (3.75)$$

According to Hypothesis 3 and the conditions of Theorem 2, the \mathbf{Z}_ℓ are symmetric, invertible, and strictly lossy (i.e., $\Re\{\mathbf{Z}_\ell\} > 0$). As known, a symmetric matrix with positive definite real part is invertible, and its inverse has the same properties (see Lemma 8 in Appendix A.1.2). Therefore, \mathbf{Z}_ℓ^{-1} is symmetric, invertible, and strictly lossy. If the sum in (3.75) is nonempty, then $\tilde{\mathbf{Y}}_t$ is symmetric, has positive definite real part, and is thus invertible. If the sum in (3.75) is empty, then $\tilde{\mathbf{Y}}_t = \mathbf{Y}_t$. In both cases, $\tilde{\mathbf{Y}}_t$ satisfies Hypothesis 3.

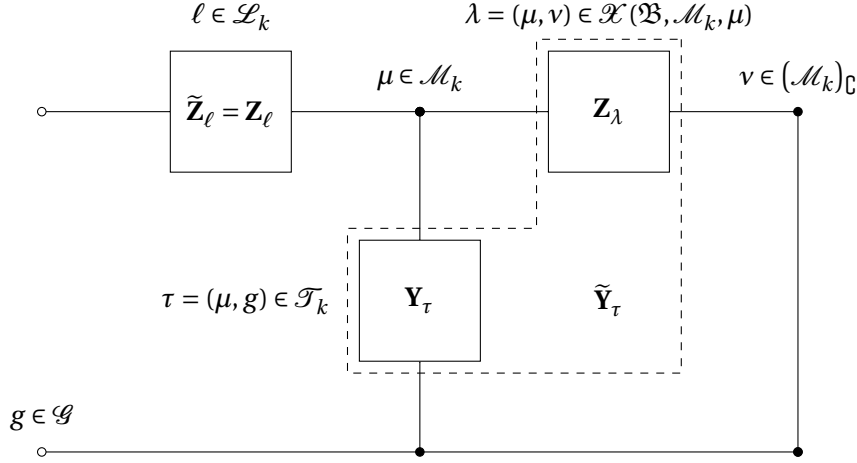


Figure 3.7 – Proof of Theorem 2: compound branch impedances $\tilde{\mathbf{Z}}_\ell$ and compound shunt admittances $\tilde{\mathbf{Y}}_\tau$ in the fictitious grid (i.e., where the polyphase nodes $(\mathcal{M}_k)_\mathbb{C}$ are grounded).

Since \mathfrak{B} is weakly connected, there exists at least one node $\mu \in \mathcal{M}_k$ in every \mathcal{M}_k such that $\mathcal{X}(\mathfrak{B}, \mathcal{M}_k, \mu)$ is nonempty. Hence, there exists a branch $\lambda \in \mathcal{X}(\mathfrak{B}, \mathcal{M}_k, \mu)$ of the original grid, whose other end is short-circuited in the fictitious grid (see Figure 3.7). Formally

$$\forall \mathcal{M}_k: \exists \mu \in \mathcal{M}_k \text{ s.t. } \mathcal{X}(\mathfrak{B}, \mathcal{M}_k, \mu) \neq \emptyset \iff \exists \lambda \in \mathcal{X}(\mathfrak{B}, \mathcal{M}_k, \mu) \quad (3.76)$$

The shunt $\tau = (\mu, g)$ has $\tilde{\mathbf{Y}}_\tau \neq \mathbf{0}$, because \mathbf{Z}_λ^{-1} contributes to $\tilde{\mathbf{Y}}_\tau$ (see Figure 3.7). In summary, the fictitious grid associated with \mathcal{M}_k consists of branch and shunt elements which satisfy Hypothesis 3, and there is at least one shunt with nonzero admittance. According to Theorem 1, its compound admittance matrix $\mathbf{Y}_{\mathcal{M}_k \times \mathcal{M}_k}$ therefore has full rank:

$$\text{rank}\left(\mathbf{Y}_{\mathcal{M}_k \times \mathcal{M}_k}\right) = |\mathcal{M}_k| |\mathcal{P}| \quad \forall k \in \mathcal{K} \quad (3.77)$$

Recall from (3.70) that $\mathbf{Y}_{\mathcal{M} \times \mathcal{M}}$ is block-diagonal with blocks $\mathbf{Y}_{\mathcal{M}_k \times \mathcal{M}_k}$. By consequence

$$\text{rank}\left(\mathbf{Y}_{\mathcal{M} \times \mathcal{M}}\right) = \sum_{k \in \mathcal{K}} \text{rank}\left(\mathbf{Y}_{\mathcal{M}_k \times \mathcal{M}_k}\right) = |\mathcal{P}| \sum_{k \in \mathcal{K}} |\mathcal{M}_k| = |\mathcal{P}| |\mathcal{M}| \quad (3.78)$$

This proves the claim. □

3.3 On the Feasibility of Kron Reduction

Recall that the compound admittance matrix \mathbf{Y} relates the nodal injected current phasors \mathbf{I} with the nodal phase-to-ground voltage phasors \mathbf{V} . Let \mathcal{Z} a set of *zero-injection nodes*, and $\mathcal{Z}_c := \mathcal{N} \setminus \mathcal{Z}$ its complement in \mathcal{N} . Accordingly, (3.34) can be written in block form as

$$\begin{bmatrix} \mathbf{I}_{\mathcal{Z}_c} \\ \mathbf{I}_{\mathcal{Z}} \end{bmatrix} = \begin{bmatrix} \mathbf{Y}_{\mathcal{Z}_c \times \mathcal{Z}_c} & \mathbf{Y}_{\mathcal{Z}_c \times \mathcal{Z}} \\ \mathbf{Y}_{\mathcal{Z} \times \mathcal{Z}_c} & \mathbf{Y}_{\mathcal{Z} \times \mathcal{Z}} \end{bmatrix} \begin{bmatrix} \mathbf{V}_{\mathcal{Z}_c} \\ \mathbf{V}_{\mathcal{Z}} \end{bmatrix} \quad (3.79)$$

where $\mathbf{I}_{\mathcal{Z}} = \mathbf{0}$ (i.e., zero injections). As known from power system analysis, the variables $\mathbf{V}_{\mathcal{Z}}$ can be eliminated via KR, if the diagonal block $\mathbf{Y}_{\mathcal{Z} \times \mathcal{Z}}$ of \mathbf{Y} is invertible (see [28] and Section 2.1). This yields a reduced system of linear equations, in which only the variables $\mathbf{V}_{\mathcal{Z}_c}$ remain.

Theorem 2 guarantees that the diagonal blocks of \mathbf{Y} have full rank, and can therefore provide a guarantee for the feasibility of KR (i.e., if the theorem applies). This is proven subsequently.

3.3.1 Reduction of a Single Set of Zero-Injection Nodes

First, consider that the entire set \mathcal{Z} is to be reduced “en bloc”. That is, KR is applied to all polyphase nodes in \mathcal{Z} in parallel. In this case, the following property holds:

Corollary 1 (KR). *Suppose that Theorem 2 applies. Let \mathcal{Z} be a set of zero-injection nodes, and \mathcal{Z}_c its complement in \mathcal{N} . That is*

$$\mathcal{Z} : \mathcal{Z} \subsetneq \mathcal{N}, \mathcal{Z} \neq \emptyset \text{ s.t. } \mathbf{I}_{\mathcal{Z}} = \mathbf{0} \quad (3.80)$$

$$\mathcal{Z}_c := \mathcal{N} \setminus \mathcal{Z} \quad (3.81)$$

Then, $\mathbf{V}_{\mathcal{Z}}$ is a linear function of $\mathbf{V}_{\mathcal{Z}_c}$, namely

$$\mathbf{V}_{\mathcal{Z}} = -\mathbf{Y}_{\mathcal{Z} \times \mathcal{Z}}^{-1} \mathbf{Y}_{\mathcal{Z} \times \mathcal{Z}_c} \mathbf{V}_{\mathcal{Z}_c} \quad (3.82)$$

and can therefore be eliminated from the admittance equation (3.34). The reduced system of linear equations is described by the Schur complement of \mathbf{Y} w.r.t. $\mathbf{Y}_{\mathcal{Z} \times \mathcal{Z}}$. Formally

$$\mathbf{I}_{\mathcal{Z}_c} = \hat{\mathbf{Y}} \mathbf{V}_{\mathcal{Z}_c}, \quad \hat{\mathbf{Y}} = \mathbf{Y} / \mathbf{Y}_{\mathcal{Z} \times \mathcal{Z}} = \mathbf{Y}_{\mathcal{Z}_c \times \mathcal{Z}_c} - \mathbf{Y}_{\mathcal{Z}_c \times \mathcal{Z}} \mathbf{Y}_{\mathcal{Z} \times \mathcal{Z}}^{-1} \mathbf{Y}_{\mathcal{Z} \times \mathcal{Z}_c} \quad (3.83)$$

Every diagonal block of the reduced compound admittance matrix $\hat{\mathbf{Y}}$ has full rank. Formally

$$\text{rank}(\hat{\mathbf{Y}}_{\mathcal{M} \times \mathcal{M}}) = |\mathcal{M}| |\mathcal{P}| \quad \forall \mathcal{M} \subsetneq \mathcal{Z}_c \quad (3.84)$$

In other words, the reduction preserves the rank property stated in Theorem 2.

Chapter 3. Analysis of Equivalent Circuits of Polyphase Power Grids

Proof. By (3.81), \mathcal{Z} and \mathcal{Z}_c form a partition of \mathcal{N} . Hence, the admittance equations (3.34) can be written in block form as

$$\begin{bmatrix} \mathbf{I}_{\mathcal{Z}_c} \\ \mathbf{I}_{\mathcal{Z}} \end{bmatrix} = \begin{bmatrix} \mathbf{Y}_{\mathcal{Z}_c \times \mathcal{Z}_c} & \mathbf{Y}_{\mathcal{Z}_c \times \mathcal{Z}} \\ \mathbf{Y}_{\mathcal{Z} \times \mathcal{Z}_c} & \mathbf{Y}_{\mathcal{Z} \times \mathcal{Z}} \end{bmatrix} \begin{bmatrix} \mathbf{V}_{\mathcal{Z}_c} \\ \mathbf{V}_{\mathcal{Z}} \end{bmatrix} \quad (3.85)$$

According to Theorem 2, $\mathbf{Y}_{\mathcal{Z} \times \mathcal{Z}}$ has full rank, and is thus invertible. So, the second block row of (3.85) can be solved for $\mathbf{V}_{\mathcal{Z}}$. This yields

$$\mathbf{V}_{\mathcal{Z}} = \mathbf{Y}_{\mathcal{Z} \times \mathcal{Z}}^{-1} \left(\mathbf{I}_{\mathcal{Z}} - \mathbf{Y}_{\mathcal{Z} \times \mathcal{Z}_c} \mathbf{V}_{\mathcal{Z}_c} \right) \quad (3.86)$$

By assumption (3.80), $\mathbf{I}_{\mathcal{Z}} = \mathbf{0}$. Therefore, (3.86) simplifies to

$$\mathbf{V}_{\mathcal{Z}} = -\mathbf{Y}_{\mathcal{Z} \times \mathcal{Z}}^{-1} \mathbf{Y}_{\mathcal{Z} \times \mathcal{Z}_c} \mathbf{V}_{\mathcal{Z}_c} \quad (3.87)$$

which proves the first claim (3.82) of Corollary 1. Substitute (3.87) into the second block row of (3.85). This yields

$$\mathbf{I}_{\mathcal{Z}_c} = \mathbf{Y}_{\mathcal{Z}_c \times \mathcal{Z}_c} \mathbf{V}_{\mathcal{Z}_c} + \mathbf{Y}_{\mathcal{Z}_c \times \mathcal{Z}} \mathbf{V}_{\mathcal{Z}} \quad (3.88)$$

$$= \left(\mathbf{Y}_{\mathcal{Z}_c \times \mathcal{Z}_c} - \mathbf{Y}_{\mathcal{Z}_c \times \mathcal{Z}} \mathbf{Y}_{\mathcal{Z} \times \mathcal{Z}}^{-1} \mathbf{Y}_{\mathcal{Z} \times \mathcal{Z}_c} \right) \mathbf{V}_{\mathcal{Z}_c} \quad (3.89)$$

$$= (\mathbf{Y} / \mathbf{Y}_{\mathcal{Z} \times \mathcal{Z}}) \mathbf{V}_{\mathcal{Z}_c} \quad (3.90)$$

which proves the second claim (3.83) of Corollary 1. As known from linear algebra, the Schur complement can be computed blockwise (see Lemma 12 in Appendix A.1.4). More precisely, the diagonal block $\hat{\mathbf{Y}}_{\mathcal{M} \times \mathcal{M}}$ of $\hat{\mathbf{Y}}$ associated with a subset $\mathcal{M} \subsetneq \mathcal{Z}_c$ is given by

$$\hat{\mathbf{Y}}_{\mathcal{M} \times \mathcal{M}} = (\mathbf{Y} / \mathbf{Y}_{\mathcal{Z} \times \mathcal{Z}})_{\mathcal{M} \times \mathcal{M}} \quad (3.91)$$

$$= \begin{bmatrix} \mathbf{Y}_{\mathcal{M} \times \mathcal{M}} & \mathbf{Y}_{\mathcal{M} \times \mathcal{Z}} \\ \mathbf{Y}_{\mathcal{Z} \times \mathcal{M}} & \mathbf{Y}_{\mathcal{Z} \times \mathcal{Z}} \end{bmatrix} / \mathbf{Y}_{\mathcal{Z} \times \mathcal{Z}} \quad (3.92)$$

$$= \mathbf{Y}_{(\mathcal{M} \cup \mathcal{Z}) \times (\mathcal{M} \cup \mathcal{Z})} / \mathbf{Y}_{\mathcal{Z} \times \mathcal{Z}} \quad (3.93)$$

From $\mathcal{M} \subsetneq \mathcal{Z}_c = \mathcal{N} \setminus \mathcal{Z}$ and $\mathcal{Z} \subsetneq \mathcal{N}$, it follows that $\mathcal{M} \cup \mathcal{Z} \subsetneq \mathcal{N}$ (i.e., $\mathcal{M} \cup \mathcal{Z}$ and \mathcal{Z} are proper subsets of \mathcal{N}). According to Theorem 2, $\mathbf{Y}_{(\mathcal{M} \cup \mathcal{Z}) \times (\mathcal{M} \cup \mathcal{Z})}$ and $\mathbf{Y}_{\mathcal{Z} \times \mathcal{Z}}$ thus have full rank. So

$$\det(\mathbf{Y}_{(\mathcal{M} \cup \mathcal{Z}) \times (\mathcal{M} \cup \mathcal{Z})}) \neq 0 \quad (3.94)$$

$$\det(\mathbf{Y}_{\mathcal{Z} \times \mathcal{Z}}) \neq 0 \quad (3.95)$$

As known from linear algebra, the determinant of $\hat{\mathbf{Y}}_{\mathcal{M} \times \mathcal{M}}$ is the product of the determinants of $\mathbf{Y}_{(\mathcal{M} \cup \mathcal{Z}) \times (\mathcal{M} \cup \mathcal{Z})}$ and $\mathbf{Y}_{\mathcal{Z} \times \mathcal{Z}}$ (see Lemma 11 in Appendix A.1.4). Accordingly

$$\det(\hat{\mathbf{Y}}_{\mathcal{M} \times \mathcal{M}}) = \det(\mathbf{Y}_{(\mathcal{M} \cup \mathcal{Z}) \times (\mathcal{M} \cup \mathcal{Z})}) \cdot \det(\mathbf{Y}_{\mathcal{Z} \times \mathcal{Z}}) \neq 0 \quad (3.96)$$

which proves the third claim (3.84) of Corollary 1. \square

3.3.2 Sequential Reduction of Multiple Sets of Zero-Injection Nodes

According to Corollary 1, the reduced compound admittance matrix $\hat{\mathbf{Y}}$ satisfies the same rank property as \mathbf{Y} (i.e., the diagonal blocks of $\hat{\mathbf{Y}}$ have full rank). Therefore, $\hat{\mathbf{Y}}$ can be reduced further, in case there are more zero-injection nodes to be eliminated.

Observation 1. *KR preserves the rank property which guarantees its feasibility (i.e., Theorem 2). Therefore, in case \mathcal{Z} is partitioned as $\{\mathcal{Z}_k \mid k \in \mathcal{K}\}$, the parts \mathcal{Z}_k can be reduced sequentially, and the (partially or fully) reduced compound admittance matrices obtained in each step also satisfy the said rank property (i.e., Theorem 2)..*

Sequential KR (i.e., rather than “en bloc”) can be computationally efficient, because the Schur complement requires a matrix inversion. This operation is computationally intensive, and scales poorly with problem size (even if the inverse is not computed explicitly).

3.4 On the Existence of Compound Hybrid Matrices

Evidently, (3.34) is in *admittance form*. That is, the nodal injected currents and the nodal phase-to-ground voltages appear in separate vectors \mathbf{I} and \mathbf{V} , which are linked by the compound admittance matrix \mathbf{Y} . In power system analysis, it is often more convenient to write the grid equations in *hybrid form* (i.e., if this is feasible). Let $\mathcal{M} \subsetneq \mathcal{N}$ be nonempty, and $\mathcal{M}_G := \mathcal{N} \setminus \mathcal{M}$. The grid equations in hybrid form (w.r.t. \mathcal{M}) read as follows:

$$\begin{bmatrix} \mathbf{V}_{\mathcal{M}} \\ \mathbf{I}_{\mathcal{M}_G} \end{bmatrix} = \begin{bmatrix} \mathbf{H}_{\mathcal{M} \times \mathcal{M}} & \mathbf{H}_{\mathcal{M} \times \mathcal{M}_G} \\ \mathbf{H}_{\mathcal{M}_G \times \mathcal{M}} & \mathbf{H}_{\mathcal{M}_G \times \mathcal{M}_G} \end{bmatrix} \begin{bmatrix} \mathbf{I}_{\mathcal{M}} \\ \mathbf{V}_{\mathcal{M}_G} \end{bmatrix} \quad (3.97)$$

The block matrix \mathbf{H} is the *compound hybrid matrix* (w.r.t. \mathcal{M}). A priori, the existence of such a matrix is not guaranteed, and may depend both on \mathbf{Y} and the choice of \mathcal{M} . To be more precise, the diagonal block $\mathbf{Y}_{\mathcal{M} \times \mathcal{M}}$ of \mathbf{Y} has to be invertible in order for \mathbf{H} to exist (see Section 2.1).

Recall from Section 2.1 that various researches have investigated the matter of hybrid matrices. Some authors merely describe how a hybrid matrix can be built, if it exists at all (e.g., [42–44]). Other authors do provide criteria for the existence of hybrid matrices, but only for some (i.e., at least one) partition of the nodes (e.g., [45–47]). The existing works exclusively deal with single-phase grids. Hence, their findings can (at best) be applied to balanced three-phase grids (i.e., to their equivalent positive-sequence equivalent circuits). In contrast, Theorem 2 guarantees the existence of \mathbf{H} for arbitrary choices of \mathcal{M} in unbalanced polyphase grids.

3.4.1 The Case of Unreduced Grid Models

For now, suppose that \mathbf{Y} is unreduced (this is the base case of Theorem 2).

Corollary 2 (Existence of \mathbf{H}). *Suppose that Theorem 2 applies. Let $\mathcal{M} \subsetneq \mathcal{N}$ be nonempty, such that \mathcal{M} and $\mathcal{M}_G := \mathcal{N} \setminus \mathcal{M}$ form a nontrivial partition of \mathcal{N} . Then, $\exists \mathbf{H}$ so that*

$$\begin{bmatrix} \mathbf{V}_{\mathcal{M}} \\ \mathbf{I}_{\mathcal{M}_G} \end{bmatrix} = \begin{bmatrix} \mathbf{H}_{\mathcal{M} \times \mathcal{M}} & \mathbf{H}_{\mathcal{M} \times \mathcal{M}_G} \\ \mathbf{H}_{\mathcal{M}_G \times \mathcal{M}} & \mathbf{H}_{\mathcal{M}_G \times \mathcal{M}_G} \end{bmatrix} \begin{bmatrix} \mathbf{I}_{\mathcal{M}} \\ \mathbf{V}_{\mathcal{M}_G} \end{bmatrix} \quad (3.98)$$

where

$$\mathbf{H}_{\mathcal{M} \times \mathcal{M}} = \mathbf{Y}_{\mathcal{M} \times \mathcal{M}}^{-1} \quad (3.99)$$

$$\mathbf{H}_{\mathcal{M} \times \mathcal{M}_G} = -\mathbf{Y}_{\mathcal{M} \times \mathcal{M}}^{-1} \mathbf{Y}_{\mathcal{M} \times \mathcal{M}_G} \quad (3.100)$$

$$\mathbf{H}_{\mathcal{M}_G \times \mathcal{M}} = \mathbf{Y}_{\mathcal{M}_G \times \mathcal{M}} \mathbf{Y}_{\mathcal{M} \times \mathcal{M}}^{-1} \quad (3.101)$$

$$\mathbf{H}_{\mathcal{M}_G \times \mathcal{M}_G} = \mathbf{Y}_{\mathcal{M}_G \times \mathcal{M}_G} - \mathbf{Y}_{\mathcal{M}_G \times \mathcal{M}} \mathbf{Y}_{\mathcal{M} \times \mathcal{M}}^{-1} \mathbf{Y}_{\mathcal{M} \times \mathcal{M}_G} = \mathbf{Y} / \mathbf{Y}_{\mathcal{M} \times \mathcal{M}} \quad (3.102)$$

Observe that the term $\mathbf{Y}_{\mathcal{M} \times \mathcal{M}}^{-1}$ appears in every block of \mathbf{H} .

3.4. On the Existence of Compound Hybrid Matrices

Proof. Write the admittance equation (3.34) in block form for \mathcal{M} and \mathcal{M}_G :

$$\begin{bmatrix} \mathbf{I}_{\mathcal{M}} \\ \mathbf{I}_{\mathcal{M}_G} \end{bmatrix} = \begin{bmatrix} \mathbf{Y}_{\mathcal{M} \times \mathcal{M}} & \mathbf{Y}_{\mathcal{M} \times \mathcal{M}_G} \\ \mathbf{Y}_{\mathcal{M}_G \times \mathcal{M}} & \mathbf{Y}_{\mathcal{M}_G \times \mathcal{M}_G} \end{bmatrix} \begin{bmatrix} \mathbf{V}_{\mathcal{M}} \\ \mathbf{V}_{\mathcal{M}_G} \end{bmatrix} \quad (3.103)$$

By Theorem 2, $\mathbf{Y}_{\mathcal{M} \times \mathcal{M}}$ has full rank. Thus, the first block row of (3.103) can be rewritten as

$$\mathbf{V}_{\mathcal{M}} = \mathbf{Y}_{\mathcal{M} \times \mathcal{M}}^{-1} \left(\mathbf{I}_{\mathcal{M}} - \mathbf{Y}_{\mathcal{M} \times \mathcal{M}_G} \mathbf{V}_{\mathcal{M}_G} \right) \quad (3.104)$$

$$= \mathbf{Y}_{\mathcal{M} \times \mathcal{M}}^{-1} \mathbf{I}_{\mathcal{M}} - \mathbf{Y}_{\mathcal{M} \times \mathcal{M}}^{-1} \mathbf{Y}_{\mathcal{M} \times \mathcal{M}_G} \mathbf{V}_{\mathcal{M}_G} \quad (3.105)$$

$$= \mathbf{H}_{\mathcal{M} \times \mathcal{M}} \mathbf{I}_{\mathcal{M}} + \mathbf{H}_{\mathcal{M} \times \mathcal{M}_G} \mathbf{V}_{\mathcal{M}_G} \quad (3.106)$$

This proves the claims w.r.t. $\mathbf{H}_{\mathcal{M} \times \mathcal{M}}$ and $\mathbf{H}_{\mathcal{M}_G \times \mathcal{M}}$.

Substitute (3.104) into the second block row of (3.103), and group the terms w.r.t. $\mathbf{I}_{\mathcal{M}}$ and $\mathbf{V}_{\mathcal{M}_G}$

$$\mathbf{I}_{\mathcal{M}_G} = \mathbf{Y}_{\mathcal{M}_G \times \mathcal{M}} \mathbf{Y}_{\mathcal{M} \times \mathcal{M}}^{-1} \left(\mathbf{I}_{\mathcal{M}} - \mathbf{Y}_{\mathcal{M} \times \mathcal{M}_G} \mathbf{V}_{\mathcal{M}_G} \right) + \mathbf{Y}_{\mathcal{M}_G \times \mathcal{M}_G} \mathbf{V}_{\mathcal{M}_G} \quad (3.107)$$

$$= \mathbf{Y}_{\mathcal{M}_G \times \mathcal{M}} \mathbf{Y}_{\mathcal{M} \times \mathcal{M}}^{-1} \mathbf{I}_{\mathcal{M}} + \left(\mathbf{Y}_{\mathcal{M}_G \times \mathcal{M}_G} - \mathbf{Y}_{\mathcal{M}_G \times \mathcal{M}} \mathbf{Y}_{\mathcal{M} \times \mathcal{M}}^{-1} \mathbf{Y}_{\mathcal{M} \times \mathcal{M}_G} \right) \mathbf{V}_{\mathcal{M}_G} \quad (3.108)$$

$$= \mathbf{H}_{\mathcal{M}_G \times \mathcal{M}} \mathbf{I}_{\mathcal{M}} + \mathbf{H}_{\mathcal{M}_G \times \mathcal{M}_G} \mathbf{V}_{\mathcal{M}_G} \quad (3.109)$$

This proves the claims w.r.t. $\mathbf{H}_{\mathcal{M}_G \times \mathcal{M}}$ and $\mathbf{H}_{\mathcal{M}_G \times \mathcal{M}_G}$. \square

3.4.2 The Case of (Partially) Reduced Grid Models

It is worthwhile noting that compound hybrid matrices \mathbf{H} do also exist if \mathbf{Y} is reduced via KR. This is due to the fact that KR preserves the rank property stated in Theorem 2.

Observation 2 (Existence of \mathbf{H} under Application of KR). *The existence of compound hybrid matrices is guaranteed by the very same rank property as the feasibility of KR (i.e., Theorem 2). Since KR preserves the said property (see Observation 1), compound hybrid matrices can also be constructed from unreduced and (partially or fully) reduced compound admittance matrices. That is, \mathbf{Y} can be replaced by $\hat{\mathbf{Y}}$ in Corollary 2.*

4 Real-Time Estimation of the Grid State by a Sequential Kalman Filter

Contributions: Control functions (e.g., voltage/current control) and protections are usually implemented into embedded systems, especially in power distribution systems. The said applications can profit from real-time knowledge of the grid state [112]. For instance, *Phasor Measurement Units* (PMUs) can be used to acquire measurements at high refresh rates [113]. In addition to the measurement units, a state estimator is required to remove measurement noise, and infer states which are not directly observed (i.e., through a measurement model). Therefore, there is an interest in embedding state estimators into the same kind of platforms that are used for control and protection. In this respect, one of the major challenges is the implementation into dedicated hardware like *Field-Programmable Gate Arrays* (FPGAs), which are widely used in embedded systems. For instance, the standard *Kalman Filter* (KF) is difficult to implement in such hardware. In this chapter, it is demonstrated that the *Sequential Kalman Filter* (SKF) is suitable for embedded systems. First, the measurement model and process model of a generic power grid, which are prerequisites for the estimation of its state, are developed. Specifically, the measurement model includes the reduced compound admittance matrix of the grid, which is obtained via *Kron Reduction* (KR) (see Section 3.3). The working hypotheses w.r.t. the statistical properties of the measurement noise and process noise are discussed. Afterwards, the essentials of minimum-mean-squared-error estimation, which lead to the standard KF, are recalled. Then, it is formally proven that the standard KF can be equivalently rewritten as the SKF, provided that the measurements can be divided into blocks whose noise variables are uncorrelated. In this respect, it is illustrated that the SKF is computationally less intensive than the standard KF. To this end, the computational complexity of these filters is quantified in terms of additions/subtractions and multiplications/divisions. Based on the detailed analysis of the operations underlying the SKF, the hardware architecture for the implementation into the FPGA is designed. In particular, it is illustrated how these operations can be parallelized and pipelined to achieve high performance. Finally, the FPGA prototype is validated using a test grid based on the IEEE 34-node distribution feeder.

Keywords: state estimation, sequential Kalman filter, embedded systems, field-programmable gate array, phasor measurement units.

Publications:

- [114] A. M. Kettner and M. Paolone, “Sequential discrete Kalman filter for real-time state estimation in power distribution systems: theory and implementation”, IEEE Trans. Instrum. Meas. ,vol. 66, no. 9, pp. 2358–2370, Sep. 2017.

4.1 Formulation of the Measurement Model

4.1.1 Structure of the Measurement Model

States

As known from classical control theory, the *measurement model* relates the measurements with the states. The state of a power system can be described by the phase-to-ground voltages, branch voltages, nodal injected currents, branch currents, or a combination of them (cf. [58]). If PMUs are used as meters, and the states and the measurements are expressed in rectangular coordinates, then the measurement model is linear. In this thesis, the grid state is described purely by phase-to-ground voltage phasors.

Recall from Section 3.3 that the phase-to-ground voltage phasors $\mathbf{V}_{\mathcal{Z}}$ in the zero-injection nodes \mathcal{Z} of a grid are a linear function of the phase-to-ground voltage phasors $\mathbf{V}_{\mathcal{Z}_c}$ in the remainder of the nodes $\mathcal{Z}_c := \mathcal{N} \setminus \mathcal{Z}$. The fact that $\mathbf{I}_{\mathcal{Z}} = \mathbf{0}$ can be considered in different ways. For instance, one can introduce pseudo-measurements, whose noise has very low variance (i.e., by several order of magnitude lower than the variance of physical measurement noise). However, this approach is prone to numerical ill-conditioning (e.g., of the gain matrix of a weighted-least-squares estimator). Another possibility is to eliminate the states associated with the zero-injection nodes, for example via LQ or QR decomposition [16] or KR [115]. These approaches reduce the size of the SE problem, and improve its numerical conditioning.

In this thesis, the KR approach is employed. More precisely, the grid state is described by the phase-to-ground voltage phasors $\mathbf{V}_{\mathcal{Z}_c}$ of the non-zero-injection nodes \mathcal{Z}_c . The *state vector* \mathbf{x} is composed of the real and imaginary parts of the said phasors:

$$\mathbf{x} := \begin{bmatrix} \Re \{ \mathbf{V}_{\mathcal{Z}_c} \} \\ \Im \{ \mathbf{V}_{\mathcal{Z}_c} \} \end{bmatrix} \quad (4.1)$$

Measurements

As previously mentioned, it is supposed that PMUs are used as meters. Suppose further that these PMUs monitor nodal quantities (i.e., phase-to-ground voltages and injected currents at the nodes \mathcal{Z}_c)¹. Let Γ_1 and Γ_2 be *indicator functions* that select which elements of $\mathbf{V}_{\mathcal{Z}_c}$ and $\mathbf{I}_{\mathcal{Z}_c}$ are measured. In analogy to the state vector \mathbf{x} , the *measurement vector* \mathbf{y} is defined as

$$\mathbf{y} = \begin{bmatrix} \mathbf{y}_1 \\ \mathbf{y}_2 \end{bmatrix}, \quad \mathbf{y}_1 \sim \begin{bmatrix} \Gamma_1 \Re \{ \mathbf{V}_{\mathcal{Z}_c} \} \\ \Gamma_1 \Im \{ \mathbf{V}_{\mathcal{Z}_c} \} \end{bmatrix}, \quad \mathbf{y}_2 \sim \begin{bmatrix} \Gamma_2 \Re \{ \mathbf{I}_{\mathcal{Z}_c} \} \\ \Gamma_2 \Im \{ \mathbf{I}_{\mathcal{Z}_c} \} \end{bmatrix} \quad (4.2)$$

where \mathbf{y}_1 and \mathbf{y}_2 correspond to the voltage and current measurements, respectively.

¹Branch currents can easily be treated, as $\mathbf{I}_{\mathcal{L}}$ can be written in function of $\mathbf{V}_{\mathcal{Z}}$ using (3.39) (i.e., $\mathbf{I}_{\mathcal{L}} = \mathbf{Y}_{\mathcal{L}} \mathbf{A}_{\mathcal{B}}^{\mathcal{L}} \mathbf{V}$) and Corollary 1 (i.e., $\mathbf{V}_{\mathcal{Z}} = -\mathbf{Y}_{\mathcal{Z} \times \mathcal{Z}}^{-1} \mathbf{Y}_{\mathcal{Z} \times \mathcal{Z}_c} \mathbf{V}_{\mathcal{Z}_c}$). However, this is not discussed here for the sake of space.

Chapter 4. Real-Time Estimation of the Grid State by a Sequential Kalman Filter

Recall from Corollary 1 that $\mathbf{I}_{\mathcal{Z}_0}$ and $\mathbf{V}_{\mathcal{Z}_0}$ are linked by $\mathbf{Y}/\mathbf{Y}_{\mathcal{Z} \times \mathcal{Z}}$. Let \mathbf{G} and \mathbf{B} denote the real and imaginary part of $\mathbf{Y}/\mathbf{Y}_{\mathcal{Z} \times \mathcal{Z}}$, respectively:

$$\mathbf{I}_{\mathcal{Z}_0} = (\mathbf{Y}/\mathbf{Y}_{\mathcal{Z} \times \mathcal{Z}})\mathbf{V}_{\mathcal{Z}_0} := (\mathbf{G} + j\mathbf{B})\mathbf{V}_{\mathcal{Z}_0} \quad (4.3)$$

If the PMUs were ideal meters

$$\mathbf{y}_1 = \mathbf{C}_1 \mathbf{x}, \quad \mathbf{C}_1 := \begin{bmatrix} \mathbf{\Gamma}_1 & \mathbf{0} \\ \mathbf{0} & \mathbf{\Gamma}_1 \end{bmatrix} \quad (\text{for ideal meters}) \quad (4.4)$$

$$\mathbf{y}_2 = \mathbf{C}_2 \mathbf{x}, \quad \mathbf{C}_2 := \begin{bmatrix} \mathbf{\Gamma}_2 & \mathbf{0} \\ \mathbf{0} & \mathbf{\Gamma}_2 \end{bmatrix} \begin{bmatrix} \mathbf{G} & -\mathbf{B} \\ \mathbf{B} & \mathbf{G} \end{bmatrix} \quad (\text{for ideal meters}) \quad (4.5)$$

The state vector \mathbf{x} and the measurement vector \mathbf{y} are related by the *output matrix* \mathbf{C}

$$\mathbf{y} = \mathbf{C}\mathbf{x}, \quad \mathbf{C} := \begin{bmatrix} \mathbf{C}_1 \\ \mathbf{C}_2 \end{bmatrix} \quad (\text{for ideal meters}) \quad (4.6)$$

In reality, phasor measurements are corrupted with noise, which originates both from the hardware (e.g., the sensors) and the software (e.g., the signal processing) of the PMUs, and from the grid (e.g., power electronic devices and the like) [116]. This can be represented by a *measurement noise vector* \mathbf{v} , which is added to $\mathbf{C}\mathbf{x}$ [58]. Moreover, as \mathbf{x} , \mathbf{y} and \mathbf{v} vary over time, they are considered to be discrete-time signals \mathbf{x}_k , \mathbf{y}_k , and \mathbf{v}_k , respectively. In summary

Hypothesis 4 (Measurement Model). *The measurement model is linear with additive noise:*

$$\mathbf{y}_k = \mathbf{C}\mathbf{x}_k + \mathbf{v}_k \quad (4.7)$$

4.1.2 Hypotheses with Respect to the Measurement Noise

In the aforesaid measurement model, there is an implicit transformation from polar to rectangular coordinates. This is due to the fact that PMUs provide measurements of magnitude and phase [113], whereas \mathbf{y} is expressed in real and imaginary parts.

The measurement noise in polar coordinates is approximately normally distributed [117]. The transformation from polar to rectangular coordinates does not preserve the normality of the probability density function. For practical values of the sensor accuracy in polar coordinates, the normality of the probability distribution is not substantially affected, though. In order for the effect to become noticeable, the standard deviation of the measurement error would have to exceed 5% [116]. PMUs are typically equipped with voltage and currents sensors of class 1 or better. Therefore, the measurement noise in rectangular coordinates is normally distributed in practice [118]. However, the coordinate transformation does affect the standard deviations. That is, the standard deviations associated with polar coordinates are functions of those associated with rectangular coordinates. The interested reader is referred to Appendix A.3, where this subject is discussed in detail.

Let $N(\boldsymbol{\mu}, \boldsymbol{\Sigma})$ denote the multivariate *normal distribution* with *mean vector* $\boldsymbol{\mu}$ and *covariance matrix* $\boldsymbol{\Sigma}$, and $E[\cdot]$ the *expected-value operator*. The measurement noise is described by the model stated below (see [58]):

Hypothesis 5 (Measurement Noise). *The measurement noise vector \mathbf{v}_k is normally distributed and white:*

$$\mathbf{v}_k \sim N(\mathbf{0}, \mathbf{R}_k) \quad (4.8)$$

$$E[\mathbf{v}_k \mathbf{v}_l^T] = \begin{cases} \mathbf{R}_k & l = k \\ \mathbf{0} & l \neq k \end{cases} \quad (4.9)$$

Note that the *measurement noise covariance matrix* \mathbf{R}_k is known (i.e., it can be derived from the metrological characteristics of the PMUs). Since \mathbf{R}_k is a covariance matrix, it is positive semidefinite: $\mathbf{R}_k \geq 0$. In general, \mathbf{R}_k is time-variant (i.e., \mathbf{v}_k is *non-stationary*) and dense (i.e., the elements of \mathbf{v}_k are *correlated*) [119–121].

4.1.3 The Necessary Condition for Observability

In order to achieve *observability* (i.e., to infer all states from the measurements), the output matrix \mathbf{C} needs to have full rank [23]. To that effect, a sufficient number of PMUs needs to be placed appropriately in the grid [122]. Hereafter, it is assumed that this is the case:

Hypothesis 6 (Observability). *The output matrix \mathbf{C} has full rank (i.e., the grid is observable).*

In this regard, it is worth mentioning that the measurement model may include critical and leverage measurements. A *critical measurement* is a measurement whose loss causes the grid to become unobservable (i.e., it decreases the rank of \mathbf{C}). The residuals (i.e., the difference between the raw and the estimated measurements, see Section 2.2) of critical measurements are identical to zero [23]. A *leverage measurement* is a measurement whose residual remains close to zero even in presence of large measurement errors (i.e., due to the structure of \mathbf{C}) [23]. Recall that bad data can be identified based on the statistical distribution of the residuals (e.g., [59,60]). Namely, a measurement is marked as bad if its residual exceeds a certain statistical threshold. Since critical and leverage measurements have residuals identical or close to zero, respectively, bad data occurring on these measurements cannot be detected. The identification and the treatment of critical and leverage measurements are well-discussed in the existing literature (e.g., [22,23]), but are beyond the scope of this thesis.

4.2 Formulation of the Process Model

4.2.1 Structure of the Process Model

As known from classical control theory, the *process model* describes the evolution of the state over time. For a *discrete-time, linear, time-invariant system*, the process model is of the form

$$\mathbf{x}_{k+1} = \mathbf{A}\mathbf{x}_k + \mathbf{B}\mathbf{u}_k + \mathbf{w}_k \quad (4.10)$$

where \mathbf{u} is the vector of *controllable variables*, \mathbf{w} is the vector of *process noise variables*, \mathbf{A} is the *system matrix*, and \mathbf{B} is the *input matrix* [58,64].

In the case of power systems, the aforesaid process model can be simplified as proposed in [58,68]. Firstly, PMUs are required to stream measurements at high refresh rates [123,124] (i.e., tens of frames per second). Therefore, the state varies only little between two consecutive time steps. Hence, a quasi-static process model can be used (i.e., \mathbf{A} is an identity matrix). Secondly, from the point of view of the state estimator, the inputs of a power system are not controllable. Accordingly, they can be ignored in the process model (i.e., \mathbf{B} is a null matrix). This yields an *Autoregressive Integrated Moving Average* (ARIMA) model of order (0,1,0) [125]:

Hypothesis 7 (Process Model). *The process model is an ARIMA model of order (0,1,0):*

$$\mathbf{x}_{k+1} = \mathbf{x}_k + \mathbf{w}_k \quad (4.11)$$

It is worthwhile noting that this process model can capture power system transients, provided that the associated time constants are reasonably longer than the time window used for the synchrophasor extraction (i.e., several cycles of the fundamental component). Typically, the windows length is 40–100 milliseconds (i.e., 2–5 cycles) [126]. Accordingly, slow transients with time constants of several hundreds of milliseconds can be treated, while fast transients with time constants of a few tens of milliseconds cannot.

4.2.2 Hypotheses with Respect to the Process Noise

With regard to the noise, there is a fundamental difference between the measurement model and the process model. The measurement noise is a statistical property of observations, which is due to both the hardware (e.g., the sensors) and the software (e.g, the signal processing). Therefore, the measurement noise can be characterized experimentally, for instance using a calibrator [127]. The process noise, on the other hand, is a virtual construct, which is related to the mathematical model of the evolution of the system state. More precisely, it captures the mismatch between the chosen process model and the true evolution of the system state. In practice, the true system state is unknown. Hence, the process noise cannot be characterized experimentally like the measurement noise. Normally, it is assumed that the process noise behaves similar to the measurement noise (e.g., [58,68]):

Hypothesis 8 (Process Noise). *The process noise \mathbf{w}_k is normally distributed and white:*

$$\mathbf{w}_k \sim \mathcal{N}(\mathbf{0}, \mathbf{Q}_k) \quad (4.12)$$

$$\mathbb{E}[\mathbf{w}_k \mathbf{w}_l^\top] = \begin{cases} \mathbf{Q}_k & l = k \\ \mathbf{0} & l \neq k \end{cases} \quad (4.13)$$

Usually, *process noise covariance matrix* \mathbf{Q}_k is assumed constant (i.e., $\mathbf{Q}_k = \mathbf{Q}$), and set to a value which ensures that the process model captures the typical dynamics well. Nevertheless, based on the aforesaid hypothesis that the process noise is normally distributed, \mathbf{Q}_k can be assessed on-line. For instance, \mathbf{Q}_k can be approximated by the sample variance of the estimated state [69], or by solving a $\log(\det(\cdot))$ optimization problem [70]. However, such methods are beyond the scope of this thesis, and are thus not considered in the following. Instead, it is simply assumed that \mathbf{Q}_k is known.

4.3 Estimation of the System State using Kalman Filters

4.3.1 Recall of the Standard Kalman Filter

The KF produces an estimate of the *true state* \mathbf{x}_k , which minimizes the mean squared error [64]. It consists of a *prediction step*, which relies only on information from the past time step $k - 1$, and an *estimation step*, which takes into account information from the present time step k . Let $\hat{\mathbf{x}}_k^-$ and $\hat{\mathbf{x}}_k^+$ be the *predicted state* and *estimated state*, respectively. The *prediction error* \mathbf{e}_k^- and the *estimation error* \mathbf{e}_k^+ are defined as the differences w.r.t. the true state \mathbf{x}_k :

$$\mathbf{e}_k^- := \hat{\mathbf{x}}_k^- - \mathbf{x}_k \quad (4.14)$$

$$\mathbf{e}_k^+ := \hat{\mathbf{x}}_k^+ - \mathbf{x}_k \quad (4.15)$$

Suppose that the said errors have zero mean (i.e., $\hat{\mathbf{x}}_k^-$ and $\hat{\mathbf{x}}_k^+$ are on average equal to \mathbf{x}_k):

$$\mathbb{E}[\mathbf{e}_k^-] = \mathbf{0} \quad (4.16)$$

$$\mathbb{E}[\mathbf{e}_k^+] = \mathbf{0} \quad (4.17)$$

Under these conditions, the *prediction error covariance matrix* \mathbf{P}_k^- and the *estimation error covariance matrix* \mathbf{P}_k^+ are given by

$$\mathbf{P}_k^- := \mathbb{E}[\mathbf{e}_k^- (\mathbf{e}_k^-)^\top] \quad (4.18)$$

$$\mathbf{P}_k^+ := \mathbb{E}[\mathbf{e}_k^+ (\mathbf{e}_k^+)^\top] \quad (4.19)$$

Derivation of the Prediction Step

Assume that the estimated state $\hat{\mathbf{x}}_{k-1}^+$ of the past step $k - 1$ is known. According to Hypothesis 7, the true state remains constant between step $k - 1$ and k (except for process noise). Therefore, one can set (see [128])

$$\hat{\mathbf{x}}_k^- = \hat{\mathbf{x}}_{k-1}^+ \quad (4.20)$$

Given this relation, the prediction error covariance matrix \mathbf{P}_k^- can be expressed in function of the estimation error covariance matrix \mathbf{P}_{k-1}^+ and the process noise covariance matrix \mathbf{Q}_{k-1} . First, substitute (4.14) and (4.20) into (4.18):

$$\mathbf{P}_k^- = \mathbb{E}[\mathbf{e}_k^- (\mathbf{e}_k^-)^\top] \quad (4.21)$$

$$= \mathbb{E}[(\hat{\mathbf{x}}_k^- - \mathbf{x}_k) (\hat{\mathbf{x}}_k^- - \mathbf{x}_k)^\top] \quad (4.22)$$

$$= \mathbb{E}[(\hat{\mathbf{x}}_{k-1}^+ - \mathbf{x}_k) (\hat{\mathbf{x}}_{k-1}^+ - \mathbf{x}_k)^\top] \quad (4.23)$$

Then, use (4.15) (i.e., $\mathbf{e}_k^+ = \hat{\mathbf{x}}_k^+ - \mathbf{x}_k$) and Hypothesis 7 (i.e., $\mathbf{x}_{k+1} = \mathbf{x}_k + \mathbf{w}_k$), and simplify:

$$\mathbf{P}_k^- = \mathbb{E} \left[(\hat{\mathbf{x}}_{k-1}^+ - \mathbf{x}_k) (\hat{\mathbf{x}}_{k-1}^+ - \mathbf{x}_k)^\top \right] \quad (4.24)$$

$$= \mathbb{E} \left[(\mathbf{x}_{k-1} + \mathbf{e}_{k-1}^+ - (\mathbf{x}_{k-1} + \mathbf{w}_{k-1})) (\mathbf{x}_{k-1} + \mathbf{e}_{k-1}^+ - (\mathbf{x}_{k-1} + \mathbf{w}_{k-1}))^\top \right] \quad (4.25)$$

$$= \mathbb{E} \left[(\mathbf{e}_{k-1}^+ - \mathbf{w}_{k-1}) (\mathbf{e}_{k-1}^+ - \mathbf{w}_{k-1})^\top \right] \quad (4.26)$$

Expanding the product yields

$$\mathbf{P}_k^- = \mathbb{E} \left[(\mathbf{e}_{k-1}^+ - \mathbf{w}_{k-1}) (\mathbf{e}_{k-1}^+ - \mathbf{w}_{k-1})^\top \right] \quad (4.27)$$

$$= \mathbb{E} \left[\mathbf{e}_{k-1}^+ (\mathbf{e}_{k-1}^+)^\top \right] + \mathbb{E} \left[\mathbf{w}_{k-1} \mathbf{w}_{k-1}^\top \right] + \mathbb{E} \left[\mathbf{e}_{k-1}^+ \mathbf{w}_{k-1}^\top \right] + \mathbb{E} \left[\mathbf{w}_{k-1} (\mathbf{e}_{k-1}^+)^\top \right] \quad (4.28)$$

If the estimation error \mathbf{e}_{k-1}^+ and the process noise \mathbf{w}_{k-1} are uncorrelated, that is

$$\mathbb{E} \left[\mathbf{e}_{k-1}^+ \mathbf{w}_{k-1}^\top \right] = \mathbf{0} \quad (4.29)$$

$$\mathbb{E} \left[\mathbf{w}_{k-1} (\mathbf{e}_{k-1}^+)^\top \right] = \mathbf{0} \quad (4.30)$$

then the prediction error covariance matrix \mathbf{P}_k^- is given by

$$\mathbf{P}_k^- = \mathbb{E} \left[\mathbf{e}_{k-1}^+ (\mathbf{e}_{k-1}^+)^\top \right] + \mathbb{E} \left[\mathbf{w}_{k-1} \mathbf{w}_{k-1}^\top \right] \quad (4.31)$$

Using (4.19) (i.e., $\mathbf{P}_k^+ = \mathbb{E} \left[\mathbf{e}_k^+ (\mathbf{e}_k^+)^\top \right]$) and Hypothesis 8 (i.e., $\mathbf{w}_k \sim N(\mathbf{0}, \mathbf{Q}_k)$), one finds

$$\mathbf{P}_k^- = \mathbf{P}_{k-1}^+ + \mathbf{Q}_{k-1} \quad (4.32)$$

Derivation of the Estimation Step

Now, the measurement \mathbf{y}_k shall be used in order to obtain the estimated state $\hat{\mathbf{x}}_k^+$. To this end, the predicted state $\hat{\mathbf{x}}_k^-$ is corrected using the mismatch between the observed measurement \mathbf{y}_k and the expected measurement $\hat{\mathbf{y}}_k = \mathbf{C} \hat{\mathbf{x}}_k^-$ (see [128]):

$$\hat{\mathbf{x}}_k^+ = \hat{\mathbf{x}}_k^- + \mathbf{K}_k (\mathbf{y}_k - \mathbf{C}_k \hat{\mathbf{x}}_k^-) \quad (4.33)$$

The selection of the *Kalman gain* \mathbf{K}_k (a.k.a. *blending factor*) is discussed later in this chapter. The estimation error covariance matrix \mathbf{P}_k^+ can be expressed in function of the prediction error covariance matrix \mathbf{P}_k^- , the output matrix \mathbf{C}_k , the measurement noise covariance matrix \mathbf{R}_k , and the Kalman gain \mathbf{K}_k . First, substitute (4.15) and (4.33) into (4.19):

$$\mathbf{P}_k^+ = \mathbb{E} \left[\mathbf{e}_k^+ (\mathbf{e}_k^+)^\top \right] \quad (4.34)$$

$$= \mathbb{E} \left[(\hat{\mathbf{x}}_k^+ - \mathbf{x}_k) (\hat{\mathbf{x}}_k^+ - \mathbf{x}_k)^\top \right] \quad (4.35)$$

$$= \mathbb{E} \left[(\hat{\mathbf{x}}_k^- + \mathbf{K}_k (\mathbf{y}_k - \mathbf{C}_k \hat{\mathbf{x}}_k^-) - \mathbf{x}_k) (\hat{\mathbf{x}}_k^- + \mathbf{K}_k (\mathbf{y}_k - \mathbf{C}_k \hat{\mathbf{x}}_k^-) - \mathbf{x}_k)^\top \right] \quad (4.36)$$

Then, use Hypothesis 4 (i.e., $\mathbf{y}_k = \mathbf{C}_k \mathbf{x}_k + \mathbf{v}_k$) and (4.14) (i.e., $\mathbf{e}_k^- = \hat{\mathbf{x}}_k^- - \mathbf{x}_k$), and simplify:

$$\mathbf{P}_k^+ = \mathbb{E} \left[\left(\hat{\mathbf{x}}_k^- + \mathbf{K}_k (\mathbf{y}_k - \mathbf{C}_k \hat{\mathbf{x}}_k^-) - \mathbf{x}_k \right) \left(\hat{\mathbf{x}}_k^- + \mathbf{K}_k (\mathbf{y}_k - \mathbf{C}_k \hat{\mathbf{x}}_k^-) - \mathbf{x}_k \right)^\top \right] \quad (4.37)$$

$$= \mathbb{E} \left[\left(\hat{\mathbf{x}}_k^- + \mathbf{K}_k (\mathbf{C}_k \mathbf{x}_k + \mathbf{v}_k - \mathbf{C}_k \hat{\mathbf{x}}_k^-) - \mathbf{x}_k \right) \left(\hat{\mathbf{x}}_k^- + \mathbf{K}_k (\mathbf{C}_k \mathbf{x}_k + \mathbf{v}_k - \mathbf{C}_k \hat{\mathbf{x}}_k^-) - \mathbf{x}_k \right)^\top \right] \quad (4.38)$$

$$= \mathbb{E} \left[\left(\hat{\mathbf{x}}_k^- - \mathbf{x}_k + \mathbf{K}_k (\mathbf{v}_k - \mathbf{C}_k (\hat{\mathbf{x}}_k^- - \mathbf{x}_k)) \right) \left(\hat{\mathbf{x}}_k^- - \mathbf{x}_k + \mathbf{K}_k (\mathbf{v}_k - \mathbf{C}_k (\hat{\mathbf{x}}_k^- - \mathbf{x}_k)) \right)^\top \right] \quad (4.39)$$

$$= \mathbb{E} \left[\left(\mathbf{e}_k^- + \mathbf{K}_k (\mathbf{v}_k - \mathbf{C}_k \mathbf{e}_k^-) \right) \left(\mathbf{e}_k^- + \mathbf{K}_k (\mathbf{v}_k - \mathbf{C}_k \mathbf{e}_k^-) \right)^\top \right] \quad (4.40)$$

$$= \mathbb{E} \left[\left((\mathbf{I} - \mathbf{K}_k \mathbf{C}_k) \mathbf{e}_k^- + \mathbf{K}_k \mathbf{v}_k \right) \left((\mathbf{I} - \mathbf{K}_k \mathbf{C}_k) \mathbf{e}_k^- + \mathbf{K}_k \mathbf{v}_k \right)^\top \right] \quad (4.41)$$

Expanding the product yields

$$\mathbf{P}_k^+ = \mathbb{E} \left[\left((\mathbf{I} - \mathbf{K}_k \mathbf{C}_k) \mathbf{e}_k^- + \mathbf{K}_k \mathbf{v}_k \right) \left((\mathbf{I} - \mathbf{K}_k \mathbf{C}_k) \mathbf{e}_k^- + \mathbf{K}_k \mathbf{v}_k \right)^\top \right] \quad (4.42)$$

$$= \begin{bmatrix} (\mathbf{I} - \mathbf{K}_k \mathbf{C}_k) \mathbb{E} \left[\mathbf{e}_k^- (\mathbf{e}_k^-)^\top \right] (\mathbf{I} - \mathbf{K}_k \mathbf{C}_k)^\top + \mathbf{K}_k \mathbb{E} \left[\mathbf{v}_k \mathbf{v}_k^\top \right] \mathbf{K}_k^\top \\ + (\mathbf{I} - \mathbf{K}_k \mathbf{C}_k) \mathbb{E} \left[\mathbf{e}_k^- \mathbf{v}_k^\top \right] \mathbf{K}_k^\top + \mathbf{K}_k \mathbb{E} \left[\mathbf{v}_k (\mathbf{e}_k^-)^\top \right] (\mathbf{I} - \mathbf{K}_k \mathbf{C}_k)^\top \end{bmatrix} \quad (4.43)$$

If the prediction error \mathbf{e}_k^- and the measurement noise \mathbf{v}_k are uncorrelated, that is

$$\mathbb{E} \left[\mathbf{e}_k^- \mathbf{v}_k^\top \right] = \mathbf{0} \quad (4.44)$$

$$\mathbb{E} \left[\mathbf{v}_k (\mathbf{e}_k^-)^\top \right] = \mathbf{0} \quad (4.45)$$

then the estimation error covariance matrix \mathbf{P}_k^+ is given by

$$\mathbf{P}_k^+ = (\mathbf{I} - \mathbf{K}_k \mathbf{C}_k) \mathbb{E} \left[\mathbf{e}_k^- (\mathbf{e}_k^-)^\top \right] (\mathbf{I} - \mathbf{K}_k \mathbf{C}_k)^\top + \mathbf{K}_k \mathbb{E} \left[\mathbf{v}_k \mathbf{v}_k^\top \right] \mathbf{K}_k^\top \quad (4.46)$$

Using (4.18) and Hypothesis 5 (i.e., $\mathbf{v}_k \sim \mathcal{N}(\mathbf{0}, \mathbf{R}_k)$), one finds

$$\mathbf{P}_k^+ = (\mathbf{I} - \mathbf{K}_k \mathbf{C}_k) \mathbf{P}_k^- (\mathbf{I} - \mathbf{K}_k \mathbf{C}_k)^\top + \mathbf{K}_k \mathbf{R}_k \mathbf{K}_k^\top \quad (4.47)$$

The prediction error covariance matrix \mathbf{P}_k^- is given at this point. Moreover, the output matrix \mathbf{C}_k and the measurement noise covariance matrix \mathbf{R}_k are known by Hypothesis 4 and Hypothesis 5, respectively. The Kalman gain \mathbf{K}_k can be selected such that the estimated state $\hat{\mathbf{x}}_k^+$ is optimal w.r.t. a given design objective.

The objective for designing the KF is to minimize the mean squared error (e.g., [128,129]):

$$\hat{\mathbf{x}}_k^+ = \arg \min \left(\mathbb{E} \left[(\mathbf{e}_k^+)^T \mathbf{e}_k^+ \right] \right) = \arg \min \left(\text{trace}(\mathbf{P}_k^+) \right) \quad (4.48)$$

To this end, the Kalman gain \mathbf{K}_k needs to satisfy the following condition:

$$\frac{d \left[\text{trace}(\mathbf{P}_k^+) \right]}{d \mathbf{K}_k} = \mathbf{0} \quad (4.49)$$

First, substitute (4.47) into trace(\mathbf{P}_k^+):

$$\text{trace}(\mathbf{P}_k^+) = \text{trace}\left((\mathbf{I} - \mathbf{K}_k \mathbf{C}_k) \mathbf{P}_k^- (\mathbf{I} - \mathbf{K}_k \mathbf{C}_k)^\top + \mathbf{K}_k \mathbf{R}_k \mathbf{K}_k^\top\right) \quad (4.50)$$

$$= \text{trace}\left(\mathbf{P}_k^- - \mathbf{K}_k \mathbf{C}_k \mathbf{P}_k^- - \mathbf{P}_k^- \mathbf{C}_k^\top \mathbf{K}_k^\top + \mathbf{K}_k \mathbf{C}_k \mathbf{P}_k^- \mathbf{C}_k^\top \mathbf{K}_k^\top + \mathbf{K}_k \mathbf{R}_k \mathbf{K}_k^\top\right) \quad (4.51)$$

$$= \text{trace}\left(\mathbf{P}_k^- - \left(\mathbf{K}_k \mathbf{C}_k \mathbf{P}_k^- + \mathbf{P}_k^- \mathbf{C}_k^\top \mathbf{K}_k^\top\right) + \mathbf{K}_k \left(\mathbf{C}_k \mathbf{P}_k^- \mathbf{C}_k^\top + \mathbf{R}_k\right) \mathbf{K}_k^\top\right) \quad (4.52)$$

$$= \text{trace}\left(\mathbf{P}_k^- - \left(\mathbf{K}_k \mathbf{C}_k \mathbf{P}_k^- + (\mathbf{K}_k \mathbf{C}_k \mathbf{P}_k^-)^\top\right) + \mathbf{K}_k \left(\mathbf{C}_k \mathbf{P}_k^- \mathbf{C}_k^\top + \mathbf{R}_k\right) \mathbf{K}_k^\top\right) \quad (4.53)$$

$$= \text{trace}(\mathbf{P}_k^-) - 2 \text{trace}(\mathbf{K}_k \mathbf{C}_k \mathbf{P}_k^-) + \text{trace}\left(\mathbf{K}_k \left(\mathbf{C}_k \mathbf{P}_k^- \mathbf{C}_k^\top + \mathbf{R}_k\right) \mathbf{K}_k^\top\right) \quad (4.54)$$

Now, the derivative of trace(\mathbf{P}_k^+) w.r.t. \mathbf{K}_k is calculated. It is known that (for proof, see [130])

$$\frac{d[\text{trace}(\mathbf{AB})]}{d\mathbf{A}} = \mathbf{B}^\top \quad \text{if } \mathbf{AB} = \text{square} \quad (4.55)$$

$$\frac{d[\text{trace}(\mathbf{ACA}^\top)]}{d\mathbf{A}} = 2\mathbf{AC} \quad \text{if } \mathbf{C} = \mathbf{C}^\top \quad (4.56)$$

It follows that

$$\frac{d[\text{trace}(\mathbf{P}_k^+)]}{d\mathbf{K}_k} = -2 \frac{d[\text{trace}(\mathbf{K}_k \mathbf{C}_k \mathbf{P}_k^-)]}{d\mathbf{K}_k} + \frac{d[\text{trace}(\mathbf{K}_k (\mathbf{C}_k \mathbf{P}_k^- \mathbf{C}_k^\top + \mathbf{R}_k) \mathbf{K}_k^\top)]}{d\mathbf{K}_k} \quad (4.57)$$

$$= -2\mathbf{P}_k^- \mathbf{C}_k^\top + 2\mathbf{K}_k (\mathbf{C}_k \mathbf{P}_k^- \mathbf{C}_k^\top + \mathbf{R}_k) \quad (4.58)$$

$$= \mathbf{0} \quad (4.59)$$

Provided that the term $\mathbf{C}_k \mathbf{P}_k^- \mathbf{C}_k^\top + \mathbf{R}_k$ is non-singular, the Kalman gain \mathbf{K}_k is obtained as

$$\mathbf{K}_k = \mathbf{P}_k^- \mathbf{C}_k^\top (\mathbf{C}_k \mathbf{P}_k^- \mathbf{C}_k^\top + \mathbf{R}_k)^{-1} \quad (4.60)$$

Formulation of the Standard Kalman Filter

In summary, the standard KF consists of the prediction step

$$\mathbf{P}_k^- = \mathbf{P}_{k-1}^+ + \mathbf{Q}_{k-1} \quad (4.61)$$

$$\hat{\mathbf{x}}_k^- = \hat{\mathbf{x}}_{k-1}^+ \quad (4.62)$$

and the estimation step

$$\mathbf{K}_k = \mathbf{P}_k^- \mathbf{C}_k^\top (\mathbf{C}_k \mathbf{P}_k^- \mathbf{C}_k^\top + \mathbf{R}_k)^{-1} \quad (4.63)$$

$$\mathbf{P}_k^+ = (\mathbf{I} - \mathbf{K}_k \mathbf{C}_k) \mathbf{P}_k^- (\mathbf{I} - \mathbf{K}_k \mathbf{C}_k)^\top + \mathbf{K}_k \mathbf{R}_k \mathbf{K}_k^\top \quad (4.64)$$

$$\hat{\mathbf{x}}_k^+ = \hat{\mathbf{x}}_k^- + \mathbf{K}_k (\mathbf{y}_k - \mathbf{C}_k \hat{\mathbf{x}}_k^-) \quad (4.65)$$

In classical control theory, various equivalent formulations of the KF are known (see [131]).

Lemma 3 (KF). *Consider a power grid, whose measurement model and process model satisfy Hypotheses 4–6 and Hypotheses 7–8, respectively. If it holds that*

$$\mathbb{E} \left[\mathbf{v}_k \mathbf{w}_l^\top \right] = \mathbf{0} \quad (4.66)$$

(i.e., the measurement noise \mathbf{v} and the process noise \mathbf{w} are uncorrelated), the KF gives an estimate with minimal mean squared error. More precisely, the KF consists of the prediction step

$$\mathbf{P}_k^- = \mathbf{P}_{k-1}^+ + \mathbf{Q}_{k-1} \quad (4.67)$$

$$\hat{\mathbf{x}}_k^- = \hat{\mathbf{x}}_{k-1}^+ \quad (4.68)$$

and the estimation step

$$\mathbf{K}_k = \mathbf{P}_k^- \mathbf{C}_k^\top \left(\mathbf{C}_k \mathbf{P}_k^- \mathbf{C}_k^\top + \mathbf{R}_k \right)^{-1} \quad (4.69)$$

$$\mathbf{P}_k^+ = (\mathbf{I} - \mathbf{K}_k \mathbf{C}_k) \mathbf{P}_k^- (\mathbf{I} - \mathbf{K}_k \mathbf{C}_k)^\top + \mathbf{K}_k \mathbf{R}_k \mathbf{K}_k^\top = (\mathbf{I} - \mathbf{K}_k \mathbf{C}_k) \mathbf{P}_k^- \quad (4.70)$$

$$\hat{\mathbf{x}}_k^+ = \hat{\mathbf{x}}_k^- + \mathbf{K}_k (\mathbf{y}_k - \mathbf{C}_k \hat{\mathbf{x}}_k^-) \quad (4.71)$$

The latter can be equivalently written as

$$(\mathbf{P}_k^+)^{-1} = (\mathbf{P}_k^-)^{-1} + \mathbf{C}_k^\top \mathbf{R}_k^{-1} \mathbf{C}_k \quad (4.72)$$

$$\mathbf{K}_k = \mathbf{P}_k^+ \mathbf{C}_k^\top \mathbf{R}_k^{-1} \quad (4.73)$$

$$\hat{\mathbf{x}}_k^+ = \hat{\mathbf{x}}_k^- + \mathbf{K}_k (\mathbf{y}_k - \mathbf{C}_k \hat{\mathbf{x}}_k^-) \quad (4.74)$$

The first formula for \mathbf{P}_k^+ in (4.70) (a.k.a. *Joseph's form*) is more complex than the second one, but grants immediate insight into the positive (semi)definiteness of \mathbf{P}_k^+ . The interested reader is referred to Appendix A.4.1, where the equivalence of the two formulas is proven.

Evidently, in order for the KF to be applicable, the inverses of \mathbf{R}_k , \mathbf{P}_k^- , \mathbf{P}_k^+ , and $\mathbf{C}_k \mathbf{P}_k^- \mathbf{C}_k^\top + \mathbf{R}_k$ have to exist. A priori, there is no guarantee for this: \mathbf{R}_k , \mathbf{P}_k^- , and \mathbf{P}_k^+ are covariance matrices, which means that they are only ensured to be positive semidefinite, and may thus be singular. In practice, the positive definiteness (and thus invertibility) of these terms can be enforced. For instance, the diagonal elements of the process noise covariance matrix \mathbf{Q}_k can be inflated, so that the error covariance matrices $\mathbf{P}_k^- / \mathbf{P}_k^+$ become positive definite. This comes at the cost of higher estimation error. In case the measurement noise covariance matrix \mathbf{R}_k is positive definite, $\mathbf{P}_k^- / \mathbf{P}_k^+$ are also guaranteed to be positive definite. The interested reader is referred to Appendix A.4.2, where this subject is discussed in detail. Hereafter, whenever the KF is utilized, it is supposed that the following hypothesis holds:

Hypothesis 9 (Positive Definiteness of \mathbf{R}_k , \mathbf{P}_k^+). *The measurement noise covariance matrix \mathbf{R}_k and the estimation error covariance matrix \mathbf{P}_k^+ are positive definite.*

Incidentally, Hypothesis 9 is the basis for the equivalence of the formulations (4.69)–(4.71) and (4.72)–(4.74) of the estimation step. The proof is given in Appendix A.4.3.

4.3.2 The Sequential Kalman Filter

Correlation of the Measurement Noise Variables

Recall that the measurement noise vector \mathbf{v}_k is additive and normally distributed with zero mean (Hypothesis 4–5), and that its covariance matrix \mathbf{R}_k is positive definite (Hypothesis 9):

$$\mathbf{v}_k \sim N(\mathbf{0}, \mathbf{R}_k), \quad \mathbf{R}_k > 0$$

So far, no assumptions have been made w.r.t. to the correlation between the elements of \mathbf{v}_k . In theory, all measurement noise variables could be correlated. That is, all elements of \mathbf{R}_k could be non-zero. In practice, most of them are zero, though. For instance, noise variables associated with different PMUs are uncorrelated. By contrast, noise variables associated with channels of the same PMU (i.e., phase-to-ground voltages and injected currents at the same node) may be correlated. Recall that PMUs provide measurements in polar coordinates (i.e., magnitude and phase) [113]. The magnitude noise variables are uncorrelated, because they stem from separate sensors. By contrast, the phase noise variables are correlated, since the phases are defined w.r.t. to the same synchronized clock [121]. Recall that the measurement model (4.2) is expressed in rectangular coordinates. If the noise variables associated with the phases of the channels of a PMU are correlated, the same holds for the noise variables associated with the real and imaginary parts.

On these grounds, the measurement noise vector \mathbf{v}_k is thought to be composed of blocks $\mathbf{v}_{k,i}$ that are mutually uncorrelated. In other words, the measurement noise covariance matrix \mathbf{R}_k is block-diagonal. Formally:

Hypothesis 10 (Diagonality of \mathbf{R}_k). *The measurement noise vector \mathbf{v}_k consists of blocks $\mathbf{v}_{k,i}$, which are mutually uncorrelated:*

$$\mathbb{E}[\mathbf{v}_{k,i} \mathbf{v}_{k,j}^\top] = \begin{cases} \mathbf{R}_{k,i} & i = j \\ \mathbf{0} & i \neq j \end{cases} \quad (4.75)$$

By consequence, the measurement noise covariance matrix \mathbf{R}_k is block-diagonal:

$$\mathbf{R}_k = \text{diag}_i(\mathbf{R}_{k,i}) \quad (4.76)$$

Sequential Treatment of the Measurements

Let $\mathbf{y}_{k,i}$ and $\mathbf{C}_{k,i}$ be the blocks of \mathbf{y}_k and \mathbf{C}_k which correspond to the block $\mathbf{v}_{k,i}$ of \mathbf{v}_k :

$$\mathbf{y}_{k,i} = \mathbf{C}_{k,i} \mathbf{x}_k + \mathbf{v}_{k,i} \quad (4.77)$$

Chapter 4. Real-Time Estimation of the Grid State by a Sequential Kalman Filter

Note that $\mathbf{y}_{k,i}$, $\mathbf{C}_{k,i}$, and $\mathbf{v}_{k,i}$ are the i -th block rows of \mathbf{y}_k , \mathbf{C}_k , and \mathbf{v}_k , respectively. Accordingly

$$\mathbf{y}_k = \text{col}_i(\mathbf{y}_{k,i}) \quad (4.78)$$

$$\mathbf{C}_k = \text{col}_i(\mathbf{C}_{k,i}) \quad (4.79)$$

$$\mathbf{v}_k = \text{col}_i(\mathbf{v}_{k,i}) \quad (4.80)$$

As it turns out, provided that the blocks of measurement noise variables $\mathbf{v}_{k,i}$ are uncorrelated, the blocks of measurements $\mathbf{y}_{k,i}$ can be processed sequentially rather than simultaneously. That is, the KF can be equivalently reformulated as the SKF. Let B be the number of blocks of the measurement model (i.e., $i = 1, \dots, B$). The SKF is as follows (see [131]):

Theorem 3 (SKF). *Suppose that the conditions of Lemma 3 are met and that Hypothesis 9 holds. If Hypothesis 10 is satisfied, the KF can be equivalently reformulated as the SKF. More precisely, the blocks of measurements $\mathbf{y}_{k,i}$ are processed sequentially (i.e., in a FOR loop that runs over i) in the estimation step. The initial values are the results of the prediction step:*

$$\mathbf{P}_{k,0}^+ = \mathbf{P}_k^- \quad (4.81)$$

$$\hat{\mathbf{x}}_{k,0}^+ = \hat{\mathbf{x}}_k^- \quad (4.82)$$

The iteration step for (4.69)–(4.71) is

$$\mathbf{K}_{k,i} = \mathbf{P}_{k,i-1}^+ \mathbf{C}_{k,i}^T (\mathbf{C}_{k,i} \mathbf{P}_{k,i-1}^+ \mathbf{C}_{k,i}^T + \mathbf{R}_{k,i})^{-1} \quad (4.83)$$

$$\mathbf{P}_{k,i}^+ = (\mathbf{I} - \mathbf{K}_{k,i} \mathbf{C}_{k,i}) \mathbf{P}_{k,i-1}^+ (\mathbf{I} - \mathbf{K}_{k,i} \mathbf{C}_{k,i})^T + \mathbf{K}_{k,i} \mathbf{R}_{k,i} \mathbf{K}_{k,i}^T = (\mathbf{I} - \mathbf{K}_{k,i} \mathbf{C}_{k,i}) \mathbf{P}_{k,i-1}^+ \quad (4.84)$$

$$\hat{\mathbf{x}}_{k,i}^+ = \hat{\mathbf{x}}_{k,i-1}^+ + \mathbf{K}_{k,i} (\mathbf{y}_{k,i} - \mathbf{C}_{k,i} \hat{\mathbf{x}}_{k,i-1}^+) \quad (4.85)$$

and the one for (4.72)–(4.74) is

$$(\mathbf{P}_{k,i}^+)^{-1} = (\mathbf{P}_{k,i-1}^+)^{-1} + \mathbf{C}_{k,i}^T \mathbf{R}_{k,i}^{-1} \mathbf{C}_{k,i} \quad (4.86)$$

$$\mathbf{K}_{k,i} = \mathbf{P}_{k,i}^+ \mathbf{C}_{k,i}^T \mathbf{R}_{k,i}^{-1} \quad (4.87)$$

$$\hat{\mathbf{x}}_{k,i}^+ = \hat{\mathbf{x}}_{k,i-1}^+ + \mathbf{K}_{k,i} (\mathbf{y}_{k,i} - \mathbf{C}_{k,i} \hat{\mathbf{x}}_{k,i-1}^+) \quad (4.88)$$

The final results of the SKF are identical to the results of the KF:

$$\mathbf{P}_k^+ = \mathbf{P}_{k,B}^+ \quad (4.89)$$

$$\hat{\mathbf{x}}_k^+ = \hat{\mathbf{x}}_{k,B}^+ \quad (4.90)$$

The term $\mathbf{C}_{k,i} \mathbf{P}_{k,i-1}^+ \mathbf{C}_{k,i}^T + \mathbf{R}_{k,i}$ is equal in size to $\mathbf{R}_{k,i}$, which is typically much smaller than \mathbf{R}_k . By contrast, $\mathbf{P}_{k,i}^+$ has the full size of \mathbf{P}_k^+ . Hence, the calculation of the inverse in (4.83) is less demanding than the calculation of the inverses in (4.86). If all measurement noise variables are uncorrelated, which means that all $\mathbf{R}_{k,i}$ have size 1×1 , the inversion in (4.83) simplifies to a division. This is beneficial w.r.t. computational complexity (see Section 4.5), and facilitates the implementation of the SKF into an FPGA (see Section 4.6).

4.4 Equivalence of the Considered Kalman Filters

Obviously, the sequential formulations (4.83)–(4.85)/(4.86)–(4.88) are structurally similar to the standard formulations (4.69)–(4.71)/(4.72)–(4.74). Nevertheless, it is not evident that the measurements can be processed sequentially, and that the sequential calculation yields the same results as the standard one. Notably, the iterations of the SKF are not independent estimations, since one block of measurement $\mathbf{y}_{k,i}$ does not suffice to infer the entire state \mathbf{x}_k (i.e., the partial measurement model $\mathbf{y}_{k,i} = \mathbf{C}_{k,i}\mathbf{x}_k + \mathbf{v}_{k,i}$ is underdetermined). Furthermore, although the SKF occasionally appears in the literature (e.g., [68,71]), a complete proof of equivalence is nowhere to be found to the best of the author’s knowledge. Therefore, the equivalence of the SKF and the standard KF is now proven.

Due to the similarity of the SKF and the standard KF, it is simple to show that the sequential formulations (4.83)–(4.85) and (4.86)–(4.88) are equivalent. In fact, the proof in Appendix A.4.3, which establishes that the standard formulations (4.69)–(4.71) and (4.72)–(4.74) are equivalent, applies with minor changes. As the sequential formulations are equivalent, it suffices to show that either of them produces the same results as one of the standard formulations. The proof of equivalence is performed separately for the estimation error covariance matrix and the estimated state vector.

4.4.1 Estimation Error Covariance Matrix

Proof. ($\mathbf{P}_k^+ = \mathbf{P}_{k,B}^+$). (4.86) is a recursion formula for $(\mathbf{P}_{k,i}^+)^{-1}$. Expanding it for $i = B$ yields

$$(\mathbf{P}_{k,B}^+)^{-1} = (\mathbf{P}_{k,B-1}^+)^{-1} + \mathbf{C}_{k,B}^\top \mathbf{R}_{k,B}^{-1} \mathbf{C}_{k,B} \quad (4.91)$$

$$= (\mathbf{P}_{k,0}^+)^{-1} \sum_{i=1}^B \mathbf{C}_k^\top \mathbf{R}_{k,i}^{-1} \mathbf{C}_k \quad (4.92)$$

Recall equation (4.79) (i.e., $\mathbf{C}_k = \text{col}_i(\mathbf{C}_{k,i})$), Hypothesis 10 (i.e., $\mathbf{R}_k = \text{diag}_i(\mathbf{R}_{k,i})$), as well as equation (4.81) (i.e., $\mathbf{P}_{k,0}^+ = \mathbf{P}_k^-$). It follows that

$$(\mathbf{P}_{k,B}^+)^{-1} = (\mathbf{P}_{k,0}^+)^{-1} + \sum_{i=1}^B \mathbf{C}_k^\top \mathbf{R}_{k,i}^{-1} \mathbf{C}_k \quad (4.93)$$

$$= (\mathbf{P}_k^-)^{-1} + \mathbf{C}_k^\top \mathbf{R}_k^{-1} \mathbf{C}_k \quad (4.94)$$

Finally, using (4.72) (i.e., $(\mathbf{P}_k^+)^{-1} = (\mathbf{P}_k^-)^{-1} + \mathbf{C}_k^\top \mathbf{R}_k^{-1} \mathbf{C}_k$), one finds that

$$(\mathbf{P}_{k,B}^+)^{-1} = (\mathbf{P}_k^-)^{-1} + \mathbf{C}_k^\top \mathbf{R}_k^{-1} \mathbf{C}_k \quad (4.95)$$

$$= (\mathbf{P}_k^+)^{-1} \quad (4.96)$$

This proves the claim w.r.t. \mathbf{P}_k^+ . □

4.4.2 Estimated State Vector

Proof. ($\hat{\mathbf{x}}_k^+ = \hat{\mathbf{x}}_{k,B}^+$). Group the terms in (4.88) w.r.t. to $\hat{\mathbf{x}}_{k,i-1}^+$ and $\mathbf{y}_{k,i}$:

$$\hat{\mathbf{x}}_{k,i}^+ = \hat{\mathbf{x}}_{k,i-1}^+ + \mathbf{K}_{k,i} (\mathbf{y}_{k,i} - \mathbf{C}_{k,i} \hat{\mathbf{x}}_{k,i-1}^+) \quad (4.97)$$

$$= (\mathbf{I} - \mathbf{K}_{k,i} \mathbf{C}_{k,i}) \hat{\mathbf{x}}_{k,i-1}^+ + \mathbf{K}_{k,i} \mathbf{y}_{k,i} \quad (4.98)$$

This is a recursion formula for $\hat{\mathbf{x}}_{k,i}^+$. Expand it for $i = B$, and use (4.82) (i.e., $\hat{\mathbf{x}}_{k,0}^+ = \hat{\mathbf{x}}_k^-$):

$$\hat{\mathbf{x}}_{k,B}^+ = (\mathbf{I} - \mathbf{K}_{k,B} \mathbf{C}_{k,B}) \hat{\mathbf{x}}_{k,B-1}^+ + \mathbf{K}_{k,B} \mathbf{y}_{k,B} \quad (4.99)$$

$$= \prod_{j=1}^{j=B} \left\{ \mathbf{I} - \mathbf{K}_{k,j} \mathbf{C}_{k,j} \right\} \hat{\mathbf{x}}_k^- + \mathbf{K}_{k,B} \mathbf{y}_{k,B} + \sum_{i=1}^{B-1} \prod_{j=i+1}^{j=B} \left\{ \mathbf{I} - \mathbf{K}_{k,j} \mathbf{C}_{k,j} \right\} \mathbf{K}_{k,i} \mathbf{y}_{k,i} \quad (4.100)$$

Note that the indices of the multiplicands are decreasing. If $\hat{\mathbf{x}}_{k,B}^+ = \hat{\mathbf{x}}_k^+$, then it must hold that

$$\prod_{i=1}^{i=B} \left\{ \mathbf{I} - \mathbf{K}_{k,i} \mathbf{C}_{k,i} \right\} \hat{\mathbf{x}}_k^- = (\mathbf{I} - \mathbf{K}_k \mathbf{C}_k) \hat{\mathbf{x}}_k^- \quad (4.101)$$

$$\mathbf{K}_{k,B} \mathbf{y}_{k,B} + \sum_{i=1}^{B-1} \prod_{j=i+1}^{j=B} \left\{ \mathbf{I} - \mathbf{K}_{k,j} \mathbf{C}_{k,j} \right\} \mathbf{K}_{k,i} \mathbf{y}_{k,i} = \mathbf{K}_k \mathbf{y}_k \quad (4.102)$$

Recall that the claim $\mathbf{P}_k^+ = \mathbf{P}_{k,B}^+$ has already been proven. Thus, (4.84) yields the same as (4.70) after B iterations. Namely

$$\prod_{i=1}^{i=B} (\mathbf{I} - \mathbf{K}_{k,i} \mathbf{C}_{k,i}) \mathbf{P}_k^- = (\mathbf{I} - \mathbf{K}_k \mathbf{C}_k) \mathbf{P}_k^- \quad (4.103)$$

By comparison of the coefficients, it follows that (4.101) holds. Now, solve (4.84) for $\mathbf{I} - \mathbf{K}_{k,i} \mathbf{C}_{k,i}$, and use the result to rewrite the product term on the left-hand side of (4.102):

$$\prod_{i+1}^{j=B} \left\{ \mathbf{I} - \mathbf{K}_{k,j} \mathbf{C}_{k,j} \right\} = \prod_{i+1}^{j=B} \left\{ \mathbf{P}_{k,j}^+ (\mathbf{P}_{k,j-1}^+)^{-1} \right\} \quad (4.104)$$

$$= \mathbf{P}_{k,B}^+ (\mathbf{P}_{k,i}^+)^{-1} \quad (4.105)$$

Therefore, the sum term on the left-hand side of (4.102) can be rewritten as follows:

$$\sum_{i=1}^{B-1} \prod_{j=i+1}^{j=B} \left\{ \mathbf{I} - \mathbf{K}_{k,j} \mathbf{C}_{k,j} \right\} \mathbf{K}_{k,i} \mathbf{y}_{k,i} = \mathbf{P}_{k,B}^+ \sum_{i=1}^{B-1} (\mathbf{P}_{k,i}^+)^{-1} \mathbf{K}_{k,i} \mathbf{y}_{k,i} \quad (4.106)$$

Substitute (4.87) (i.e., $\mathbf{K}_{k,i} = \mathbf{P}_{k,i}^+ \mathbf{C}_{k,i}^\top \mathbf{R}_{k,i}^{-1}$) into the aforesaid equation:

$$\mathbf{P}_{k,B}^+ \sum_{i=1}^{B-1} (\mathbf{P}_{k,i}^+)^{-1} \mathbf{K}_{k,i} \mathbf{y}_{k,i} = \mathbf{P}_{k,B}^+ \sum_{i=1}^{B-1} \mathbf{C}_{k,i}^\top \mathbf{R}_{k,i}^{-1} \mathbf{y}_{k,i} \quad (4.107)$$

4.4. Equivalence of the Considered Kalman Filters

So, the left-hand side of (4.102) can be simplified as follows:

$$\mathbf{K}_{k,B} \mathbf{y}_{k,B} + \sum_{i=1}^{B-1} \prod_{i+1}^{j=B} \left\{ \mathbf{I} - \mathbf{K}_{k,j} \mathbf{C}_{k,j} \right\} \mathbf{K}_{k,i} \mathbf{y}_{k,i} = \mathbf{P}_{k,B}^+ \sum_{i=1}^B \mathbf{C}_{k,i}^T \mathbf{R}_{k,i}^{-1} \mathbf{y}_{k,i} \quad (4.108)$$

From (4.79) (i.e., $\mathbf{C}_k = \text{col}_i(\mathbf{C}_{k,i})$), Hypothesis 9 (i.e., $\mathbf{R}_k = \text{diag}(\mathbf{R}_{k,i})$), and the first claim (i.e., $\mathbf{P}_k^+ = \mathbf{P}_{k,B}^+$), it follows that

$$\mathbf{P}_{k,B}^+ \sum_{i=1}^B \mathbf{C}_{k,i}^T \mathbf{R}_{k,i}^{-1} \mathbf{y}_{k,i} = \mathbf{P}_k^+ \mathbf{C}_k^T \mathbf{R}_k^{-1} \mathbf{y}_k \quad (4.109)$$

Using (4.87) (i.e., $\mathbf{K}_k = \mathbf{P}_k^+ \mathbf{C}_k^T \mathbf{R}_k^{-1}$), it is found that

$$\mathbf{P}_k^+ \mathbf{C}_k^T \mathbf{R}_k^{-1} \mathbf{y}_k = \mathbf{K}_k \mathbf{y}_k \quad (4.110)$$

which is the right-hand side of (4.102). Since (4.101) and (4.102) hold, $\hat{\mathbf{x}}_{k,B}^+ = \hat{\mathbf{x}}_k^+$ as claimed. \square

4.5 Computational Complexity of the Considered Kalman Filters

4.5.1 Performance Limitations due to Matrix Inversions

Recall that both the standard KF and the SKF involve matrix inversions. Let S be the size of \mathbf{x}_k (i.e., the number of states), M the size of \mathbf{y}_k (i.e., the number of measurements), and M_i the size of $\mathbf{y}_{k,i}$. The following inverses need to be calculated (see Lemma 3 and Theorem 3):

- KF, version (4.69)–(4.71): $(\mathbf{C}_k \mathbf{P}_k^- \mathbf{C}_k^\top + \mathbf{R}_k)^{-1}$ ($M \times M$), calculated once.
- KF, version (4.72)–(4.74): $(\mathbf{P}_k^+)^{-1} / (\mathbf{P}_k^-)^{-1}$ ($S \times S$) and \mathbf{R}_k^{-1} ($M \times M$), calculated once.
- SKF, version (4.83)–(4.85): $(\mathbf{C}_{k,i} \mathbf{P}_{k,i-1}^+ \mathbf{C}_{k,i}^\top + \mathbf{R}_{k,i})^{-1}$ ($M_i \times M_i$), calculated B times.
- SKF, version (4.86)–(4.88): $(\mathbf{P}_{k,i}^+)^{-1}$ ($S \times S$) and $(\mathbf{R}_{k,i})^{-1}$ ($M_i \times M_i$), calculated B times.

The majority of the aforementioned matrices are *dense* (i.e., they have few nonzero elements), and hence inefficient w.r.t. storage and treatment. Matrix inversion is known to scale poorly, because the computational complexity is high, and the memory access pattern is irregular. Indeed, the performance of the standard KF is limited by the calculation of the inverses [132]. Version (4.86)–(4.88) of the SKF is even more impractical, because $\mathbf{P}_{k,i}^+$, which has the same size as \mathbf{P}_k^+ , needs to be inverted in every iteration. By contrast, the terms $\mathbf{C}_{k,i} \mathbf{P}_{k,i-1}^+ \mathbf{C}_{k,i}^\top + \mathbf{R}_{k,i}$ have the same size as the $\mathbf{R}_{k,i}$, which are usually smaller than \mathbf{R}_k , because only few measurement noise variables are correlated (i.e., $M_i \ll M$). For this reason, the calculation of the inverse is less critical for version (4.83)–(4.85) of the SKF. In case the measurement noise variables are uncorrelated, the matrix inversion even simplifies to a division. In light of these observations, the standard KF is clearly unsuitable for implementation in dedicated hardware (e.g., FPGAs). By contrast, the SKF is suitable if the measurement noise variables are largely uncorrelated.

4.5.2 Assumption of Uncorrelated Measurement Noise Variables

In [121], it is investigated how state estimators perform when the correlations are considered (i.e., if \mathbf{R}_k is block-diagonal) or not (i.e., if \mathbf{R}_k is diagonal). Traditional measurement units as well as PMUs are examined. In both cases, it is found that the inclusion of the correlation into the measurement model yields virtually no improvement in terms of estimation accuracy. Even in a hypothetical case study with high correlation factors and large measurement errors, no significant improvement is achieved. Hence, the correlation between measurement noise variables can be neglected in practice. So, the SKF processes the elements $y_{k,i}$ of \mathbf{y}_k sequentially

$$\mathbf{y}_{k,i} = y_{k,i} := (\mathbf{y}_k)_i \quad (4.111)$$

$$\mathbf{C}_{k,i} = \text{row}_i(\mathbf{C}_{k,i}) \quad (4.112)$$

$$\mathbf{R}_{k,i} = R_{k,i} := (\mathbf{R}_k)_{ii} \quad (4.113)$$

4.5. Computational Complexity of the Considered Kalman Filters

Table 4.1 – Computational complexity of the prediction step.

Operation	+ -	× ÷
$\mathbf{P}_k^- = \mathbf{P}_{k-1}^+ + \mathbf{Q}_{k-1}$	S^2	0
$\hat{\mathbf{x}}_k^- = \hat{\mathbf{x}}_{k-1}^+$	0	0

4.5.3 Analysis of the Computational Complexity

The computational complexity is quantified by the number of scalar additions/subtractions (+|-) and scalar multiplications/divisions (×|÷).

Prediction Step

First, recall the prediction step (4.67)–(4.68), which is the same for the standard KF and SKF. Its computational complexity is illustrated in Table 4.1.

Estimation Step of the Standard Kalman Filter

Now, recall the estimation step (4.69)–(4.71) of the standard KF:

$$\begin{aligned} \mathbf{K}_k &= \mathbf{P}_k^- \mathbf{C}_k^\top \left(\mathbf{C}_k \mathbf{P}_k^- \mathbf{C}_k^\top + \mathbf{R}_k \right)^{-1} \\ \mathbf{P}_k^+ &= (\mathbf{I} - \mathbf{K}_k \mathbf{C}_k) \mathbf{P}_k^- \\ \hat{\mathbf{x}}_k^+ &= \hat{\mathbf{x}}_k^- + \mathbf{K}_k (\mathbf{y}_k - \mathbf{C}_k \hat{\mathbf{x}}_k^-) \end{aligned}$$

For ease of understanding, the calculations are divided into sequences of simple operations. Operands which have been calculated in a previous step are marked with rectangular brackets. To give an example, $\mathbf{AB} + \mathbf{CD}$ can be calculated as follows: 1) \mathbf{AB} , 2) \mathbf{CD} , and 3) $[\mathbf{AB}] + [\mathbf{CD}]$. The results for the above-stated equations are given in Table 4.2. The complexity of the inverse is indicated as $\mathcal{O}(M^3)$, because the exact numbers depend on the algorithm.

Estimation Step of the Sequential Kalman Filter

For uncorrelated measurement noise, the estimation step (4.83)–(4.85) of the SKF becomes

$$\begin{aligned} \mathbf{K}_{k,i} &= \mathbf{P}_{k,i-1}^+ \mathbf{C}_{k,i}^\top \left(\mathbf{C}_{k,i} \mathbf{P}_{k,i-1}^+ \mathbf{C}_{k,i}^\top + R_{k,i} \right)^{-1} \\ \mathbf{P}_{k,i}^+ &= (\mathbf{I} - \mathbf{K}_{k,i} \mathbf{C}_{k,i}) \mathbf{P}_{k,i-1}^+ \\ \hat{\mathbf{x}}_{k,i}^+ &= \hat{\mathbf{x}}_{k,i-1}^+ + \mathbf{K}_{k,i} (y_{k,i} - \mathbf{C}_{k,i} \hat{\mathbf{x}}_{k,i-1}^+) \end{aligned}$$

Observe that the term $\mathbf{C}_{k,i} \mathbf{P}_{k,i-1}^+ \mathbf{C}_{k,i}^\top + R_{k,i}$ is a scalar, so the inversion is actually a division. The number of scalar operations required for one iteration are provided in Table 4.3.

Chapter 4. Real-Time Estimation of the Grid State by a Sequential Kalman Filter

Table 4.2 – Computational complexity of the estimation step of the standard KF.

Variable	Operation	+ -	× ÷
-	$\mathbf{C}_k \mathbf{P}_k^-$	$S(S-1)M$	S^2
\mathbf{K}_k	$[\mathbf{C}_k \mathbf{P}_k^-] \mathbf{C}_k^\top$	$(S-1)M^2$	SM^2
dito	$[\mathbf{C}_k \mathbf{P}_k^- \mathbf{C}_k^\top] + \mathbf{R}_k$	M^2	0
dito	$[\mathbf{C}_k \mathbf{P}_k^- \mathbf{C}_k^\top + \mathbf{R}_k]^{-1}$	$\mathcal{O}(M^3)$	$\mathcal{O}(M^3)$
dito	$[(\mathbf{C}_k \mathbf{P}_k^-)^\top] [(\mathbf{C}_k \mathbf{P}_k^- \mathbf{C}_k^\top + \mathbf{R}_k)^{-1}]$	$SM(M-1)$	SM^2
\mathbf{P}_k^+	$[\mathbf{K}_k] [\mathbf{C}_k \mathbf{P}_k^-]$	$S^2(M-1)$	S^2M
dito	$\mathbf{P}_k^- - [\mathbf{K}_k \mathbf{C}_k \mathbf{P}_k^-]$	S^2	0
$\hat{\mathbf{x}}_k^+$	$\mathbf{C}_k \hat{\mathbf{x}}_k^-$	$(S-1)M$	SM
dito	$\mathbf{y}_k - [\mathbf{C}_k \hat{\mathbf{x}}_k^-]$	M	0
dito	$[\mathbf{K}_k] [\mathbf{y}_k - \mathbf{C}_k \hat{\mathbf{x}}_k^-]$	$S(M-1)$	SM
dito	$\hat{\mathbf{x}}_k^- + [\mathbf{K}_k (\mathbf{y}_k - \mathbf{C}_k \hat{\mathbf{x}}_k^-)]$	S	0

Table 4.3 – Computational complexity of one iteration of the estimation step of the SKF.

Variable	Operation	+ -	× ÷
-	$\mathbf{C}_{k,i} \mathbf{P}_{k,i-1}^+$	$S(S-1)$	S^2
$\mathbf{K}_{k,i}$	$[\mathbf{C}_{k,i} \mathbf{P}_{k,i-1}^+] \mathbf{C}_{k,i}^\top$	$S-1$	S
dito	$[\mathbf{C}_{k,i} \mathbf{P}_{k,i-1}^+ \mathbf{C}_{k,i}^\top] + R_{k,i}$	1	0
dito	$[\mathbf{C}_{k,i} \mathbf{P}_{k,i-1}^+ \mathbf{C}_{k,i}^\top + R_{k,i}]^{-1}$	0	1
dito	$[(\mathbf{C}_{k,i} \mathbf{P}_{k,i-1}^+)^\top] [(\mathbf{C}_{k,i} \mathbf{P}_{k,i-1}^+ \mathbf{C}_{k,i}^\top + R_{k,i})^{-1}]$	0	S
$\mathbf{P}_{k,i}^+$	$[\mathbf{K}_{k,i}] [\mathbf{C}_{k,i} \mathbf{P}_{k,i-1}^+]$	0	S^2
dito	$\mathbf{P}_{k,i-1}^+ - [\mathbf{K}_{k,i} \mathbf{C}_{k,i} \mathbf{P}_{k,i-1}^+]$	S^2	0
$\hat{\mathbf{x}}_{k,i}^+$	$\mathbf{C}_{k,i} \hat{\mathbf{x}}_{k,i-1}^+$	$S-1$	S
dito	$y_{k,i} - [\mathbf{C}_{k,i} \hat{\mathbf{x}}_{k,i-1}^+]$	1	0
dito	$[\mathbf{K}_{k,i}] [y_{k,i} - \mathbf{C}_{k,i} \hat{\mathbf{x}}_{k,i-1}^+]$	0	S
dito	$\hat{\mathbf{x}}_{k,i-1}^+ + [\mathbf{K}_{k,i} (y_{k,i} - \mathbf{C}_{k,i} \hat{\mathbf{x}}_{k,i-1}^+)]$	S	0

4.5. Computational Complexity of the Considered Kalman Filters

Table 4.4 – Comparison of the computational complexity of the standard KF and the SKF.

KF	+ -	× ÷	SKF (\sum_i)	+ -	× ÷
\mathbf{P}_k^-	S^2	0	\mathbf{P}_k^-	S^2	0
$\hat{\mathbf{x}}_k^-$	0	0	$\hat{\mathbf{x}}_k^-$	0	0
$\mathbf{C}_k \mathbf{P}_k^-$	$S(S-1)M$	S^2M	$\mathbf{C}_{k,i} \mathbf{P}_{k,i-1}^+$	$S(S-1)M$	S^2M
\mathbf{K}_k	$SM(2M-1) + \mathcal{O}(M^3)$	$2SM^2 + \mathcal{O}(M^3)$	$\mathbf{K}_{k,i}$	SM	$(2S+1)M$
\mathbf{P}_k^+	S^2M	S^2M	$\mathbf{P}_{k,i}^+$	S^2M	S^2M
$\hat{\mathbf{x}}_k^+$	$2SM$	$2SM$	$\hat{\mathbf{x}}_{k,i}^+$	$2SM$	$2SM$

Comparison of the Computational Complexity

For ease of comparison, the detailed results from Tables 4.1–4.3 are summarized in Table 4.4. Note that only the number of operations needed to calculate \mathbf{K}_k and $\mathbf{K}_{k,i}$ ($\forall i$) are different. Moreover, the SKF requires fewer scalar operations than the standard KF:

$$(+|-) \quad SM < SM(2M-1) + \mathcal{O}(M^3) \quad (4.114)$$

$$(\times|\div) \quad (2S+1)M < 2SM^2 + \mathcal{O}(M^3) \quad (4.115)$$

According to Hypothesis 6, the output matrix \mathbf{C}_k must have full rank in order for the grid to be observable. Since \mathbf{C}_k has size $M \times S$, full rank implies that $M \geq S$. For security reasons, operators ensure ample redundancy of the measurements, so in practice $M \gg S$. As a result, the cubic terms constitute the lion's share of the computational burden of the standard KF [132]. In summary, the SKF is computationally more efficient than the standard KF.

Furthermore, since the measurement noise variables are uncorrelated, the SKF only requires elementary matrix operations plus divisions. In contrast to matrix inversions, these operations are easy to implement in dedicated hardware. Notably, they can be parallelized and pipelined to ensure fast execution and high throughput (these nontrivial implementation aspects are discussed next in Section 4.6). In that sense, the SKF facilitates the implementation of a real-time state estimator for power grids into an FPGA.

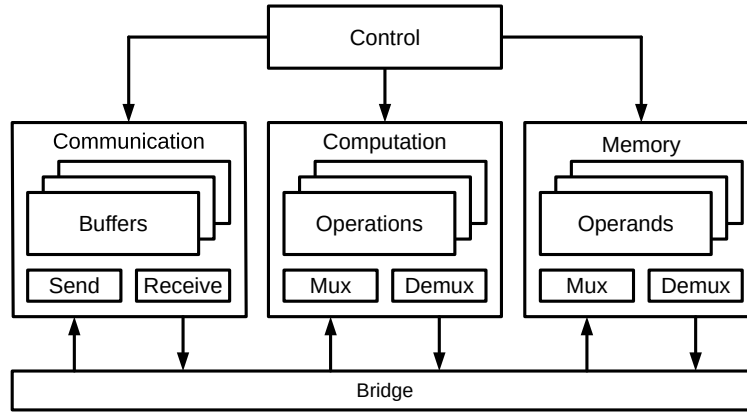


Figure 4.1 – Architecture of the FPGA prototype of the SKF. Dedicated modules take care of communication, computation, memory, and control (i.e., of the first three modules).

4.6 Implementation of the Sequential Filter into an FPGA

The SKF is implemented into a NI cRIO-9033 microcontroller. This device is equipped with an FPGA (Xilinx Kintex-7 7K160T) and a CPU (Intel Atom E3825) [133]. Thus, it can host both the prototype implementation (see Section 4.6.1) and the test infrastructure (see Section 4.6.2).

4.6.1 Prototype Implementation

The architecture of the FPGA prototype of the SKF is shown in Figure 4.1. The functionality is divided into communication, computation, memory, and control.

Communication Module

The communication module handles the transfer of data between the CPU and the FPGA. More precisely, *First-In/First-Out* (FIFO) buffers hosted in the *Random Access Memory* (RAM) of the FPGA are used. The low-level coordination of the data transfer is managed by a *Direct Memory Access* (DMA) controller, and the high-level coordination by a handshake protocol.

Computation Module

The computation module provides the mathematical operations. Namely:

1. Matrix addition/subtraction: $\mathbf{M}_1 \pm \mathbf{M}_2$.
2. Vector addition/subtraction: $\mathbf{v}_1 \pm \mathbf{v}_2$.
3. Outer product: $\mathbf{v}_1 \mathbf{v}_2^\top$.
4. Inner product: $\mathbf{v}_1^\top \mathbf{v}_2$.
5. Matrix-vector product: $\mathbf{M}\mathbf{v}$.
6. Scalar-vector product: $s \cdot \mathbf{v}$.

4.6. Implementation of the Sequential Filter into an FPGA

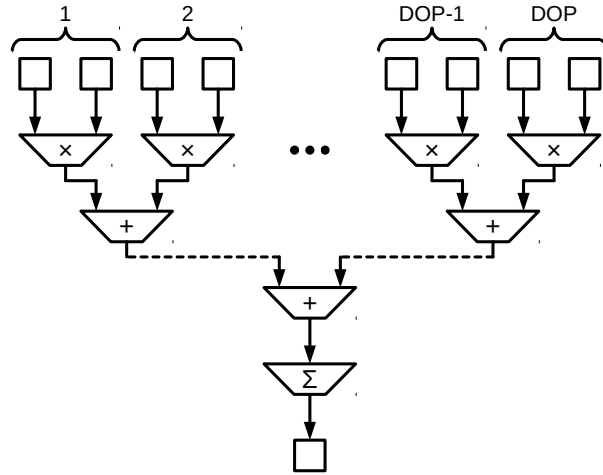


Figure 4.2 – Parallelized implementation of the inner product.

In order to achieve fast execution and high throughput, these operations are parallelized and pipelined. As parallel data processing requires parallel data access, the operands need to be partitioned into blocks, which are stored in separate memories. More precisely, since the SKF treats the measurements sequentially, the parallelization is done w.r.t. the states. Note that the *Degree Of Parallelism* (DOP) is a design parameter of the FPGA architecture. The matrix operands (i.e., \mathbf{P}_k^- and $\mathbf{P}_{k,i}^+$) are split into 2D arrays of $\text{DOP} \times \text{DOP}$ blocks, and the vector operands (i.e., $[\mathbf{C}_{k,i} \mathbf{P}_{k,i}^+]$, $\mathbf{C}_{k,i}$, $\mathbf{K}_{k,i}$, $\hat{\mathbf{x}}_k^-$, and $\hat{\mathbf{x}}_k^+$) into 1D arrays of $\text{DOP} \times 1$ blocks. Accordingly, the operations 1, 3, and 5 are accelerated by a factor of DOP^2 , whereas the operations 2, 4, and 6 are accelerated by a factor of DOP. The matrix addition/subtraction, the vector addition/subtraction, and the scalar-vector product are implemented of arrays of adders or multipliers, respectively. The inner product is built from an array of multipliers, a tree of adders, and one accumulator as shown in Figure 4.2. The matrix-vector product is constructed from DOP replicas of the inner product.

For the synthesis of the fundamental arithmetic blocks (i.e., adders/subtractors, multipliers, accumulators, and dividers), optimized libraries for *Single-Precision Floating-Point* (SGL) operations, which utilize the *Digital Signal Processor* (DSP) slices of the FPGA, are used [134]. When the fundamental arithmetic blocks are configured, a trade-off has to be made w.r.t. throughput, latency, and resource consumption. In this particular case, high throughput and low resource consumption are crucial. The resulting specifications are listed in Table 4.5. Note that the resource consumption is quantified by the number of DSPs, *Look-Up Tables* (LUTs), and *Flip-Flops* (FFs).

Table 4.5 – Specifications of the fundamental arithmetic blocks.

Operation	Throughput	Latency	DSPs	LUTs	FFs
\pm	1/cycle	5 cycles	2	228	224
\times	1/cycle	2 cycles	3	81	49
Σ	1/cycle	20 cycles	9	–	–
\div	1/cycle	20 cycles	8	–	–

Table 4.6 – Occupation of FPGA resources for DOP = 4.

Resource	Available	Occupied	Percentage
DSPs	600	357	59.5
RAMs	325	262	80.6
LUTs	101'400	43'166	42.6
FFs	202'800	49'088	24.2

Memory Module

The memory module consists of the storage for the operands. As a rule of thumb, it is advisable to use block memory (i.e., RAMs) for large operands like matrices and vectors, and registers (i.e., FFs) for small operands like scalars. In order to increase the performance, some of the calculation steps in Table 4.3 are contracted in the FPGA implementation. For this reason, not all intermediate results need to be stored. Thanks to the said simplifications, it suffices to store $\mathbf{Q}_k, \mathbf{R}_k, \mathbf{C}_k, \mathbf{y}_k, [\mathbf{C}_{k,i} \mathbf{P}_{k,i}^+], \mathbf{K}_k, \hat{\mathbf{x}}_k^- / \hat{\mathbf{x}}_{k,i}^+, \mathbf{P}_k^- / \mathbf{P}_{k,i}^+, (\mathbf{C}_{k,i} \mathbf{P}_{k,i}^+ \mathbf{C}_{k,i}^T + R_{k,i})^{-1}$, and $[\mathbf{C}_{k,i} \hat{\mathbf{x}}_{k,i}^+]$. Recall that some of these operands need to be partitioned into blocks, and stored in separate memories to allow for parallel data processing. Therefore, both the capacity and the organization of the available RAMs impose restrictions on the DOP. Firstly, the total capacity of the RAM slices needs to be large enough to store the operands. Secondly, there need to be sufficiently many RAM slices for parallel read/write access (i.e., DOP \times DOP or DOP \times 1 accesses in parallel).

Resource Occupation of the Entire Architecture

With the resources available in the FPGA of the NI cRIO-9033, DOP = 4 can be achieved. Table 4.6. lists the FPGA resources occupied by the SKF prototype. Clearly, the DSPs and the RAMs are most critical. Indeed, these resources limit the DOP to 4 (i.e., the architecture for DOP =5 does not fit on the FPGA). The large number of DSPs is mainly due to the operations which consist of DOP \times DOP arrays of arithmetic blocks (i.e., matrix addition/subtraction, outer product, and matrix-vector product). The large amount of RAMs is mostly due to the operands $\mathbf{P}_k^- / \mathbf{P}_k^+$ and \mathbf{C}_k , which consist of $S \times S$ and $M \times S$ elements, respectively. The LUTs and FFs are principally used as shift registers for the pipeline stages. Obviously, the occupation of these resources is not critical.

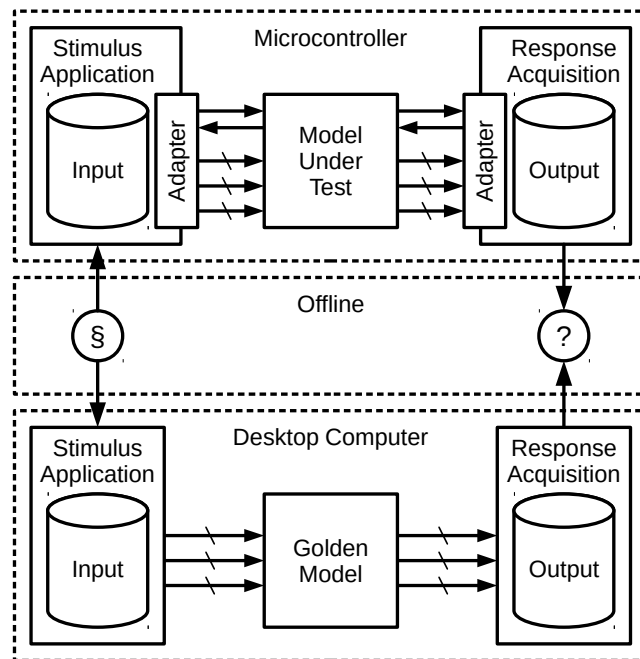


Figure 4.3 – Architecture of the TB setup.

4.6.2 Test Bench

The architecture of the *Test Bench* (TB) is shown in Figure 4.3. It is composed of two parts, which correspond to the *Model Under Test* (MUT) and the *Golden Model* (GM), respectively. Note that, since the stimuli and responses are stored in files, the MUT and the GM can be run independently. So, the analysis of the results can be performed offline.

The MUT part consists of the FPGA prototype plus some CPU software. This part is located on the cRIO-9033, which runs NI Linux Real-Time and NI LabVIEW. The purpose of the CPU software is twofold. Firstly, it provides input/output routines for reading the stimuli for the MUT and writing the responses of the MUT. These processes are facilitated by protocol adapters, which abstract the interface between the high-level data on the CPU and the low-level data on the FPGA. Secondly, it coordinates the communication between the CPU and the FPGA for the application of the stimuli and the acquisition of the responses.

The GM part consists of a MATLAB code of the standard KF. This part is located on a desktop machine, which runs Mac OSX.

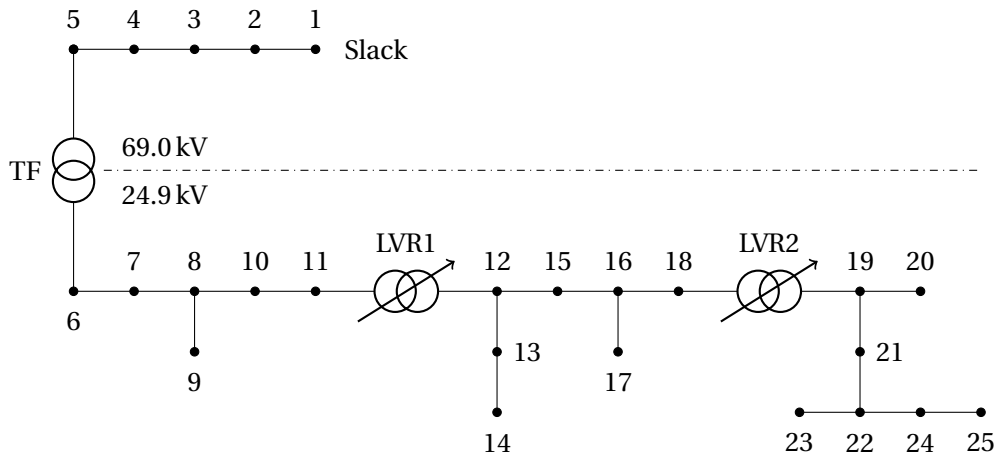


Figure 4.4 – Schematic of the benchmark power grid. Note that the 24.9 kV subsystem is a modified version of the IEEE 34-node distribution feeder.

4.7 Validation of the Hardware Prototype

The validation of the FPGA prototype of the SKF is done in two parts. Firstly, the functionality of the state estimator needs to be verified (see Section 4.7.1). To this end, the FPGA prototype of the SKF is compared with a CPU implementation of the standard KF. The test data are obtained through simulation of a benchmark power grid. Secondly, the scalability of the hardware architecture has to be analyzed (see Section 4.7.2). For this purpose, the FPGA prototype is fed with estimation problems of different sizes. These test data are produced using a random number generator.

4.7.1 Verification of the Functionality

Description of the Benchmark Power Grid

The schematic of the benchmark power grid is depicted in Figure 4.4. As shown, the benchmark power grid consists of two subsystems, which are interfaced through a transformer:

1. Upper-level subsystem (nodes 1–5) with nominal voltage 69.0 kV (phase-to-phase).
2. Lower-level subsystem (nodes 6–25) with nominal voltage 24.9 kV (phase-to-phase).

The former is a linear feeder built of transposed overhead lines. The latter is a modified version of the IEEE 34-node distribution feeder, which consists of untransposed overhead lines and *Line Voltage Regulators* (LVRs) [135]. The specifications of the grid are provided in Appendix A.5. For the sake of simplicity, it is assumed that the tap ratios of the LVRs are equal to 1.0, and that the topology of the grid does not change. By consequence, the compound admittance matrix is constant: $\mathbf{Y}_k = \mathbf{Y}$.

4.7. Validation of the Hardware Prototype

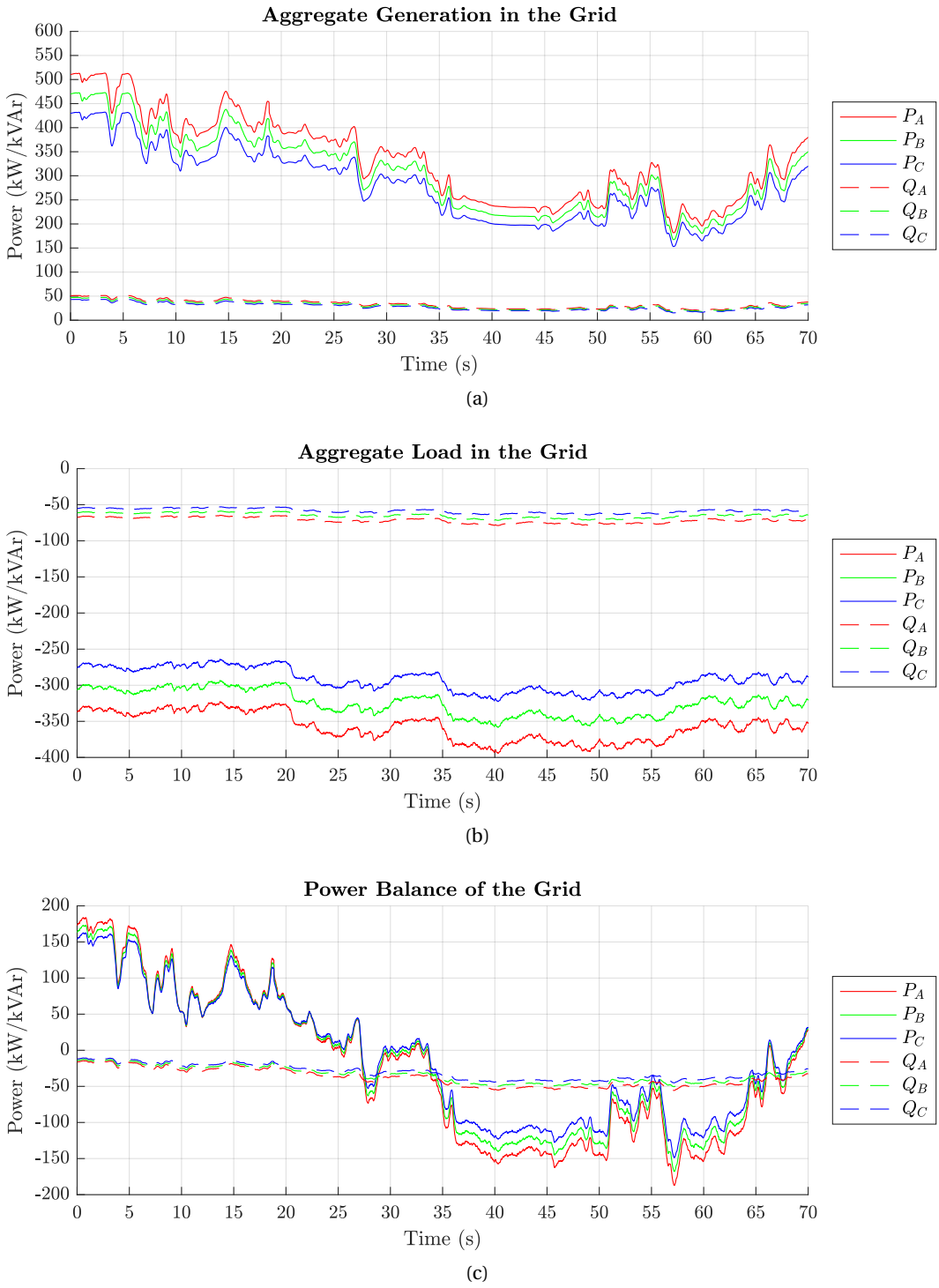


Figure 4.5 – Power profiles used for the validation of the SKF prototype: (4.5a) aggregate generation, (4.5b) aggregate load, and (4.5c) power balance of the benchmark power grid.

The primary substation, which acts as slack node, is in node 1. It has a short-circuit power of 100 MVA. Its *Thévenin Equivalent* (TE) consists of a positive-sequence voltage source, which is rated at nominal voltage, and a diagonal compound impedance matrix with equal diagonal entries, for which $R/X = 0.1$. In the lower-level subsystem, there are three nodes with distributed generation (i.e., 6, 12, and 16) and six nodes with distributed load (i.e., 9, 14, 17, 20, 23, and 25). All the other nodes of the power grid are zero-injection nodes. Accordingly

$$\mathcal{Z} = \{2 - 5, 7 - 8, 10 - 11, 13, 15, 18 - 19, 21 - 22, 24\}$$

$$\mathcal{Z}_0 = \{1, 6, 9, 12, 14, 16, 17, 20, 23, 25\}$$

It is assumed that both the distributed generators and the distributed loads are of constant-power type. The profiles of the aggregate generation, aggregate load, and power balance are shown in Figure 4.5. They correspond to a window of 70 seconds at 50 frames per second (i.e., 3500 samples per profile). The profiles are derived from power measurements recorded in the medium-voltage grid of the EPFL campus in Lausanne, Switzerland [136]. More precisely, the load is a mixture of offices and workshops, and the generation is photovoltaic.

Recall from Section 4.1 that the zero-injection nodes \mathcal{Z} are reduced via KR. The corresponding nodal phase-to-ground voltages can be reconstructed as follows:

$$\mathbf{V}_{\mathcal{Z}} = -\mathbf{Y}_{\mathcal{Z} \times \mathcal{Z}}^{-1} \mathbf{Y}_{\mathcal{Z} \times \mathcal{Z}_0} \mathbf{V}_{\mathcal{Z}_0}$$

The non-zero-injection nodes \mathcal{Z}_0 are equipped with PMUs, which measure the nodal phase-to-ground voltages and nodal injected currents in all phases. In this case, the grid is observable. The PMUs are equipped with voltage/current sensors of class 0.1, which results in a maximum magnitude error of 10^{-3} pu and a maximum phase error of $1.5 \cdot 10^{-3}$ rad [137–139].

As common in power-system analysis, all electrical quantities are expressed in per unit (pu). The base power is chosen as 10 MVA. The base voltage is set to $69.0/\sqrt{3}$ kV (phase-to-ground) for the upper-level system, and $24.9/\sqrt{3}$ kV (phase-to-ground) for the lower-level subsystem.

Preparation of the Test Data

The admittance matrix \mathbf{Y} and the profiles of the nodal injected powers \mathbf{S}_k define power-flow problems, whose solution yields the profiles of the true nodal phase-to-ground voltages \mathbf{V}_k .

The measurements \mathbf{y}_k are created by corrupting the true values with noise, whose statistical properties correspond to the metrological properties of the PMUs and their sensors. More precisely, the standard deviations are set to 1/3 of the assumed maximum errors: $1/3 \cdot 10^{-3}$ pu for the magnitude and $0.5 \cdot 10^{-3}$ rad for the phase. Recall from Section 4.1 that the measurement model is formulated in rectangular coordinates, whereas the characteristics of the measurement noise are given in polar coordinates. The measurement noise covariance matrix \mathbf{R}_k is

obtained using the projection from Appendix A.3. To this end, it is assumed that

$$V_{n,1,k} = 1 \angle 0 \text{ pu}, V_{n,2,k} = 1 \angle -\frac{2\pi}{3} \text{ pu}, V_{n,3,k} = 1 \angle \frac{2\pi}{3} \text{ pu}$$

The process noise covariance matrix \mathbf{Q}_k is assumed to be a constant diagonal matrix with all entries equal to 10^{-6} pu. Lastly, the state estimator requires initial values. One can use $\mathbf{P}_0^+ = \mathbf{Q}$, and set $\hat{\mathbf{x}}_0^+$ to a flat voltage profile.

Finally, the responses $\hat{\mathbf{x}}_k^+|_{\text{MUT}}$ and $\hat{\mathbf{x}}_k^+|_{\text{GM}}$ of the MUT and the GM are produced with the TB. Thus, the estimated nodal phase-to-ground voltages $\hat{\mathbf{V}}_k|_{\text{MUT}}$ and $\hat{\mathbf{V}}_k|_{\text{GM}}$ are obtained (recall that this process involves inverse KR for the zero-injection nodes).

Discussion of the Results

The key performance indicators for the are estimation error of the SKF (i.e., the difference between the estimated and the true state), and the numerical mismatch between the SKF and the standard KF (i.e., the difference between the responses of the MUT and the GM). Moreover, the normalized residuals of the measurements are investigated to perform a sanity check of the measurement model (i.e., the change from polar to rectangular coordinates).

Figure 4.6 shows the statistical distribution of the estimation error in magnitude and phase. The results are shown for selected nodes (i.e, 1, 12, and 20), the non-zero-injection nodes \mathcal{Z}_c , whose voltages are estimated by the SKF, and the zero-injection nodes \mathcal{Z} , whose voltages are reconstructed via inverse KR. Evidently, the estimation error is low in magnitude and phase: roughly half of the samples are within $\pm 1.0 \cdot 10^{-4}$ pu and $\pm 1.0 \cdot 10^{-4}$ rad, respectively. Notably, the estimation errors are substantially lower than the voltage measurement noise of the PMUs. Moreover, the error distributions comparable for the selected nodes and the sets \mathcal{Z}_c and \mathcal{Z} . This demonstrates that the SKF is tracking the state correctly, and that the inverse KR used to reconstruct $\mathbf{V}_{\mathcal{Z}}$ from $\mathbf{V}_{\mathcal{Z}_c}$ does not introduce any noticeable errors.

Figure 4.7 illustrates the statistical distribution of the normalized measurement residuals. With the exception of a few outliers, the residuals are within ± 3 standard deviations, and more than half of them are within ± 1 standard deviation. As a rule of thumb, the normalized residuals should be within ± 3 to ± 4 standard deviations if there are no bad data or model errors (see [16]). The fact that these limits are well respected indicates that the change of coordinates does not introduce noticeable errors to the measurement model.

Figure 4.8 depicts the statistical distribution of the numerical mismatch between the SKF (i.e., the MUT) and the standard KF (i.e., the GM). Except for outliers, the mismatches are within $\pm 1 \cdot 10^{-6}$ pu for $\hat{\mathbf{x}}_k^+$ and $\pm 1 \cdot 10^{-7}$ pu for \mathbf{P}_k^+ . Recall that the SKF works with SGL precision (on the FPGA), and the KF with DBL precision (on the CPU). As known, SGL and DBL precision give 6–9 and 15–17 significant digits, respectively. Thus, the observed mismatches confirm that the FPGA SKF is equivalent to the CPU KF within the available numerical accuracy.

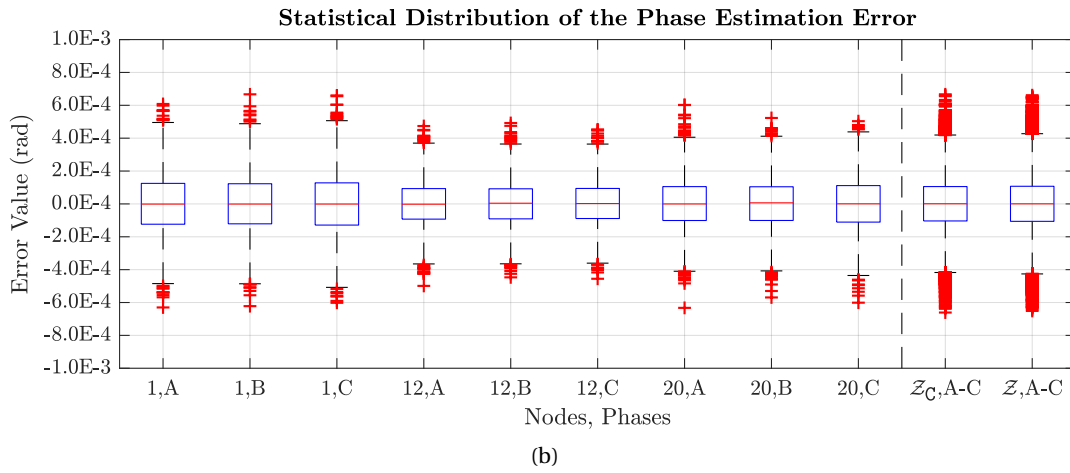
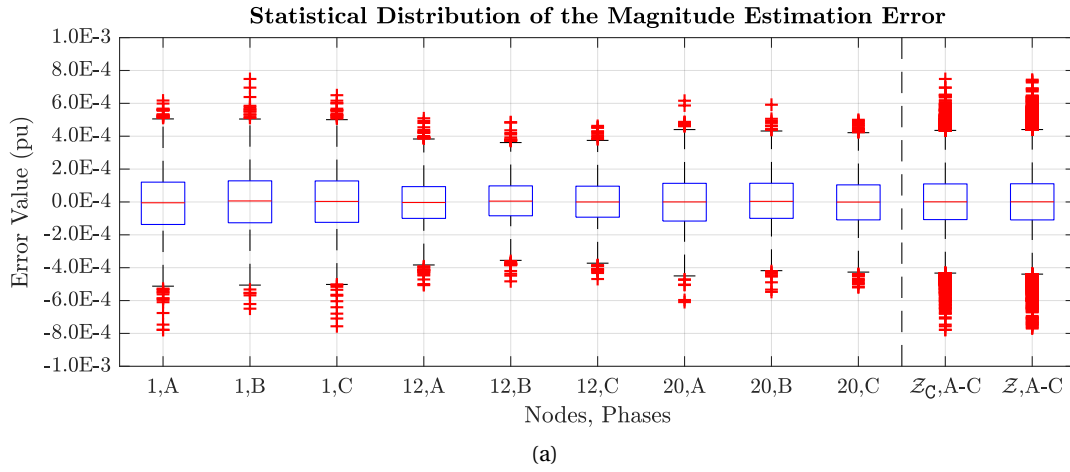


Figure 4.6 – Statistical distribution of the estimation error: (4.6a) magnitude and (4.6b) phase. The distributions are shown for selected nodes (i.e., 1, 12, and 20, and for the sets \mathcal{Z}_C and \mathcal{Z} . The edges of the boxes correspond to the 25th and 75th percentile, respectively.

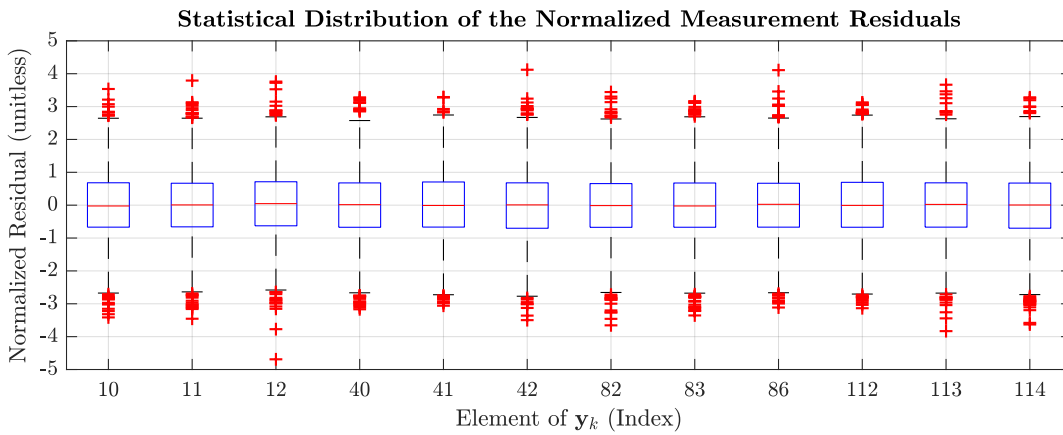


Figure 4.7 – Statistical distribution of the normalized residuals of selected measurements in \mathbf{y}_k . The edges of the boxes correspond to the 25th and 75th percentile, respectively.

4.7. Validation of the Hardware Prototype

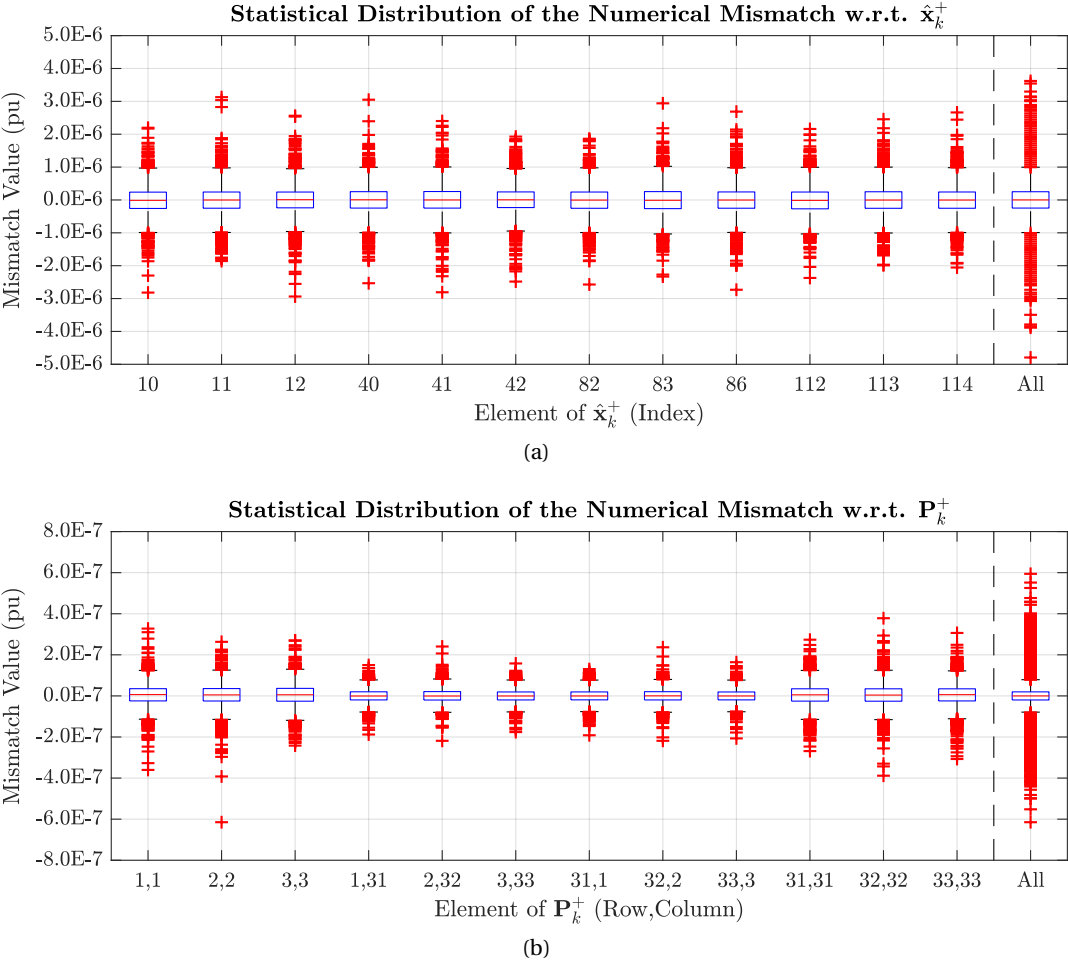


Figure 4.8 – Statistical distribution of the numerical mismatch between SKF and standard KF: (4.8a) \hat{x}_k^+ and (4.8b) P_k^+ . The distributions are shown for selected elements, and for the entire vector/matrix. The edges of the boxes correspond to the 25th and 75th percentile, respectively.

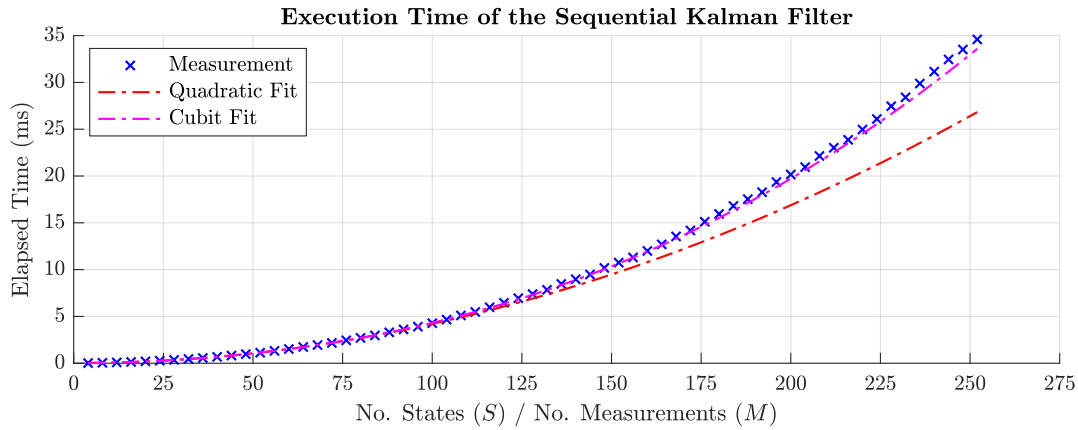


Figure 4.9 – Execution time of the SKF prototype for $S < 256$ and $M = S$. The quadratic fit and the cubic fit are calculated from the measurements for which $S \leq 80$.

4.7.2 Analysis of the Scalability

Description of the Test Procedure

The scalability of the hardware architecture is analyzed by measuring the execution time of the SKF prototype for estimation problems of different size. As benchmark power grids of arbitrary size are not readily available, the test data are produced using a random number generator, while ensuring that the working hypotheses of the SKF hold (e.g., C_k has full rank). For the sake of simplicity, it is assumed that $M = S$ in this test (i.e., a physical system would be observable with no redundancy). The problem size which the SKF prototype can handle is limited by the amount of RAM available on the FPGA. If $M = S$ as assumed, estimation problems with $S < 256$ states can be treated. For a three-phase grid, this would correspond to $\lfloor 255 / (3 \cdot 2) \rfloor = 42$ non-zero-injection nodes (recall from Section 4.1 that the zero-injection nodes are reduced using KR).

The execution time of the SKF is defined as the time which passes between reading the inputs and writing the outputs on the FPGA. This time is measured using an on-chip counter, which is driven by the master clock of the FPGA. Since the frequency of the master clock is known precisely, the execution time can be inferred from the state of the counter.

Discussion of the Results

The evolution of the execution time over the problem size is plotted in Figure 4.9. To visualize the computational complexity, a quadratic and a cubic curve are fit to the portion $S \leq 80$. Note that the cubic fit is virtually congruent with the measurements, which means that the computational complexity is of third order. This is in accordance with the analysis performed in Section 4.5. Moreover, note that the cubic fit does not differ much from the quadratic one, which implies that the cubic term is not dominant. This is due to the fact that the operations

4.7. Validation of the Hardware Prototype

are heavily parallelized and pipelined on the FPGA. That is, the execution time is dominated by the filling of the pipeline rather than the processing of the elements. Finally, note that the execution time is below 20 ms for $S \leq 200$ (i.e., $\lfloor 200/(3 \cdot 2) \rfloor = 33$ non-zero-injection nodes) and equal to 35 ms for $S = 256$ (i.e., 42 non-zero-injection nodes). That is, the state estimator is fast enough to support real-time applications like fault detection and location [112].

5 Real-Time Assessment of the Voltage Stability by a Voltage Stability Index

Contributions: It is known that voltage stability can be a concern in the operation of power distribution systems. Notably, it has been documented that voltage instability can occur while the thermal ratings of lines and transformers are respected [11]. Therefore, real-time control methods for power distribution systems require real-time situation awareness w.r.t. the system stability. To this end, computationally efficient *Voltage Stability Assessment (VSA)* methods are needed. In particular, such VSA methods have to account for the particular characteristics of power distribution systems (e.g., unbalances of the grid components and power injections), and be capable of real-time operation (i.e., refresh rates of tens of frames per second). Classical *Continuation Power Flow (CPF)* methods and conventional *Voltage Stability Indices (VSIs)* do not comply with these requirements. The former work with detailed system models, but are computationally intensive. The latter are computationally efficient, but work with simplistic system models, such as positive-sequence equivalent circuits. In this chapter, a novel VSI, which is suitable for generic unbalanced polyphase power systems, is proposed. More precisely, the proposed VSI is a generalized formulation of the well-known *L-index* [18]. The grid is described by a compound hybrid matrix. In this respect, the theorems discussed in Chapter 3 are leveraged to substantiate the existence of the said compound hybrid matrix. Slack nodes and resource nodes are represented by *Thévenin Equivalent*s (TEs) and *Polynomial Models* (PMs), respectively. In this way, the polyphase nature of the grid and the aggregate behavior of common types of nodes can be adequately modeled. The proposed VSI is obtained by incorporating these models into the classical formulation of the *L-index*. By comparison with CPF study, it is verified that the proposed VSI is able to correctly detect voltage instability. This analysis is performed on a test grid that is based on the IEEE 34-node distribution feeder.

Keywords: voltage stability assessment, voltage stability index, polyphase power systems, unbalanced power systems, *L-index*, Thévenin equivalent, polynomial load model.

Chapter 5. Real-Time Assessment of the Voltage Stability by a Voltage Stability Index

Publications:

- [140] A. M. Kettner and M. Paolone, "A generalized index for static voltage stability of unbalanced polyphase power systems including Thévenin equivalents and polynomial models", accepted for publication in IEEE Trans. Power Syst.
- [115] A. M. Kettner and M. Paolone, "Performance assessment of Kron reduction in the numerical analysis of polyphase power systems", accepted for presentation in IEEE PES PowerTech Conf., Milano, LOM, IT, Jun. 2019.

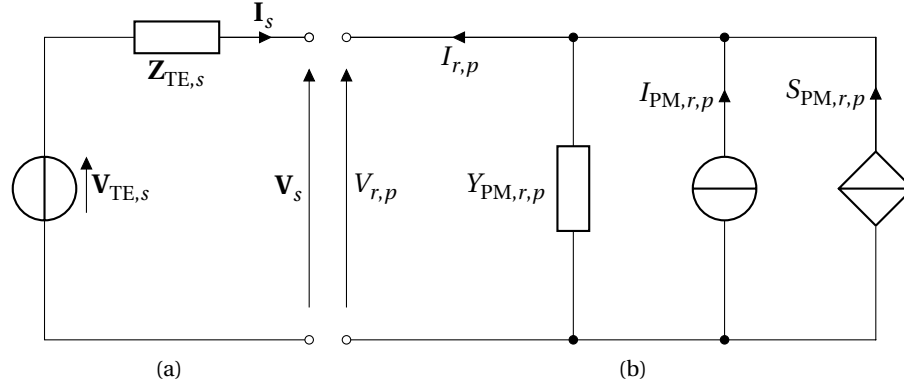


Figure 5.1 – Representation of the aggregate behavior of the nodes: (5.1a) Thévenin equivalent of a slack node $s \in \mathcal{S}$, (5.1b) polynomial model of phase $p \in \mathcal{P}$ in a resource node $r \in \mathcal{R}$.

5.1 The System Model

5.1.1 Electrical Grid

As explained in Chapter 3, the grid is represented by a polyphase equivalent circuit, which consists of polyphase branches and polyphase shunts. Recall that the polyphase branches connect pairs of polyphase nodes, and that the polyphase shunts connect the polyphase nodes with the ground node. The grid can be described by a compound admittance matrix or a compound hybrid matrix (i.e., provided that the respective hypotheses hold).

5.1.2 Aggregate Behavior of the Polyphase Nodes

The nodes \mathcal{N} are divided into three sets based on their generic behavior. Namely

$$\mathcal{N} = \mathcal{S} \cup \mathcal{R} \cup \mathcal{Z} \quad (5.1)$$

where \mathcal{Z} stands for *zero-injection nodes*, \mathcal{S} for *slack nodes*, and \mathcal{R} for *resource nodes*.

Slack Nodes

At the slack nodes $s \in \mathcal{S}$, voltage and frequency are imposed, for instance by a synchronous machine [103], a power electronic converter [141], or a connection to the bulk grid. That is, the slack nodes correspond to $V\delta$ buses in classical power system analysis. These nodes behave like finite-power voltage sources, and are thus modeled by TE[s]:

$$\mathbf{V}_s = \mathbf{V}_{\text{TE},s} - \mathbf{Z}_{\text{TE},s} \mathbf{I}_s \quad (5.2)$$

where $\mathbf{V}_{\text{TE},s}$ and $\mathbf{Z}_{\text{TE},s}$ are the TE voltage sources and impedances, respectively (see Fig. 5.1a). In this respect, it is assumed that these quantities can be either computed or measured.

Resource Nodes

At the resource nodes $r \in \mathcal{R}$, non-zero power is injected, but the voltage is not imposed. That is, resource nodes correspond to PQ buses in classical power systems analysis. In general, these nodes behave like voltage-dependent power sources, which can be approximated by PMs (e.g., [142–144]). Assuming that these equivalent sources have no coupling among the phases, the active power $P_{r,p}$ and reactive power $Q_{r,p}$ injected into phase $p \in \mathcal{P}$ of resource node $r \in \mathcal{R}$ are given by

$$P_{r,p} = \lambda_{r,p} P_{0,r,p} \left(\alpha_{\Re,r,p} \left| \frac{V_{r,p}}{V_{0,r,p}} \right|^2 + \beta_{\Re,r,p} \left| \frac{V_{r,p}}{V_{0,r,p}} \right| + \gamma_{\Re,r,p} \right) \quad (5.3)$$

$$Q_{r,p} = \lambda_{r,p} Q_{0,r,p} \left(\alpha_{\Im,r,p} \left| \frac{V_{r,p}}{V_{0,r,p}} \right|^2 + \beta_{\Im,r,p} \left| \frac{V_{r,p}}{V_{0,r,p}} \right| + \gamma_{\Im,r,p} \right) \quad (5.4)$$

where λ is the loading factor, $\alpha_{\Re/\Im}$, $\beta_{\Re/\Im}$, and $\gamma_{\Re/\Im}$ are normalized polynomial coefficients (i.e., $\alpha_{\Re/\Im} + \beta_{\Re/\Im} + \gamma_{\Re/\Im} = 1$), V_0 is a reference voltage, and P_0 and Q_0 are the reference powers for $\lambda = 1$ and $|V| = V_0$. P_0 and Q_0 follow the generator sign convention. That is, a positive sign indicates injection of power, whereas a negative sign indicates absorption of power.

For a given loading factor, the nodal injected power $S_{r,p} = P_{r,p} + jQ_{r,p}$ can be rewritten as

$$S_{r,p} \approx -Y_{\text{PM},r,p}^* \left| V_{r,p} \right|^2 + V_{r,p} I_{\text{PM},r,p}^* + S_{\text{PM},r,p} \quad (5.5)$$

where Y_{PM} , I_{PM} , and S_{PM} are *Constant Impedance (CZ)*, *Constant Current (CI)*, and *Constant Power (CP)* terms, respectively (see Figure 5.1b). Hence, PMs are also known as ZIP models.

Note that, in case white-box models of the connected devices are available, the TE and PM parameters can be computed numerically or analytically. Otherwise, they can be estimated from measurements, for example through least-squares regression (e.g., [145]). In this thesis, it is assumed that these parameters are known, irrespective of how they have been obtained.

Zero-Injection Nodes

The zero-injection nodes $z \in \mathcal{Z}$ have zero nodal injected current (as the name suggests):

$$\mathbf{I}_z = \mathbf{0} \quad (5.6)$$

5.2 Recall of the Continuation Power Flow Approach

As mentioned before, traditional VSA relies on CPF methods. The essentials of this approach are recalled below.

5.2.1 Parametrization of the Power-Flow Equations

Mismatch Equations in Complex Space

The admittance equations $\mathbf{I} = \mathbf{Y}\mathbf{V}$, TEs (5.2), PMs (5.3)–(5.4), and zero-injection nodes (5.6) define the power-flow equations. The nodal injected powers \mathbf{S} are given by

$$\mathbf{S}(\mathbf{V}) := \mathbf{V} \circ (\mathbf{Y}\mathbf{V})^* \quad (5.7)$$

where \circ is the *Hadamard product*.

The nodal injected powers can also be expressed using the models of the aggregate behavior of the nodes. For the slack nodes $s \in \mathcal{S}$, define

$$\mathbf{S}_{\text{TE}}(\mathbf{V}_{\mathcal{S}}) := \text{col}_{s \in \mathcal{S}} (\mathbf{S}_{\text{TE},s}(\mathbf{V}_s)) \quad (5.8)$$

$$\mathbf{S}_{\text{TE},s}(\mathbf{V}_s) := \mathbf{V}_s \circ (\mathbf{Y}_{\text{TE},s}(\mathbf{V}_{\text{TE},s} - \mathbf{V}_s))^* \quad (5.9)$$

As the TEs represent finite-power voltage sources, it is supposed that the equivalent admittance matrices $\mathbf{Y}_{\text{TE},s} := \mathbf{Z}_{\text{TE},s}^{-1}$ do exist. Similarly, for the resource nodes $r \in \mathcal{R}$, define

$$\mathbf{S}_{\text{PM}}(\mathbf{V}_{\mathcal{R}}, \boldsymbol{\lambda}) := \text{col}_{r \in \mathcal{R}} (\mathbf{S}_{\text{PM},r}(\mathbf{V}_r, \boldsymbol{\lambda}_r)) \quad (5.10)$$

$$\mathbf{S}_{\text{PM},r}(\mathbf{V}_r, \boldsymbol{\lambda}_r) := \text{col}_{p \in \mathcal{P}} (\mathbf{S}_{\text{PM},r,p}(V_{r,p}, \lambda_{r,p})) \quad (5.11)$$

$$\mathbf{S}_{\text{PM},r,p}(V_{r,p}, \lambda_{r,p}) := \lambda_{r,p} \begin{bmatrix} P_{0,r,p} \left(\alpha_{\Re,r,p} \left| \frac{V_{r,p}}{V_{0,r,p}} \right|^2 + \beta_{\Re,r,p} \left| \frac{V_{r,p}}{V_{0,r,p}} \right| + \gamma_{\Re,r,p} \right) \\ + j Q_{0,r,p} \left(\alpha_{\Im,r,p} \left| \frac{V_{r,p}}{V_{0,r,p}} \right|^2 + \beta_{\Im,r,p} \left| \frac{V_{r,p}}{V_{0,r,p}} \right| + \gamma_{\Im,r,p} \right) \end{bmatrix} \quad (5.12)$$

For the zero-injection nodes $z \in \mathcal{Z}$, the nodal injected powers are zero.

An equilibrium point (if it exists) is characterized by zero mismatch $\Delta \mathbf{S}$ between the nodal injected powers calculated using the grid model and the node models, respectively:

$$\Delta \mathbf{S}(\mathbf{V}, \boldsymbol{\lambda}) := \mathbf{S}(\mathbf{V}) - \begin{bmatrix} \mathbf{S}_{\text{TE}}(\mathbf{V}_{\mathcal{S}}) \\ \mathbf{0} \\ \mathbf{S}_{\text{PM}}(\mathbf{V}_{\mathcal{R}}, \boldsymbol{\lambda}) \end{bmatrix} = \mathbf{0} \quad (5.13)$$

These are the *mismatch equations* of the power system. Note that (5.13) is directly derived by applying the law of conservation of energy to the grid under study.

Transformation into Real Space

Observe that (5.13) is a system of complex-valued functions in complex-valued variables. Express $\Delta\mathbf{S}$ in rectangular coordinates and \mathbf{V} in polar coordinates:

$$\Delta\mathbf{S}(\mathbf{V}, \boldsymbol{\lambda}) := \Delta\mathbf{P}(\mathbf{V}, \boldsymbol{\lambda}) + j\Delta\mathbf{Q}(\mathbf{V}, \boldsymbol{\lambda}) \quad (5.14)$$

$$\mathbf{V} := \mathbf{E}\angle\boldsymbol{\theta} \quad (5.15)$$

Thus, (5.13) can be restated as a system of real-valued functions in real-valued variables:

$$\begin{bmatrix} \Delta\mathbf{P}(\mathbf{E}, \boldsymbol{\theta}, \boldsymbol{\lambda}) \\ \Delta\mathbf{Q}(\mathbf{E}, \boldsymbol{\theta}, \boldsymbol{\lambda}) \end{bmatrix} = \mathbf{0} \quad (5.16)$$

Furthermore, define

$$\mathbf{f}(\mathbf{E}, \boldsymbol{\theta}, \boldsymbol{\lambda}) := \begin{bmatrix} \Delta\mathbf{P}(\mathbf{E}, \boldsymbol{\theta}, \boldsymbol{\lambda}) \\ \Delta\mathbf{Q}(\mathbf{E}, \boldsymbol{\theta}, \boldsymbol{\lambda}) \end{bmatrix} \quad (5.17)$$

$$\boldsymbol{\xi} := \begin{bmatrix} \mathbf{E} \\ \boldsymbol{\theta} \end{bmatrix} \quad (5.18)$$

and suppose that $\boldsymbol{\lambda}$ follows a trajectory which is parametrized as $\boldsymbol{\lambda}(\zeta)$. Using these definitions, (5.16) can be written compactly as

$$\mathbf{f}(\boldsymbol{\xi}, \zeta) = \mathbf{0} \quad (5.19)$$

5.2.2 Determination of Loadability Limits via Numerical Continuation

The *loadability limit* ζ_{\max} along the trajectory $\boldsymbol{\lambda}(\zeta)$ is the solution of the nonlinear program

$$\begin{aligned} &\max \zeta \\ &\text{s.t. } \mathbf{f}(\boldsymbol{\xi}, \zeta) = \mathbf{0} \end{aligned} \quad (5.20)$$

It can reasonably be supposed that $\mathbf{f}(\boldsymbol{\xi}, \zeta)$ is continuous and differentiable w.r.t. $\boldsymbol{\xi}$ and ζ [85]. That is, the derivatives $D_{\boldsymbol{\xi}}\mathbf{f}$ and $D_{\zeta}\mathbf{f}$ of \mathbf{f} w.r.t. $\boldsymbol{\xi}$ and ζ , respectively, are defined. In this case, the maximization problem can be solved via numerical continuation. Here, the CPF method proposed in [79], which follows a predictor-corrector approach, is considered as benchmark. For ease of reference, the pseudocode is provided in Algorithm 1.

The predictor extrapolates another solution from a known solution $\boldsymbol{\xi}_k, \zeta_k$. To be more precise, it takes a step of length σ tangent to the solution path. The tangent direction is defined by

$$D_{\boldsymbol{\xi}}\mathbf{f}(\boldsymbol{\xi}_k, \zeta_k)d\boldsymbol{\xi} + D_{\zeta}\mathbf{f}(\boldsymbol{\xi}_k, \zeta_k)d\zeta = \mathbf{0} \quad (5.21)$$

To obtain the unit tangent vector, set $d\zeta = 1$, solve for $d\boldsymbol{\xi}$, and normalize with $\sqrt{\|d\boldsymbol{\xi}\|^2 + 1}$.

5.2. Recall of the Continuation Power Flow Approach

Algorithm 1 Continuation method.

```

procedure CONTINUATION( $f(\xi, \zeta)$ ,  $\xi_0, \zeta_0$ ) ▷ Starting point  $\xi_0, \zeta_0$ .
  for  $k \geq 0$  do
    # Predictor
     $d\xi \leftarrow \text{solve}(D_\xi f(\xi_k, \zeta_k)d\xi = -D_\zeta f(\xi_k, \zeta_k), d\xi)$  ▷ Determine tangent direction.
     $\begin{bmatrix} \xi_{k+1}^- \\ \zeta_{k+1}^- \end{bmatrix} = \begin{bmatrix} \xi_k \\ \zeta_k \end{bmatrix} + \sigma \left( \frac{1}{\sqrt{\|d\xi\|^2 + 1}} \begin{bmatrix} d\xi \\ 1 \end{bmatrix} \right)$  ▷ Take step of length  $\sigma$ .
    # Corrector
     $\mathbf{g}(\xi, \zeta) := \begin{bmatrix} f(\xi, \zeta) \\ \|\xi - \xi_k\|^2 + (\zeta - \zeta_k)^2 - \sigma^2 \end{bmatrix}$ 
     $[\xi_{k+1}^+, \zeta_{k+1}^+] \leftarrow \text{NEWTONRAPHSON}(\mathbf{g}(\xi, \zeta), \xi_{k+1}^-, \zeta_{k+1}^-)$  ▷ Solve  $\mathbf{g}(\xi, \zeta) = \mathbf{0}$ .
     $\begin{bmatrix} \xi_{k+1} \\ \zeta_{k+1} \end{bmatrix} \leftarrow \begin{bmatrix} \xi_{k+1}^+ \\ \zeta_{k+1}^+ \end{bmatrix}$ 
    if  $\text{sign}(\zeta_{k+1} - \zeta_k) \leq 0$  then ▷ Maximum of  $\zeta$  found.
      break
    end if
  end for
  return  $\{\xi_k, \zeta_k\}$  ▷ Continuum of solutions  $\{\xi_k, \zeta_k\}$ .
end procedure

```

The corrector finds an actual solution at distance σ from ξ_k, ζ_k . To this end, it solves

$$\mathbf{g}(\xi, \zeta) := \begin{bmatrix} f(\xi, \zeta) \\ \|\xi - \xi_k\|^2 + (\zeta - \zeta_k)^2 - \sigma^2 \end{bmatrix} = \mathbf{0} \quad (5.22)$$

using the Newton-Raphson method, taking the predicted solution $\xi_{k+1}^-, \zeta_{k+1}^-$ as initial value.

Observe that both the continuation method and the Newton-Raphson method are iterative. Every step of the continuation method requires the following calculations:

- The calculation of the Jacobian matrices $D_\xi f$ and $D_\zeta f$ of f .
- The solution of the systems of linear equations (5.21). This process is direct.
- The solution of the system of nonlinear equations (5.22) using the Newton-Raphson method. This process is iterative.

Every iteration of the Newton-Raphson method requires the following calculations:

- The calculation of the Jacobian matrices $D_\xi \mathbf{g}$ and $D_\zeta \mathbf{g}$ of \mathbf{g} .
- The solution of a system of nonlinear equations (i.e., to update equation).

This hints at why CPF methods are computationally intensive.

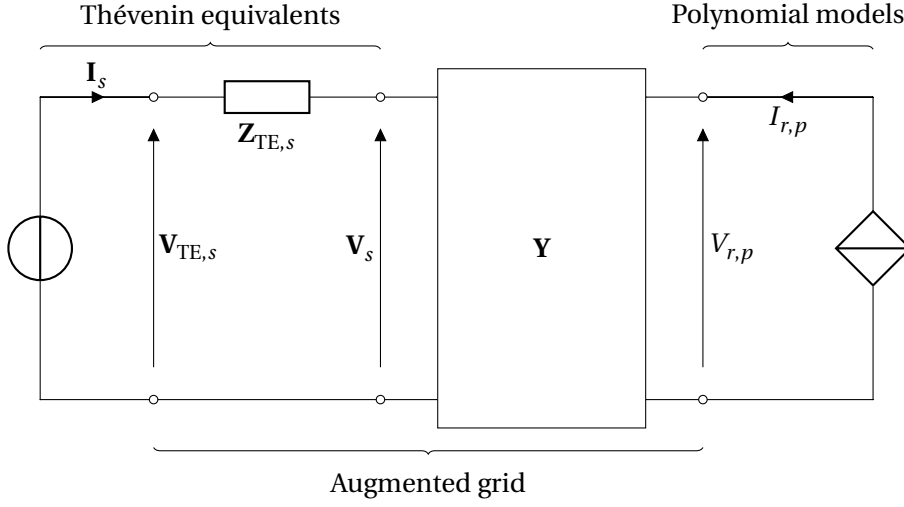


Figure 5.2 – Schematic of the system model for the derivation of the voltage stability index.

5.3 The Generalized Formulation of the L-Index

5.3.1 Reformulation of the System Model

Augmentation of the Grid Model

Summarizing Section 5.1, the power system is described by

$$\mathbf{I} = \mathbf{Y}\mathbf{V} \quad (5.23)$$

$$\mathbf{V}_s = \mathbf{V}_{TE,s} - \mathbf{Z}_{TE,s}\mathbf{I}_s \quad s \in \mathcal{S} \quad (5.24)$$

$$\mathbf{I}_z = \mathbf{0} \quad z \in \mathcal{Z} \quad (5.25)$$

$$I_{r,p} = -Y_{PM,r,p}V_{r,p} + I_{PM,r,p} + \frac{S_{PM,r,p}^*}{V_{r,p}^*} \quad r \in \mathcal{R}, p \in \mathcal{P} \quad (5.26)$$

Provided that the $\mathbf{Z}_{TE,s}$ comply with Hypothesis 3, that is

Hypothesis 11 (TE). *The TE impedance matrices $\mathbf{Z}_{TE,s}$ are symmetric, invertible, and lossy:*

$$\forall s \in \mathcal{S} : \begin{cases} \mathbf{Z}_{TE,s} = \mathbf{Z}_{TE,s}^T \\ \exists \mathbf{Y}_{TE,s} = \mathbf{Z}_{TE,s}^{-1} \\ \Re \{ \mathbf{Z}_{TE,s} \} \geq 0 \end{cases} \quad (5.27)$$

They can be interpreted as compound impedance matrices of additional polyphase branches. This defines an *augmented grid*, which connects the TE voltage sources with the PMs (see Figure 5.2).

Write the admittance equations (5.23) in block form w.r.t. to \mathcal{S} , \mathcal{I} , and \mathcal{R} :

$$\begin{bmatrix} \mathbf{I}_{\mathcal{S}} \\ \mathbf{I}_{\mathcal{I}} \\ \mathbf{I}_{\mathcal{R}} \end{bmatrix} = \begin{bmatrix} \mathbf{Y}_{\mathcal{S} \times \mathcal{S}} & \mathbf{Y}_{\mathcal{S} \times \mathcal{I}} & \mathbf{Y}_{\mathcal{S} \times \mathcal{R}} \\ \mathbf{Y}_{\mathcal{I} \times \mathcal{S}} & \mathbf{Y}_{\mathcal{I} \times \mathcal{I}} & \mathbf{Y}_{\mathcal{I} \times \mathcal{R}} \\ \mathbf{Y}_{\mathcal{R} \times \mathcal{S}} & \mathbf{Y}_{\mathcal{R} \times \mathcal{I}} & \mathbf{Y}_{\mathcal{R} \times \mathcal{R}} \end{bmatrix} \begin{bmatrix} \mathbf{V}_{\mathcal{S}} \\ \mathbf{V}_{\mathcal{I}} \\ \mathbf{V}_{\mathcal{R}} \end{bmatrix} \quad (5.28)$$

Moreover, define

$$\mathbf{V}_{\text{TE}} := \text{col}_{s \in \mathcal{S}} (\mathbf{V}_{\text{TE},s}) \quad (5.29)$$

$$\mathbf{Y}_{\text{TE}} := \text{diag}_{s \in \mathcal{S}} (\mathbf{Y}_{\text{TE},s}) \quad (5.30)$$

where Hypothesis 11 ensures the existence of the $\mathbf{Y}_{\text{TE},s}$. Thus, the TE equations (5.24) can be written compactly as

$$\mathbf{I}_{\mathcal{S}} = \mathbf{Y}_{\text{TE}} (\mathbf{V}_{\text{TE}} - \mathbf{V}_{\mathcal{S}}) \quad (5.31)$$

Through combination of (5.28), (5.31), and (5.25), one obtains the admittance equations of the augmented grid:

$$\begin{bmatrix} \mathbf{I}_{\mathcal{S}} \\ \mathbf{0} \\ \mathbf{0} \\ \mathbf{I}_{\mathcal{R}} \end{bmatrix} = \begin{bmatrix} \mathbf{Y}_{\text{TE}} & -\mathbf{Y}_{\text{TE}} & \mathbf{0} & \mathbf{0} \\ -\mathbf{Y}_{\text{TE}} & \mathbf{Y}_{\text{TE}} + \mathbf{Y}_{\mathcal{S} \times \mathcal{S}} & \mathbf{Y}_{\mathcal{S} \times \mathcal{I}} & \mathbf{Y}_{\mathcal{S} \times \mathcal{R}} \\ \mathbf{0} & \mathbf{Y}_{\mathcal{I} \times \mathcal{S}} & \mathbf{Y}_{\mathcal{I} \times \mathcal{I}} & \mathbf{Y}_{\mathcal{I} \times \mathcal{R}} \\ \mathbf{0} & \mathbf{Y}_{\mathcal{R} \times \mathcal{S}} & \mathbf{Y}_{\mathcal{R} \times \mathcal{I}} & \mathbf{Y}_{\mathcal{R} \times \mathcal{R}} \end{bmatrix} \begin{bmatrix} \mathbf{V}_{\text{TE}} \\ \mathbf{V}_{\mathcal{S}} \\ \mathbf{V}_{\mathcal{I}} \\ \mathbf{V}_{\mathcal{R}} \end{bmatrix} \quad (5.32)$$

Note that the slack nodes \mathcal{S} are zero-injection nodes in the augmented grid.

Kron Reduction and Hybrid Parameters

It can reasonably be assumed that the branch impedances and the TE impedances are lossy. That is, the augmented grid model satisfies the conditions of Corollaries 1–2. By Corollary 1, the slack nodes \mathcal{S} and the zero-injection nodes \mathcal{I} can be eliminated from the model of the augmented grid through *Kron Reduction* (KR). This yields

$$\begin{bmatrix} \mathbf{I}_{\mathcal{S}} \\ \mathbf{I}_{\mathcal{R}} \end{bmatrix} = \begin{bmatrix} \hat{\mathbf{Y}}_{\mathcal{S} \times \mathcal{S}} & \hat{\mathbf{Y}}_{\mathcal{S} \times \mathcal{R}} \\ \hat{\mathbf{Y}}_{\mathcal{R} \times \mathcal{S}} & \hat{\mathbf{Y}}_{\mathcal{R} \times \mathcal{R}} \end{bmatrix} \begin{bmatrix} \mathbf{V}_{\text{TE}} \\ \mathbf{V}_{\mathcal{R}} \end{bmatrix} \quad (5.33)$$

By Corollary 2, the aforesaid equation can be rewritten in hybrid form:

$$\begin{bmatrix} \mathbf{I}_{\mathcal{S}} \\ \mathbf{V}_{\mathcal{R}} \end{bmatrix} = \begin{bmatrix} \hat{\mathbf{H}}_{\mathcal{S} \times \mathcal{S}} & \hat{\mathbf{H}}_{\mathcal{S} \times \mathcal{R}} \\ \hat{\mathbf{H}}_{\mathcal{R} \times \mathcal{S}} & \hat{\mathbf{H}}_{\mathcal{R} \times \mathcal{R}} \end{bmatrix} \begin{bmatrix} \mathbf{V}_{\text{TE}} \\ \mathbf{I}_{\mathcal{R}} \end{bmatrix} \quad (5.34)$$

Note that $\hat{\mathbf{Y}}$ and $\hat{\mathbf{H}}$ are constant as long as the compound electrical parameters and the topology of the augmented grid remain unchanged.

5.3.2 Development of the Voltage Stability Index

Approximation of the Power-Flow Equations by Complex Quadratic Equations

For a given resource node $r \in \mathcal{R}$, the second row of (5.34) reads

$$\mathbf{V}_r = \sum_{i \in \mathcal{S}} \hat{\mathbf{H}}_{ri} \mathbf{V}_{\text{TE},i} + \sum_{j \in \mathcal{R}} \hat{\mathbf{H}}_{rj} \mathbf{I}_j \quad (5.35)$$

where $\hat{\mathbf{H}}_{ri}$ ($i \in \mathcal{S}$) and $\hat{\mathbf{H}}_{rj}$ ($j \in \mathcal{R}$) are blocks of $\hat{\mathbf{H}}_{\mathcal{R} \times \mathcal{S}}$ and $\hat{\mathbf{H}}_{\mathcal{R} \times \mathcal{R}}$, respectively. Accordingly, for a given phase $p \in \mathcal{P}$ of node r , it holds that

$$V_{r,p} = \sum_{i \in \mathcal{S}} \text{row}_p(\hat{\mathbf{H}}_{ri}) \mathbf{V}_{\text{TE},i} + \sum_{j \in \mathcal{R}} \text{row}_p(\hat{\mathbf{H}}_{rj}) \mathbf{I}_j \quad (5.36)$$

Recall that the elements $I_{j,q}$ of \mathbf{I}_j ($j \in \mathcal{R}$, $q \in \mathcal{P}$) are given by the PMs (5.26). Namely

$$I_{j,q} = -Y_{\text{PM},j,q} V_{j,q} + I_{\text{PM},j,q} + \frac{S_{\text{PM},j,q}^*}{V_{j,q}^*} \quad (5.37)$$

This PM is a function of $V_{j,q}$. By introducing

$$\tilde{Y}_{\text{PM},j,q} := \frac{V_{j,q}}{V_{r,p}} Y_{\text{PM},j,q} \quad (5.38)$$

$$\tilde{S}_{\text{PM},j,q} := \frac{V_{r,p}}{V_{j,q}} S_{\text{PM},j,q} \quad (5.39)$$

$I_{j,q}$ can be restated as a function of $V_{r,p}$ instead:

$$I_{j,q} = -\tilde{Y}_{\text{PM},j,q} V_{r,p} + I_{\text{PM},j,q} + \frac{\tilde{S}_{\text{PM},j,q}^*}{V_{r,p}^*} \quad (5.40)$$

Analogously, define

$$\tilde{\mathbf{Y}}_{\text{PM},j} := \text{col}_{q \in \mathcal{P}}(\tilde{Y}_{\text{PM},j,q}) \quad (5.41)$$

$$\mathbf{I}_{\text{PM},j} := \text{col}_{q \in \mathcal{P}}(I_{\text{PM},j,q}) \quad (5.42)$$

$$\tilde{\mathbf{S}}_{\text{PM},j} := \text{col}_{q \in \mathcal{P}}(\tilde{S}_{\text{PM},j,q}) \quad (5.43)$$

and rewrite \mathbf{I}_j as a function of $V_{r,p}$:

$$\mathbf{I}_j = \tilde{\mathbf{Y}}_{\text{PM},j} V_{r,p} + \mathbf{I}_{\text{PM},j} + \frac{\tilde{\mathbf{S}}_{\text{PM},j}^*}{V_{r,p}^*} \quad (5.44)$$

Substituting (5.44) into (5.36) yields

$$V_{r,p} = -a_{r,p} V_{r,p} + b_{r,p} + \frac{c_{r,p}}{V_{r,p}^*} \quad (5.45)$$

$$a_{r,p} := \sum_{j \in \mathcal{R}} \text{row}_p(\hat{\mathbf{H}}_{rj}) \tilde{\mathbf{Y}}_{\text{PM},j} \quad (5.46)$$

$$b_{r,p} := \sum_{i \in \mathcal{L}} \text{row}_p(\hat{\mathbf{H}}_{ri}) \mathbf{V}_{\text{TE},i} + \sum_{j \in \mathcal{R}} \text{row}_p(\hat{\mathbf{H}}_{rj}) \mathbf{I}_{\text{PM},j} \quad (5.47)$$

$$c_{r,p} := \sum_{j \in \mathcal{R}} \text{row}_p(\hat{\mathbf{H}}_{rj}) \tilde{\mathbf{S}}_{\text{PM},j}^* \quad (5.48)$$

Equation (5.45) can be rearranged as follows

$$\left| V_{r,p} \right|^2 - \frac{b_{r,p}}{1 + a_{r,p}} V_{r,p}^* = \frac{c_{r,p}}{1 + a_{r,p}} \quad (5.49)$$

Thus, the power-flow equations can be locally approximated by complex quadratic equations.

Solvability of the Complex Quadratic Equations

As shown in [18], a complex quadratic equations of the form (5.49) is solvable if the index $L_{r,p}$, which is defined as

$$L_{r,p} := \left| 1 - \frac{b_{r,p}}{1 + a_{r,p}} \frac{1}{V_{r,p}} \right| = \left| \frac{c_{r,p}}{1 + a_{r,p}} \frac{1}{V_{r,p}^2} \right| \quad (5.50)$$

lies in the range $L_{r,p} \leq 1$. Namely, (5.49) has two solutions if $L_{r,p} < 1$ and one solution if $L_{r,p} = 1$. In case there are two solutions, $L_{r,p} < 1$ for both of them (i.e., the VSI is defined both on the high-voltage and the low-voltage branch of the nose curve). In that sense, the $L_{r,p}$ are local indicators for the solvability of the power-flow equations. A critical point is reached if at least one of them is equal to 1. Hence

$$L := \max_{r \in \mathcal{R}} \max_{p \in \mathcal{P}} L_{r,p} \quad (5.51)$$

is a VSI for the power system. Namely, $L < 1$ in the stable region and $L = 1$ on the stability boundary.

Compared to the original L -index [18] and the existing extensions [103,104], the proposed generalized formulation applies to more generic systems. Namely, it can handle unbalanced polyphase systems, whose nodes are represented by TEs or PMs, respectively. In this context, Hypotheses 1–11 and Corollaries 1–2 ensure the existence of the compound hybrid matrix $\hat{\mathbf{H}}$, which is required for the calculation of the VSI.

Computational Complexity

Suppose that the nodal voltages $V_{r,p}$, the compound admittance matrix $\hat{\mathbf{Y}}$, the TE parameters $\mathbf{V}_{\text{TE},s}$ and $\mathbf{Z}_{\text{TE},s}$ ($s \in \mathcal{S}$), and the PM parameters $Y_{\text{PM},r,p}$, $I_{\text{PM},r,p}$, and $S_{\text{PM},r,p}$ ($r \in \mathcal{R}$) are known. Then, the VSI requires the following calculations:

- A Schur complement for $\hat{\mathbf{H}}$.
- Multiplications and divisions for $\tilde{Y}_{\text{PM},r,p}$ and $\tilde{S}_{\text{PM},r,p}$.
- Inner products for $a_{r,p}$, $b_{r,p}$, and $c_{r,p}$.
- Additions, divisions, and absolute values for $L_{r,p}$.
- A maximum value for L .

Note that $\hat{\mathbf{H}}$ does not need to be refreshed while the electrical parameters and the topology of the augmented grid remain unchanged. Unlike the CPF method, the VSI does not involve any iterative methods (i.e., which require the calculation of Jacobian matrices, and the solution of the associated systems of linearized equations). Hence, the proposed VSI is computationally less intensive than classical VSA methods, such as the CPF method discussed in Section 5.2.

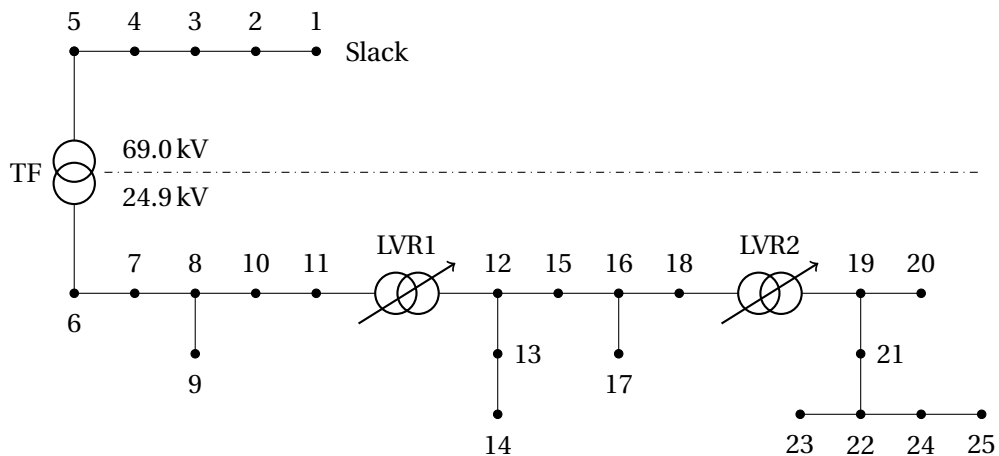


Figure 5.3 – Schematic of the benchmark power grid. Note that the 24.9 kV subsystem is a modified version of the IEEE 34-node distribution feeder.

5.4 Validation of the Proposed Voltage Stability Index

5.4.1 Description of the Benchmark Power Grid

The VSI is validated using the same benchmark power grid already used in Chapter 4. For ease of reference, the schematic is provided in Figure 5.3. Recall that the benchmark power grid consists of two subsystems with nominal voltage of 69.0 kV phase-to-phase (nodes 1–5) and 24.9 kV phase-to-phase (nodes 6–25), respectively. The first subsystem is a linear feeder, which is built of transposed overhead lines. The second subsystem is a modified version of the IEEE 34-node distribution feeder, which consists of untransposed overhead lines and *Line Voltage Regulators* (LVRs) [135]. The detailed specifications of the grid are provided in Appendix A.5. For the sake of simplicity, it is supposed that the tap ratios of the LVRs are fixed to 1.05, and that the topology of the grid does not change (i.e., there are no disconnections of lines or transformers). In case the tap ratios are changed (e.g., due to voltage control), one can simply rebuild the compound admittance matrix and compound hybrid matrix, respectively.

The slack node is the primary substation in node 1. Its TE consists of a positive-sequence voltage source, which is defined by the rated voltage, and a diagonal compound impedance matrix with equal diagonal entries, which are defined by the short-circuit parameters. The substation is characterized by the short-circuit power of 100 MVA at $R/X = 0.1$. The resource nodes are located in the 24.9 kV subsystem, and host loads and compensators. Generators are not considered, since voltage instability due to generation is unlikely in a lossy grid like this one [82]. The PMs are specified in Tables 5.1–5.2. The load coefficients are taken from [142] (i.e., the means of zones 11–16 and 21–26). These values are derived from real measurements. The compensators are assumed to be *Static Synchronous Compensators* (STATCOMs), which supply constant reactive power.

Table 5.1 – Reference values of the utilized polynomial models.

Node	V_0 (kV)	$P_{0,A}, P_{0,B}, P_{0,C}$ (kW)	$Q_{0,A}, Q_{0,B}, Q_{0,C}$ (kVAR)	Type
9	14.4	-60, -50, -40	-30, -25, -20	Load
14	14.4	-75, -60, -45	-40, -30, -21	Load
17	14.4	-90, -70, -50	-50, -35, -22	Load
20	14.4	-105, -80, -55	-60, -40, -23	Load
23	14.4	-120, -90, -60	-70, -45, -24	Load
25	14.4	-135, -100, -65	-80, -50, -25	Load
12	14.4	0, 0, 0	100, 100, 100	Compensator
19	14.4	0, 0, 0	100, 100, 100	Compensator

Table 5.2 – Normalized coefficients of utilized polynomial models.

Type	$\alpha_{\Re}, \beta_{\Re}, \gamma_{\Re}$	$\alpha_{\Im}, \beta_{\Im}, \gamma_{\Im}$
Load	-0.067, 0.251, 0.816	1.064, -0.088, 0.025
Compensator	0.000, 0.000, 0.000	0.000, 0.000, 1.000

5.4.2 Validation Method

The VSI proposed in Section 5.3 is validated against the CPF method explained in Section 5.2. Following common practice, the trajectory $\lambda(\zeta)$ is chosen as uniform load increase [83,85]. That is, $\lambda_{r,p} = \zeta$ for the PMs that represent loads, and $\lambda_{r,p} = 1$ for the PMs that represent compensators. The VSI is evaluated along the continuum of solutions produced by the CPF method. At the loadability limit (i.e., $\zeta = \zeta_{\max}$), the VSI at the critical phase of the critical node is expected to be (approximately) equal 1.

Furthermore, the loadability limit is verified graphically and numerically. For the graphical validation, the nose curves of the system and the characteristic curves of the loads are plotted. These curves are tangent at a loadability limit. For the numerical validation, the singular values of the Jacobian matrix of the power-flow equations are calculated. Recall from Section 2.3 that the Jacobian matrix becomes singular when a loadability limit is approached. By consequence, at least one of its singular values must tend to zero.

5.4.3 Discussion of the Results

The CPF method identifies the loadability limit as $\zeta_{\max} = 1.759$. The maximum value of the VSI occurs in phase A of node 25, that is $L = L_{25,A} = 1.017$. In view of the radial topology and the load distribution, this is plausible: node 25 is furthest away from the slack node (see Figure 5.3), and phase A bears the highest load (see Table 5.1).

5.4. Validation of the Proposed Voltage Stability Index

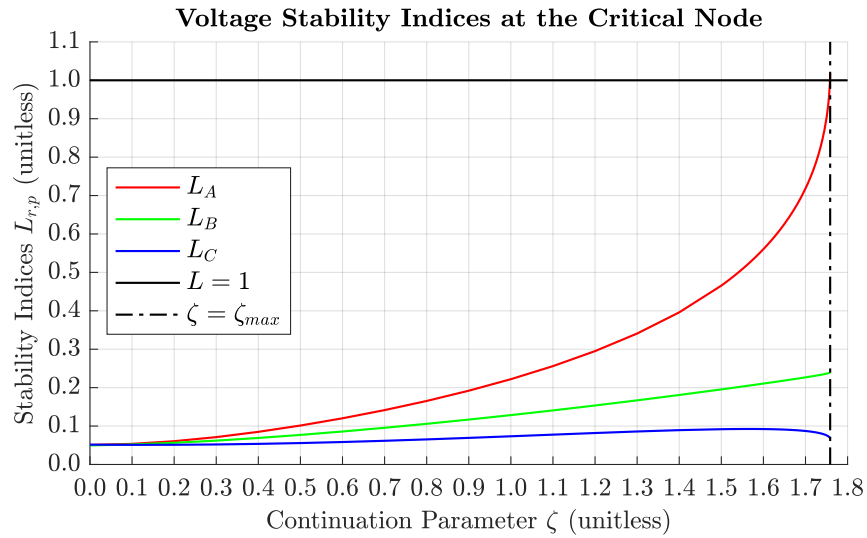


Figure 5.4 – Evolution of the proposed voltage stability index at the critical node (i.e., node 25), and comparison with the loadability limit computed with the continuation power flow method.

The evolution of the VSIs at this node is shown in Fig. 5.4. Clearly, only $L_{25,A}$ tends to 1 as ζ increases, whereas $L_{25,B}$ and $L_{25,C}$ remain much lower. This behavior is consistent with what has been observed for original L -index in [18]. The VSIs in the other nodes of the system behave similarly. That is, the indices in phase A are higher than those in phases B and C , and all of them are lower than those in node 25.

As mentioned before, the Jacobian matrix of the power-flow equations is expected to become singular when a loadability limit reached. To confirm this, the evolution of the maximum, minimum, and mean of the singular values of the Jacobian matrix is shown in Fig. 5.5. Evidently, the maximum and mean singular value do not change much over the range $[0, \zeta_{max}]$. In contrast, the minimum singular value progressively diminishes as ζ increases, and finally plummets as ζ reaches ζ_{max} . Thus, it can be concluded that the Jacobian matrix of the power-flow equations is indeed singular. This confirms the results obtained using the CPF method and the VSI, respectively.

Moreover, the nose curves and the characteristic curves of the loads (i.e., for $\zeta = \zeta_{max}$) are expected to be tangent at the critical phase of the critical node. The nose curves are obtained by evaluating the PMs on the continuum of solutions $\{\xi_k, \zeta_k\}$. The characteristic curves of the loads are produced by evaluating the PMs for $\zeta = \zeta_{max}$ over a range of (fictitious) voltage magnitudes. The results are shown in Figure 5.6. Clearly, the curves in phase A of node 25 are tangent. This confirms that the CPF has identified a valid loadability limit, and that the VSI correctly detects it. It is worth noting that the nose curves of phase A are bent downward (i.e., towards lower voltage), whereas those of phases B and C start bending upward (i.e., towards higher voltage) as $\zeta \rightarrow \zeta_{max}$. The change of curvature is clearly visible in phase B . This behavior is in accordance with the CPF studies of unbalanced triphase systems in [83,84].

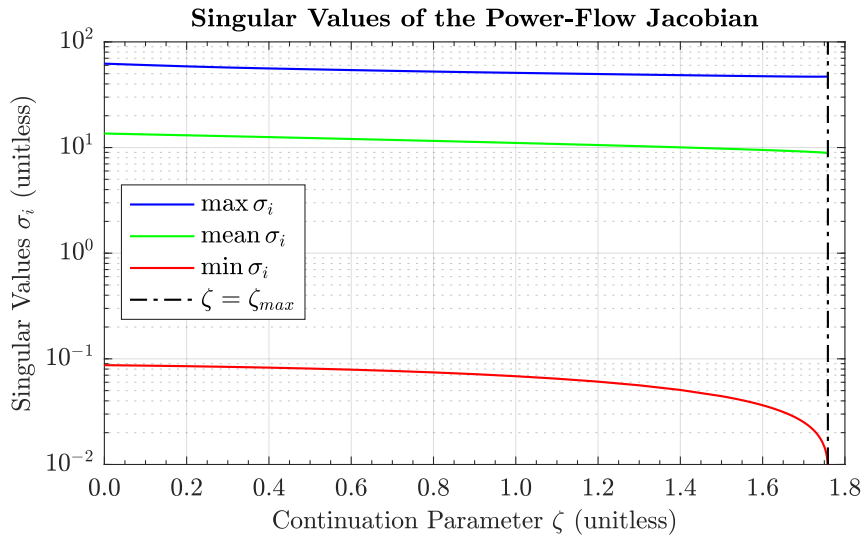


Figure 5.5 – Evolution of the singular values of the Jacobian matrix of the power-flow equations.

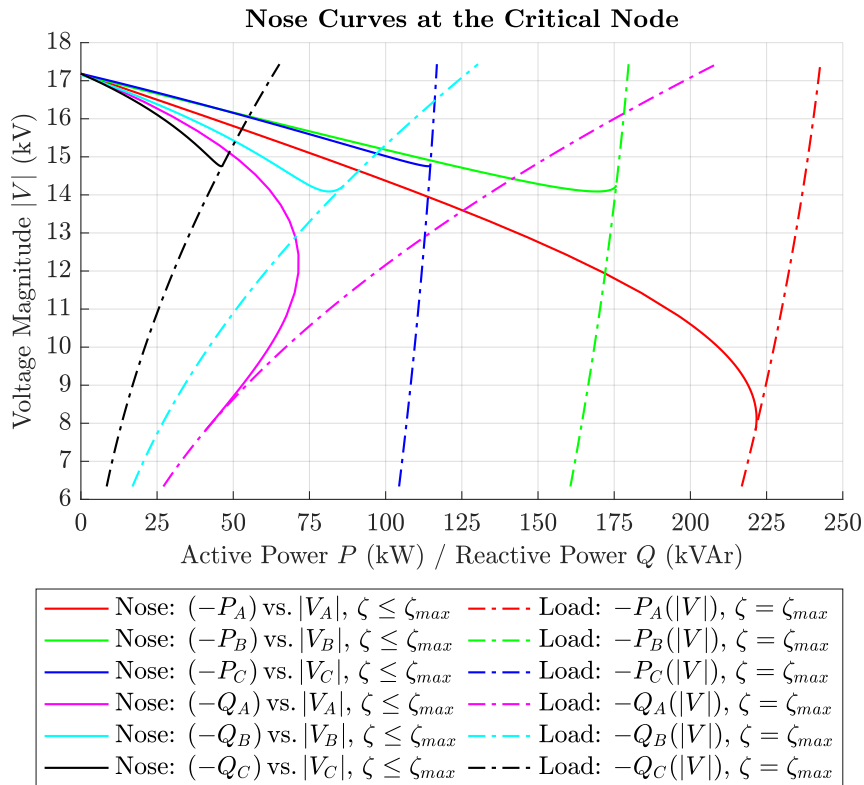


Figure 5.6 – Nose curves and characteristic curves of the loads at the critical node (i.e., node 25).

5.4. Validation of the Proposed Voltage Stability Index

Table 5.3 – Magnitudes of the phase-to-ground voltages at the load nodes for $\zeta = \zeta_{\max}$.

Node	V_A (kV)	V_B (kV)	V_C (kV)	V_{nominal} (kV)
9	12.1	14.1	14.4	14.4
14	9.9	14.1	14.5	14.4
17	8.8	13.9	14.3	14.4
20	8.1	14.3	14.8	14.4
23	7.9	14.3	14.8	14.4
25	7.8	14.3	14.8	14.4

Table 5.4 – Magnitudes of the conductor currents in selected lines for $\zeta = \zeta_{\max}$.

Line	I_A (A)	I_B (A)	I_C (A)	I_{rated} (A)
1–2	40.8	21.1	18.4	300
5–6	120.6	60.8	40.9	230
8–10	111.9	54.1	36.1	230
12–15	95.3	45.5	29.0	180
16–18	78.3	36.1	22.7	180
19–21	54.2	26.0	16.0	180
22–24	28.8	13.7	8.4	180

Finally, there are some comments to be made regarding the practicality of the obtained results. As one can see in Figure 5.6, the voltage in phase A of node 25 is low: roughly 8 kV, which corresponds to around 55% of the nominal voltage. This value lies outside the range desired for regular operation. Table 5.3 lists the magnitudes of the phase-to-ground voltages at the load nodes, which are observed at the loadability limit (i.e., for $\zeta = \zeta_{\max}$). Low voltages only occur in phase A, which bears the highest load (recall Table 5.1). In phases B and C, on the other hand, the voltages remain close to the nominal value. Table 5.4 lists the magnitudes of the conductor currents in selected lines, which are observed at the loadability limit (i.e., for $\zeta = \zeta_{\max}$). Moreover, the rated currents of the conductors are respected with ample margin throughout the system. In view of these observations, the identified loadability limit is deemed to be of practical interest. Lastly, it is worth noting that voltage instability may well occur at close-to-nominal voltage in power distribution systems, as documented in [11]. As known, the location of the critical point depends on the characteristics of the grid and the load [146].

6 Practical Deployment into a Real-Scale Microgrid

Contributions: In order to lower the operational cost and improve the service quality to the customers, distribution system operators are expected to equip their grids with automation technology. This automation effort implicates a large-scale deployment of measurement, monitoring, and control devices. In this regard, embedded systems are a key technology, because they are low-cost, which is crucial for minimizing the investment cost. However, as compared to workstation computers or servers, embedded systems have very limited processing power. Therefore, it is crucial to verify that applications like *State Estimation* (SE), see Chapter 4, or *Voltage Stability Assessment* (VSA), see Chapter 5, do indeed run in real time (i.e., at refresh rates of tens of frames per second) on such embedded platforms. Specifically, the latency of these applications has to be quantified. To this end, the methods developed in this thesis are deployed into the microgrid facility of the *Distributed Electrical Systems Laboratory* (DESL) at the *École Polytechnique Fédérale de Lausanne* (EPFL) in Switzerland. This microgrid is a real-scale implementation of the low-voltage benchmark grid defined by the *Conseil International des Grands Réseaux d'Électricité* (CIGRÉ) [19]. To be more precise, the *Sequential Kalman Filter* (SKF) presented in Chapter 4 and the *Voltage Stability Index* (VSI) presented in Chapter 5 are deployed into an industrial real-time controller, and coupled with a low-latency *Phasor Data Concentrator* (PDC) [15] and high-accuracy *Phasor Measurement Units* (PMUs) [14].

Keywords: microgrids, real-time operation, latency assessment, COMMELEC framework.

Publications:

- [147] L. E. Reyes Chamorro, A. Bernstein, N. J. Boumann, E. Scolari, A. M. Kettner, B. Cathiard, J.-Y. Le Boudec, and M. Paolone, “Experimental Validation of an Explicit Power-Flow Primary Control in Microgrids”, *IEEE Trans. Ind. Informat.*, vol. 14, no. 11, pp. 4779–4791, Nov. 2018.
- [148] L. E. Reyes Chamorro, W. Saab, R. Rudnik, A. M. Kettner, M. Paolone and J.-Y. Le Boudec, “Slack Selection for Unintentional Islanding: Practical Validation in a Benchmark Microgrid”, *Proc. Power Syst. Comput. Conf.*, Dublin, L, IE, Jun. 2018.

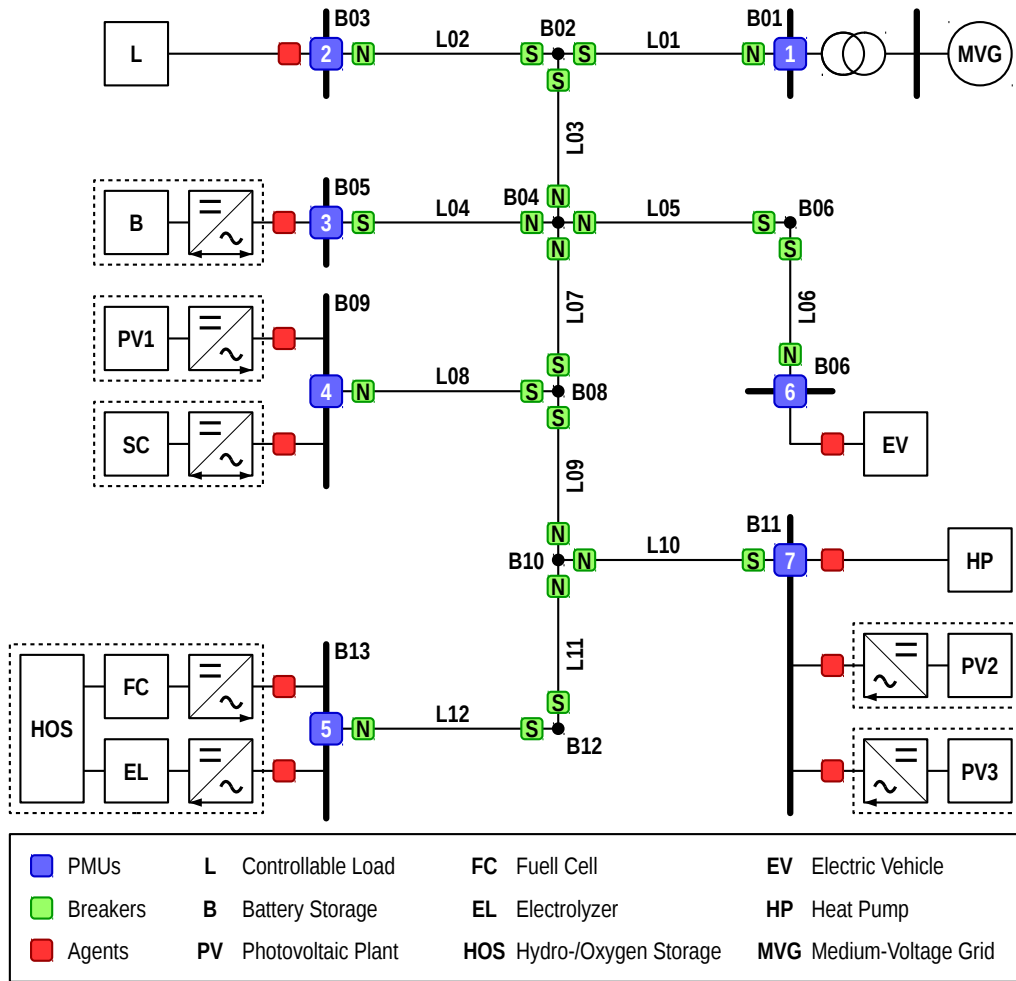


Figure 6.1 – Schematic diagram of the real-scale microgrid of DESL at EPFL.

6.1 Overview of the Microgrid Setup

The practical deployment is done in the microgrid facility of DESL at EPFL in Switzerland. This microgrid is a real-scale implementation of the low-voltage benchmark grid given in [19], which has been defined by the CIGRÉ. In the following, an overview of the experimental facility is presented. For further information, the interested reader is referred to [17,147].

6.1.1 Architecture

Figure 6.1 shows the schematic diagram of the microgrid. The microgrid is a three-phase low-voltage grid operated at 400 V (nominal phase-to-phase voltage), and connected to the medium-voltage grid operated at 20 kV (nominal phase-to-phase voltage) of the EPFL campus through a transformer (i.e., in node B01). The topology is radial, with 13 nodes (B01–13) and 12 lines (L01–12) in total.

Resources

The following resources are connected to the microgrid:

- A controllable load (L) with 24 kW peak power. The load consists of three single-phase power converters, which emulate the consumption of a residential building with an electric heating system.
- A battery storage (B) with 25 kW rated power and 25 kWh storage capacity. The battery consists of Lithium-Titanate cells, which are interfaced with a four-quadrant power converter, which can operate in grid-forming and grid-following mode.
- A supercapacitor storage (SC) with 50 kW rated power and 0.8 kWh storage capacity. The supercapacitor bank consists of six modules (3000 F capacitance each) connected in series, and is interfaced through a four-quadrant power converter, which can operate in grid-forming and grid-following mode (like the one of the battery storage).
- Three photovoltaic generators (PV1–3) with 13 kW (PV1), 20 kW (PV2), and 7 kW (PV3) peak power, respectively. PV1–2 are installed on the roof, and PV3 on the facade of the ELL building of EPFL (i.e., where DESL is located). PV1 is equipped with a four-quadrant power converter (i.e., controllable), whereas PV2–3 are equipped with maximum-power-point-tracking inverters (i.e., uncontrollable).
- A fuel cell (FC) with 15 kW rated power and an electrolyzer (EL) with 6 kW rated power. These are coupled with a hydrogen/oxygen storage (HOS) operated at 30 bar pressure, which has 0.8 MWh storage capacity (i.e., equivalent electrical energy). The fuel cell and electrolyzer are based on proton-exchange-membrane technology.
- An air-to-water heat pump (HP) with 10 kW rated power. This is a controllable load.

Grid

The resources are interconnected through cables. Table 6.1 lists their lengths, ampacities, and per-unit-length positive-sequence parameters. It is worth mentioning that the cables are located under the raised floor of the laboratory. The cables are shielded (i.e., to avoid electromagnetic interference), and connected such that there are no loops.

Chapter 6. Practical Deployment into a Real-Scale Microgrid

Table 6.1 – Data of the cables installed in the microgrid.

Line	Length (m)	Ampacity (A)	R'_p (Ω/km)	X'_p (Ω/km)
L01	70	207	0.272	0.119
L02	30	44	3.300	0.141
L03	35	207	0.272	0.119
L04	30	108	0.780	0.126
L05	105	82	1.210	0.132
L06	30	82	1.210	0.132
L07	70	135	0.554	0.123
L08	30	207	0.272	0.119
L09	105	82	1.210	0.132
L10	30	44	3.300	0.141
L11	35	82	1.210	0.132
L12	30	82	1.210	0.132

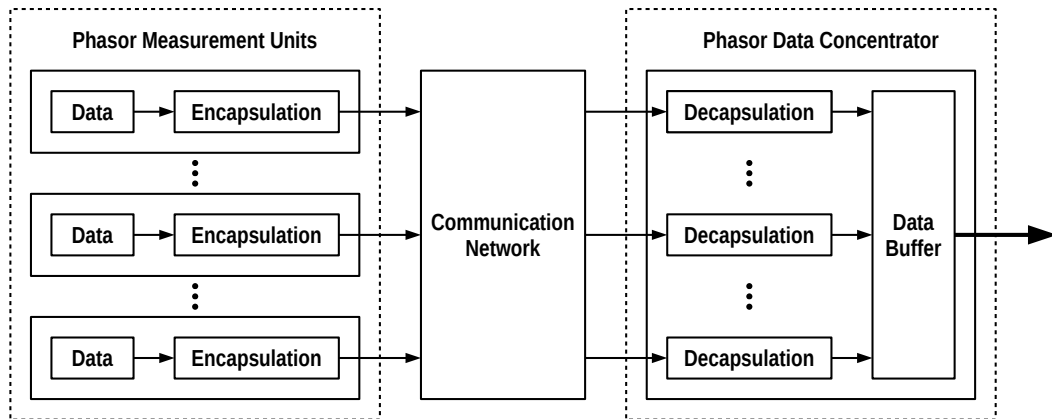


Figure 6.2 – Conceptual diagram of the metering system. The PMUs stream encapsulated synchrophasor data, which are decapsulated and time-aligned by the PDC.

6.1.2 Metering System

The metering infrastructure consists of high-accuracy PMUs and a low-latency PDC, which are described subsequently. The architecture of the metering system is shown in Figure 6.2.

Phasor Measurement Units

The PMUs are based on the interpolated discrete Fourier transform [14]. Specifically, the hardware implementation presented in [149], which complies with the industry standards [123,124], is used. The PMUs are implemented in NI cRIO-9068 real-time controllers, which are equipped both with a *Central Processing Unit* (CPU) and a *Field-Programmable Gate Array* (FPGA) [150]. Data acquisition (i.e., sampling of voltage/current waveforms) and signal processing (i.e., synchrophasor estimation) are performed on the FPGA, whereas the communication (i.e., data encapsulation and streaming) are done on the CPU. For data acquisition, voltage transducers of type LEM CV 3-1000 ($\pm 0.2\%$ accuracy) [151] and current transducers of type LEM LF 205-S/SP1 ($\pm 0.5\%$ accuracy) [152] are used. For time synchronization of the PMUs, Trimble Bullet III GPS antennas [153] are utilized. The synchrophasors are encapsulated into *User Datagram Protocol* (UDP) datagrams according to [124] and broadcast over Ethernet. The streaming rate is 50 frames per second.

Phasor Data Concentrator

The PDC decapsulates the UDP datagrams sent by the PMUs, and time-aligns them using a timeout-based circular buffer [15]. Moreover, the PDC replaces missing measurements, in order to provide complete and consistent sets of data at low latency. Specifically, the software implementation presented in [154] is used. This application is implemented in the NI LabVIEW programming environment.

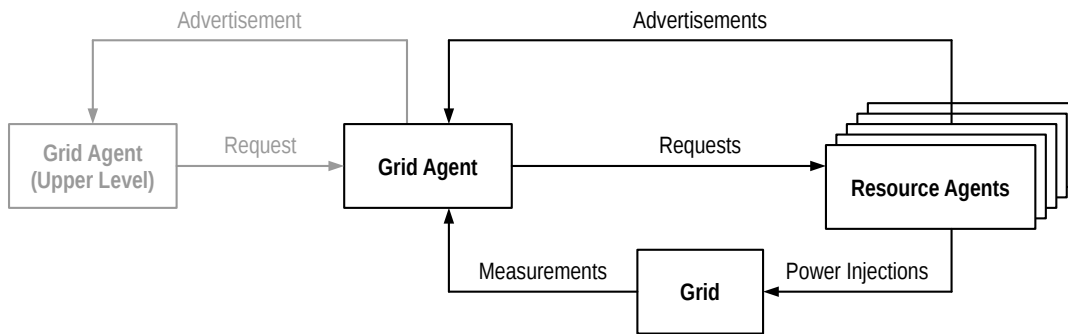


Figure 6.3 – Flow chart of the COMMELEC framework. The GA calculates requests based on the advertisements of its follower RAs, measurements of the grid state, and the request of its leader agent (in case there is one).

6.1.3 COMMELEC Framework

The resources are controlled using the so-called COMMELEC framework proposed in [155,156]. COMMELEC is a hierarchical, agent-based method for real-time control of active distribution networks using explicit power setpoints. The work of this thesis was carried out within the context of the COMMELEC project, which was supported by the Swiss National Science Foundation through the National Research Programme NRP-70 “Energy Turnaround”.

Working Principles

The COMMELEC agents are divided into *Resource Agents* (RAs), which manage individual resources, and *Grid Agents* (GAs), which handle an entire subsystem (i.e., a group of resources and the grid they are connected to).

The agents are organized in a strict hierarchy (see Figure 6.3). RAs are *followers* of a GA, to whom they send advertisements, and from whom they receive requests. A GA is a *leader* w.r.t. its assigned RAs, and can be a follower w.r.t. to an upper-level GA. In this case, the follower GA aggregates its subsystem, and acts like an RA toward the upper-level GA.

The agents communicate using an advertisement/request protocol. A *request* consists of an active/reactive power setpoint. An *advertisement* is composed of a *PQ profile*, a *belief function*, and a *virtual cost function*. The *PQ profile* is a subset of the (P, Q) -plane, which consists of all setpoints that a resource can deploy. The belief function characterizes the uncertainty of the deployment process. More precisely, for every deployable setpoint (i.e., every point in the *PQ profile*), it returns a set wherein the actually implemented setpoint will lie with overwhelming probability. The virtual cost function quantifies the willingness of a resource to implement the setpoints (i.e., lower cost indicates higher willingness). In this way, generic resources (i.e., generators, loads, or storage systems) can be represented. Indeed, this abstraction is one of the main strengths of the COMMELEC framework.

The GA determines the setpoints for the resources such that

1. The total virtual cost of the RAs is minimized.
2. The PQ profiles of the RAs are respected.
3. The setpoint requested by an upper-level GA is met (i.e., if there is an upper-level GA).
4. The grid is in a feasible and safe state of operation (i.e., line current ratings are respected, and nodal voltages are within predefined bounds).

Within the limits imposed by the aforesaid constraints, the GA can exploit the flexibility advertised by the RAs in order to optimize the operation. Thanks to this generic approach, the COMMELEC framework can support different modes of operation, such as safe and optimal operation in grid-connected and islanded mode, real-time dispatch of an agreed-upon plan, primary frequency support, as well as generic objectives defined by the user (see [147]).

The RAs are hosted on NI cRIO-9068 real-time controllers [150] (like the PMUs). Specifically, low-level tasks like data acquisition or signal processing are executed by the FPGA, whereas high-level tasks like data encapsulation, decapsulation, and streaming are done by the CPU. The GA is hosted on a workstation computer that runs on Scientific Linux 7.2. More precisely, the GA consists of three components. The core functionality of the COMMELEC framework (i.e., the communication protocol and the control method) are provided by a C++ application. The situation awareness w.r.t. the grid state is provided by the aforementioned low-latency PDC [154], and a standard *Kalman Filter* (KF) [136]. Both the PDC and the KF are implemented in the NI LabVIEW programming environment.

Application Example: Real-Time Dispatch

For illustration, one of the applications of the COMMELEC framework presented in [147], namely real-time dispatch, is summarized here.

In this experiment, the controllable load L , the battery storage B , and the photovoltaic plant $PV1$ are considered (see Figure 6.1). The objective of real-time dispatch is to follow a given plan of active/reactive values at node B01 (i.e., the point of connection), because deviations from this plan are penalized (i.e., since they require the activation of reserve). In order to emulate grid congestion, the ampacity of line L01 is artificially lowered from 207 A to 30 A.

The results of this experiment are shown in Figure 6.4. Evidently, the COMMELEC framework is able to track the external reference with high accuracy, except when the current in line L01 approaches the (virtual) ampacity. In these cases, the external reference is not tracked exactly, because the penalty for approaching the ampacity limit outweighs the penalty for deviating from the dispatch plan (see [147] and [155,156] for further details).

Chapter 6. Practical Deployment into a Real-Scale Microgrid

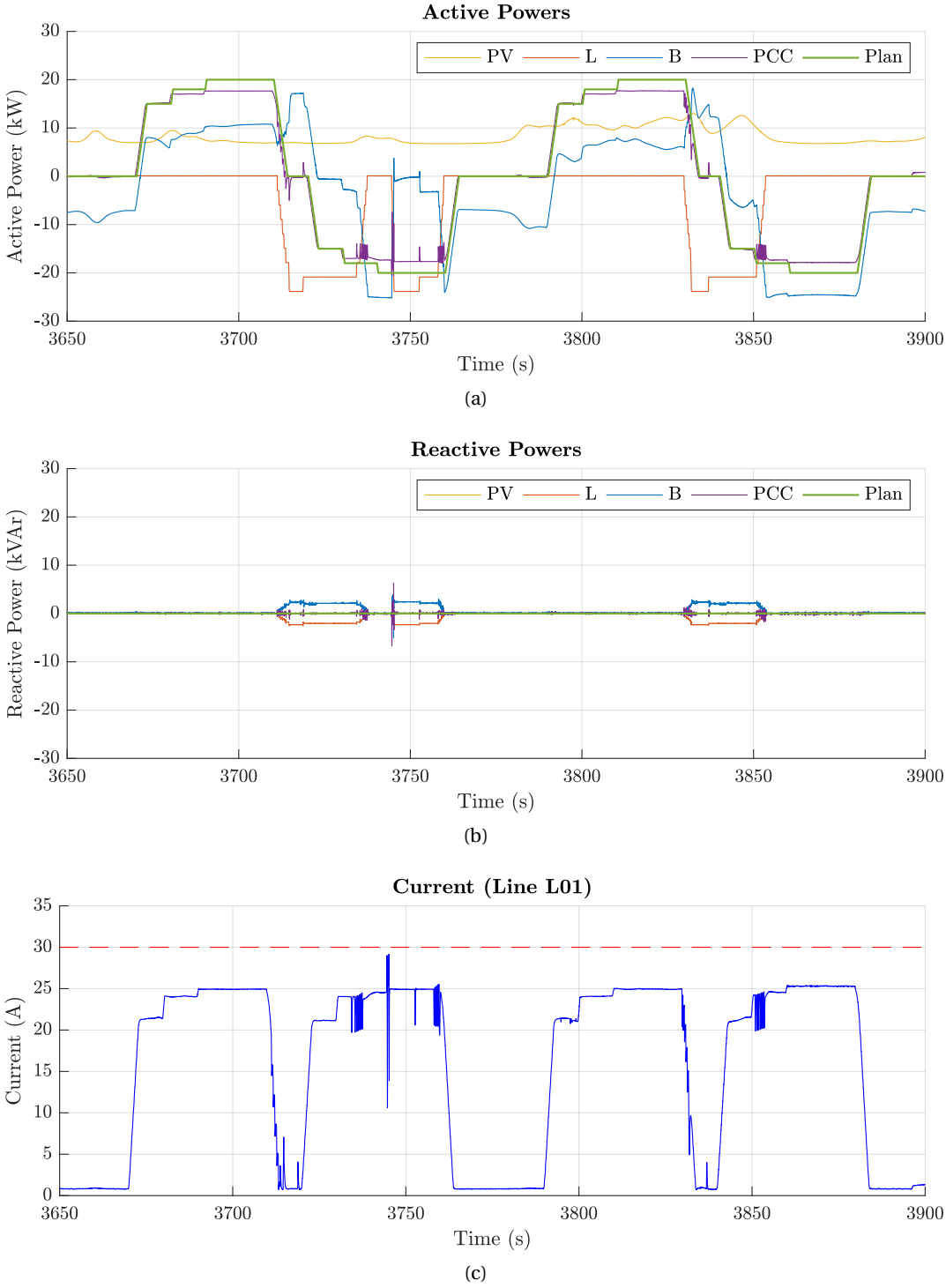


Figure 6.4 – Real-time dispatch using the COMMELEC framework (as presented in [147]): (6.4a) active powers, (6.4b) reactive powers, and (6.4c) current in line L01.

6.2 Experimental Validation of the Real-Time Capability

Subsequently, the real-time capability of the SKF presented in Chapter 4 and the VSI presented in Chapter 5 is validated. To this end, these methods are deployed into the microgrid facility described in Section 6.1.

6.2.1 Description of the Method

More precisely, the SKF and the VSI are deployed into an NI cRIO-9033 real-time controller, which is equipped with a CPU and an FPGA [133] (recall that the SKF is implemented in FPGA hardware). As explained in Section 6.1, a PDC is required to perform the time-alignment of the PMU measurements. Specifically, the low-latency PDC discussed in [154] is used. Following the modularity principle, the PDC, SKF, and VSI are embedded into separate applications. Namely:

- PDC application. This module includes the low-latency PDC, plus a wrapper layer for interfacing it with the other applications. The entire application is executed on the CPU.
- SE application. This module consists of the SKF and the associated circuit analysis methods (i.e., construction of \mathbf{Y} , and \mathbf{KR}). The SKF is executed on the FPGA, the rest of the application on the CPU.
- VSA application. This module consists of the VSI and the associated circuit analysis methods (i.e., construction of \mathbf{Y} and \mathbf{H} , and \mathbf{KR}). The entire application runs on the CPU.

The aforesaid applications are implemented in the NI LabVIEW programming environment.

In order to validate the real-time capability of these applications, the latency of the processing chain PDC-SE-VSA is assessed. To this end, the data are time-stamped at the following instants:

1. When the PDC application receives a PMU data frame.
2. When the PDC application releases a time-aligned set of synchrophasors.
3. When the SE application releases the results of the SKF calculation.
4. When the VSA application releases the results of the VSI calculation.

As suggested in [136], the latency is expressed w.r.t. to the center of the signal window used for the synchrophasor extraction. For this purpose, the clock of the real-time controller that hosts the PDC/SE/VSA applications is synchronized using the *Precision Time Protocol* (PTP) with a TEKRON TTM 01-G master clock [157], which is equipped with a Trimble Bullet III GPS antenna (like the PMUs).

6.2.2 Discussion of the Results

Figure 6.5 depicts the *Cumulative Distribution Functions* (CDFs) of the obtained latencies. These CDFs are obtained from 20'000 samples each. The median latencies of the PMU, PDC, SE, and VSA data are ca. 38.5 ms, 58.5 ms, 65.5 ms, and 67.5 ms, respectively. That is, the PDC, SE, and VSA application have execution times of ca. 20 ms, 8 ms, and 2 ms, respectively. Note that the CDFs of the latencies of the PDC, SE, and VSA data are very steep. More precisely, the jitter is in the sub-millisecond range. This means that the execution time of these applications is very deterministic. Notably, the applications can keep up with the streaming rate of the PMUs (i.e., 50 frames per second). In conclusion, these results confirm that the proposed methods are indeed real-time capable when deployed into an embedded system.

For comparison, the results of the latency assessment of the COMMELEC framework from [147] are shown in Figure 6.6. These CDFs are obtained from 15'000 samples each. Note that these values are calculated w.r.t. the beginning of the COMMELEC cycle (i.e., when the GA sends new requests to the RAs), not w.r.t. the center of the PMU signal windows. Nevertheless, the shape of the CDF of the SE latency illustrates the advantage of the real-time controller over the workstation computer. Namely, the execution on the real-time controller is much more deterministic (i.e., the CDF of the latency is much steeper). This is due to two reasons. Firstly, the SKF is implemented mostly on the FPGA, whereas the standard KF used by COMMELEC is implemented on the CPU. As known, the execution on FPGAs is deterministic, whereas the execution on CPUs is not. Secondly, the real-time controller works with real-time operating system, whereas the workstation computer works with a conventional one. Therefore, the execution of programs on the CPU of the real-time controller is more deterministic than on the CPU of the workstation computer.

The comparison of the results shown in Figure 6.5 versus those shown in Figure 6.6 clearly demonstrates the effectiveness of the proposed methods and their implementation into embedded hardware, both w.r.t. computational efficiency and time-determinism.

6.2. Experimental Validation of the Real-Time Capability

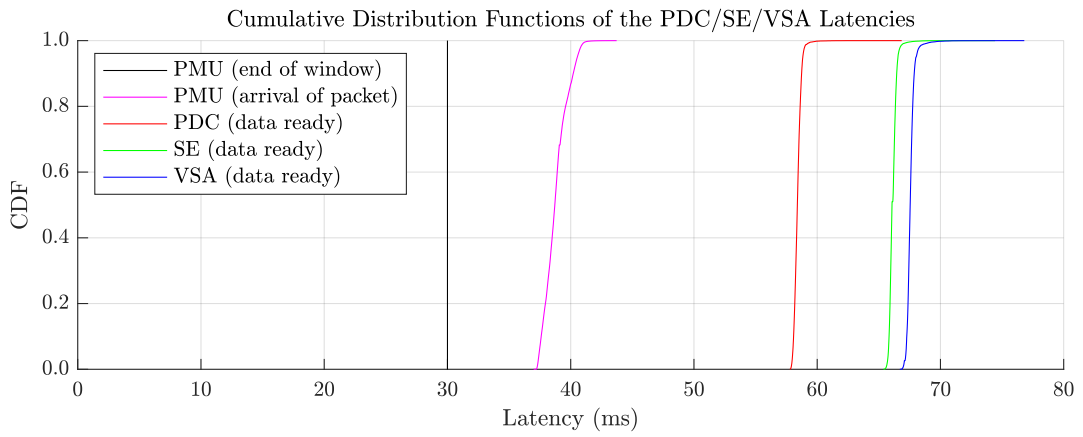


Figure 6.5 – Assessment of the latencies of the PDC/SE/VSA applications.

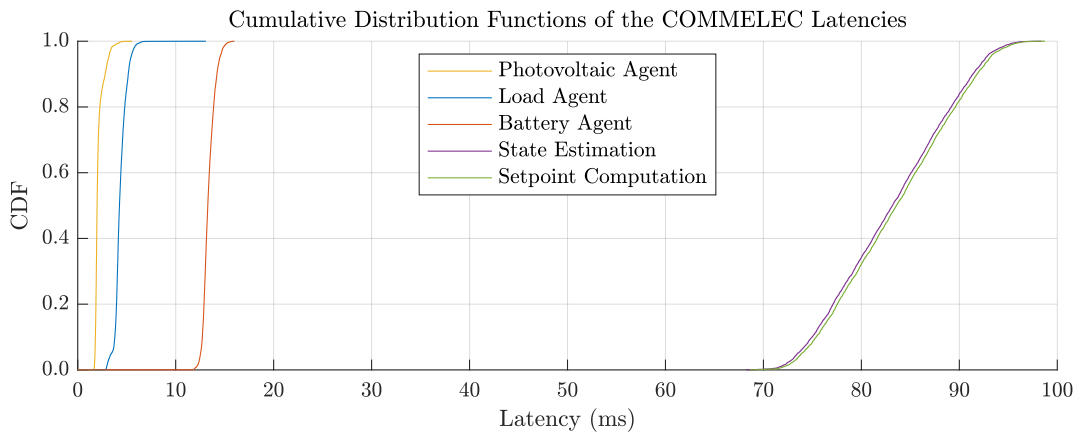


Figure 6.6 – Assessment of the latencies of the COMMELEC applications (as presented in [147]).

7 Conclusions

7.1 Synopsis of the Main Findings

This thesis developed, validated, and deployed real-time methods for *State Estimation* (SE) and *Voltage Stability Assessment* (VSA), which can support the automation of passive and active power distribution systems.

Chapter 3 discusses fundamental properties of the compound admittance matrix of polyphase power grids. First, it is shown that such grids can be represented by equivalent circuits built of polyphase branch and shunt elements. Moreover, it is argued that the compound electrical parameters of these elements are symmetric, invertible, and lossy. Based on these properties, and the hypothesis that the branch graph is weakly connected, it is formally proven that the compound admittance matrix has full rank if there is at least one shunt element, and that its diagonal blocks always have full rank. Building upon these findings, it is formally proven that *Kron Reduction* (KR) is feasible for any set of zero-injection nodes, and that a compound hybrid matrix exists for any partition of the nodes. These findings establish a rigorous theoretical foundation for the methods developed in the rest of this thesis.

Chapter 4 presents a *Field-Programmable Gate Array* (FPGA) implementation of a real-time state estimator for polyphase power grids, which is based on a *Sequential Kalman Filter* (SKF). First, the essentials of SE in general and *Kalman Filter* (KF) theory in particular are recalled. Specifically, the properties of the measurement and process model, as well as the derivation of the standard KF are discussed. Then, the SKF is introduced, and it is formally proven that the SKF and the standard KF produce identical estimates if the measurement noise variables are uncorrelated. Afterwards, the computational complexity of the SKF and the standard KF are analyzed and compared. Notably, it is demonstrated that the SKF has lower computational complexity, and the SKF (as opposed to the standard KF) is suitable for implementation into FPGAs, because it only requires elementary operations of linear algebra. Finally, the FPGA implementation of the SKF is presented, and validated against a *Central Processing Unit* (CPU) implementation of the standard KF. In particular, it is found that the results of the FPGA SKF are in accordance with those of the CPU KF, except for negligible differences due to the lower numerical precision available on the FPGA.

Chapter 7. Conclusions

Chapter 5 introduces a *Voltage Stability Index* (VSI) for assessing the voltage stability of polyphase power systems. First, the system model for VSA is described. It is illustrated that the non-zero-injection nodes can be classified into slack nodes, which behave like voltage sources with finite output impedances, and resource nodes, which behave like voltage-dependent power sources. The former are represented by *Thévenin Equivalents* (TEs), and the latter by *Polynomial Models* (PMs). Then, the classical *Continuation Power Flow* (CPF) approach to VSA is recalled. In view of the computationally intensive iterative methods required for the numerical continuation, it is concluded that CPF is not suitable for real-time applications. The VSI is proposed as a computationally efficient solution to the VSA problem. To this end, the power-flow equations are locally approximated by complex quadratic equations using the compound hybrid matrix of the grid. The proposed VSI is obtained through generalization of the well-known *L-index*, which works with similar complex quadratic equations. Finally, the VSI is validated against the classical CPF approach. The results of these methods are found to be in good agreement. That is, the proposed VSI does correctly detect voltage instability in polyphase power systems.

Chapter 6 illustrates the deployment of the proposed methods into a real-scale experimental microgrid. To this end, an overview of the equipment available in the microgrid is given in order to support the reader for a potential replication of the results. For the deployment, the metering system, which consists of *Phasor Measurement Units* (PMUs) coupled with a *Phasor Data Concentrator* (PDC), is of particular importance. The SKF and the VSI are embedded into modular applications for SE and VSA, which are deployed into an industrial real-time controller along with the PDC. To validate the real-time capability of this setup, the latencies of the PDC–SE–VSA processing chain are measured w.r.t. the PMU timestamps. The results show that the execution times of the SE and VSA applications are in the order of a few milliseconds, and deterministic (i.e., with sub-millisecond jitter).

7.2 Outlook on Future Work

In continuation of the work presented in this thesis, the following topics are suggested for further investigation:

- The earthing systems could be included into the grid model, in order to account for nonzero neutral-to-ground voltages. To this end, the neutral conductor and the ground node need to be modeled as separate elements, and the impedance of the earthing systems need to be considered.
- The SKF can be coupled with methods for the identification/correction of bad data and the assessment of the process noise covariance matrix. These aspects are not considered in this thesis, but solutions are available in the literature.
- The slack/resource nodes should be identified dynamically, and the TE/PM parameters can be estimated online. In this thesis, the roles of the nodes and the parameters of their models are assumed to be known, but this may not be the case in practice.
- The PDC, SE, and VSA applications can be integrated together into the FPGA, in order to simplify the communication between them, and ensure fully deterministic execution. As the PDC is essentially a circular buffer, and that the VSI only requires basic algebraic operations, this appears well feasible.
- The developed methods can be used for real-time protection, monitoring, and control. For instance, the SE functionality can support fault detection and location [112], and the VSA functionality could be integrated into the COMMELEC framework [155,156].

A Appendix

A.1 Essentials of Linear Algebra

A.1.1 Rank and Inverse

The so-called rank (\mathbf{M}) of a matrix \mathbf{M} is the number of its linearly independent rows or columns. A square matrix \mathbf{A} with full rank is *invertible* (or *nonsingular*) and has a unique *inverse* \mathbf{A}^{-1} .

The following properties hold (for proofs, see [158]):

Lemma 4. For any matrix \mathbf{M} , it holds that $\text{rank}(\mathbf{M}^T \mathbf{M}) = \text{rank}(\mathbf{M})$.

Lemma 5. If \mathbf{M} is arbitrary, and \mathbf{A} , \mathbf{B} are nonsingular (and of appropriate size), it holds that $\text{rank}(\mathbf{A}\mathbf{M}) = \text{rank}(\mathbf{M}) = \text{rank}(\mathbf{M}\mathbf{B})$.

Lemma 6 (Woodbury Matrix Identity). If \mathbf{A} , \mathbf{B} are invertible, and \mathbf{U} , \mathbf{V} are such that the terms $\mathbf{A} + \mathbf{U}\mathbf{B}\mathbf{V}$ and $\mathbf{B}^{-1} + \mathbf{V}\mathbf{A}^{-1}\mathbf{U}$ are invertible, then it holds that

$$(\mathbf{A} + \mathbf{U}\mathbf{B}\mathbf{V})^{-1} = \mathbf{A}^{-1} - \mathbf{A}^{-1}\mathbf{U}(\mathbf{B}^{-1} + \mathbf{V}\mathbf{A}^{-1}\mathbf{U})\mathbf{V}\mathbf{A}^{-1} \quad (\text{A.1})$$

A.1.2 Positive-Definite and Negative-Definite Matrices

The *transpose* \mathbf{M}^T is obtained by flipping \mathbf{M} over its diagonal. If $\mathbf{M} = \mathbf{M}^T$, then \mathbf{M} is *symmetric*. A symmetric real matrix \mathbf{M} is *positive definite* ($\mathbf{M} > 0$) or *negative definite* ($\mathbf{M} < 0$) if

$$\mathbf{M} > 0: \quad \mathbf{x}^T \mathbf{M} \mathbf{x} > 0 \quad \forall \mathbf{x} \neq \mathbf{0} \quad (\text{A.2})$$

$$\mathbf{M} < 0: \quad \mathbf{x}^T \mathbf{M} \mathbf{x} < 0 \quad \forall \mathbf{x} \neq \mathbf{0} \quad (\text{A.3})$$

If 0 is included, \mathbf{M} is *positive semidefinite* ($\mathbf{M} \geq 0$) or *negative semidefinite* ($\mathbf{M} \leq 0$), respectively.

For positive definite matrices, the following property holds (see [159]):

Lemma 7. If $\mathbf{A} > 0$ and \mathbf{B} is nonsingular (and of appropriate size), then $\mathbf{B}^T \mathbf{A} \mathbf{B} > 0$.

Appendix A. Appendix

For complex symmetric matrices with positive-definite real or imaginary part, the following properties hold (for proof, see [160] and [161] respectively):

Lemma 8. *If \mathbf{M} is complex symmetric and $\Re\{\mathbf{M}\} > 0$, then \mathbf{M} is nonsingular and $\Re\{\mathbf{M}^{-1}\} > 0$.*

Lemma 9. *If \mathbf{M} is complex symmetric and $\Im\{\mathbf{M}\} > 0$, then \mathbf{M} is nonsingular and $\Im\{\mathbf{M}^{-1}\} < 0$.*

A.1.3 Unitary Matrices

A nonsingular complex matrix \mathbf{M} is *unitary* if $\mathbf{M}^{-1} = (\mathbf{M}^*)^T$. It holds that (for proof, see [162]):

Lemma 10 (Autonne-Takagi Factorization). *If \mathbf{M} is complex symmetric, it can be factorized as $\mathbf{M} = \mathbf{U}^T \mathbf{D} \mathbf{U}$, where \mathbf{U} is unitary and \mathbf{D} is nonnegative diagonal. Additionally, if \mathbf{M} is nonsingular, then \mathbf{D} is positive diagonal.*

A.1.4 Block Matrices

Let \mathbf{M} be a block matrix of the form

$$\mathbf{M} = \begin{bmatrix} \mathbf{A} & \mathbf{B} \\ \mathbf{C} & \mathbf{D} \end{bmatrix} \quad (\text{A.4})$$

If \mathbf{D} is invertible, the *Schur complement* \mathbf{M}/\mathbf{D} of \mathbf{D} in \mathbf{M} is defined as

$$\mathbf{M}/\mathbf{D} := \mathbf{A} - \mathbf{B}\mathbf{D}^{-1}\mathbf{C} \quad (\text{A.5})$$

The following properties hold (for proof, see [163]):

Lemma 11. $\det(\mathbf{M}) = \det(\mathbf{M}/\mathbf{D}) \det(\mathbf{D})$.

Lemma 12. *If \mathbf{A} is composed of blocks \mathbf{A}_{ij} , \mathbf{B} of row blocks \mathbf{B}_i , and \mathbf{C} of column blocks \mathbf{C}_j (i.e., of compatible size), then the Schur complement can be computed blockwise:*

$$(\mathbf{M}/\mathbf{D})_{ij} = \mathbf{A}_{ij} - \mathbf{B}_i \mathbf{D}^{-1} \mathbf{C}_j = \begin{bmatrix} \mathbf{A}_{ij} & \mathbf{B}_i \\ \mathbf{C}_j & \mathbf{D} \end{bmatrix} / \mathbf{D} \quad (\text{A.6})$$

The *Kronecker product* $\mathbf{A} \otimes \mathbf{B}$ of two matrices \mathbf{A} and \mathbf{B} is a block matrix, whose blocks $(\mathbf{A} \otimes \mathbf{B})_{ij}$ are the products of the corresponding element A_{ij} of \mathbf{A} and \mathbf{B} :

$$\mathbf{A} \otimes \mathbf{B}: \quad (\mathbf{A} \otimes \mathbf{B})_{ij} = A_{ij} \cdot \mathbf{B} \quad (\text{A.7})$$

The following property holds (for proof, see [164]).

Lemma 13. $\text{rank}(\mathbf{A} \otimes \mathbf{B}) = \text{rank}(\mathbf{A}) \cdot \text{rank}(\mathbf{B})$.

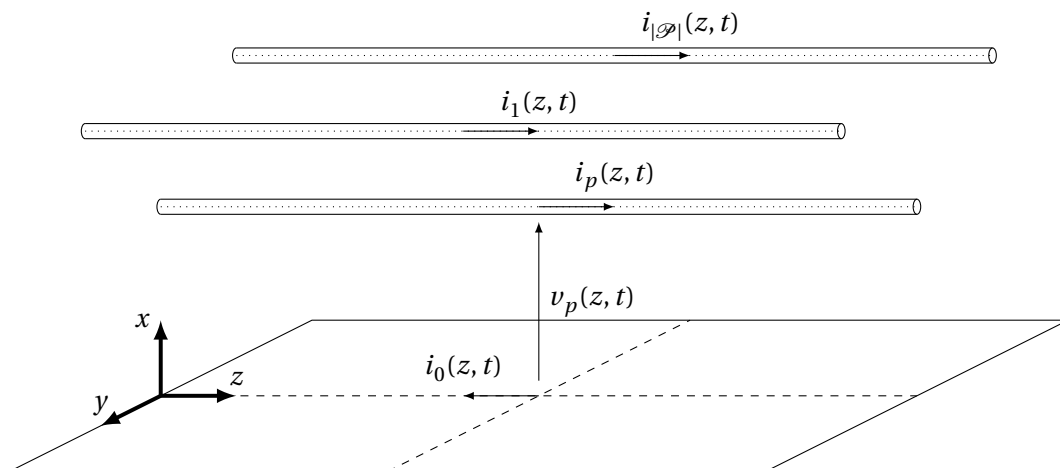


Figure A.1 – Schematic of a polyphase transmission line. The conductors are parallel to each other and to the ground plane. The x -axis and the y -axis are perpendicular to the conductors, and the z -axis is parallel to the conductors.

A.2 Modeling of Power System Components

A.2.1 Transmission Lines

Telegrapher's Equations

Consider a polyphase transmission line, whose conductors are parallel to each other and the ground plane, and have infinite length. Define the orthogonal coordinate axes x , y , and z s.t. the z -axis is parallel to the conductors (see Figure A.1). Label the conductors as $p \in \mathcal{P}$, and the ground plane as 0. Suppose the following:

Hypothesis 12 (Longitudinal Wave Propagation). *The transverse dimensions of the conductors (i.e., their diameters and distances) are substantially smaller than the wavelengths of interest, so that only longitudinal propagation (i.e., along the z -axis) needs to be considered.*

Hypothesis 13 (Transverse Electromagnetic Field). *The electric field $\vec{\mathbf{E}}$ and magnetic field $\vec{\mathbf{B}}$ outside of the conductors, which result from the charges and currents inside of the conductors, are purely transverse (i.e., $E_z = 0$ and $B_z = 0$).*

Hypothesis 14 (Linear, Homogeneous, Isotropic Materials). *The conductors and the ambient dielectric are linear, homogeneous, and isotropic. That is, the conductivity σ of the conductors, as well as the permittivity ϵ and the permeability μ of the dielectric, are finite scalar constants.*

Under these conditions, the *phase-to-ground voltages* $v_p(z, t)$ are uniquely defined. Moreover, the sum of the *conductor currents* $i_p(z, t)$ plus the *ground current* $i_0(z, t)$ equals zero:

$$i_0(z, t) = - \sum_{p \in \mathcal{P}} i_p(z, t) \tag{A.8}$$

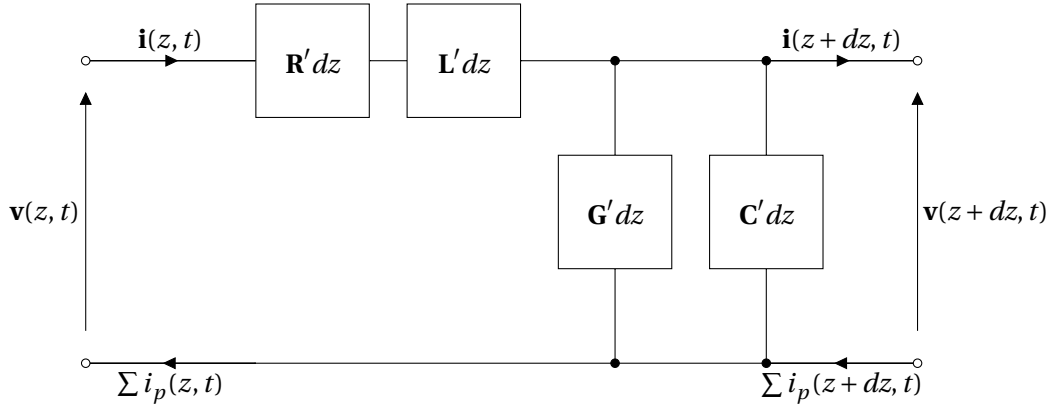


Figure A.2 – Polyphase equivalent circuit of an infinitesimal line segment.

Define $\mathbf{v}(z, t)$ and $\mathbf{i}(z, t)$ as the vectors of all $v_p(z, t)$ and $i_p(z, t)$, respectively:

$$\mathbf{v}(z, t) := \text{col}_{p \in \mathcal{P}} \left(v_p(z, t) \right) \quad (\text{A.9})$$

$$\mathbf{i}(z, t) := \text{col}_{p \in \mathcal{P}} \left(i_p(z, t) \right) \quad (\text{A.10})$$

As known from transmission line theory (for proof, see [165,166]):

Lemma 14 (Telegrapher's Equations). *If Hypotheses 12–14 hold, Maxwell's equations simplify to the so-called telegrapher's equations*

$$\frac{\partial}{\partial z} \mathbf{v}(z, t) := - \left(\mathbf{R}' + \mathbf{L}' \frac{\partial}{\partial t} \right) \mathbf{i}(z, t) \quad (\text{A.11})$$

$$\frac{\partial}{\partial z} \mathbf{i}(z, t) := - \left(\mathbf{G}' + \mathbf{C}' \frac{\partial}{\partial t} \right) \mathbf{v}(z, t) \quad (\text{A.12})$$

\mathbf{R}'/\mathbf{L}' are the *per-unit-length resistance/inductance matrices* of the conductors and the ground, and \mathbf{G}'/\mathbf{C}' *per-unit-length conductance/capacitance matrices* of the dielectric. These matrices are symmetric: $\mathbf{R}' = (\mathbf{R}')^\top$, $\mathbf{L}' = (\mathbf{L}')^\top$, $\mathbf{G}' = (\mathbf{G}')^\top$, and $\mathbf{C}' = (\mathbf{C}')^\top$ (see [165]).

Energy in the Fields and Losses in the Materials

The line can be thought to be composed of infinitesimal segments of length dz (see Figure A.2).

Let $E_{\mathbf{L}'}(z, t)$ and $E_{\mathbf{C}'}(z, t)$ be the *energy stored in the magnetic and electric field*, respectively, of an infinitesimal segment located at position z . They are given by (see [165] and Figure A.2)

$$E_{\mathbf{L}'}(z, t) = \frac{1}{2} \mathbf{i}(z, t)^\top \mathbf{L}' \mathbf{i}(z, t) dz \quad (\text{A.13})$$

$$E_{\mathbf{C}'}(z, t) = \frac{1}{2} \mathbf{v}(z, t)^\top \mathbf{C}' \mathbf{v}(z, t) dz \quad (\text{A.14})$$

The energy stored in the field is zero only if there is no field: $E_{\mathbf{L}'}(z, t) = \mathbf{0}$ iff $\vec{\mathbf{B}}(z, t) = \mathbf{0}$, and $E_{\mathbf{C}'}(z, t) = \mathbf{0}$ iff $\vec{\mathbf{E}}(z, t) = \mathbf{0}$. Since $\vec{\mathbf{B}}(z, t) = \mathbf{0}$ requires $\mathbf{i}(z, t) = \mathbf{0}$, and $\vec{\mathbf{E}}(z, t) = \mathbf{0}$ implies $\mathbf{v}(z, t) = \mathbf{0}$, it follows that $E_{\mathbf{L}'}(z, t) > 0 \forall \mathbf{i}(z, t) \neq \mathbf{0}$ and $E_{\mathbf{C}'}(z, t) > 0 \forall \mathbf{v}(z, t) \neq \mathbf{0}$. As \mathbf{L}' and \mathbf{C}' are symmetric, they are thus positive definite: $\mathbf{L}' > 0$ and $\mathbf{C}' > 0$.

Let $P_{\mathbf{R}'}(z, t)$ and $P_{\mathbf{G}'}(z, t)$ be the losses dissipated in the conductors and dielectric, respectively, of an infinitesimal segment located at position z . They are given by (see [165] and Figure A.2)

$$P_{\mathbf{R}'}(z, t) = \frac{1}{2} \mathbf{i}(z, t)^\top \mathbf{R}' \mathbf{i}(z, t) dz \quad (\text{A.15})$$

$$P_{\mathbf{G}'}(z, t) = \frac{1}{2} \mathbf{v}(z, t)^\top \mathbf{G}' \mathbf{v}(z, t) dz \quad (\text{A.16})$$

If the materials are lossy (i.e., $\mathbf{R}' \neq \mathbf{0}$ and $\mathbf{G}' \neq \mathbf{0}$), the losses are zero only if no currents flow. That is, $P_{\mathbf{R}'}(z, t) = 0$ iff $\mathbf{i}(z, t) = \mathbf{0}$, and $P_{\mathbf{G}'}(z, t) = 0$ iff $\mathbf{v}(z, t) = \mathbf{0}$. As \mathbf{R}' and \mathbf{G}' are symmetric, they are thus positive definite: $\mathbf{R}' > 0$ and $\mathbf{G}' > 0$.

Approximate Lumped-Element Model of a Short Line

Now, consider a line of finite length, which runs from z_m to z_n (i.e., m and n are polyphase nodes of a grid). Let $\Delta z := |z_m - z_n|$ denote the length of the line. For a given frequency ω , define \mathbf{X}' and \mathbf{B}' as

$$\mathbf{X}' := \omega \mathbf{L}' \quad (\text{A.17})$$

$$\mathbf{B}' := \omega \mathbf{B}' \quad (\text{A.18})$$

Since \mathbf{L}' and \mathbf{C}' are positive definite, \mathbf{X}' and \mathbf{B}' are positive definite: $\mathbf{X}' = (\mathbf{X}')^\top$ and $\mathbf{B}' = (\mathbf{B}')^\top$.

As known from transmission line theory (see [165]):

Lemma 15 (Electrically Short Line). *If a line is electrically short (i.e., its length is substantially shorter than the wavelengths of interest), it can be approximated by a Π -section equivalent circuit, whose shunt and branch elements correspond to the transversal electrical parameters \mathbf{G}' and \mathbf{B}' and the longitudinal electrical parameters \mathbf{R}' and \mathbf{X}' , respectively (see Figure A.3).*

The parameters of the polyphase Π -section equivalent circuit are given by (see Figure A.3)

$$\mathbf{Z}_{\Pi, (m, n)} = (\mathbf{R}' + j\mathbf{X}') \Delta z \quad (\text{A.19})$$

$$\mathbf{Y}_{\Pi, m | (m, n)} = \frac{1}{2} (\mathbf{G}' + j\mathbf{B}') \Delta z \quad (\text{A.20})$$

$$\mathbf{Y}_{\Pi, n | (m, n)} = \frac{1}{2} (\mathbf{G}' + j\mathbf{B}') \Delta z \quad (\text{A.21})$$

Since \mathbf{R}' , \mathbf{X}' , \mathbf{G}' , and \mathbf{B}' are positive definite, $\mathbf{Z}_{\Pi, (m, n)}$, $\mathbf{Y}_{\Pi, m | (m, n)}$, and $\mathbf{Y}_{\Pi, n | (m, n)}$ are symmetric and have positive definite real parts. Therefore, according to Lemma 8, they are invertible. This is in accordance with Hypothesis 3.

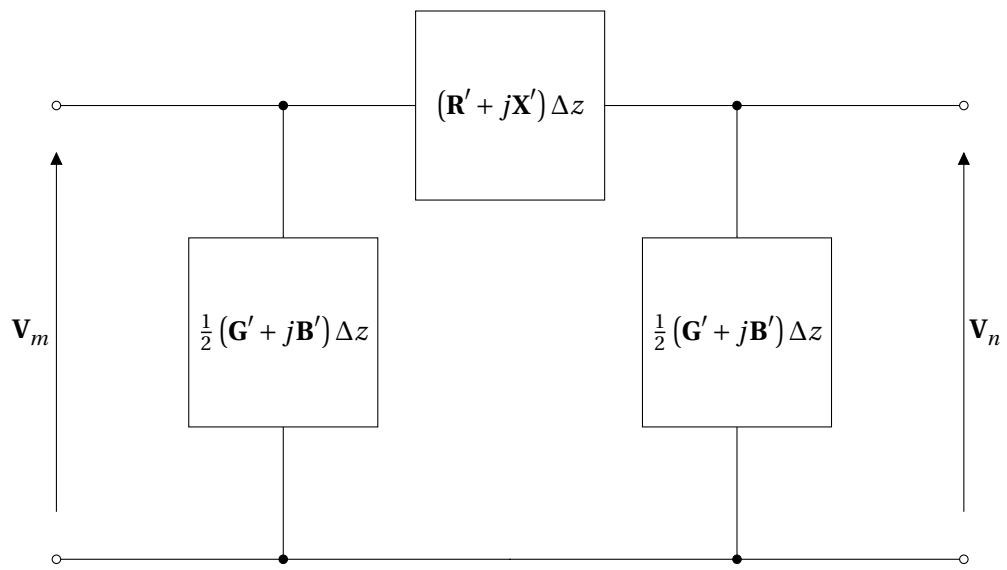


Figure A.3 – Polyphase Π -section equivalent circuit of a short line.

A.2.2 Transformers

Lumped-Element Model of a Lossless Transformer

Consider a polyphase transformer, whose *primary side* P and *secondary side* S are configured as grounded stars. Let $\mathbf{v}_p(t)$ and $\mathbf{v}_s(t)$ be the vectors of the *phase-to-ground terminal voltages*, and $\mathbf{i}_p(t)$ and $\mathbf{i}_s(t)$ the vectors of the *injected terminal currents*. Suppose the following:

Hypothesis 15 (Linear, Homogeneous, Isotropic Materials). *The windings and the core are made from linear, homogeneous, isotropic materials (i.e., the conductivity σ of the windings and the permeability μ of the core are finite scalar constants).*

For the moment, neglect the losses in the windings and the core. Under these conditions, the terminal voltages and currents on the primary and secondary side are related by (see [167]):

$$\begin{bmatrix} \mathbf{v}_p(t) \\ \mathbf{v}_s(t) \end{bmatrix} = \begin{bmatrix} \mathbf{L}_{PP} & \mathbf{L}_{PS} \\ \mathbf{L}_{SP} & \mathbf{L}_{SS} \end{bmatrix} \frac{\partial}{\partial t} \begin{bmatrix} \mathbf{i}_p(t) \\ \mathbf{i}_s(t) \end{bmatrix} \quad (\text{A.22})$$

\mathbf{L}_{PP} and \mathbf{L}_{SS} are the matrices of *self-inductances* of the primary and secondary windings, and \mathbf{L}_{PS} and \mathbf{L}_{SP} are the matrices of *mutual inductances* between them. The following symmetries hold: $\mathbf{L}_{PP} = \mathbf{L}_{PP}^T$, $\mathbf{L}_{SS} = \mathbf{L}_{SS}^T$, and $\mathbf{L}_{PS} = \mathbf{L}_{SP}^T$.

Furthermore, assume the following:

Hypothesis 16 (Symmetric Core). *The core is magnetically symmetric. That is, $\mathbf{L}_{PS} = \mathbf{L}_{SP} = \mathbf{M}$.*

Hypothesis 17 (Equal Turn Ratios). *The turn ratios η_p of the primary and secondary windings of all phases are equal: $\eta_p = N_{s,p}/N_{p,p} = \eta \forall p \in \mathcal{P}$.*

In this case, \mathbf{L}_{PP} , \mathbf{L}_{SS} , and \mathbf{M} are positive definite: $\mathbf{L}_{PP} > 0$, $\mathbf{L}_{SS} > 0$, and $\mathbf{M} > 0$ (see [168]). Moreover, (A.22) can be represented by an equivalent circuit. Rewrite the first row of (A.22) as

$$\mathbf{v}_p(t) = \mathbf{L}_{PP} \frac{\partial}{\partial t} \mathbf{i}_p(t) + \mathbf{M} \frac{\partial}{\partial t} \mathbf{i}_s(t) \quad (\text{A.23})$$

$$= \left(\mathbf{L}_{PP} - \frac{1}{\eta} \mathbf{M} \right) \frac{\partial}{\partial t} \mathbf{i}_p(t) + \mathbf{M} \frac{\partial}{\partial t} \left(\frac{1}{\eta} \mathbf{i}_p(t) + \mathbf{i}_s(t) \right) \quad (\text{A.24})$$

$$= \left(\mathbf{L}_{PP} - \frac{1}{\eta} \mathbf{M} \right) \frac{\partial}{\partial t} \mathbf{i}_p(t) + \frac{1}{\eta} \mathbf{M} \frac{\partial}{\partial t} (\mathbf{i}_p(t) + \eta \mathbf{i}_s(t)) \quad (\text{A.25})$$

Similarly, rewrite the second row of (A.22) as

$$\mathbf{v}_s(t) = \mathbf{M} \frac{\partial}{\partial t} \mathbf{i}_p(t) + \mathbf{L}_{SS} \frac{\partial}{\partial t} \mathbf{i}_s(t) \quad (\text{A.26})$$

$$= \mathbf{M} \frac{\partial}{\partial t} (\mathbf{i}_p(t) + \eta \mathbf{i}_s(t)) + (\mathbf{L}_{SS} - \eta \mathbf{M}) \frac{\partial}{\partial t} \mathbf{i}_s(t) \quad (\text{A.27})$$

$$= \eta \left(\frac{1}{\eta} \mathbf{M} \frac{\partial}{\partial t} (\mathbf{i}_p(t) + \eta \mathbf{i}_s(t)) \right) + (\mathbf{L}_{SS} - \eta \mathbf{M}) \frac{\partial}{\partial t} \mathbf{i}_s(t) \quad (\text{A.28})$$

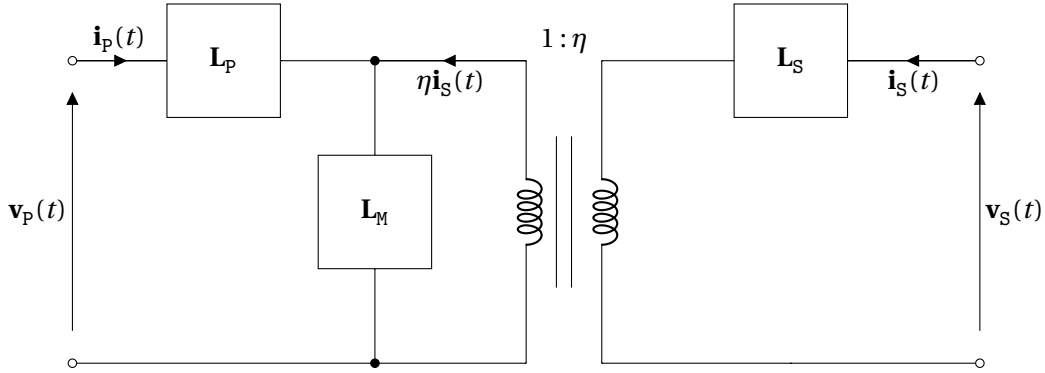


Figure A.4 – Polyphase equivalent circuit of a lossless transformer in absolute units.

Define the *leakage inductances* \mathbf{L}_P and \mathbf{L}_S and the *magnetization inductance* \mathbf{L}_M as

$$\mathbf{L}_P := \mathbf{L}_{PP} - \frac{1}{\eta} \mathbf{M} \quad (\text{A.29})$$

$$\mathbf{L}_S := \mathbf{L}_{SS} - \eta \mathbf{M} \quad (\text{A.30})$$

$$\mathbf{L}_M := \frac{1}{\eta} \mathbf{M} \quad (\text{A.31})$$

Since \mathbf{L}_{PP} , \mathbf{L}_{SS} , and \mathbf{M} are positive definite, \mathbf{L}_P and \mathbf{L}_S are symmetric, and \mathbf{L}_M is positive definite: $\mathbf{L}_P = \mathbf{L}_P^T$, $\mathbf{L}_S = \mathbf{L}_S^T$, and $\mathbf{L}_M > 0$ (\mathbf{L}_P and \mathbf{L}_S need not be positive definite due to the subtraction). Using these definitions, (A.25) and (A.28) simplify to

$$\mathbf{v}_P(t) = \mathbf{L}_P \frac{\partial}{\partial t} \mathbf{i}_P(t) + \mathbf{L}_M \frac{\partial}{\partial t} \left(\frac{1}{\eta} \mathbf{i}_P(t) + \mathbf{i}_S(t) \right) \quad (\text{A.32})$$

$$\mathbf{v}_S(t) = \eta \left(\mathbf{L}_M \frac{\partial}{\partial t} (\mathbf{i}_P(t) + \eta \mathbf{i}_S(t)) \right) + \mathbf{L}_S \frac{\partial}{\partial t} \mathbf{i}_S(t) \quad (\text{A.33})$$

This corresponds to the equivalent circuit shown in Figure A.4. The equivalent circuit consists of the lumped elements \mathbf{L}_P , \mathbf{L}_S , and \mathbf{L}_M , as well as an ideal transformer with turn ratio $1 : \eta$.

Per-Unit Model

The presence of the ideal transformer in the equivalent circuit in Figure A.4 is due to the fact that $\mathbf{v}_P(t)$ and $\mathbf{v}_S(t)$ are expressed absolute units. If the voltages and currents are expressed in relative units (i.e., w.r.t. to a *per-unit basis*), the ideal transformer can be eliminated from the equivalent circuit. To this end, assuming that the same *base power* P_b is used for both sides, the ratio of the *secondary base voltage* $V_{S,b}$ and the *primary base voltage* $V_{P,b}$ must be equal to the turn ratio of the transformer (for proof, see [169]). That is

$$\frac{V_{S,b}}{V_{P,b}} = \eta \quad (\text{A.34})$$

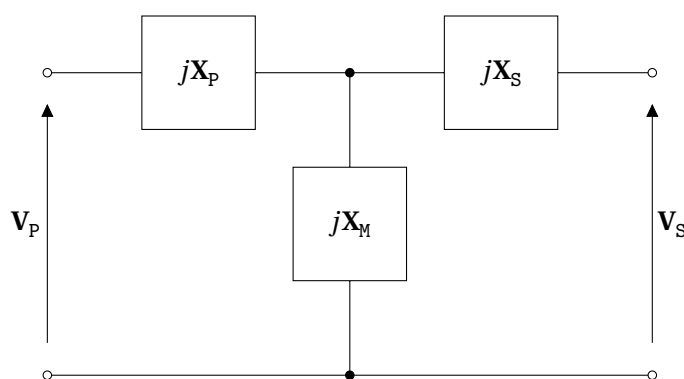


Figure A.5 – Polyphase T-section equivalent circuit of a lossless transformer in relative units.

Using the per-unit basis, define the per-unit phasors

$$\mathbf{V}_P \sim \frac{\mathbf{v}_P(t)}{V_{P,b}} \quad (\text{A.35})$$

$$\mathbf{V}_S \sim \frac{\mathbf{v}_S(t)}{V_{S,b}} \quad (\text{A.36})$$

and the per-unit reactances (i.e., for a given frequency ω)

$$\mathbf{X}_P := \frac{\omega \mathbf{L}_P}{Z_{P,b}} \quad (\text{A.37})$$

$$\mathbf{X}_S := \frac{\omega \mathbf{L}_S}{Z_{S,b}} \quad (\text{A.38})$$

$$\mathbf{X}_M := \frac{\omega \mathbf{L}_M}{Z_{P,b}} \quad (\text{A.39})$$

where $Z_{P,b}$ and $Z_{S,b}$ are the absolute values of the base impedances. The equivalent circuit shown in Figure A.4 can be transformed into the one shown in Figure A.5 (see [169]).

Note that, since \mathbf{L}_P and \mathbf{L}_S are symmetric, \mathbf{X}_P and \mathbf{X}_S are symmetric, too: $\mathbf{X}_P = \mathbf{X}_P^T$ and $\mathbf{X}_S = \mathbf{X}_S^T$. Moreover, since \mathbf{L}_M is positive definite, \mathbf{X}_M is positive definite, too: $\mathbf{X}_M > 0$. Therefore, according to Lemmata 8–9, $j\mathbf{X}_M$ has the inverse $-j\mathbf{B}_M$, where $\mathbf{B}_M > 0$ (i.e., the impedance parameters $j\mathbf{X}_M$ can be replaced by the admittance parameters $-j\mathbf{B}_M$).

Losses in the Windings and the Core

The winding losses are represented by compound resistance matrices \mathbf{R}_P and \mathbf{R}_S connected in series with the compound reactance matrices \mathbf{X}_P and \mathbf{X}_S , see Figure A.6. The Ohmic losses depend only on the current flowing in the respective conductor, so \mathbf{R}_P and \mathbf{R}_S are diagonal. Furthermore, given that the conductors are lossy, the Ohmic losses are zero iff no current flows. Accordingly, \mathbf{R}_P and \mathbf{R}_S are positive diagonal, and hence positive definite: $\mathbf{R}_P > 0$ and $\mathbf{R}_S > 0$.

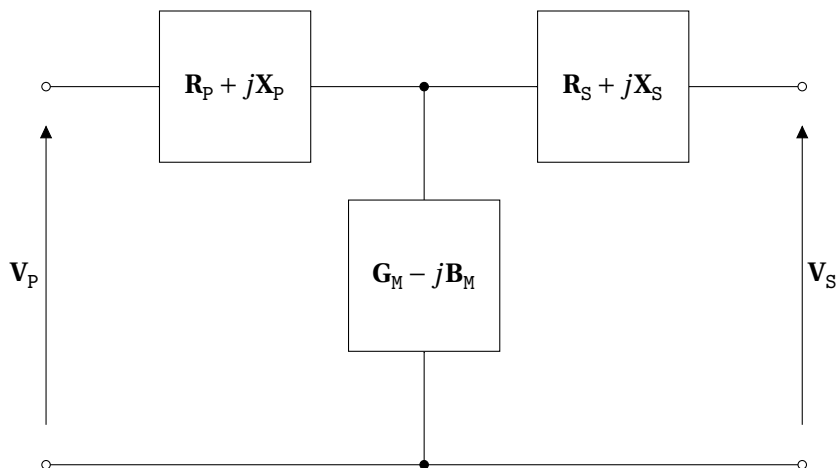


Figure A.6 – Polyphase T-section equivalent circuit of a lossy transformer in relative units.

The core losses are represented by a compound conductance matrix \mathbf{G}_M connected in parallel with the compound susceptance matrix \mathbf{B}_M , see Figure A.6. As known \mathbf{G}_M can be derived from the equivalent magnetic circuit of the transformer [170]. Since the magnetic flux in a leg of the core is a superposition of contributions originating from all windings, \mathbf{G}_M is a dense matrix (i.e., its off-diagonal elements are nonzero). Moreover, due to symmetry of the magnetic interaction, \mathbf{G}_M is symmetric (this property is guaranteed by the manufacturers). Furthermore, given that the core is lossy, the magnetization losses are zero iff the magnetic fluxes are zero. By consequence, \mathbf{G}_M is positive definite: $\mathbf{G}_M > 0$.

Following the notation in Figure 3.1b, label the primary side as m , the secondary side as n , and the internal node as x (i.e., m and n are physical nodes, and x is a virtual node of a grid). The parameters of the polyphase T-section equivalent circuit are given by

$$\mathbf{Z}_{T,(m,x)} = \mathbf{R}_P + j\mathbf{X}_P \tag{A.40}$$

$$\mathbf{Z}_{T,(n,x)} = \mathbf{R}_S + j\mathbf{X}_S \tag{A.41}$$

$$\mathbf{Y}_{T,x} = \mathbf{G}_M - j\mathbf{B}_M \tag{A.42}$$

Recall that \mathbf{R}_P and \mathbf{R}_S are positive definite, and \mathbf{X}_P and \mathbf{X}_S are symmetric. By consequence, $\mathbf{Z}_{T,(m,x)}$ and $\mathbf{Z}_{T,(n,x)}$ are symmetric with positive definite real part. Thus, according to Lemma 8, they are invertible. Further, recall that \mathbf{G}_M is positive definite, and \mathbf{B}_M is symmetric. Therefore, $\mathbf{Y}_{T,x}$ is symmetric with positive definite real part. Hence, according to Lemma 8, it is invertible, too. This is in accordance with Hypothesis 3.

A.2.3 Series Compensators and Shunt Compensators

There exist three categories of FACTS devices: *series compensators*, *shunt compensators*, and combined *series-and-shunt compensators* [171]. Hereafter, the first two cases are discussed.

Recall from Appendix A.2.1 that a polyphase line is characterized by the following compound electrical parameters:

$$\mathbf{Z}_{\Lambda,(m,n)} := (\mathbf{R}' + j\mathbf{X}') \Delta z \quad (\text{A.43})$$

$$\mathbf{Y}_{\Lambda,m|(m,n)} := \frac{1}{2} (\mathbf{G}' + j\mathbf{B}') \Delta z \quad (\text{A.44})$$

$$\mathbf{Y}_{\Lambda,n|(m,n)} := \frac{1}{2} (\mathbf{G}' + j\mathbf{B}') \Delta z \quad (\text{A.45})$$

These parameters satisfy Hypothesis 3. If the line is equipped with a series compensator, its branch impedance is modified. Let $\mathbf{Z}_{\Gamma,(m,n)}$ denote the *compound series impedance matrix* of the compensator. Then, as shown in Figure A.7

$$\mathbf{Z}_{\Pi,(m,n)} = \mathbf{Z}_{\Lambda,(m,n)} + \mathbf{Z}_{\Gamma,(m,n)} \quad (\text{A.46})$$

Similarly, if the line is equipped with shunt compensators, its shunt admittances are modified. Let $\mathbf{Y}_{\Gamma,m}$ and $\mathbf{Y}_{\Gamma,n}$ denote the *compound shunt admittance matrices* of these compensators. Then, as shown in Figure A.8

$$\mathbf{Z}_{\Pi,m|(m,n)} = \mathbf{Z}_{\Lambda,m|(m,n)} + \mathbf{Z}_{\Gamma,m} \quad (\text{A.47})$$

$$\mathbf{Y}_{\Pi,n|(m,n)} = \mathbf{Y}_{\Lambda,n|(m,n)} + \mathbf{Y}_{\Gamma,n} \quad (\text{A.48})$$

Usually, such compensators are built of banks of capacitors or inductors. Due to the symmetry of electromagnetic interactions (which is a consequence of Maxwell's equations), such devices are symmetrical w.r.t. the phases. Moreover, they are lossy (like every physical system). Hence

$$\text{series compensation : } \begin{cases} \mathbf{Z}_{\Gamma,(m,n)} = \mathbf{Z}_{\Gamma,(m,n)}^{\top} \\ \Re \{ \mathbf{Z}_{\Gamma,(m,n)} \} > 0 \end{cases} \quad (\text{A.49})$$

$$\text{shunt compensation : } \begin{cases} \mathbf{Y}_{\Gamma,m/n} = \mathbf{Y}_{\Gamma,m/n}^{\top} \\ \Re \{ \mathbf{Y}_{\Gamma,m/n} \} > 0 \end{cases} \quad (\text{A.50})$$

Since $\mathbf{Z}_{\Gamma,(m,n)}$, $\mathbf{Y}_{\Gamma,m}$ and $\mathbf{Y}_{\Gamma,n}$ have positive definite real parts, by Lemma 8, they are invertible. Therefore, they satisfy Hypothesis 3. The addition in (A.47)–(A.48) preserve the symmetry of the matrices and the positive definiteness of the real part of $\mathbf{Z}_{\Pi,(m,n)}$, $\mathbf{Y}_{\Pi,m}$, and $\mathbf{Y}_{\Pi,n}$. Therefore, by Lemma 8, they are invertible. So, the obtained parameters satisfy Hypothesis 3.

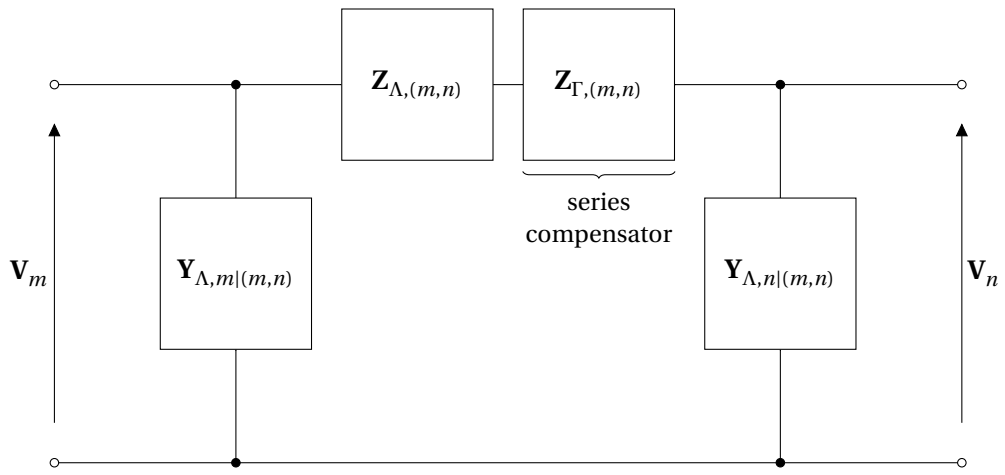


Figure A.7 – Equivalent circuit of a line equipped with a series compensator.

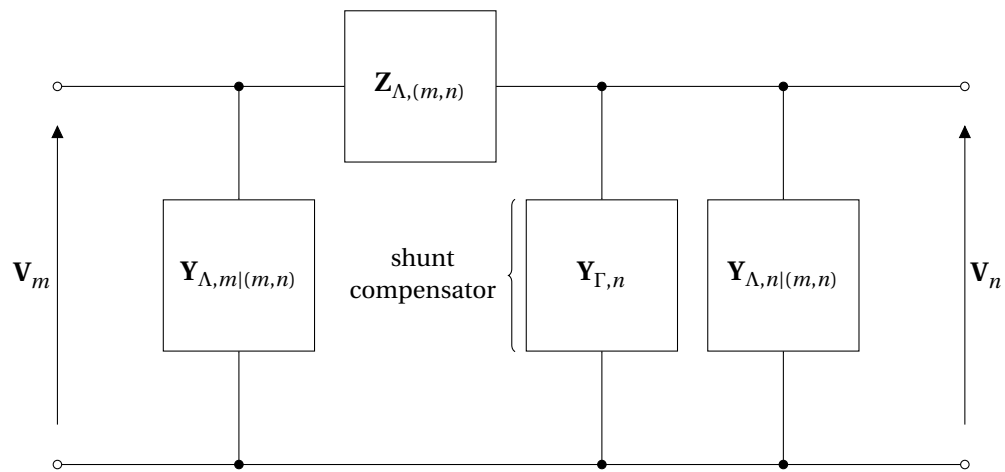


Figure A.8 – Equivalent circuit of a line equipped with shunt compensators. For the sake of simplicity, only one compensator is shown.

A.3 Measurement Noise in Different Coordinate Systems

In the following, voltage measurements are considered for illustration. Current measurements can be treated analogously.

Let V be the true value of a voltage phasor, which is expressed in polar coordinates as $V := E \angle \theta$. Suppose that the measurement process introduces a *magnitude error* \tilde{E} and a *phase error* $\tilde{\theta}$

$$\text{measurement of } V : (E + \tilde{E}) \angle (\theta + \tilde{\theta}) \quad (\text{A.51})$$

where \tilde{E} and $\tilde{\theta}$ are normally distributed with zero mean

$$\tilde{E} \sim \mathcal{N}(0, \sigma_E^2) \quad (\text{A.52})$$

$$\tilde{\theta} \sim \mathcal{N}(0, \sigma_\theta^2) \quad (\text{A.53})$$

Alternatively, V can be expressed in rectangular coordinates as $V := V_{\text{re}} + jV_{\text{im}}$. Analogously

$$\text{measurement of } V : (V_{\text{re}} + \tilde{V}_{\text{re}}) + j(V_{\text{im}} + \tilde{V}_{\text{im}}) \quad (\text{A.54})$$

According to Euler's formula

$$\tilde{V}_{\text{re}} = (E + \tilde{E}) \cos(\theta + \tilde{\theta}) - E \cos \theta \quad (\text{A.55})$$

$$\tilde{V}_{\text{im}} = (E + \tilde{E}) \sin(\theta + \tilde{\theta}) - E \sin \theta \quad (\text{A.56})$$

If \tilde{E} and $\tilde{\theta}$ are independent, the standard deviations $\sigma_{V_{\text{re}}}$ and $\sigma_{V_{\text{im}}}$ of \tilde{V}_{re} and \tilde{V}_{im} , respectively, are given by (for derivation, see [58])

$$\sigma_{V_{\text{re}}}^2 = \begin{bmatrix} E^2 \exp(-\sigma_\theta^2) (\cos^2 \theta (\cosh(\sigma_\theta^2) - 1) + \sin^2 \theta \sinh(\sigma_\theta^2)) \\ + \sigma_E^2 \exp(-\sigma_\theta^2) (\cos^2 \theta \cosh(\sigma_\theta^2) + \sin^2 \theta \sinh(\sigma_\theta^2)) \end{bmatrix} \quad (\text{A.57})$$

$$\sigma_{V_{\text{im}}}^2 = \begin{bmatrix} E^2 \exp(-\sigma_\theta^2) (\sin^2 \theta (\cosh(\sigma_\theta^2) - 1) + \cos^2 \theta \sinh(\sigma_\theta^2)) \\ + \sigma_E^2 \exp(-\sigma_\theta^2) (\sin^2 \theta \cosh(\sigma_\theta^2) + \cos^2 \theta \sinh(\sigma_\theta^2)) \end{bmatrix} \quad (\text{A.58})$$

Observe that $\sigma_{V_{\text{re}}}$ and $\sigma_{V_{\text{im}}}$ depend on σ_E and σ_θ as well as E and θ (i.e., the true magnitude and phase). In practice, the true values E and θ are unknown, but (A.57)–(A.58) can be evaluated using estimates \hat{E} and $\hat{\theta}$ of E and θ , or using assumed values.

A.4 Properties of the Kalman Filter

A.4.1 Joseph's Form of the Error Covariance Update

Lemma 16 (Joseph's form). *Recall the KF from Lemma 3. It holds that*

$$\mathbf{P}_k^+ = (\mathbf{I} - \mathbf{K}_k \mathbf{C}_k) \mathbf{P}_k^- (\mathbf{I} - \mathbf{K}_k \mathbf{C}_k)^\top + \mathbf{K}_k \mathbf{R}_k \mathbf{K}_k^\top \iff \mathbf{P}_k^+ = (\mathbf{I} - \mathbf{K}_k \mathbf{C}_k) \mathbf{P}_k^- \quad (\text{A.59})$$

Proof. Recall from (4.69) that the Kalman gain \mathbf{K}_k is given by

$$\mathbf{K}_k = \mathbf{P}_k^- \mathbf{C}_k^\top (\mathbf{C}_k \mathbf{P}_k^- \mathbf{C}_k^\top + \mathbf{R}_k)^{-1} \quad (\text{A.60})$$

Joseph's form can be rewritten as follows

$$\mathbf{P}_k^+ = (\mathbf{I} - \mathbf{K}_k \mathbf{C}_k) \mathbf{P}_k^- (\mathbf{I} - \mathbf{K}_k \mathbf{C}_k)^\top + \mathbf{K}_k \mathbf{R}_k \mathbf{K}_k^\top \quad (\text{A.61})$$

$$= \mathbf{P}_k^- - \mathbf{K}_k \mathbf{C}_k \mathbf{P}_k^- - \mathbf{P}_k^- \mathbf{C}_k^\top \mathbf{K}_k^\top + \mathbf{K}_k \mathbf{C}_k \mathbf{P}_k^- \mathbf{C}_k^\top \mathbf{K}_k^\top + \mathbf{K}_k \mathbf{R}_k \mathbf{K}_k^\top \quad (\text{A.62})$$

$$= \mathbf{P}_k^- - \mathbf{K}_k \mathbf{C}_k \mathbf{P}_k^- - \mathbf{P}_k^- \mathbf{C}_k^\top \mathbf{K}_k^\top + \mathbf{K}_k (\mathbf{C}_k \mathbf{P}_k^- \mathbf{C}_k^\top + \mathbf{R}_k) \mathbf{K}_k^\top \quad (\text{A.63})$$

$$= \mathbf{P}_k^- - \mathbf{K}_k \mathbf{C}_k \mathbf{P}_k^- - \mathbf{P}_k^- \mathbf{C}_k^\top \mathbf{K}_k^\top + \mathbf{P}_k^- \mathbf{C}_k^\top \mathbf{K}_k^\top \quad (\text{A.64})$$

$$= \mathbf{P}_k^- - \mathbf{K}_k \mathbf{C}_k \mathbf{P}_k^- \quad (\text{A.65})$$

$$= (\mathbf{I} - \mathbf{K}_k \mathbf{C}_k) \mathbf{P}_k^- \quad (\text{A.66})$$

This proves the claim. \square

A.4.2 Positive Definiteness of the Estimation Error Covariance Matrix

In the following, the validity of Hypothesis 9 is substantiated. More precisely, it is proven that the KF preserves the positive definiteness of the prediction error covariance matrix \mathbf{P}_k^- and of the estimation error covariance matrix \mathbf{P}_k^+ . Formally:

Lemma 17 ($\mathbf{P}_k^+ > 0$). *Recall the KF from Lemma 3. If $\mathbf{R}_k > 0$ and $\mathbf{P}_0^+ > 0$, then $\mathbf{P}_k^+ > 0$ for $k > 0$.*

Proof. (Formulation (4.69)–(4.71)). Provided that \mathbf{P}_{k-1}^+ is positive definite, $\mathbf{P}_k^- = \mathbf{P}_{k-1}^+ + \mathbf{Q}_{k-1}$ is positive definite, because \mathbf{Q}_{k-1} positive semidefinite. The Kalman gain \mathbf{K}_k is given by (4.69) as

$$\mathbf{K}_k = \mathbf{P}_k^- \mathbf{C}_k^\top (\mathbf{C}_k \mathbf{P}_k^- \mathbf{C}_k^\top + \mathbf{R}_k)^{-1} \quad (\text{A.67})$$

Since the system is observable, \mathbf{C}_k has full rank. Hence, the term $\mathbf{C}_k \mathbf{P}_k^- \mathbf{C}_k^\top$ is positive definite (see Lemma 7, Appendix A.1.2). Moreover, the term $\mathbf{C}_k \mathbf{P}_k^- \mathbf{C}_k^\top + \mathbf{R}_k$ is positive definite, and thus has full rank. Accordingly, \mathbf{K}_k has full rank (see Lemma 5, Appendix A.1.1). The estimation error covariance matrix \mathbf{P}_k^+ is given by (4.70) as

$$\mathbf{P}_k^+ = (\mathbf{I} - \mathbf{K}_k \mathbf{C}_k) \mathbf{P}_k^- (\mathbf{I} - \mathbf{K}_k \mathbf{C}_k)^\top + \mathbf{K}_k \mathbf{R}_k \mathbf{K}_k^\top \quad (\text{A.68})$$

The first summand is positive semidefinite, as \mathbf{P}_k^- is positive definite. The second summand is positive definite, as \mathbf{R}_k is positive definite and \mathbf{C}_k has full rank (see Lemma 7, Appendix A.1.2). In summary, $\mathbf{P}_{k-1}^+ > 0$ implies $\mathbf{P}_k^+ > 0$. By induction, it follows that $\mathbf{P}_k^+ > 0$ for $k > 0$ if $\mathbf{P}_0^+ > 0$. This proves the claim. \square

Proof. (Formulation (4.72)–(4.74)). The procedure is analogous. By (4.72)

$$(\mathbf{P}_k^+)^{-1} = (\mathbf{P}_k^-)^{-1} + \mathbf{C}_k^T \mathbf{R}_k^{-1} \mathbf{C}_k \quad (\text{A.69})$$

The inverse matrices on the right-hand side are positive definite, because the original matrices are positive definite. Moreover, \mathbf{C}_k has full rank. Therefore, the term $\mathbf{C}_k^T \mathbf{R}_k^{-1} \mathbf{C}_k$ is positive definite (see Lemma 7, Appendix A.1.2). Accordingly, $(\mathbf{P}_k^+)^{-1}$ is positive definite, and so is \mathbf{P}_k^+ . By induction, it follows that $\mathbf{P}_k^+ > 0$ for $k > 0$ if $\mathbf{P}_0^+ > 0$, which proves the claim. \square

A.4.3 Equivalent Formulations of the Estimation Step

Lemma 18. Consider the KF as stated in Lemma 3. If Hypothesis A.4.2 holds, then

$$\begin{cases} \mathbf{K}_k = \mathbf{P}_k^- \mathbf{C}_k^T (\mathbf{C}_k \mathbf{P}_k^- \mathbf{C}_k^T + \mathbf{R}_k)^{-1} \\ \mathbf{P}_k^+ = (\mathbf{I} - \mathbf{K}_k \mathbf{C}_k) \mathbf{P}_k^- \\ \hat{\mathbf{x}}_k^+ = \hat{\mathbf{x}}_k^- + \mathbf{K}_k (\mathbf{y}_k - \mathbf{C}_k \hat{\mathbf{x}}_k^-) \end{cases} \iff \begin{cases} (\mathbf{P}_k^+)^{-1} = (\mathbf{P}_k^-)^{-1} + \mathbf{C}_k^T \mathbf{R}_k^{-1} \mathbf{C}_k \\ \mathbf{K}_k = \mathbf{P}_k^+ \mathbf{C}_k^T \mathbf{R}_k^{-1} \\ \hat{\mathbf{x}}_k^+ = \hat{\mathbf{x}}_k^- + \mathbf{K}_k (\mathbf{y}_k - \mathbf{C}_k \hat{\mathbf{x}}_k^-) \end{cases} \quad (\text{A.70})$$

The equivalence holds if the obtained \mathbf{P}_k^+ and \mathbf{K}_k are the same for both formulations.

Proof. (Part 1: \mathbf{P}_k^+). Inverting the equation defining $(\mathbf{P}_k^+)^{-1}$ yields \mathbf{P}_k^+ as

$$\mathbf{P}_k^+ = \left((\mathbf{P}_k^-)^{-1} + \mathbf{C}_k^T \mathbf{R}_k^{-1} \mathbf{C}_k \right)^{-1} \quad (\text{A.71})$$

Hypothesis 9 ensures that \mathbf{R}_k , \mathbf{P}_k^- , $(\mathbf{P}_k^-)^{-1} + \mathbf{C}_k^T \mathbf{R}_k^{-1} \mathbf{C}_k$, and $\mathbf{C}_k \mathbf{P}_k^- \mathbf{C}_k^T + \mathbf{R}_k$, are positive definite, and hence invertible. Therefore, the Woodbury matrix identity (see Lemma 6, Appendix A.1.1) can be applied using $\mathbf{A} := (\mathbf{P}_k^-)^{-1}$, $\mathbf{B} := \mathbf{R}_k^{-1}$, $\mathbf{U} := \mathbf{C}_k$, and $\mathbf{V} := \mathbf{C}_k$:

$$\mathbf{P}_k^+ = \left((\mathbf{P}_k^-)^{-1} + \mathbf{C}_k^T \mathbf{R}_k^{-1} \mathbf{C}_k \right)^{-1} \quad (\text{A.72})$$

$$= \mathbf{P}_k^- - \mathbf{P}_k^- \mathbf{C}_k^T (\mathbf{C}_k \mathbf{P}_k^- \mathbf{C}_k^T + \mathbf{R}_k)^{-1} \mathbf{C}_k \mathbf{P}_k^- \quad (\text{A.73})$$

$$= \mathbf{P}_k^- - \mathbf{K}_k \mathbf{C}_k \mathbf{P}_k^- \quad (\text{A.74})$$

$$= (\mathbf{I} - \mathbf{K}_k \mathbf{C}_k) \mathbf{P}_k^- \quad (\text{A.75})$$

This proves the equivalence for \mathbf{P}_k^+ . \square

Appendix A. Appendix

Proof. (Part 2: \mathbf{K}_k). Reformulate the expression for \mathbf{K}_k as follows

$$\mathbf{K}_k = \mathbf{P}_k^+ \mathbf{C}_k^T \mathbf{R}_k^{-1} \quad (\text{A.76})$$

$$= \mathbf{P}_k^- \mathbf{C}_k^T \mathbf{R}_k^{-1} \left(\mathbf{C}_k \mathbf{P}_k^- \mathbf{C}_k^T + \mathbf{R}_k \right) \left(\mathbf{C}_k \mathbf{P}_k^- \mathbf{C}_k^T + \mathbf{R}_k \right)^{-1} \quad (\text{A.77})$$

$$= \mathbf{P}_k^+ \mathbf{C}_k^T \mathbf{R}_k^{-1} \left(\mathbf{C}_k \mathbf{P}_k^- \mathbf{C}_k^T \mathbf{R}_k^{-1} + \mathbf{I} \right) \mathbf{R}_k \left(\left(\mathbf{C}_k \mathbf{P}_k^- \mathbf{C}_k^T \mathbf{R}_k^{-1} + \mathbf{I} \right) \mathbf{R}_k \right)^{-1} \quad (\text{A.78})$$

$$= \mathbf{P}_k^+ \mathbf{C}_k^T \mathbf{R}_k^{-1} \left(\mathbf{C}_k \mathbf{P}_k^- \mathbf{C}_k^T \mathbf{R}_k^{-1} + \mathbf{I} \right) \left(\mathbf{C}_k \mathbf{P}_k^- \mathbf{C}_k^T \mathbf{R}_k^{-1} + \mathbf{I} \right)^{-1} \quad (\text{A.79})$$

$$= \mathbf{P}_k^+ \left(\mathbf{C}_k^T \mathbf{R}_k^{-1} \mathbf{C}_k \mathbf{P}_k^- \mathbf{C}_k^T \mathbf{R}_k^{-1} + \mathbf{C}_k^T \mathbf{R}_k^{-1} \right) \left(\mathbf{C}_k \mathbf{P}_k^- \mathbf{C}_k^T \mathbf{R}_k^{-1} + \mathbf{I} \right)^{-1} \quad (\text{A.80})$$

$$= \mathbf{P}_k^+ \left(\mathbf{C}_k^T \mathbf{R}_k^{-1} \mathbf{C}_k + (\mathbf{P}_k^-)^{-1} \right) \mathbf{P}_k^- \mathbf{C}_k^T \mathbf{R}_k^{-1} \left(\mathbf{C}_k \mathbf{P}_k^- \mathbf{C}_k^T \mathbf{R}_k^{-1} + \mathbf{I} \right)^{-1} \quad (\text{A.81})$$

$$= \mathbf{P}_k^+ (\mathbf{P}_k^+)^{-1} \mathbf{P}_k^- \mathbf{C}_k^T \mathbf{R}_k^{-1} \left(\mathbf{C}_k \mathbf{P}_k^- \mathbf{C}_k^T \mathbf{R}_k^{-1} + \mathbf{I} \right)^{-1} \quad (\text{A.82})$$

$$= \mathbf{P}_k^- \mathbf{C}_k^T \left(\left(\mathbf{C}_k \mathbf{P}_k^- \mathbf{C}_k^T \mathbf{R}_k^{-1} + \mathbf{I} \right) \mathbf{R}_k \right)^{-1} \quad (\text{A.83})$$

$$= \mathbf{P}_k^- \mathbf{C}_k^T \left(\mathbf{C}_k \mathbf{P}_k^- \mathbf{C}_k^T + \mathbf{R}_k \right)^{-1} \quad (\text{A.84})$$

This proves the equivalence for \mathbf{K}_k . □

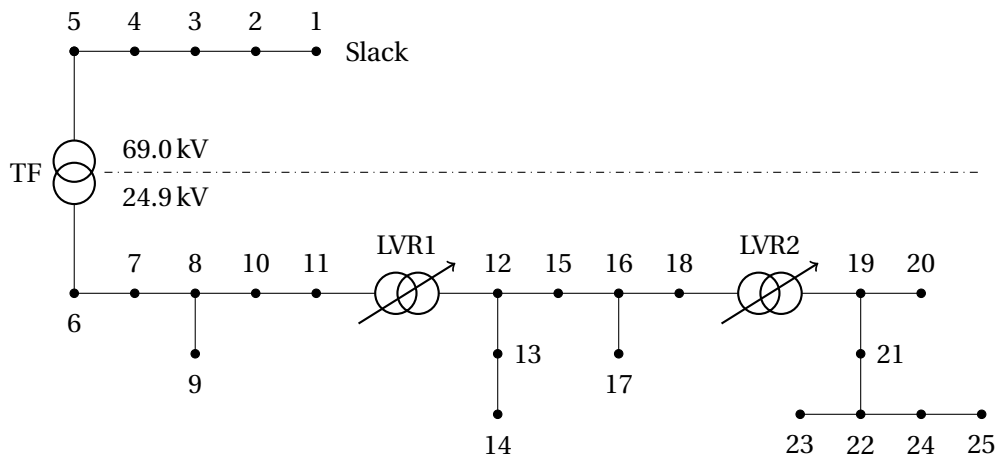


Figure A.9 – Schematic of the benchmark power grid.

A.5 Benchmark Power Grid

The same benchmark power grid is used for all simulation studies presented in this thesis. As shown in Figure A.9, it consists of two subsystems:

1. Upper-level subsystem (nodes 1–5) with nominal voltage 69.0 kV (phase-to-phase).
2. Lower-level subsystem (nodes 6–25) with nominal voltage 24.9 kV (phase-to-phase).

The former is a linear feeder built of transposed overhead lines. The latter is a modified version of the IEEE 34-node distribution feeder, which consists of untransposed overhead lines and *Line Voltage Regulators* (LVRs) [135]. These subsystems are interfaced by a conventional transformer (i.e., without a tap changer). Tables A.1–A.3 list the specifications of the nodes, lines, and transformers, respectively.

The transposed overhead lines are characterized by the sequence parameters given in Table A.4. These values are for aluminum/steel conductors with a cross-sectional area of 435 mm^2 [172], which translates to a rated current of 300 A. The untransposed overhead lines are specified in detail in [135]. They have rated currents of 230 A (IEEE-300) and 180 A (IEEE-301) per conductor. The transformers are wye-connected and effectively grounded on both the primary and secondary side. Therefore, the sequence impedances are equal. Here, typical values are used: $R = 5E-3 \text{ pu}$ and $X = 0.1 \text{ pu}$ (w.r.t. the base impedance defined by the rated power and the nominal voltage) [172].

Table A.1 – Specification of the nodes.

Node	Name (IEEE)	Node	Name (IEEE)
1–5	–		
6	800	16	854
7	806	17	856
8	808	18	852
9	810	19	832
10	812	20	890
11	814	21	858
12	816	22	834
13	820	23	848
14	822	24	836
15	824	25	838

Table A.2 – Specification of the lines.

Line	Length (km)	Parameters	Line	Length (km)	Parameters
1–2	25.000	Table A.4	12–13	15.197	IEEE-301
2–3	25.000	Table A.4	13–14	4.188	IEEE-301
3–4	25.000	Table A.4	12–15	3.112	IEEE-301
4–5	25.000	Table A.4	15–16	6.645	IEEE-301
6–7	1.314	IEEE-300	16–17	7.111	IEEE-301
7–8	9.851	IEEE-300	16–18	11.226	IEEE-301
8–9	1.769	IEEE-300	19–20	3.219	IEEE-301
8–10	11.430	IEEE-300	19–21	1.494	IEEE-301
10–11	9.062	IEEE-300	21–22	1.777	IEEE-301
			22–23	1.768	IEEE-301
			22–24	1.433	IEEE-301
			24–25	1.567	IEEE-301

Table A.3 – Specification of the transformers.

Name	Connection (I–II)	Rated Power (MVA)	Nominal Voltage (kV)
TF	5–6	12.0	69.0 (I), 24.9 (II)
LVR1	11–12	9.0	24.9 (I+II)
LVR2	18–19	9.0	24.9 (I+II)

Table A.4 – Sequence parameters of the transposed lines.

Sequence	R' (Ω/km)	X' (Ω/km)	B' ($\mu\text{S}/\text{km}$)
Positive + Negative	0.071	0.379	3.038
Homopolar	0.202	0.884	1.740

Bibliography

- [1] F. F. Wu, K. Moslehi, and A. Bose, "Power system control centers: Past, present, and future," *Proc. IEEE*, vol. 93, no. 11, pp. 1890–1908, Oct. 2005.
- [2] R. H. Park and E. H. Bancker, "System stability as a design problem," *Trans. AIEE*, vol. 48, no. 1, pp. 170–193, Jan. 1929.
- [3] E. W. Kimbark, *Power System Stability, Volume 1: Elements of Stability Calculations*. Hoboken, NJ, USA: Wiley, 1948.
- [4] ———, *Power System Stability, Volume 2: Power Circuit Breakers and Protective Relays*. Hoboken, NJ, USA: Wiley, 1948.
- [5] ———, *Power System Stability, Volume 3: Synchronous Machines*. Hoboken, NJ, USA: Wiley, 1948.
- [6] IEEE, "IEEE recommended practice for grounding of industrial and commercial power systems," 2007, IEEE Standard 142–2007.
- [7] ———, "IEEE recommended practice for protection and coordination of industrial and commercial power systems," 2001, IEEE Standard 242–2001.
- [8] ———, "IEEE recommended practice for design of reliable industrial and commercial power systems," 2007, IEEE Standard 493–2007.
- [9] CIGRÉ WG C6.11, "Development and operation of active distribution networks," CIGRÉ, Paris, IDF, FR, Tech. Rep. 457, Apr. 2011.
- [10] A. Bose and K. A. Clements, "Real-time modeling of power networks," *Proc. IEEE*, vol. 75, no. 12, pp. 1607–1622, Dec. 1987.
- [11] R. B. Prada and L. J. Souza, "Voltage stability and thermal limit: Constraints on the maximum loading of electrical energy distribution feeders," *IEE Proc.–Gener. Transm. Distrib.*, vol. 145, no. 5, pp. 573–577, Sep. 1998.
- [12] CIGRÉ WG C4.34, "Application of phasor measurement units for monitoring power system dynamic performance," CIGRÉ, Paris, IDF, FR, Tech. Rep. 702, Sep. 2017.

Bibliography

- [13] CIGRÉ/CIREN JWG C6/B5.25, “Control and automation systems for electricity distribution networks of the future,” CIGRÉ, Paris, IDF, FR, Tech. Rep. 711, Dec. 2017.
- [14] P. Romano, “DFT-based synchrophasor estimation algorithms and their integration in advanced phasor measurement units for the real-time monitoring of active distribution networks,” Ph.D. thesis, École Polytechnique Fédérale de Lausanne (EPFL), Lausanne, VD, CH, 2016.
- [15] M. Pignati, “Resilient synchrophasor networks for the real-time monitoring, protection and control of power grids: From theory to validation,” Ph.D. dissertation, École Polytechnique Fédérale de Lausanne (EPFL), Lausanne, VD, CH, 2017.
- [16] L. Zanni, “Power-system state estimation based on PMU, static and dynamic approaches: From theory to real implementation,” Ph.D. dissertation, École Polytechnique Fédérale de Lausanne (EPFL), Lausanne, VD, CH, 2017.
- [17] L. E. Reyes Chamorro, “Real-time control framework for active distribution networks: Theoretical definition and experimental validation,” Ph.D. dissertation, École Polytechnique Fédérale de Lausanne (EPFL), Lausanne, VD, CH, 2016.
- [18] P. Kessel and H. Glavitsch, “Estimating the voltage stability of a power system,” *IEEE Trans. Power Del.*, vol. 1, no. 3, pp. 346–354, Jul. 1986.
- [19] K. Strunz *et al.*, “Benchmark systems for network integration of renewable and distributed energy resources,” CIGRÉ, Paris, IDF, FR, Tech. Rep. 575, 2014.
- [20] B. Stott, “Review of load-flow calculation methods,” *Proc. IEEE*, vol. 62, no. 7, pp. 916–929, Jul. 1974.
- [21] F. F. Wu, “Power system state estimation: A survey,” *Int. J. Elect. Power Energy Syst.*, vol. 12, no. 2, pp. 80–87, Apr. 1990.
- [22] A. J. Monticelli, *State Estimation in Electric Power Systems: A Generalized Approach*. Berlin, BE, DE: Springer, 1999.
- [23] A. Abur and A. Gómez Expósito, *Power System State Estimation: Theory and Implementation*. Boca Raton, FL, USA: CRC Press, 2004.
- [24] P. S. Kundur, *Power System Stability and Control*, N. J. Balu and M. G. Lauby, Eds. New York City, NY, USA: McGraw-Hill, 1994.
- [25] P. M. Anderson and A.-A. Fouad, *Power System Stability and Control*, 2nd ed. Hoboken, NJ, USA: Wiley, 2002.
- [26] T. Van Cutsem and C. Vournas, *Voltage Stability of Electric Power Systems*. Berlin, BER, DE: Springer, 1998.

-
- [27] J. B. Ward, "Equivalent circuits for power-flow studies," *Trans. AIEE*, vol. 68, no. 1, pp. 373–382, Jul. 1949.
- [28] G. Kron, *Tensors for Circuits*, 2nd ed. Mineola, NY, USA: Dover Publications, 1959.
- [29] S. K. Khaitan and A. Gupta, Eds., *High-Performance Computing in Power and Energy Systems*. Berlin, BER, DE: Springer, 2013.
- [30] C. P. Steinmetz, "Complex quantities and their use in electrical engineering," in *Proc. Int. Elect. Congr., Chicago, IL, USA*, 1893, pp. 33–74.
- [31] J. Arrillaga and C. P. Arnold, *Computer Analysis of Power Systems*. Hoboken, NJ, USA: Wiley, 1990.
- [32] C. L. Fortescue, "Method of symmetrical coordinates applied to the solution of polyphase networks," *Trans. AIEE*, vol. 37, no. 2, pp. 1027–1140, Jun. 1918.
- [33] M. A. Laughton and A. O. M. Saleh, "Unified phase-coordinate load-flow and fault analysis of polyphase networks," *Int. J. Elect. Power Energy Syst.*, vol. 2, no. 4, pp. 181–192, 1980.
- [34] A. P. Sakis Meliopoulos and F. Zhang, "Multiphase power flow and state estimation for power distribution systems," *IEEE Trans. Power Syst.*, vol. 11, no. 2, pp. 939–946, May 1996.
- [35] S. N. Tiwari and L. P. Singh, "Mathematical modelling and analysis of multiphase systems," *IEEE Trans. Power App. Syst.*, no. 6, pp. 1784–1793, Jun. 1982.
- [36] F. Dörfler and F. Bullo, "Kron reduction of graphs with applications to electrical networks," *IEEE Trans. Circuits Syst. I: Reg. Papers*, vol. 60, no. 1, pp. 150–163, Jan. 2013.
- [37] C. Wang, A. Bernstein, J.-Y. Le Boudec, and M. Paolone, "Existence and uniqueness of load-flow solutions in three-phase distribution networks," *IEEE Trans. Power Syst.*, vol. 32, no. 4, pp. 3319–3320, Jul. 2017.
- [38] M. Bazrafshan and N. Gatsis, "Comprehensive modeling of three-phase distribution systems via the bus admittance matrix," *IEEE Trans. Power Syst.*, vol. 33, no. 2, pp. 2015–2029, Mar. 2018.
- [39] R. J. Duffin, D. Hazony, and N. Morrison, "Network synthesis through hybrid matrices," *SIAM J. Appl. Mathematics*, vol. 14, no. 2, pp. 390–413, Mar. 1966.
- [40] R. J. Duffin and G. E. Trapp, "Hybrid addition of matrices – network theory concept," *Applicable Anal.*, vol. 2, no. 3, pp. 241–254, 1972.
- [41] A. E. Sen and Y. Tokad, "The existence and the determination of terminal equations for hybrid-connected n -ports," *Int. J. Circuit Theory Applicat.*, vol. 8, no. 3, pp. 205–217, Jul. 1980.

Bibliography

- [42] I. N. Hajj, "Computation of hybrid equations of linear multiports," *IEEE Trans. Circuits Syst.*, vol. 24, no. 11, pp. 655–656, Nov. 1977.
- [43] S. Q. Sun and L. Y. Qian, "Formulation of generalised state equations and multiport equations: A novel approach," *IEE Proc. G – Circuits Devices Syst.*, vol. 137, no. 1, pp. 49–52, Feb. 1990.
- [44] J. A. S. Augusto and C. F. B. Almeida, "Use of modified nodal analysis to write multiport hybrid matrix," *IET Electron. Lett.*, vol. 27, no. 19, pp. 1750–1752, Sep. 1991.
- [45] H. C. So, "On the hybrid description of a linear n -port resulting from the extraction of arbitrarily specified elements," *IEEE Trans. Circuit Theory*, vol. 12, no. 3, pp. 381–387, Sep. 1965.
- [46] J. Zuidweg, "Every passive time-invariant linear n -port has at least one h -matrix," *IEEE Trans. Circuit Theory*, vol. 12, no. 1, pp. 131–132, Mar. 1965.
- [47] B. Anderson, R. Newcomb, and J. Zuidweg, "On the existence of h matrices," *IEEE Trans. Circuit Theory*, vol. 13, no. 1, pp. 109–110, Mar. 1966.
- [48] F. C. Schweppe and E. J. Handschin, "Static state estimation in electric power systems," *Proc. IEEE*, vol. 62, no. 7, pp. 972–982, Jul. 1974.
- [49] A. J. Monticelli, "Electric power system state estimation," *Proc. IEEE*, vol. 88, no. 2, pp. 262–282, Feb. 2000.
- [50] J. F. Dopazo, O. A. Klitin, G. W. Stagg, and L. S. Van Slyck, "State calculation of power systems from line-flow measurements. part I," *IEEE Trans. Power App. Syst.*, vol. 89, no. 7, pp. 1698–1708, Sep. 1970.
- [51] J. F. Dopazo, O. A. Klitin, and L. S. Van Slyck, "State calculation of power systems from line-flow measurements. part II," *IEEE Trans. Power App. Syst.*, vol. 91, no. 1, pp. 145–151, Jan. 1972.
- [52] F. C. Schweppe and J. Wildes, "Power system static-state estimation. part I: Exact model," *IEEE Trans. Power App. Syst.*, vol. 89, no. 1, pp. 120–125, Jan. 1970.
- [53] F. C. Schweppe and D. B. Rom, "Power system static-state estimation. part II: Approximate model," *IEEE Trans. Power App. Syst.*, vol. 89, no. 1, pp. 125–130, Jan. 1970.
- [54] F. C. Schweppe, "Power system static-state estimation. part III: Implementation," *IEEE Trans. Power App. Syst.*, vol. 89, no. 1, pp. 130–135, Jan. 1970.
- [55] M. E. Baran and A. W. Kelley, "A branch-current-based state estimation method for distribution systems," *IEEE Trans. Power Syst.*, vol. 10, pp. 483–491, Feb. 1995.
- [56] D. A. Haughton and G. T. Heydt, "A linear state estimation formulation for smart distribution systems," *IEEE Trans. Power Syst.*, vol. 28, no. 2, pp. 1187–1195, May 2013.

- [57] C. N. Lu, J. H. Teng, and W.-H. E. Liu, "Distribution system state estimation," *IEEE Trans. Power Syst.*, vol. 10, no. 1, pp. 229–240, Feb. 1995.
- [58] M. Paolone, J.-Y. Le Boudec, S. Sarri, and L. Zanni, "Static and recursive PMU-based state estimation processes for transmission and distribution grids," in *Advanced Techniques for Power System Modelling, Control and Stability Analysis*, F. Milano, Ed. Stevenage, ENG, UK: IET, 2016, ch. 6, pp. 189–239.
- [59] T. Van Cutsem, L. Mili, and M. Ribbens-Pavella, "Hypothesis testing identification: A new method for bad data analysis in power system state estimation," *IEEE Trans. Power App. Syst.*, no. 11, pp. 3239–3252, Nov. 1984.
- [60] —, "Bad data identification methods in power system state estimation – a comparative study," *IEEE Trans. Power App. Syst.*, no. 11, pp. 3037–3049, Nov. 1985.
- [61] P. Rousseaux, D. Mallieu, T. Van Cutsem, and M. Ribbens-Pavella, "Dynamic state prediction and hierarchical filtering for power system state estimation," *Automatica*, vol. 24, no. 5, pp. 595–618, 1988.
- [62] N. G. Bretas, "An iterative dynamic state estimation and bad data processing," *Int. J. Elect. Power Energy Syst.*, vol. 11, no. 1, pp. 70–74, 1989.
- [63] E. Ghahremani and I. Kamwa, "Dynamic state estimation in power system by applying the extended kalman filter with unknown inputs to phasor measurements," *IEEE Trans. Power Syst.*, vol. 26, no. 4, pp. 2556–2566, Nov. 2011.
- [64] R. E. Kalman, "A new approach to linear filtering and prediction problems," *J. Basic Eng.*, vol. 82, no. 1, pp. 35–45, 1960.
- [65] G. Valverde and V. Terzija, "Unscented kalman filter for power system dynamic state estimation," *IET Gener. Transm. Distrib.*, vol. 5, no. 1, pp. 29–37, 2011.
- [66] R. E. Larson, W. F. Tinney, and J. Peschon, "State estimation in power systems. part I: Theory and feasibility," *IEEE Trans. Power App. Syst.*, vol. 89, no. 3, pp. 345–352, Mar. 1970.
- [67] R. E. Larson, W. F. Tinney, L. P. Hajdu, and D. S. Piercy, "State estimation in power systems. part II: Implementation and applications," *IEEE Trans. Power App. Syst.*, vol. 89, no. 3, pp. 353–363, Mar. 1970.
- [68] A. S. Debs and R. E. Larson, "A dynamic estimator for tracking the state of a power system," *IEEE Trans. Power App. Syst.*, vol. 89, no. 7, pp. 1670–1678, Sep./Oct. 1970.
- [69] L. Zanni, S. Sarri, M. Pignati, R. Cherkaoui, and M. Paolone, "Probabilistic assessment of the process noise covariance matrix of discrete-kalman-filter state estimation of active distribution networks," in *Proc. Int. Conf. Probabilistic Meth. Appl. Power Syst. (PMAPS)*, Durham, ENG, UK, Jul. 2014, pp. 1–6.

Bibliography

- [70] L. Zanni, J.-Y. Le Boudec, R. Cherkaoui, and M. Paolone, "A prediction-error covariance estimator for adaptive kalman filtering in step-varying processes: Application to power-system state estimation," *IEEE Trans. Control Syst. Technol.*, vol. 25, no. 5, pp. 1683–1697, Sep. 2017.
- [71] A. S. Debs, R. E. Larson, and L. P. Hajdu, "Online sequential state estimation for power systems," in *Proc. Power Syst. Comput. Conf. (PSCC), Grenoble, ARA, FR*, Sep. 1972, pp. 1–32.
- [72] P. Kundur, J. Paserba, V. Ajjarapu, G. Andersson, A. Bose, C. Canizares, N. Hatziargyriou, D. Hill, A. Stankovic, C. Taylor, T. Van Cutsem, and V. Vital, "Definition and classification of power system stability," *IEEE Trans. Power Syst.*, vol. 19, no. 3, pp. 1387–1401, May 2004.
- [73] P. W. Sauer, B. C. Lesieutre, and M. A. Pai, "Maximum loadability and voltage stability in power systems," *Int. J. Elect. Power Energy Syst.*, vol. 15, no. 3, pp. 145–153, 1993.
- [74] P. W. Sauer and M. A. Pai, "Power system steady-state stability and the load-flow Jacobian," *IEEE Trans. Power Syst.*, vol. 5, no. 4, pp. 1374–1383, Nov. 1990.
- [75] T. Van Cutsem, "Voltage instability: Phenomena, countermeasures, and analysis methods," *Proc. IEEE*, vol. 88, no. 2, pp. 208–227, Feb. 2000.
- [76] V. Venkatasubramanian, H. Schättler, and J. Zaborsky, "Dynamics of large constrained nonlinear systems – a taxonomy theory," *Proc. IEEE*, vol. 83, no. 11, pp. 1530–1561, Nov. 1995.
- [77] V. Ajjarapu and C. Christy, "The continuation power flow: A tool for steady-state voltage stability analysis," *IEEE Trans. Power Syst.*, vol. 7, no. 1, pp. 416–423, Feb. 1992.
- [78] C. A. Cañizares and F. L. Alvarado, "Point-of-collapse and continuation methods for large AC/DC systems," *IEEE Trans. Power Syst.*, vol. 8, no. 1, pp. 1–8, Feb. 1993.
- [79] H.-D. Chiang, A. J. Flueck, K. S. Shah, and N. J. Balu, "CPFLOW: A practical tool for tracing power-system steady-state stationary behavior due to load and generation variations," *IEEE Trans. Power Syst.*, vol. 10, no. 2, pp. 623–634, May 1995.
- [80] S.-H. Li and H.-D. Chiang, "Nonlinear predictors and hybrid corrector for fast continuation power flow," *IET Gener. Transm. Distrib.*, vol. 2, no. 3, pp. 341–354, May 2008.
- [81] P. Xu, X. Wang, and V. Ajjarapu, "Continuation power flow with adaptive stepsize control via convergence monitor," *IET Gener. Transm. Distrib.*, vol. 6, no. 7, pp. 673–679, Jul. 2012.
- [82] V. C. Nikolaidis, N. A. Tsouris, and C. D. Vournas, "Continuation power flow incorporating dispersed generation," in *Proc. IEEE PowerTech, Lausanne, VD, CH*, 2007, pp. 573–578.

-
- [83] X.-P. Zhang, P. Ju, and E. Handschin, "Continuation three-phase power flow: A tool for voltage stability analysis of unbalanced three-phase power systems," *IEEE Trans. Power Syst.*, vol. 20, no. 3, pp. 1320–1329, Aug. 2005.
- [84] H. Sheng and H.-D. Chiang, "CDFLOW: A practical tool for tracing stationary behaviors of general distribution networks," *IEEE Trans. Power Syst.*, vol. 29, no. 3, pp. 1365–1371, May 2014.
- [85] R. J. Avalos, C. A. Cañizares, F. Milano, and A. J. Conejo, "Equivalency of continuation and optimization methods to determine saddle-node and limit-induced bifurcations in power systems," *IEEE Trans. Circuits Syst. I: Reg. Papers*, vol. 56, no. 1, pp. 210–223, Jan. 2009.
- [86] G. D. Irisarri, X. Wang, J. Tong, and S. Mokhtari, "Maximum loadability of power systems using interior-point nonlinear optimization method," *IEEE Trans. Power Syst.*, vol. 12, no. 1, pp. 162–172, Feb. 1997.
- [87] T. Van Cutsem, "A method to compute reactive-power margins with respect to voltage collapse," *IEEE Trans. Power Syst.*, vol. 6, no. 1, pp. 145–156, Feb. 1991.
- [88] C. D. Vournas, M. Karystianos, and N. G. Maratos, "Bifurcation points and loadability limits as solutions of constrained optimization problems," in *Proc. IEEE PES Summer Meeting, Seattle, WA, USA*, vol. 3, 2000, pp. 1883–1888.
- [89] C. Desoer, "The maximum power transfer theorem for n -ports," *IEEE Trans. Circuit Theory*, vol. 20, no. 3, pp. 328–330, May 1973.
- [90] K. Vu, M. Begović, D. Novosel, and M. M. Saha, "Use of local measurements to estimate voltage stability margin," *IEEE Trans. Power Syst.*, vol. 14, no. 3, pp. 1029–1035, Aug. 1999.
- [91] B. Milošević and M. Begović, "Voltage stability protection and control using a wide-area network of phasor measurements," *IEEE Trans. Power Syst.*, vol. 18, no. 1, pp. 121–127, Feb. 2003.
- [92] M. H. Haque, "Novel method of assessing voltage stability of a power system using stability boundary in pq plane," *Elect. Power Syst. Research*, vol. 64, no. 1, pp. 35–40, Jan. 2003.
- [93] C. D. Vournas, "Maximum power transfer in the presence of network resistance," *IEEE Trans. Power Syst.*, vol. 30, no. 5, pp. 2826–2827, Sep. 2015.
- [94] Y. Wang, I. R. Pordanjani, W. Li, W. Xu, T. Chen, E. Vaahedi, and J. Gurney, "Voltage stability monitoring based on the concept of coupled single-port circuit," *IEEE Trans. Power Syst.*, vol. 26, no. 4, pp. 2154–2163, Nov. 2011.
- [95] B. Cui and Z. Wang, "Voltage stability assessment based on improved coupled single-port method," *IET Gener. Transm. Distrib.*, vol. 11, no. 10, pp. 2703–2711, Nov. 2017.

Bibliography

- [96] J.-H. Liu and C.-C. Chu, "Wide-area measurement-based voltage stability indicators by modified coupled single-port models," *IEEE Trans. Power Syst.*, vol. 29, no. 2, pp. 756–764, Mar. 2014.
- [97] S. Grijalva, "Individual branch and path necessary conditions for saddle-node bifurcation voltage collapse," *IEEE Trans. Power Syst.*, vol. 27, no. 1, pp. 12–19, Feb. 2012.
- [98] S. Bolognani and S. Zampieri, "On the existence and linear approximation of the power-flow solution in power distribution networks," *IEEE Trans. Power Syst.*, vol. 31, no. 1, pp. 163–172, Jan. 2016.
- [99] J. E. Machado, R. Griñó, N. Barabanov, R. Ortega, and B. Polyak, "On existence of equilibria of multi-port linear AC networks with constant-power loads," *IEEE Trans. Circuits Syst. I: Reg. Papers*, vol. 64, no. 10, pp. 2772–2782, Oct. 2017.
- [100] C. Wang, A. Bernstein, J.-Y. Le Boudec, and M. Paolone, "Explicit conditions on existence and uniqueness of load-flow solutions in distribution networks," *IEEE Trans. Smart Grid*, vol. 9, pp. 953–962, Mar. 2018.
- [101] B. Gao, G. K. Morison, and P. S. Kundur, "Voltage stability evaluation using modal analysis," *IEEE Trans. Power Syst.*, vol. 7, no. 4, pp. 1529–1542, Nov. 1992.
- [102] P.-A. Löf, G. Andersson, and D. J. Hill, "Voltage stability indices for stressed power systems," *IEEE Trans. Power Syst.*, vol. 8, no. 1, pp. 326–335, Feb. 1993.
- [103] Y. Wang, C. Wang, F. Lin, W. Li, L. Y. Wang, and J. Zhao, "Incorporating generator equivalent model into voltage stability analysis," *IEEE Trans. Power Syst.*, vol. 28, no. 4, pp. 4857–4866, Jul. 2013.
- [104] J. Hongjie, Y. Xiaodan, and Y. Yixin, "An improved voltage stability index and its application," *Int. J. Elect. Power Energy Syst.*, vol. 27, no. 8, pp. 567–574, Oct. 2005.
- [105] M. M. El-Kateb, S. Abdelkader, and M. S. Kandil, "Linear indicator for voltage collapse in power systems," *IEE Proc.—Gener. Transm. Distrib.*, vol. 144, no. 2, pp. 139–146, Mar. 1997.
- [106] A. R. R. Matavalam and V. Ajjarapu, "Calculating the long-term voltage stability margin using a linear index," in *Proc. IEEE PES General Meeting, Denver, CO, USA*, 2015, pp. 1–5.
- [107] A. M. Kettner and M. Paolone, "On the properties of the power systems nodal admittance matrix," *IEEE Trans. Power Syst.*, vol. 33, no. 1, pp. 1130–1131, Jan. 2018.
- [108] —, "On the properties of the compound nodal admittance matrix of polyphase power systems," *IEEE Trans. Power Syst.*, vol. 34, no. 1, pp. 444–453, Jan. 2019.
- [109] J. C. Das and R. H. Osman, "Grounding of AC and DC low-voltage and medium-voltage drive systems," *IEEE Trans. Ind. Appl.*, vol. 34, no. 1, pp. 205–216, Jan. 1998.

-
- [110] T.-H. Chen and W.-C. Yang, "Analysis of multi-grounded four-wire distribution systems considering the neutral grounding," *IEEE Trans. Power Del.*, vol. 16, no. 4, pp. 710–717, Oct. 2001.
- [111] C. Desoer and E. Kuh, *Basic Circuit Theory*. New York City, NY, USA: McGraw-Hill, 1969.
- [112] M. Pignati, L. Zanni, P. Romano, R. Cherkaoui, and M. Paolone, "Fault detection and faulted line identification in active distribution networks using synchrophasor-based real-time state estimation," *IEEE Trans. Power Del.*, vol. 32, no. 1, pp. 381–392, Feb. 2017.
- [113] A. G. Phadke and J. S. Thorp, *Synchronized Phasor Measurements and their Applications*, 2nd ed. Berlin, BER, DE: Springer, 2017.
- [114] A. M. Kettner and M. Paolone, "Sequential discrete Kalman filter for real-time state estimation in power distribution systems: Theory and implementation," *IEEE Trans. Instrum. Meas.*, vol. 66, no. 9, pp. 2358–2370, Sep. 2017.
- [115] —, "Performance assessment of Kron reduction in the numerical analysis of polyphase power systems," in *IEEE PES PowerTech, Milano, LOM, IT*, Jun. 2019, pp. 1–6, accepted for presentation.
- [116] S. Sarri, "Methods and performance assessment of PMU-based real-time state estimation of active distribution networks," Ph.D. dissertation, École Polytechnique Fédérale de Lausanne (EPFL), Lausanne, VD, CH, 2016.
- [117] G. Frigo, A. Derviškić, A. Bach, and M. Paolone, "Statistical model of measurement noise in real-world PMU-based acquisitions," in *IEEE Int. Conf. Smart Grid Synchron. Meas. Analytics (SGSMA), Houston, TX, USA*, May 2019, pp. 1–6, accepted for presentation.
- [118] A. Mingotti, L. Peretto, and R. Tinarelli, "Low-power voltage transformer accuracy class effects on the residual voltage measurement," in *IEEE Int. Instrum. Meas. Technol. Conf. (I2MTC), Houston, TX, USA*, May 2018, pp. 1–6.
- [119] E. Caro Huertas, A. J. Conejo Navarro, and R. Mínguez Solana, "Power-system state estimation considering measurement dependencies," *IEEE Trans. Power Syst.*, vol. 24, no. 4, pp. 1875–1885, Nov. 2009.
- [120] G. Valverde Mora, A. T. Sarić, and V. Terzija, "Stochastic monitoring of distribution networks including correlated input variables," *IEEE Trans. Power Syst.*, vol. 28, no. 1, pp. 246–255, Feb. 2013.
- [121] C. Muscas, M. Pau, P.A. Pegoraro, and S. Sulis, "Effects of measurements and pseudomeasurements correlation in distribution-system state estimation," *IEEE Trans. Instrum Meas.*, vol. 63, no. 12, pp. 2813–2823, Dec. 2014.
- [122] N. M. Manousakis, G. N. Korres, and P. S. Georgilakis, "Taxonomy of PMU placement methodologies," *IEEE Trans. Power Syst.*, vol. 27, no. 2, pp. 1070–1077, May 2012.

Bibliography

- [123] IEEE PES, “IEEE standard for synchrophasor measurements for power systems,” 2011, IEEE Standard C37.118.1-2011.
- [124] —, “IEEE standard for synchrophasor data transfer for power systems,” 2011, IEEE Standard C37.118.2-2011.
- [125] G. E. P. Box and G. M. Jenkins, *Time-Series Analysis: Forecasting and Control*. San Francisco, CA, USA: Holden-Day, 1970.
- [126] D. Belega and D. Petri, “Accuracy analysis of the multicycle synchrophasor estimator provided by the interpolated dft algorithm,” *IEEE Trans. Instrum Meas.*, vol. 62, no. 5, pp. 942–953, May 2013.
- [127] G. Frigo, D. Colangelo, A. Derviškić, M. Pignati, C. Narduzzi, and M. Paolone, “Definition of accurate reference synchrophasors for static and dynamic characterization of pmus,” *IEEE Trans. Instrum. Meas.*, vol. 66, no. 9, pp. 2233–2246, Sep. 2017.
- [128] R. G. Brown and P. Y. C. Hwang, *Introduction to Random Signals and Applied Kalman Filtering*, 4th ed. Hoboken, NJ, USA: Wiley, 2012.
- [129] H. W. Sorenson, “Least-squares estimation: From Gauss to Kalman,” *IEEE Spectr.*, vol. 7, no. 7, pp. 63–68, Jul. 1970.
- [130] J. R. Magnus and H. Neudecker, “Matrix differential calculus with applications in statistics and econometrics,” 1999.
- [131] D. Simon, *Optimal State Estimation: Kalman, H_∞ , and Nonlinear Approaches*. Hoboken, NJ, USA: John Wiley & Sons, 2006.
- [132] J. N. Mendel, “Computational requirements for a discrete Kalman filter,” *IEEE Trans. Autom. Control*, vol. 16, no. 6, pp. 748–758, Dec. 1971.
- [133] National Instruments, “NI cRIO-9033,” 2019, user manual.
- [134] Xilinx, *7 Series DSP48E1 Slice*, 2016, user guide UG 479 (Version 1.9).
- [135] W. H. Kersting, “Radial distribution test feeders,” *IEEE Trans. Power Syst.*, vol. 6, no. 3, pp. 975–985, Aug. 1991.
- [136] M. Pignati, M. Popovic, S. Barreto, R. Cherkaoui, G. D. Flores, J.-Y. Le Boudec, M. Mohiuddin, M. Paolone, P. Romano, S. Sarri, T. Tesfay, D.-C. Tomozei, and L. Zanni, “Real-time state estimation of the EPFL-campus medium-voltage grid by using PMUs,” in *Proc. IEEE PES Innov. Smart Grid Tech. Conf. (ISGT)*, Washington, DC, USA, Feb. 2015, pp. 1–5.
- [137] IEC, “Instrument transformers. part 1: General requirements,” 2007, IEC Standard 61869-1:2007.
- [138] —, “Instrument transformers. part 2: Additional requirements for current transformers,” 2012, IEC Standard 61869-2:2012.

-
- [139] —, “Instrument transformers. part 3: Additional requirements for inductive voltage transformers,” 2011, IEC Standard 61869-3:2011.
- [140] A. M. Kettner and M. Paolone, “A generalized index for static voltage stability of unbalanced polyphase power systems including Thévenin equivalents and polynomial models,” *IEEE Trans. Power Syst.*, accepted for publication, preprint available under <https://arxiv.org/abs/1809.09922>.
- [141] J. Rocabert, A. Luna, F. Blaabjerg, and P. Rodriguez, “Control of power converters in AC microgrids,” *IEEE Trans. Power Electron.*, vol. 27, no. 11, pp. 4734–4749, Nov. 2012.
- [142] W. W. Price, K. A. Wirgau, A. Murdoch, J. V. Mitsche, E. Vaahedi, and M. El-Kady, “Load modeling for power-flow and transient stability computer studies,” *IEEE Trans. Power Syst.*, vol. 3, no. 1, pp. 180–187, Feb. 1988.
- [143] L. M. Hajagos and B. Danai, “Laboratory measurements and models of modern loads and their effect on voltage stability studies,” *IEEE Trans. Power Syst.*, vol. 13, no. 2, pp. 584–592, May 1998.
- [144] A. J. Collin, “Advanced load modelling for power system studies,” Ph.D. dissertation, University of Edinburgh, Edinburgh, SCT, UK, 2013.
- [145] I. Džafić, M. Gilles, R. A. Jabr, B. C. Pal, and S. Henselmeyer, “Real-time estimation of loads in radial and unsymmetrical three-phase distribution networks,” *IEEE Trans. Power Syst.*, vol. 28, no. 4, pp. 4839–4848, Nov. 2013.
- [146] T. J. Overbye, “Effects of load modelling on analysis of power-system voltage stability,” *Int. J. Elect. Power Energy Syst.*, vol. 16, no. 5, pp. 329–338, Oct. 1994.
- [147] L. Reyes Chamorro, A. Bernstein, N. J. Bouman, E. Scolari, A. M. Kettner, B. Cathiard, J.-Y. Le Boudec, and M. Paolone, “Experimental validation of an explicit power-flow primary control in microgrids,” *IEEE Trans. Ind. Informat.*, vol. 14, no. 11, pp. 4779–4791, Nov. 2018.
- [148] L. E. Reyes Chamorro, W. Saab, R. Rudnik, A. M. Kettner, M. Paolone, and J.-Y. Le Boudec, “Slack selection for unintentional islanding: Practical validation in a benchmark microgrid,” in *Proc. Power Syst. Comput. Conf. (PSCC), Dublin, L, IE*, Jun. 2018, pp. 1–7.
- [149] P. Romano and M. Paolone, “Enhanced interpolated DFT for synchrophasor estimation in FPGAs: Theory, implementation, and validation of a PMU prototype,” *IEEE Trans. Instrum. Meas.*, vol. 63, no. 12, pp. 2824–2836, May 2014.
- [150] National Instruments, “NI cRIO-9068,” 2016, user manual.
- [151] LEM, “Voltage transducer CV 3-1000,” 2017, datasheet.
- [152] —, “Current transducer LF 205-S/SP1,” 2017, datasheet.

Bibliography

- [153] Trimble, “Bullet III GPS antenna,” 2015, datasheet.
- [154] A. Derviškić, P. Romano, M. Pignati, and M. Paolone, “Architecture and experimental validation of a low-latency phasor data concentrator,” *IEEE Trans. Smart Grid*, vol. 9, pp. 2885–2893, Jul. 2018.
- [155] A. Bernstein, L. E. Reyes Chamorro, J.-Y. Le Boudec, and M. Paolone, “A composable method for real-time control of active distribution networks with explicit power set-points. part i: Framework,” *Elect. Power Syst. Research*, vol. 125, pp. 254–264, 2015.
- [156] L. E. Reyes Chamorro, A. Bernstein, J.-Y. Le Boudec, and M. Paolone, “A composable method for real-time control of active distribution networks with explicit power set-points. part ii: Implementation and validation,” *Elect. Power Syst. Research*, vol. 125, pp. 265–280, 2015.
- [157] Tekron, “TTM 01-G compact substation clock,” 2019, datasheet.
- [158] G. Strang, *Linear Algebra and its Applications*, 4th ed. Boston, MA, USA: Cengage, 2005.
- [159] T. H. Kerr, “Fallacies in computational testing of matrix positive definiteness/semidefiniteness,” *IEEE Trans. Aerosp. Electron. Syst.*, vol. 26, no. 2, pp. 415–421, Mar. 1990.
- [160] D. London, “A note on matrices with positive definite real part,” *Proc. AMS*, vol. 82, pp. 322–324, Jul. 1981.
- [161] K. Fan, “Generalized Cayley transforms and strictly dissipative matrices,” *Lin. Alg. Applicat.*, vol. 5, no. 2, pp. 155–172, 1972.
- [162] R. A. Horn and C. R. Johnson, *Matrix Analysis*, 2nd ed. Cambridge, ENG, UK: Cambridge Univ. Press, 2012.
- [163] F. Zhang, *The Schur Complement and its Applications*. Berlin, BER, DE: Springer, 2006.
- [164] A. Graham, *Kronecker Products and Matrix Calculus with Applications*. Mineola, NY, USA: Dover Publications, 1981.
- [165] C. R. Paul, *Analysis of Multiconductor Transmission Lines*. Hoboken, NJ, USA: Wiley, 2008.
- [166] A. Borghetti, F. Napolitano, C. A. Nucci, F. Rachidi, and M. Rubinstein, “Telegrapher’s equations for field-to-transmission-line interaction,” in *Advanced Techniques for Power System Modelling, Control and Stability Analysis*, F. Milano, Ed. Stevenage, ENG, UK: IET, 2016, ch. 1, pp. 3–44.
- [167] M. J. Heathcote, *The Johnson & Phillips Transformer Book*, 13th ed. Oxford, ENG, UK: Newnes, 2007.
- [168] Y. Tokad and M. B. Reed, “Criteria and tests for realizability of the inductance matrix,” *Trans. AIEE, Part I: Commun. Electron.*, vol. 78, no. 6, pp. 924–926, Jan. 1960.

- [169] J. J. Grainger and W. D. Stevenson, *Power System Analysis*. New York City, NY, USA: McGraw-Hill, 1994.
- [170] K. T. Compton, *Magnetic Circuits and Transformers*. Cambridge, MA, USA: MIT Press, 1943.
- [171] S. Gerbex, R. Cherkaoui, and A. J. Germond, "Optimal location of multi-type FACTS devices in a power system by means of genetic algorithms," *IEEE Trans. Power Syst.*, vol. 16, no. 3, pp. 537–544, Aug. 2001.
- [172] R. Roeper, *Short-Circuit Currents in Three-Phase Systems*, 2nd ed., F. Mitlehner, B. Ehmcke, and A. Webs, Eds. München, BY, DE: Siemens, 1985.

Andreas Martin Kettner

EPFL-STI-IEL-DESL
Station 11
CH-1015 Lausanne

Office: ELL 037
Phone: +41 21 693 41 62
E-Mail: andreas.kettner@epfl.ch

Curriculum Vitae



Personal Details

Name	Andreas Martin Kettner
Date of birth	21.07.1989
Hometown	Zürich
Citizenship	Swiss

Education

- 01/2015 – 06/2019 **Swiss Federal Institute of Technology in Lausanne (EPF Lausanne)**
DISTRIBUTED ELECTRICAL SYSTEMS LABORATORY (PROF. MARIO PAOLONE)
Doctor of Science
Ph.D. thesis:
*Real-Time State Estimation and Voltage Stability Assessment of Power Grids:
From Theoretical Foundations to Practical Applications*
Fields of research:
- Power system automation
 - Real-time state estimation
 - Real-time voltage stability assessment
- 05/2013 – 12/2013 **Swiss Federal Institute of Technology in Zürich (ETH Zürich)**
POWER SYSTEMS LABORATORY (PROF. GÖRAN ANDERSSON)
Master of Science
M.Sc. thesis:
Negotiated Predictive Dispatch with Power Node Unit Participants
Fields of research:
- Optimum dispatch / optimal power flow
 - Locational marginal pricing
 - Model predictive control
- 09/2008 – 12/2013 **Swiss Federal Institute of Technology in Zürich (ETH Zürich)**
DEPARTMENT OF ELECTRICAL ENGINEERING AND INFORMATION TECHNOLOGY
Master/Bachelor Studies

Andreas Martin Kettner

EPFL-STI-IEL-DESL
Station 11
CH-1015 Lausanne

Office: ELL 037
Phone: +41 21 693 41 62
E-Mail: andreas.kettner@epfl.ch

Work Experience

02/2014 – 12/2014

Supercomputing System AG

DEPARTMENT FOR ENERGY SYSTEMS (MR. STEPHAN MOSER)
Development Engineer

Activities:

- Modeling and analysis of power and energy systems
- Development of simulation software
- Supervision of semester projects and diploma theses

09/2011 – 06/2012

Swiss Federal Institute of Technology in Zürich (ETH Zürich)

ELECTRONICS LABORATORY (PROF. GERHARD TRÖSTER)
Assistant Researcher

Activities:

- Data acquisition and analysis with multi-modal hearing aids
- Usability tests with hearing-impaired people

10/2012 – 04/2013

Supercomputing Systems AG

DEPARTMENT FOR ENERGY SYSTEMS (MR. STEPHAN MOSER)
Student Apprentice

Activities:

- Study of the Swiss electricity sector
- Development of simulation software

Language Skills

German	Native speaker
English	Excellent written and oral command
French	Excellent written and oral command

Awards & Honors

01/2018

International Journal of Electrical Power and Energy Systems (IJEPES)

2017 BEST REVIEWER
Editor-in-Chief: Prof. Vladimir Terzija

02/2009

Swiss Youth in Science (Schweizer Jugend Forscht)

1ST INTERNATIONAL SWISS TALENT FORUM (ISTF)
Topic: The Energy Challenge

05/2008

Swiss Federal Institute of Technology in Zürich (ETH Zürich)

EXHIBITION OF MATURA PROJECTS IN SCIENCE AND ENGINEERING
Title: Construction of a Boat with a Magnetohydrodynamic Propulsion System
and of a Measurement Unit

Publications

Journal Papers

- [1] [A. M. Kettner](#) and M. Paolone, *A Generalized Index for Static Voltage Stability of Unbalanced Polyphase Power Systems including Thévenin Equivalents and Polynomial Models*, IEEE Transactions on Power Systems, 2019 (accepted for publication).
- [2] [A. M. Kettner](#) and M. Paolone, *On the Properties of the Compound Nodal Admittance Matrix of Polyphase Power Systems*, IEEE Transactions on Power Systems, vol. 34, no. 1, pp. 444-453, 2019.
- [3] L. E. Reyes Chamorro, A. Bernstein, N. J. Bouman, E. Scolari, [A. M. Kettner](#), B. Cathiard, J.-Y. Le Boudec, and M. Paolone, *Experimental Validation of an Explicit Power-Flow Primary Control in Microgrids*, IEEE Transactions on Industrial Informatics, vol. 14, no. 11, pp. 4779-4791, 2018.
- [4] [A. M. Kettner](#) and M. Paolone, *Sequential Discrete Kalman Filter for Real-Time State Estimation in Power Distribution Systems: Theory and Implementation*, IEEE Transactions on Instrumentation and Measurement, vol. 66, no. 9, pp. 2358-2370, 2017.

Letters

- [5] [A. M. Kettner](#) and M. Paolone, *On the Properties of the Power Systems Nodal Admittance Matrix*, IEEE Transactions on Power Systems, vol. 33, no. 1, pp. 1130-1131, 2018.

Conference Papers

- [6] [A. M. Kettner](#) and M. Paolone, *Performance Assessment of Kron Reduction in the Numerical Analysis of Polyphase Power Systems*, IEEE PES PowerTech Conference, Milano, Italy, June 2019 (accepted for presentation).
- [7] L. E. Reyes Chamorro, W. Saab, R. Rudnik, [A. M. Kettner](#), M. Paolone, and J.-Y. Le Boudec, *Slack Selection for Unintentional Islanding: Practical Validation in a Benchmark Microgrid*, Power Systems Computation Conference, Dublin, Ireland, June 2018.

Peer Review

- IEEE Transactions on Power Systems
- IEEE Transactions on Smart Grid
- IEEE Transactions on Power Electronics
- IEEE Transactions on Industrial Electronics
- IEEE Transactions on Industrial Informatics
- IEEE Transactions on Instrumentation and Measurement
- International Journal of Electrical Power and Energy Systems (Elsevier journal)
- Sustainable Energy, Grids, and Networks (Elsevier journal)
- Optimal Control: Applications and Methods (Wiley journal)

